Metal-Organic Frameworks and Related Composites for Molecular Storage, Separation, and Water Harvesting

A Thesis Submitted for the Degree of

Doctor of Philosophy

by

Subhajit Laha

JNCASR

Chemistry and Physics of Materials Unit (CPMU)

Jawaharlal Nehru Centre for Advanced Scientific Research

(A Deemed University)

Bangalore-560064

September 2021

Dedicated to 'Molecular Materials Laboratory' on the occasion of XV anniversary celebration.

DECLARATION

I hereby declare that the matter embodied in the thesis entitled **"Metal-Organic Frameworks and Related Composites for Molecular Storage, Separation, and Water Harvesting"** is the result of investigations carried out by me at the Chemistry and Physics of Materials Unit, Jawaharlal Nehru Centre for Advanced Scientific Research, Bangalore, India, under the supervision of Prof. Tapas K. Maji and that it has not been submitted elsewhere for the award of any degree or diploma.

In keeping with the general practice in reporting the scientific observations, due acknowledgment has been made whenever the work described is based on the findings of other investigators. Any omission that might have occurred due to oversight or error in judgment is regretted.

Subhajit Laha

Subhajit Laha

Date: 07-09-2021

Place: Bangalore

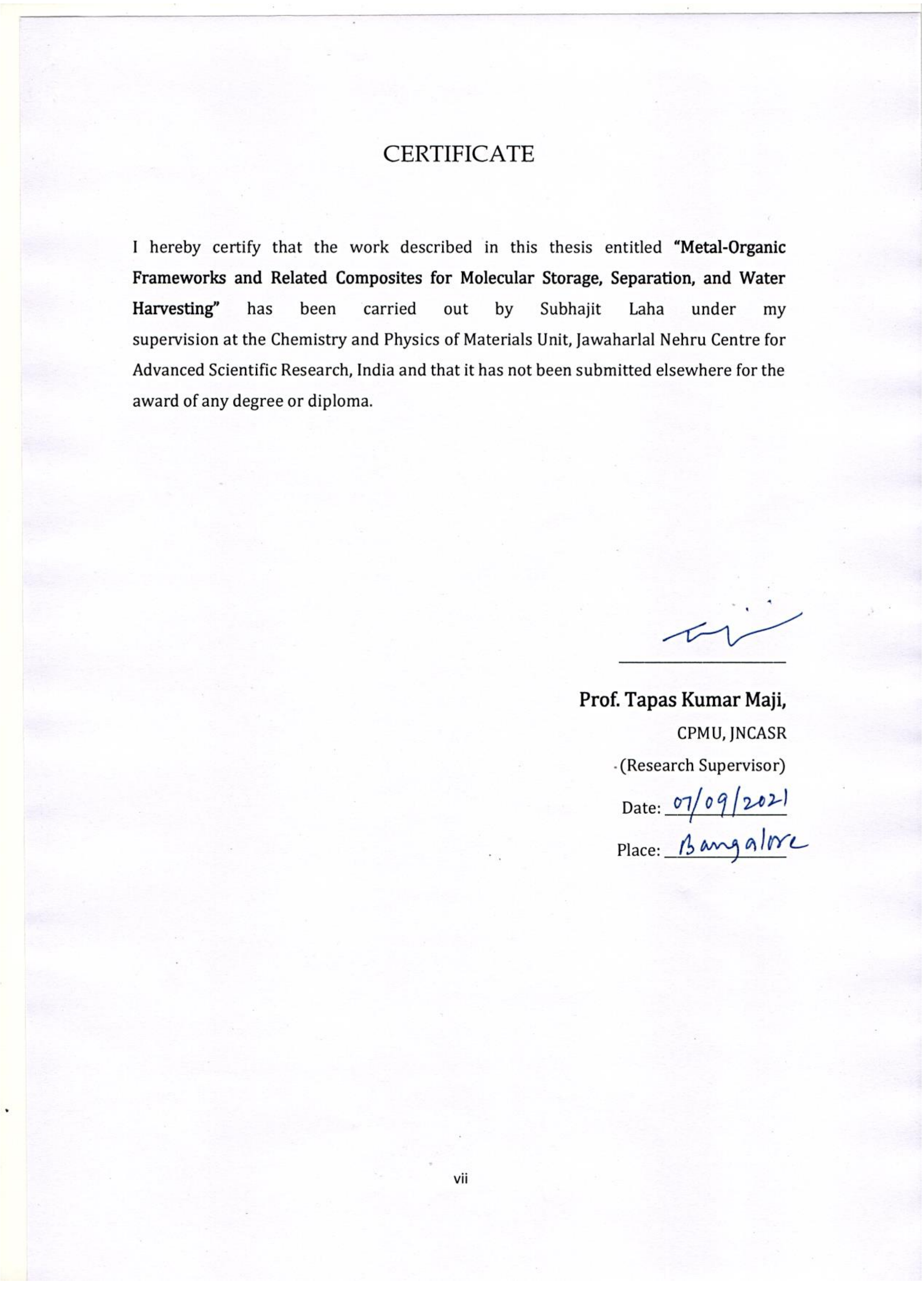

CERTIFICATE

I hereby certify that the work described in this thesis entitled **"Metal-Organic Frameworks and Related Composites for Molecular Storage, Separation, and Water Harvesting"** has been carried out by Subhajit Laha under my supervision at the Chemistry and Physics of Materials Unit, Jawaharlal Nehru Centre for Advanced Scientific Research, India and that it has not been submitted elsewhere for the award of any degree or diploma.

Prof. Tapas Kumar Maji,
CPMU, JNCASR
(Research Supervisor)
Date: 07/09/2021
Place: Bangalore

ACKNOWLEDGEMENTS

I wish to express sincere gratitude to my supervisor Prof. Tapas Kumar Maji for his constant guidance, mentoring, and encouragement. He has provided the freedom to indulge my ideas and facilitated me to inculcate a strong sense of dedication. I am thankful to him for allowing me to work under his guidance.

I thank Prof. C. N. R. Rao, FRS, who has been a constant source of inspiration.

I express my sincere thank to the past and present chairman of CPMU: Prof. Chandrabhas Narayana and Prof. A. Sundaresan for allowing me to avail myself the facilities of the Centre and also for motivating me all through.

I am thankful to all my Ph.D. course instructors: Prof. T. K. Maji, Dr. S. S. Agasti, Prof. S. J. George, and Prof. S. C. Peter, whose courses have been extremely helpful for carrying out the research work.

I am also greatly thankful to the technical staff members of JNCASR, namely, Mr. Anil, Mr. Vasu, Ms. Usha, Ms. Selvi, Mr. Mahesh, Mr. Deepak, Mr. Rahul and Mr. Shivakumar for their help with instruments and measurements.

I thank the JNCASR library, Computer Lab, Hostel, DG, IPMC, Dhanvantari, Security, Academic Section and Administrative Section for providing and maintaining the great facilities of the centre, which have made my life comfortable and easy in many ways during this journey.

I also thank my collaborators: Prof. Balasubramanian Sundaram, Prof. Chandrabhas Narayana, Prof. Eswaramoorthy Muthusamy, Prof. Rajamnai Krishna (University of Amsterdam), Mr. Nimish Dwarkanath, Dr. Abhishek Sharma, Dr. Kesavan Kamali, Dr. Sonu Kizhakkepura, who were always ready to discuss research issues and were always prompt in making quick communication of research work.

I am especially grateful to Prof. Diwakar S. V., for the technical discussions regarding water harvesting device fabrication and Mr. Moorthy, Mr. Shivananda (Prateetya Electronics) and Mr. Rajkumar, Mr. A. Srinivas from JNCASR for fabricating harvesting and high-pressure moisture capture device.

I am thankful to Mr. Yogesh, Mr. Vikash, Mr. Sandeep and Mr. Zubin (Ingersoll Rand/ Trane Technology) for promoting concept of dehumidification by utilizing our material and contributing in the fabrication of high-pressure moisture capture prototype.

I am grateful to Mr. S. P. Pal (Anton-Paar), Mr. K. Viswanathan (Metrohm) and Mr. Guruprasad D. (Agilent) for technical support, whenever I faced hurdles with tackling instruments especially during pandemic days.

I want to convey my heartfelt gratitude to the amazing past and present members of the Molecular Materials Lab. I owe a lot to my seniors Dr. Suresh, Dr. Nivedita, Dr. Syamantak, Dr. Papri, Dr. Sohini and in particular Dr. Anindita and Dr. Papri who have taught me the way to understand research during my early days. I am also grateful to Parul, Sanchita, Faruk, Anupam, Rohan, Tarak, Adrija, Argha, Tarandeep, Alolika, Mrinal, Sneha, Dr. Ashish, Dr. Rambabu, Dr. Debabrata, Dr. Subarna, Dr. Vasu, Dr. Soumitra, Dr. Sandip, Dr. Kamal, Dr. Siddhartha, Dr. Sajad, and Dr. Chayanika for providing a wonderful working atmosphere. I want to thank the very enthusiastic summer/project students, particularly Sweeny and Subhajit, who worked with me at various times.

My special thanks to Dr. Arpan and Dr. Ritesh for helping me with various research hurdles. Although we haven't shared the same lab time, their wisdom enriched me a lot.

I am deeply indebted to my alma maters Serampore Union Institution, Scottish Church College, Kolkata and IIT Hyderabad whose lessons I shall carry with me all through my life.

My friends from IIT, college, school and colony deserve a special mention.

I thank Supriti Madam for always being a lovely host and Neel-Sonai for their love.

I thank my friends from Cricket, Badminton and Bengali drama group in JNCASR. A special mention to Koyel, Subham, Biswanath, Arka, Moinak, Monodeep, Sourav, Satyajit, Niloy, Arindam, Paribesh, Saikatda, Soumalyada and many others.

Last, but not least, my warm and heartfelt thanks go to my family for their tremendous support and hope they had given to me. Cordial honor to my parents, Srikanta Laha and Snigdha Laha for their sacrifices which allowed me to carry out research in Bangalore with a peaceful mind.

PREFACE

The thesis has been organized into five chapters that describe various metal-organic frameworks and related composites for multifarious applications such as storage, separation, and water harvesting. Different MOFs and composites have been synthesized with different ligands through conventional and alternative approaches to avail hierarchy in pore geometry, diversity in structural architecture, and composition towards wide applicability.

Chapter 1 provides a brief introduction to MOF in terms of their structure and applications. This chapter has been classified into three sub-categories. The first segment discloses three types of hierarchy in MOFs, comprising hierarchy in pores, architectural hierarchy, and compositional hierarchy. It also identifies current as well as conventional approaches to MOF preparation and the recent application in the environmental domain with a brief roadmap for future research.

Chapter 2 comprises the novel strategy for designing hierarchical micro-mesoporous metal-organic frameworks and their different applications.

Chapter 2.1 describes a unique methodology of combining perturbation-assisted nanofusion (PNF) with microwave (MW) stimuli to generate wide additional pores from (5−18) nm in the prototype microporous MOF, NiMOF-74. An optimized combination of microwave exposure, perturbation in form of stirring, and solvent effect induce additional mesoscale porosity by fusion of MOF nanoparticles. The effect of microwaves is realized by varying reaction time and medium using a range of solvents having different dielectric constants. This additional mesopore, thus generated, has been utilized by encapsulating 4.6 μmol/g of large biomolecule Vitamin B_{12} (VB_{12}).

Chapter 2.2 demonstrates various hierarchical micro/mesoporous MOFs based on $\{[Al(\mu\text{-}OH)(1,4\text{-}NDC)]\cdot H_2O\}$ (Al-MOF) with tunable porosities (pore volume and surface area) have been synthesized by assembling Al(III) and 1,4-NDC (1,4-naphthalenedicarboxylate) under microwave irradiation by varying water/ethanol solvent ratio. Additional mesopore has been exploited for the stabilization of $MAPbBr_3$ (MA=methylammonium) perovskite quantum dots (PQDs).

Chapter 3 exclusively deals with aliphatic and aromatic hydrocarbon separation with real-time column/membrane breakthrough experiments under the vapor and liquid phase.

Chapter 3.1 puts forward the synthesis and characterization of Al-MOF by modulating reaction time under microwave to achieve maximum surface area. The framework shows excellent light hydrocarbon adsorption performance under ambient conditions. Further, due to the interplay of strong and week Lewis-acid base interaction between metal center and adsorbate, it shows captivating stepwise dynamic column breakthrough separation for bi-component (CH_4/CO_2, CH_4/C_2H_6, C_2H_2/CO_2, C_2H_4/C_2H_6) and multi-component ($CO_2/CH_4/C_2H_4/C_2H_6$, $CO_2/C_2H_2/C_2H_4/C_2H_6$) mixture combinations. It further reports the fabrication of MOF-based mixed matrix membrane for H_2/ CO_2 and CO_2/CH_4 separation.

Chapter 3.2 reports the synthesis of a novel three-dimensional Ni-based metal−organic framework $\{[Ni_4(\mu_3\text{-}OH)_2(\mu\text{-}H_2O)_2(1,4\text{-}ndc)_3](3H_2O)\}_n$. The 1D pore channel decorated with unsaturated pore center and pendent oxygen atoms of the ndc-ligand shows gate opening type abrupt adsorption for polar CO_2, but not for other non-polar hydrocarbons like C_2H_2 and CH_4. The selectivity study of CO_2 and C_2H_2 is extremely challenging due to their similar kinetic diameter and this separation is rarely ported. The hydrophilic pore environment leads the inverse selectivity of CO_2 over C_2H_2 as studied through dynamic column breakthrough separation.

Chapter 3.3 demonstrates "dynamic chemical clip" in a supramolecular framework ([Zn(o-phen)(2,6-ndc)·DMF] (o-phen = 9,10-phenantholine, 2,6-ndc = 2,6-naphthalenedicarboxylate, DMF = N,N'-dimethylformamide)) capable of thermodynamic and kinetics-based chemical separation. The far-reaching competency was revealed by BTEX (benzene, toluene, ethylbenzene, *o/m/p*-xylene) and associated alkyl aromatic (styrene-ethylbenzene, benzene-toluene, benzene-cyclohexane) separation through a cooperative experimental and computational approach.

Chapter 4 is partitioned into two sub-chapters, both containing the construction of nano MOF composite and customized device fabrication for adsorbing moisture under ambient and high-pressure conditions.

Chapter 4.1 introduces an atmospheric water generation (AWG), beyond the arid region, under indoor humidity and temperature regime. It demonstrates a ternary MOF nanocomposite with enhanced hydrothermal stability with 63.4% of utmost water harvesting efficiency by blending aminoclay (Aminopropyl-functionalized magnesium phyllosilicate) and graphene with MOF. The study further extrapolates the water collection dynamics by varying ambient humidity, release temperature, and on-demand sorption/desorption cycle under the ordinary indoor condition without any solar irradiation with a maximum value of 0.445 L/g indoor water collections per day.

Chapter 4.2 unfolds the design and manifestation of a prototype device based on MOF (UiO-66; prepared through both solvothermal and microwave conditions) and MOF-composite (UiO-66@Aminoclay) that captures moisture from compressed air under ambient to 7 Bar pressure. The device exhibits a 54 % improvement in operational time and a 44% increase in moisture sorption efficiency (5.42 g/m^3 of moisture capture per gram of material) in comparison to commercially used activated alumina.

Chapter 5 summarizes the entire thesis work. It also contains a discussion about future work that can be done taking the concepts and methods given in the thesis.

|| Table of Contents ||

Hydrocarbon Capture, Separation and Purification

An Adsorbate Biased Dynamic 3D Porous Framework for Inverse CO_2 Sieving over C_2H_2

Water-Energy Nexus: Storage, Harvesting and Dehumidification

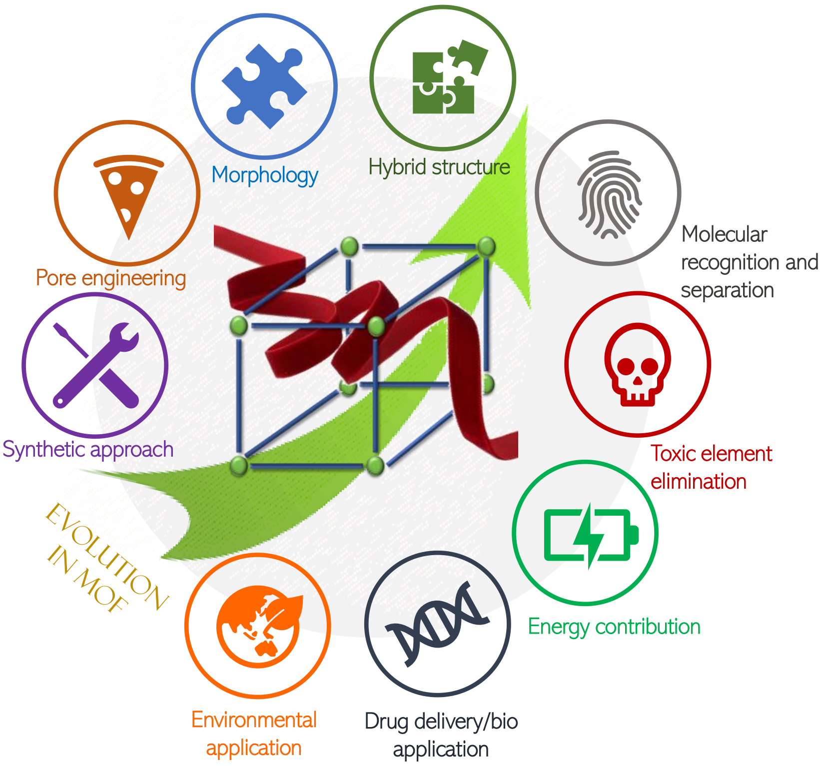

Chapter 1

Introduction

Evolution in MOF: an overview

The reticular chemistry of metal-organic frameworks (MOFs), or porous coordination polymers (PCPs), has developed an emerging class of porous material to address global energy and environmental issues.[1] They are commonly constructed by assembling molecular structural blocks such as secondary building units (SBU), metal cation salts or inorganic clusters and polydentate organic linkers through strong coordination-type interactions.[2] Explicitly, the understanding of MOFs has reached a certain stage such that the careful selection of constituents and the interplay between structure and desired properties allow the MOF to be chemically rehabilitated for use in storage, separation, purification, delivery and catalysis, among other applications.[3]

The first attempt in this field was carried out by Kitagawa *et al.* by demonstrating the gas storage properties in porous coordination polymers.[4] Followed by this work, in 1999, Yaghi and co-workers reported robust MOFs, MOF-5 and HKUST-1 with permanent porosity as well as different net topology and pore environment.[2d, 5] Employing the simple "node-and-linker" approach originated by using organic linkers of similar geometry but different lengths and functional groups, families of isoreticular MOFs (IRMOFs)[2c, 6], ZIFs,[7] MILs,[8] MCFs,[9] UiO,[10] series can be derived and further design of organic linkers resulted in mesoporous or macroscopic frameworks with cage-like structures.[11] Consequently, the MOF's surface area can typically vary from hundreds to the currently reported ultrahigh surface area of 10,577 m^2g^{-1}[12] with pore size ranging from angstroms to nanometers.

This chapter will concisely discuss how unique design strategies and different synthetic approaches of MOFs can be utilized to impart materials' functionalities for improving performance and fundamental understanding in addressing environmental concerns. The chapter has been classified into three sub-categories. The first segment discloses three types of hierarchy in MOFs, comprising hierarchy in pores, architectural hierarchy and compositional hierarchy. Then, the current and conventional approaches to MOF preparations have been identified. Finally, this chapter will be concluded with the recent application of MOFs in the environmental domain with a brief roadmap for future research (Scheme 1).

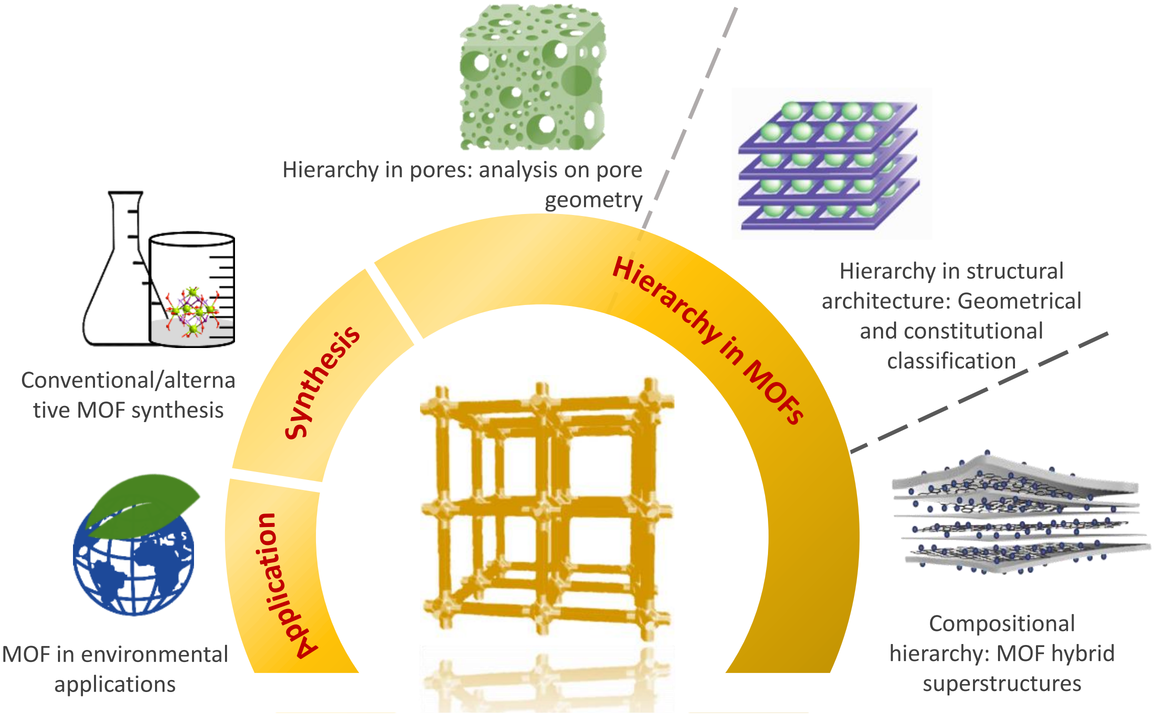

Scheme 1: Evolution in MOF: Hierarchy in pore, architecture and composition with synthetic approach and environmental applications.

1.1: Structural engineering: hierarchy in MOFs

The hierarchy of materials on porosity, structure, composition and morphology is the key element for high performance and wide applicability. Here, this segment portrays the conceptual outlook of hierarchy into the design approach of metal-organic framework (MOF) materials. Starting with a background and utility of the pores at a molecular length scale, this chapter will further discuss the geometrical and constitutional divisions of structural architecture and their synergistic combination with other functional components.

1.1.1: Hierarchy in pores

Presently, research on the evolution of hierarchically porous materials is of great interest due to enhanced versatile application in separation, catalysis, delivery and energy storage.[13] Hierarchically porous structures are usually found in living creatures such as diatom, butterfly, leaf etc., and are of key importance to achieve functional adaptation of the structure at all levels of hierarchy (Figure 1a). According to IUPAC, pores are designated as micro (pore widths less than 2 nm), meso (widths between 2 to 50 nm) and as macropores (beyond 50 nm widths).[14] In the case of a hierarchical porous system, micropores contribute to the overall surface area, while meso and macropores provide the required accessibility of larger molecules through faster diffusion or mass transfer kinetics. To date, most of the reported MOFs are microporous, and augmentation of their pores to the mesoscale range remains a formidable challenge. Several attempts have been made to introduce hierarchical porosity in MOFs, the first can be either intrinsically formed by the assembly of building blocks commonly known as ligand extension method[15] or by template-assisted synthesis.[16] In the former case, the material exhibits intrinsic mesopores by extending the length of the linear organic linker.[17] At the same time, the expanded framework either became fragile upon guest (or solvent) removal or often yield interpenetrating structures with small pore size aperture.[15b, 18] On the other hand, hierarchical MOF structures were obtained by assembling a template directing amphiphilic molecule or surfactant with metal nodes and ligand building blocks.[19] Upon calcination, solvent extraction or hydrolysis, the template is partially or completely removed leaving mesopores in the crystals/frameworks.[20] However, such methods are ridden with drawbacks like irregular pore structure with disordered pore distribution, energy-inefficient high-temperature template extraction, time-consuming and the multi-step synthetic methodology that hinders upscale production of hierarchical MOFs. Such drawbacks encourage the scientific community to design a parallel approach for designing hierarchical MOFs by neglecting ligand-extension as well as template-assisted technique. The template-free strategy typically depends on the solvent (more precisely; solvent functionality, polarity and concentration) and associated reaction parameters to obtain structural bimodality within MOF. All these methods can be broadly categorized into two classes, namely, direct and indirect solvent contribution methods. Developing bimodality within MOF pores through solvents/solvent-adjustment method,[21] hydrolytic transformation route,[22] ionic liquid/supercritical CO_2 emulsion route,[23] or CO_2-expanded liquids as switchable solvents[24] are considered under the first type, whereas the latter includes acid-base adjustment routes,[25] microwave heating process,[26] perturbation assisted nano-fusion method.[21c, 27] While the indirect solvent method mostly induces random mesopore generation with a wide pore size distribution, direct solvent participation can restrict the mesopore dimension and adjust it depending on solvent size and functionality. Credibly, for the class of indirect solvent method, solvent acted as a subordinate leading factor, whereas other modulators such as metal–ligand additional coordination, microwave stimuli, and fusion of neonate nanoparticles

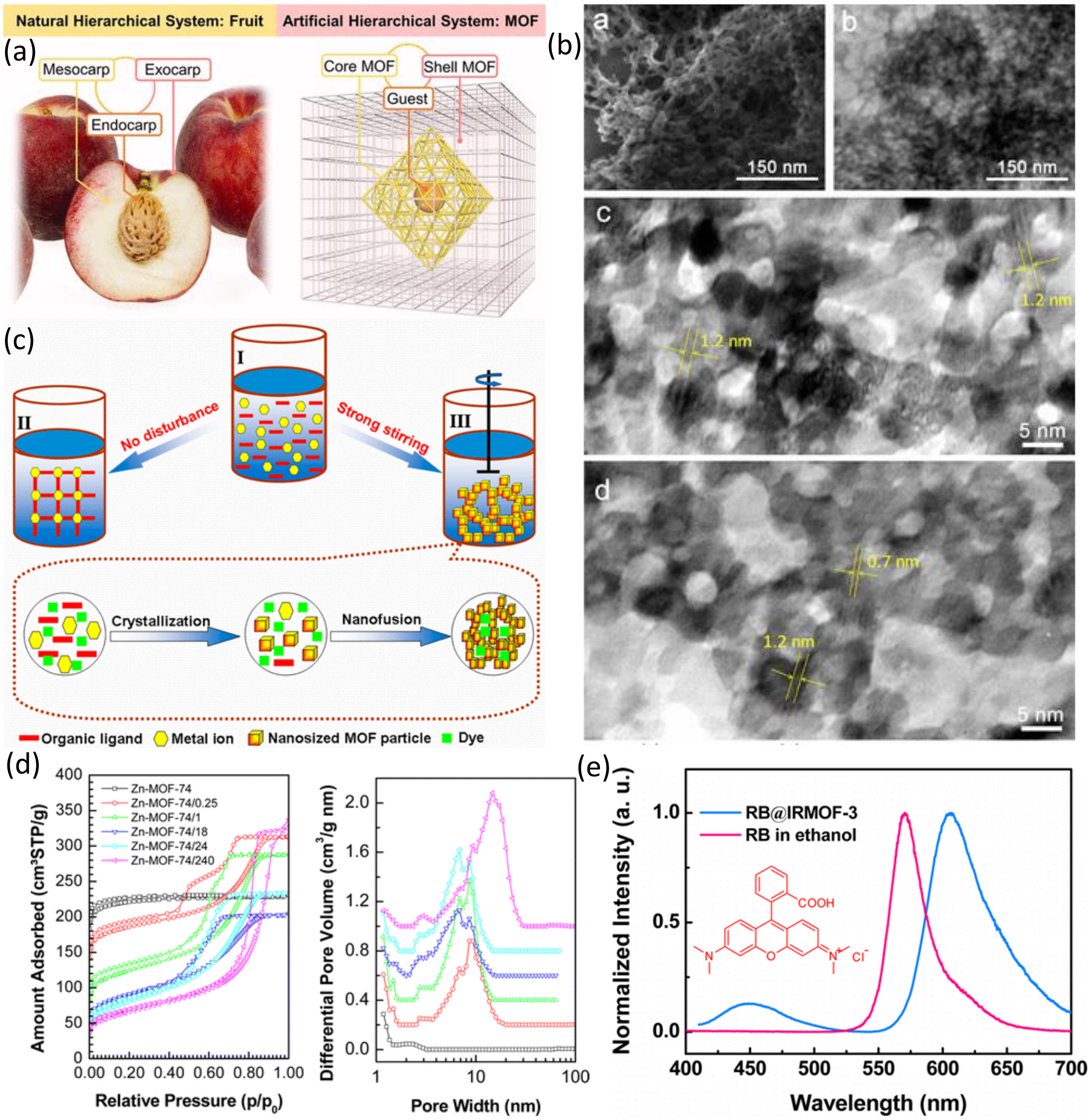

Figure 1: (a) Schematic representation of a natural peach with an artificial MOF that is arranged as a core-shell system. (b) Morphology of one representative hierarchical MOF, Zn-MOF-74. Lattice fringes are highlighted in yellow (a-d). (c) Illustrative mechanism of PNF synthesis of hierarchical MOF with encapsulated large dye molecule. (d) N_2 adsorption isotherm at 77 K and corresponding pore size distribution exhibits structural bimodality and its change with perturbation time for microporous Zn-MOF-74 and Zn-MOF-74/t. (e) Emission spectra of encapsulated dye in hierarchical MOF. Reproduced from reference 27 with permission from the American Chemical Society.

played a crucial role to direct the dimensions of mesopores. Nevertheless, for the class of direct solvent method, the solvent is majorly responsible for inducing mesopores, which is evident in the successful formation of ordered and controllable mesopores. One typical example to demonstrate the beneficial integration of mesoporosity within one benchmark microporous MOF (e.g., MOF-74, IRMOF) for the encapsulation of large dye molecule (Figure 1).[28] During MOF synthesis, strong stirring as perturbation has been introduced that restricts the formation of large crystals that would occur without stirring (Figure 1b-d). The kinetic preference over the formation and dissolution of SBUs, induced system perturbation which played the key role for the development and aggregation of small polymorphic microporous crystals, termed as nanofusion. Authors anticipated that the presence of keto functionality in solvent is responsible for generating random mesopores by pore etching and demonstrated remarkable dye uptake ability of bimodal MOF compared to microporous one (Figure 1e). Research on evolution of bimodal, multimodal or multivariate MOFs is still at an embryonic stage, creating the need for more sophisticated synthetic techniques towards formation of hierarchical MOFs, which can offer profound mechanistic understanding.

1.1.2: Architectural hierarchy

1.1.2.1: Geometrical classification

Recently, miniaturization of MOF down to the nanometre length scale regime attracts significant interest as it offers new prospects for application in microenvironments such as catalysis, sensing, drug delivery, diagnostics, light-harvesting, molecular sieving, sensing, etc.[29] By controlling the kinetics of nucleation and growth, designing their physical architecture rather than varying composition, MOF superstructures with distinct morphology can be prepared. In this brief outlook, the discussion has been restricted to extended metal-organic structures, crystalline or non-crystalline, constructed from the supramolecular assembly of inorganic and organic (organic ligand/polymer/biomolecule) units by regulating crystallization condition and other accompanying reaction environments. The term ‘nanoscale’ is mostly used for the crystal size between 1 to 100 nm, while for some special cases it could be extended up to 1000 nm depending on size and shape-dependent properties and characteristics.[30]

Hence, such materials have been classified in four dimensionalities: (a) zero-dimension characterized as nanoparticles and hollow microspheres, (b) one-dimensional architecture such as fibre, tube or rod-type morphology, (c) two-dimensional architecture for instance layered structure, thin film or membrane, (d) three-dimensional architecture as continuous or extended system (Figure 2a-b).[31] From the

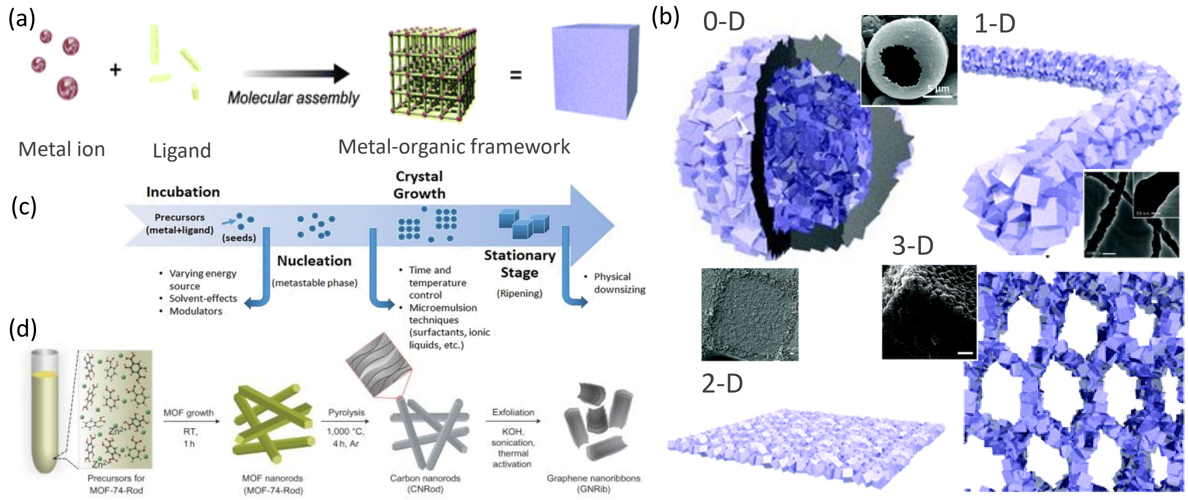

Figure 2: (a, b) Illustration of structuring MOF at different dimensionality. (c) Diagram summarizing the major steps of MOF downsizing. (d) Synthesis scheme of MOF-74-Rod, carbon nanorods and graphene nanoribbons. Adapted from reference 31 and 34 with permission from Springer Nature and Royal Society of Chemistry, respectively.

fundamental and applicatory point of view, 0-D and 1-D MOF nanostructures are found to be most promising as they could be further expanded by hydrogen bonding, π-π stacking, electrostatic and van der Waals interactions.[30-31] Synthetic strategy accounts for the most important parameter, the main challenge in structuring MOF superstructures has been in developing appropriate synthesis conditions that localize such coordination reactions within desired dimensionality and space. A class of the fascinating synthesis approaches, crystal downsizing, are categorized under the segment of 'top down' and 'bottom-up', by tailoring morphology, size distribution and pore accessibility (Figure 2c).[32] Liu *et al.* developed a strategy of synthesizing nanocarbons by heating secondary carbon precursor (FA, molecular dimensions $8.43 \times 6.44 \times 4.28$ Å^3) within the pores of MOF.[33] Adapting a similar methodology, Xu and co-workers moved beyond the limitation of MOF-derived carbon, allowing the greater varieties of morphology, from MOF to rod-shaped morphology to one-dimensional carbon nanorods (Figure 2d).[34] Finally, with high-temperature activation layered graphene nanostructures are formed with 2 to 6 sheets. Nevertheless, such top-down deconstruction technique was often followed for the generation of MOF nanosheets by integrating functional nanosheets such as clay minerals, layered double hydroxides or graphene derivatives.[35] Most recently, Kaskel and his group were able to identify timescale (*t-axis*) as an adjustable dimension in MOF and coined them as novel 4-D metal-organic frameworks by engineering spatio-temporal evolution within a dynamic framework.[36]

1.1.2.2: Constitutional classification

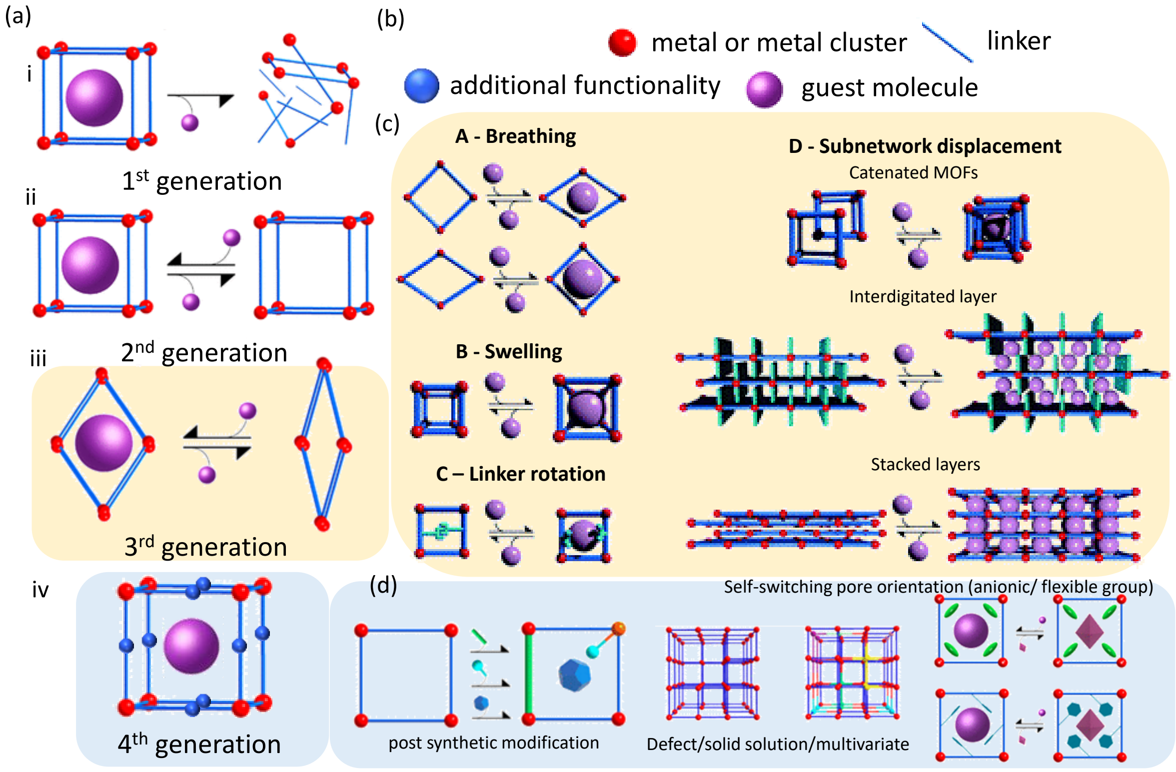

Figure 3: (a, b) Division of constitutional classification. Schematic representation of 1st (i), 2nd (ii), 3rd(iii) and 4th generation (iv) MOF. (c, d) Representative categories of 3rd and 4th generation of MOF. Represented in reference 42 and 52 with the permission from American Chemical Society and Royal Society of Chemistry, respectively.

In the late 90's, Kitagawa and Kondo classified MOFs primarily in three categories based on their structural response upon guest/solvent removal (Figure 3).[37] The 1st generation materials readily collapsed after guest removal and became nonporous. The 2nd generation possesses structural rigidity over guest removal and usually exhibits characteristics type-I adsorption isotherm profile. Generally, these materials show structural rigidity in presence of other external force fields such as temperature, interactions with light, mechanical stress, etc. and exhibit high surface area with great potential as storage material.[38] The 3rd generation of MOF was denoted as 'soft' since their framework demonstrates structural transformation with the removal of solvent, guest, template or under other external stimuli. Interpenetrated three dimensional as well as integrated and stacked two-dimensional frameworks are also conserved under the 'soft' category as they showed 'stepped' or 'S-shaped' isotherms.[39] Flexible MOFs consolidate the crystalline order of the coordination framework with amendable structural transformability and thus widely known as soft porous crystal (SPC).[40] Note that, any kind of structural or physical transition in particular crystal to crystal, crystal to amorphous, open pore to large, narrow or closed pore transformation are considered under this category. The versatility of flexible MOF was first conceptualized by Kitagawa *et al.*, published in 2004.[39c] In early days of MOF, these SPCs are exclusively used for the separation of gas, small molecules and molecular recognition due to characteristic gated or stepwise adsorption behavior.[41] The flexibility mode can be further classified as breathing, swelling, linker rotation and subnetwork displacement (Figure 3c).[42] Breathing is associated between two states (expansion and contraction), accompanied by a change in unit cell volume with atom displacement. This kind of flexibility is well-explored for MIL family ([M(bdc)(OH)]$_n$; where bdc stands for 1,4-benzenedicarboxylate and M could be any transition metal as Al, Fe, Cr, Sc, Ga, In). For instance, MIL-47(V) exhibited a remarkable difference in cell volume depending on the oxidation state of the metal centre. This material appeared to prevent oxidation of V^{III} to V^{IV}, yielding a material with composition $V^{III}(OH)(bdc)$.[43] The chromium version of MIL-53 (MIL-53(Cr)

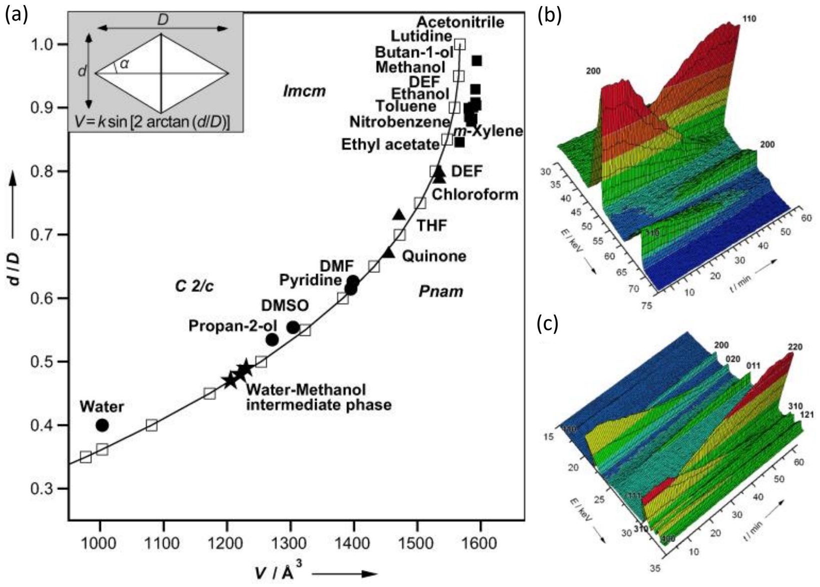

Figure 4: (a) Comparison of the theoretical evolution of the cell volume versus d/D (□ and —) with the experimental volumes associated with the changes of symmetry and space groups during swelling •, $C2/c$; ▴, *Pnam*; ▪, *Imcm*). Therefore, the ratio d/D of the two diagonals d (smallest distances between chains) and D characterizes the extent of breathing. (b) Evolution of powder X-ray pattern measured during the

uptake of lutidine by MIL-53(Fe), H_2O from the detector at a) $2\theta=1.495°$ and (c) $2\theta=4.340°$. The d spacing (Å) is related to the energy E (keV) by $E=6.11926/(d\sin\theta)$. Reprinted with permission[44]. ©2008. Willey Online Library.

$[Cr(OH)(COO_2)_2]_n$) is one of the most studied flexible MOF that changes dynamically with temperature. As-synthesized MIL-53, known as MIL-53*as*, contains terephthalate and solvent in the pore. After activating at 300 ˚C, the large pore framework was obtained (MIL-53*ht*) which upon further cooling yields narrow pore MIL-53*lt* due to adsorption of moisture. The structural transformation happens due to a change in the dihedral angle between SBU and linker as bdc is considered a rigid ligand. The calculated pore volume reduces approximately by 473.7 Å^3 from large to small pore.[45] Millange and co-workers studied the time-resolved diffraction studies of the breathing of MIL-53(Fe).[44] Initiating from the hydrated form, the sample was immersed and placed under synchrotron radiation, the solvent molecules are introduced drop-by-drop and corresponding powder X-ray patterns were collected to detect structural evolution of cell-volume exchange (Figure 4). Recently, Sikdar *et al.* demonstrated a reversible electron-transfer phenomenon in a redox active MOF, $[Zn_2(adc)_2(bpNDI)].7DMF.2H_2O]_n$, synthesized using adc and bpNDI as donor-acceptor pair, respectively.[46] It undergoes guest responsive structural transformation, rearranges donor and acceptor geometry to facile electron transfer in an unprecedented reversible fashion at room temperature. The wide collection of structure directing metal nodes and linker derivatives, the different architectural structure with building flexibility has been extensively studied from both practical and computational point of view and few synonymous terms that correlate with the phenomenon 'breathing' such as 'dynamic framework', 'accordion', 'spring or sponge like' have also been labeled by few authors. Gradual enlargement of unit cell volume by keeping shape and space group of the unit cell constant is considered is swelling.[42] One of the prototypical examples of this kind of flexibility is observed in MIL-88 family. The structure based on unit cell formula $M_3O(H_2O)_2X^{6+}$($M = Fe^{3+}$, Cr^{3+}; X = F, OH), are interconnected by fumaric acid (MIL-88A), dicarboxylic acid (MIL-88B), 2,6-naphthalenedicarboxylate (MIL-88C) or 4,4'-biphenyldicarboxylate (MIL-88D).[47] Starting from the activated structure of MIL-88A, the volume of unit cell increases from 1135 Å^3 to 1840, 1970, 2090 and 2110 Å^3 after soaking in n-butanol, ethanol, methanol and water, respectively.[48] The third category is linker rotation where the special alignment of the linker changed due to turning around a rotational axis. A variety of organic connectors with multiple carboxylate groups have been used to produce flexibility in MOF by bridging between inorganic building units. In particular, the simplest dicarboxylic ligand, 1,4-benzendicarboxylate or bdc, is utilized to construct various MOF for example MOF-5, Al-MOFs, [$Zn_2(BDC)_2$DABCO] and [$Cu_2(BDC)_2$DABCO] (DABCO = 1,4-diazabicyclo[2,2,2]octane).[2d, 49] By using solid-state NMR as a tool, Yaghi and others experimentally approximated the rotational energy of bdc in MOF-5 to be 47.3± 8.4 $kJmol^{-1}$, which was further confirmed by DFT calculations to be in the range of 51 to 62.8 $kJmol^{-1}$. The rotation of the pillar, eventually ends up in gating of the pore by opening the pore space and selectively adsorbs certain guest molecule depending upon size, shape, polarity and affinity towards the metal centre or inner pore environment. The final category of this flexible segment is subnetwork displacement. Such relocation is restricted to the systems, which are connected by non-covalent supramolecular interactions and as a result the subnet can relocate or shift in regard to each other. As for instance, a 2D bilayer threefold interpenetrated framework, ([$Cu(bpe)_{1.5}$(1,4-napdc)]$(H_2O)_n$ (bpe = 1,2-bis(4-pyridyl)ethane; 1,4-napdc = 1,4-naphthalenedicarboxilic acid) based on a mixed ligand system, while the interpenetrated nets are alleviated by C-H···π and π···π interactions. Such interpenetration induces reduction in pore aperture by allowing selective H_2O vapor diffusion by completely rejecting N_2, CO_2 and MeOH by the framework.[50] However, by altering adsorption sites, confining pore space or pore window, and also by matching the cavity of the framework to the targeted/eliminated species can be regulated.

The evolution of MOF further introduced a new segment, 'fourth generation MOF', first introduced by Liu *et al.*[51] They mostly defined such category under recently developed post-synthetic modification, largely considered under the umbrella of post-processed MOFs that can uphold underlying topology and structural integrity towards several post-modifications. In addition, other scientists such as Kitagawa, and Zaworotko, defined such materials by including MOFs affected by material anisotropy, structural defect and self-switching pore (anionic/functional group) orientation (Figure 3d).[37, 52] The field was pioneered by Lee and co-workers in the year of 1995 by developing a class of MOF-like solid consist of Ag(I) nodes and nitrile containing ligands.[53] In 2007, the term 'post-synthetic modification' was first introduced by Wang and Cohen to describe the reaction of IRMOF-3 with acetic anhydride.[54] Fourth generation MOFs are typically considered as a hybrid of 2nd and 3rd generations, highly triggering MOF catalysis to a new peak, possibly because diverse post-synthetic and post-functionalization strategies pave a novel path for catalytic reactions. The conceptual approaches to gain catalytically active materials are; (a) Using catalytic metal ion as node in framework, (b) integrating existing homogeneous or transition metal catalysis in organic struts and (c) loading of MOFs with active species.[51, 55] Karmakar *et al.* recently developed an efficient photocatalyst system by grafting the Re^{I}-based molecular catalyst and Ru^{II}-based photosensitizer into post-synthetically modified robust and water-stable Zr-MOF (MOF-808). The direct tethering of light harvesting unit and catalytic centre in the confined space of the MOF resulted in highly efficient CO_2-to-CO formation with a maximum production rate of 440 μmol $g^{-1}\ h^{-1}$ (with selectivity>99%, QE = 0.11). Nonetheless, the production of CO in water medium demonstrated the advantage and uniqueness of the catalytic assembly in nanoscopic void is an impressive example of the power of PSM.[56]

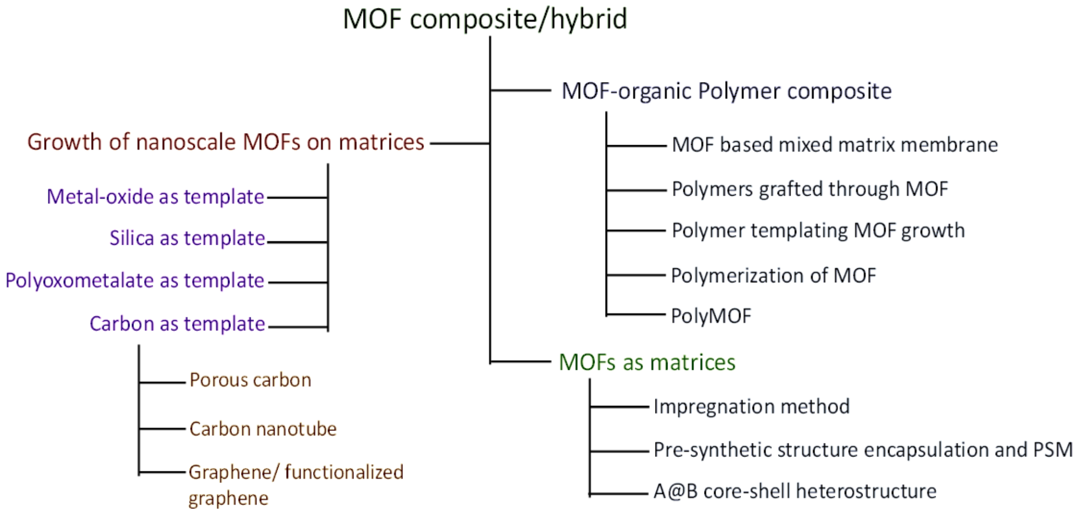

Figure 5: Major classification of MOF composites and their sub-divisions.

1.1.3: Compositional hierarchy

A great deal of research has been aimed at preparing new fascinating MOF structures and exploring various applications. Adjustable integration of MOFs and other functional material is leading to the formation of a new multifunctional assembly termed composite or hybrid. It is well reported that such optimized blending fortunately, combines the merits and mitigates the faults of individual components.[57]

Composite and *hybrid*, sound mutually synonymous, but they do not mean the same. Composite is expressed as a combination of two or more constituents with different physical or chemical properties, while hybrid usually refers to the constituents at the nano or molecular level. Integrating multiscale components, the resulting hybrid materials mostly acquire completely new properties, tailored by the specific physical and chemical characteristics of both the components. Whereas, composite creates a new physicochemical property that was not present in any of the individual components.[58] However, multivariate synthetic strategy and functionalities are introduced into the MOF by integration of several functional species in the development of such materials, both the characteristics of hybrid and composite were observed. Thus, for this case, both the terms *hybrid* and *composite* are considered analogous. Primarily, composites can be fabricated either by growing MOF on a matrix or utilizing MOF as a support for growth and impregnation of other functional materials. Based on this, MOF-composites are classified into three divisions; MOF-Polymer composite, Growth and stabilization of nanoscale MOF on different templates, and MOFs as matrices (Figure 5).

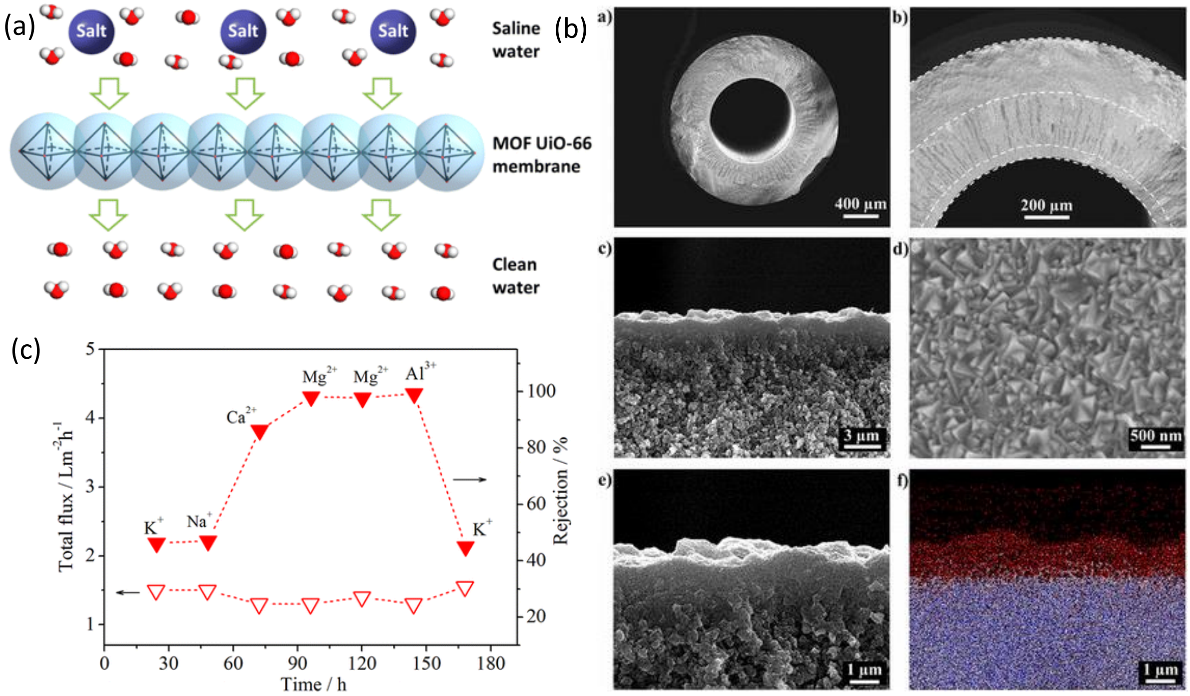

Figure 6: (a) Schematic representation of desalination by MOF-supported membrane. (b) SEM images (a–c and e, cross section; d, top view) and EDXS mapping (f) of the alumina hollow fiber supported UiO-66 membranes. Zr signal, red; Al signal, light blue. Reproduced from reference 66b with the permission from ©2015 American Chemical Society.

MOF-Polymer composite: When MOF is used as a functional species, most commonly it is blended with organic polymer, producing MOF-polymer composites such as ZIF-8/PI,[59] ZIF-8/PSU, [60] ZIF-90/matrimid, HKUST-1/PMMA,[61] and MOF-5/matrimid.[62] Pioneering work has been performed by Kitagawa *et al.*, where MOFs with different pore, shapes, dimensions and nanochannel are utilized as a nanoreactor to confine the polymerization process.[63] The versatility in design fabrication and application generates several scopes of MOF-polymer integration through the (a) synthesis of mixed matrix membrane (MMMs), (b) polymers grafted through MOFs, (c) polymers templating MOF growths, (d) polymerization of MOFs and (e) synthesis of MOFs using polymer ligand or polyMOFs. For MOF based mixed matrix membrane, it consists a polymer combined with a porous solid filler with higher flux and better selectivity. The goal of MOF-based membrane fabrication has expanded rapidly due to its versatile utilization in carbon capture,[64] hydrocarbon separation,[65] desalination,[66] dye[67] and toxic[68] heavy metal capture for water purification. Covalent attachments of polymer chains to MOF surface have been synthesized through two common routes; grafting-to and grafting-from. In general, the grafting-to strategy is simpler, where pre-synthesized polymers with reactive terminal functionalization result in MOF surface with polymer brushing. On the contrary, grafting from strategies are versatile and start with functionalizing the surface with initiator groups from which the polymer is grown. The field of stimuli-responsive polymers has rapidly expanded recently and also reflected upon MOF composite. One of the early examples of this field is demonstrating thermally responsive polymers conjugated to MOF surfaces. Zhu and co-workers grafted 2-(2-methoxyethoxy)ethyl methacrylate and oligo(ethylene glycol) methacrylate on the surface of MIL-101(Al)-NH_2 using atom transfer radical polymerization (ATRP) method.[69] The resultant particles were readily dispersed at room temperature but precipitate beyond 45 °C and showed unprecedented recyclability upon temperature treatment. Distribution of repeating units and the inter-/ intramolecular connection within the polymer structure can completely modify the physical properties of the resulting composites. For example, a lanthanide-based MOF, $[Tb(btb)]_n$ (btb = 1,3,5-benzenetrisbenzoate)was permeated with a mixture of methyl methacrylate (MMA) and styrene, while the ratio of monomer was tuned in the resulting copolymer by altering polymerization conditions. Interestingly, copolymerization under 70 °C could not differ from bulk polymerization, whereas light-induced room temperature polymerization provides high ratios of MMA over styrene,

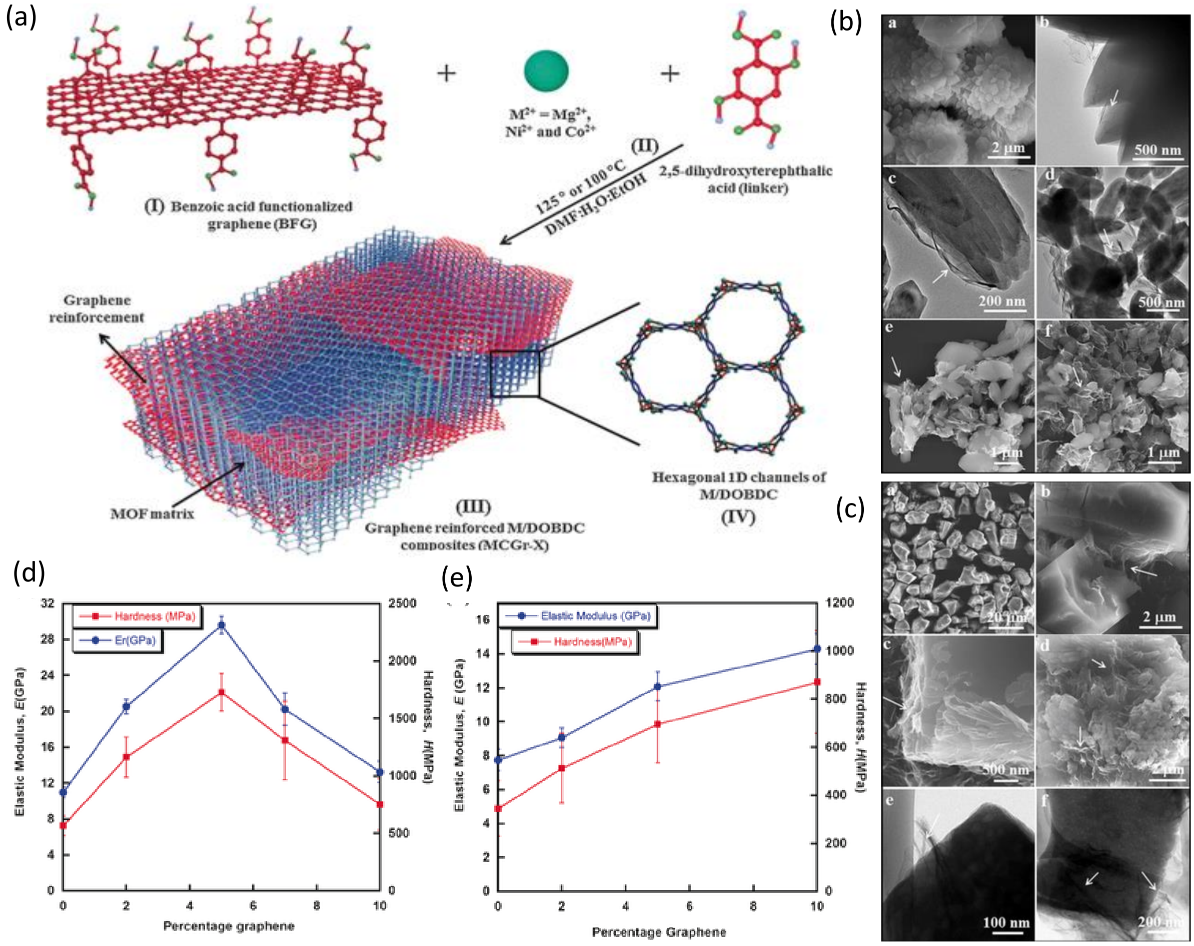

Figure 7: (a) Schematic representation of covalently linked MOF-composite. (b, c) Morphology of M/DOBDC (M= Mg^{2+}(b)-a, Ni^{2+}(c)-a) and its change with increasing concentration of graphene reinforcement. (d, e) Elastic modulus and hardness analysis of Mg/DOBDC (red-d), MgCGr-X (blue-d), Ni/DOBDC (red-e), and NiCGr-X (blue-e), respectively. Reproduced from reference 77 with the permission from ©2016 Willey Online Library.

significantly differing from initial feed ratios. The temperature-dependent FT-IR ensures the dissociation of MMA from the coordination site above 40 °C by ignoring MOF influence on polymerization.[70]

Growth and stabilization of nanoscale MOF on different templates: Apart from organic polymers, other functional materials as metal-oxide nanoparticles,[71] silica,[72] polyoxometalate,[73] carbon including porous carbon,[33, 74] carbon nanotubes,[75] graphene[76] and functionalized graphene[77] are extensively used for fabrication MOF-composites. Most of the study reveals that the matrices are used as a template to grow nanoscale MOF by reducing the probability of augmentation and an improved surface-to-volume ratio. One of the representative examples is fabricating composite of M/DOBDC (M = Mg^{2+}, Ni^{2+}, and Co^{2+}; DOBDC = 2,5-dioxido-1,4-benzene dicarboxylate) with benzoic acid functionalized graphene (Figure 7).[77] The result exhibits significantly improved surface area, enhanced gas adsorption with significantly improved hardness and elastic modulus. Maji *et al*. exclusively adapted such technique to stabilize nanoscale MOF on various layered matrices such as nanoclay[78], aminoclay[79], graphene oxide[80], and functional graphene oxide.[81] Another additional methodology of depositing MOF thin films on a substrate turned out fascinating in recent times for highly desirable application in catalytic coating, chemical sensors and smart membrane has paved the way for MOF-based nanotechnological device fabrication.[82]

MOFs as matrices: MOF can act as matrix material by hosting metal ions or small molecules in their accessible pore. By using this method, Suh's group manifested the fabrication of small palladium nanoparticles (2.6 to 3.4 nm) in a redox-active MOF ($[Zn_3(ntb)_2(EtOH)_2]\cdot 4EtOH$ or SNU-3) in absence of capping and additional reducing agent.[83] The composite showed enhanced H_2 adsorption uptake, owing to redox-activity of Pd^{2+} by 4,4′,4″-nitrilotrisbenzoate (ntb^{3-}), which can be tuned by the doping amount of Pd nanoparticles in the composite by varying the immersion time of SNU-3 in the $Pd(NO_3)_2$ solution. But such an impregnation strategy lacks the opportunity to incorporate few parameters like quantum size effect, optimizing size and shape in encapsulated species and thus constricts their application. To address this, a simple 'build-bottle-around-ship' technique was adapted to produce a series of crystalline materials with successful inclusion of protonated polyoxometalate (POM) one-step hydrothermal reaction of Copper-nitrate, 1,3,5-benzenetricarboxylate and different types of POMs. The composite reveals extraordinary thermal stability with high loading amount of POM, exceeds the record of traditional POM supported catalysis.[84] Moreover, the fabrication of A@B core-shell heterostructures is not only integrating a new functionality in the framework but could help to retain the pristine characteristics of the host structure itself. Herein, if A is considered as a MOF, then B could be any porous material such as MOF, COF (covalent-organic framework), MCM (mobile composition of matter), mesoscopic framework, enzyme or biomolecules.[85]

1.2: Synthesis technique

The principal objective in MOF synthesis is to design a synthetic condition that led to desired inorganic building blocks not affecting the stability of organic linker and at the same time to allow the nucleation and growth of crystallization of defined phase to take place. Here, it will briefly depict the evolution of synthesis technique starting from convention heating to new age methodology i.e., microwave heating, electrochemical or mechanical synthesis procedure and further move towards pilot-scale MOF production (Figure 8-9).

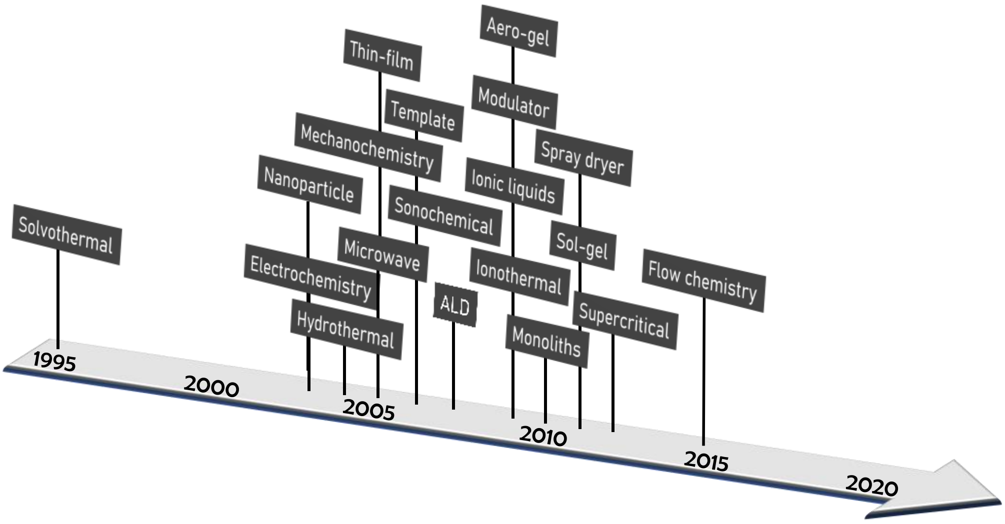

Figure 8: Timeline of common synthesis techniques patented/published for preparation of MOF.[86]

The term conventional synthesis is applied for such cases where reactions are carried out *via* electric heating without any parallelization of reactions. Under this category, MOF synthesis is subdivided into two categories; solvothermal and non-solvothermal. Prof. Albrecht Rabenau defines that the reaction takes place in a close vessel above the boiling point of the solvent and under autogenous pressure typically above 1 bar is called solvothermal or hydrothermal (water as only solvent or co-solvent) reaction.[87] Consequently, the non-solvothermal reaction takes place below or at the boiling point of the solvent under ambient pressure.[87] Some well-known MOFs have been synthesized at room temperature such as ZIF-8, HKUST-1, MOF-5, MOF-74, etc.[88] Variation of reaction temperature strongly influence product formation, crystallinity and morphology.[89] Hoskins and Robenson relied on low-temperature routes for MOF crystal formation.[90] However, this method was well-studied to grow ionic or molecular crystal as it offers the opportunity to tune the rate of nucleation and crystal growth. A jump in higher reaction temperature is also necessary to obtain preferred reaction kinetics and crystallinity. As mentioned above the influence of temperature affects the crystal morphology and even prolonged experimental time can lead to structural degradation.[91]

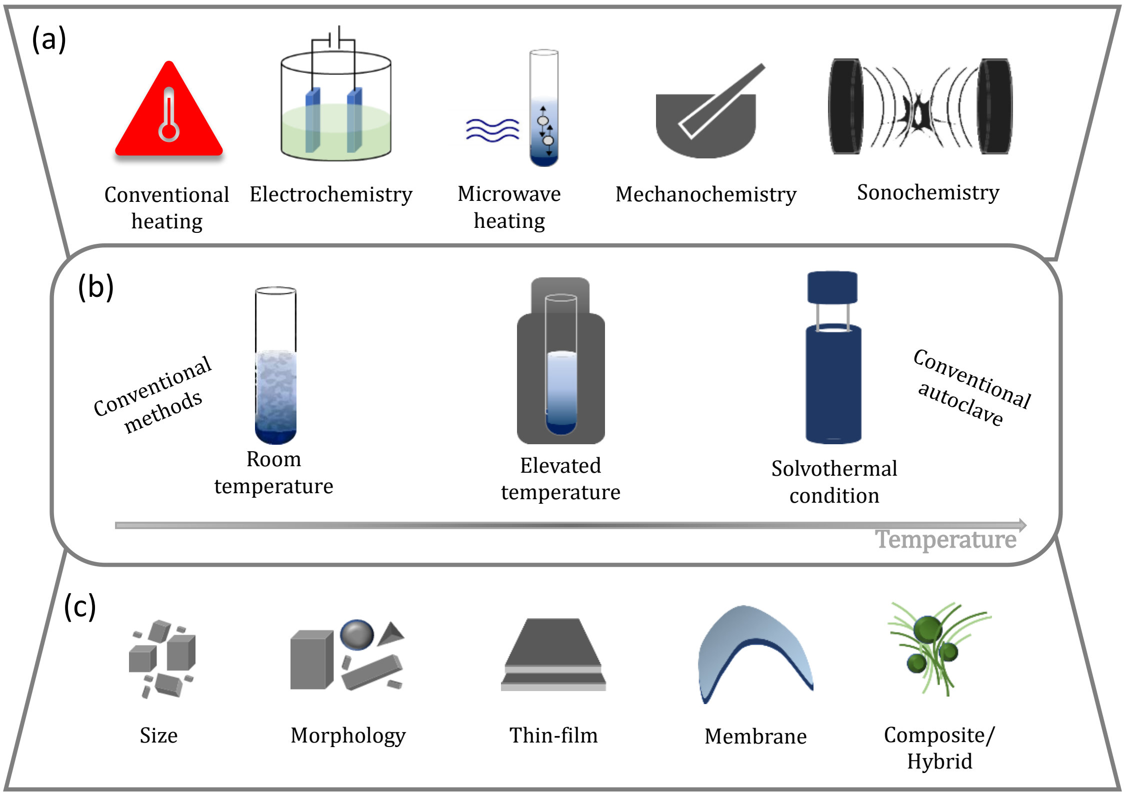

Figure 9: Overview of synthesis methods (a), possible reaction temperatures (b), and (c) final reaction products in MOF synthesis.

The main objective to adapt an alternative synthesis method is to explore material with different shapes and size distributions that can influence its characteristics. For example, decrease in particle size helps to enhance the surface-to-volume ratio that can control the diffusion kinetics of guest molecules that directly affecting in storage, separation and catalysis. Nontoxic, nanocrystalline MOF has been rapidly explored these days in biochemical or biomedical applications. One of the promising alternatives to conventional heating is microwave-assisted synthesis. It is based on the interaction of electromagnetic waves with mobile electric charges (polar solvent molecules, residual ionic charge in solution or solid) in the reaction medium. Such direct interaction induces the collision between molecules, which leads to an increase in kinetic energy i.e., the temperature in the reaction system. Moreover, microwave heating provides a higher and faster heating rate with homogeneous distribution and the complete process is highly energy efficient compared to conventional electric heating. For instance, an *ex-situ* and time-resolved *in-situ* crystallization method were executed on both MIL-53(Fe) and CAU-1-$(OH)_2$, resulting in a faster reaction rate with respect to CE heating.[92] Metal(II)carboxylate-based MOFs such as IRMOF, HKUST were frequently synthesized by applying microwave stimuli. One early study reported the synthesis of cubic microcrystals of IRMOF-1 with 24 μm length in 9 min at 95 °C under microwave irradiation.[93] In another work, Ni and Masel reported the way to reduce both the size and regularity of cubic microcrystals of IRMOF-1 up to 1 μm.[94] Recently, one microwave-assisted method yielded higher quality of IRMOF crystals with enhanced CO_2 uptake compared to ambient pressure dynamic CE heating.[95] Electrochemical synthesis became fascinating in recent times because of the possibility to run a continuous cycle with increased product yield compared to conventional batch reactions, aimed for industrial-scale production. In a comparative study, HKUST-1 was prepared through solvothermal and electrochemical routes in pure ethanol and ethanol-water solvent mixture.[96] In another method, a pattern growth of metallic Cu deposited on a glass slide followed by spin-coating reaction solution of ligand (H_3BTC), solvent (DMSO) and $AgNO_3$ that oxidized the copper by Ag^+ ion and further evaporation of solvent offered a dense film of small octahedron crystallites with 100-200 nm sizes.[97] The interest in mechanochemically synthesized MOF are increasing because of its unique key features like; (a) most of the synthesis were performed under ambient condition, (b) solvent-free method, (c) faster synthesis time, (d) formation of smaller particles with high surface area.[98] HKSUT-1 has been extensively synthesized by the mechanochemical method. Starting from 3:2 ligand-metal ratio, MOF was prepared by ligand assisted grinding and other factors such as precursor concentration, grinding condition, solvent participation and its nature were thoroughly studied.[98-99] Recently, Bhattacharyya *et al.* demonstrated few examples of solvent-free mechanochemical perovskite quantum dot-MOF composite synthesis where MOF serves the purpose of template to control the growth and stabilization of hybrid PQD.[100] Sonochemical synthesis was another approach where the product was gained upon utilization of high-energy ultrasound. Very few MOFs (MOF-5, MOF-177, HKUST-1) were synthesized by this method and the results are comparable to the product obtained by previously mentioned method.[88b, 96] The wide application with high thermal and mechanical stability insists the group of researchers to translate MOF synthesis from laboratory scale to pilot-scale production with required purity, price and time for implication. In 2002, first successful bulk-up was demonstrated at 80 g scale for HKUST-1.[101] The recently published review by Hill and his team elaborately explain the modified techniques by using novel synthetic routes, namely electrochemical, spray drying, mechanochemical and most promising continuous reaction cycle or flow chemistry have been elected for megaton scale MOF production.[86a] Other than synthesis, activation of MOFs is very important to unlock full potential especially for storage and separation application. Generally, it is performed at above boiling point of guest or solvent molecule with additive vacuum or by replacing with low boiling point solvent i.e., solvent exchange technique. In the case of PSM, activation is very important to diminish the number of side reactions that can take place. However, other structure defining synthesis approaches such as template or solvent directed method have not been covered yet as it was already mentioned in earlier sections.

1.3: MOF in environmental application

Addressing environmental issues has become one of the utmost challenges for human survival in this century. Traditional porous materials e.g., activated alumina, silica, carbon or zeolite have been extensively utilized as a host to entrap environmental pollutants selectively from safer counterparts due to high porosity and molecular-scale functional void. MOF, being a promising porous substance, scores over conventional candidates due to its advanced structural flexibility. Moreover, the major bottle neck in chasing them for understanding real life application has been structural stability under high operating temperature and exposure to high or moderate humid environment. In recent times, there has been a serious effort in the field that encourages an improved understanding of structural stability under such extreme conditions. Apart from structural stability, flexible and composite based MOFs have received better attention, and more intense study motivates to propel the advanced strategies to construct devices from microcrystalline MOF powder. Here, our discussion is restricted on three issues that, if improved, would gain great global benefits; (a) Carbon capture, separation and conversion, (b) Industrially important molecular (gas or liquid) separation, (c) Water stable MOFs for application in purification, desalination, harvesting, dehumidification and heat pump.

1.3.1: Carbon capture, separation and conversion

More than 40% of total consumed energy in the chemical industry is utilized exclusively for separation and purification. This is approximately equal to 15% of total energy production and is anticipated to increase almost triple times by 2050.[102] Global energy demand is being met largely by burning fossil fuel and anthropogenic CO_2 is the major key by-product of such combustion. Recent statistics reveal that the atmospheric CO_2 concentration has enhanced 310 to more than 400 ppm and is expected to reach 600 ppm in the next 50 years.[103] In past decades, several porous substances including MOF for CO_2 capture and conversion applications. The employment of MOFs has undergone three development stages, (a) High CO_2 uptake capacity with (b) tunable selectivity towards separation from other competitive gases such as CO_2 from CO_2/H_2 (pre-combustion C-capture), CO_2/CH_4 (natural gas purification), or CO_2/N_2 gas mixtures (post-combustion C-capture), and (c) attempts to explore possible CO_2 transformation reaction by optimizing its catalytic performance and conversion efficiency.[3e, 104]

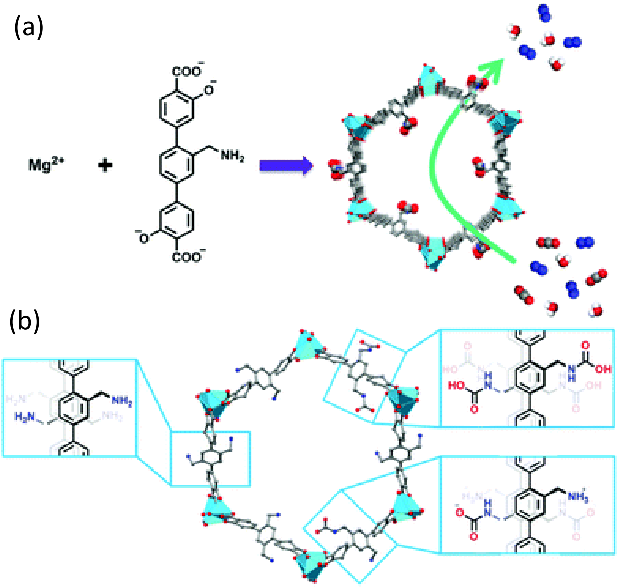

Figure 10: (a) Synthesis of IRMOF-74-III-CH_2NH_2 from Mg(II) and amine-functionalized linker. (b) Crystallographic c-axis view of modelled MOF-$(CH_2NH_2)_2$ depicts three pore environments under varied conditions. Adapted from reference 109 with the permission form American Chemical Society.

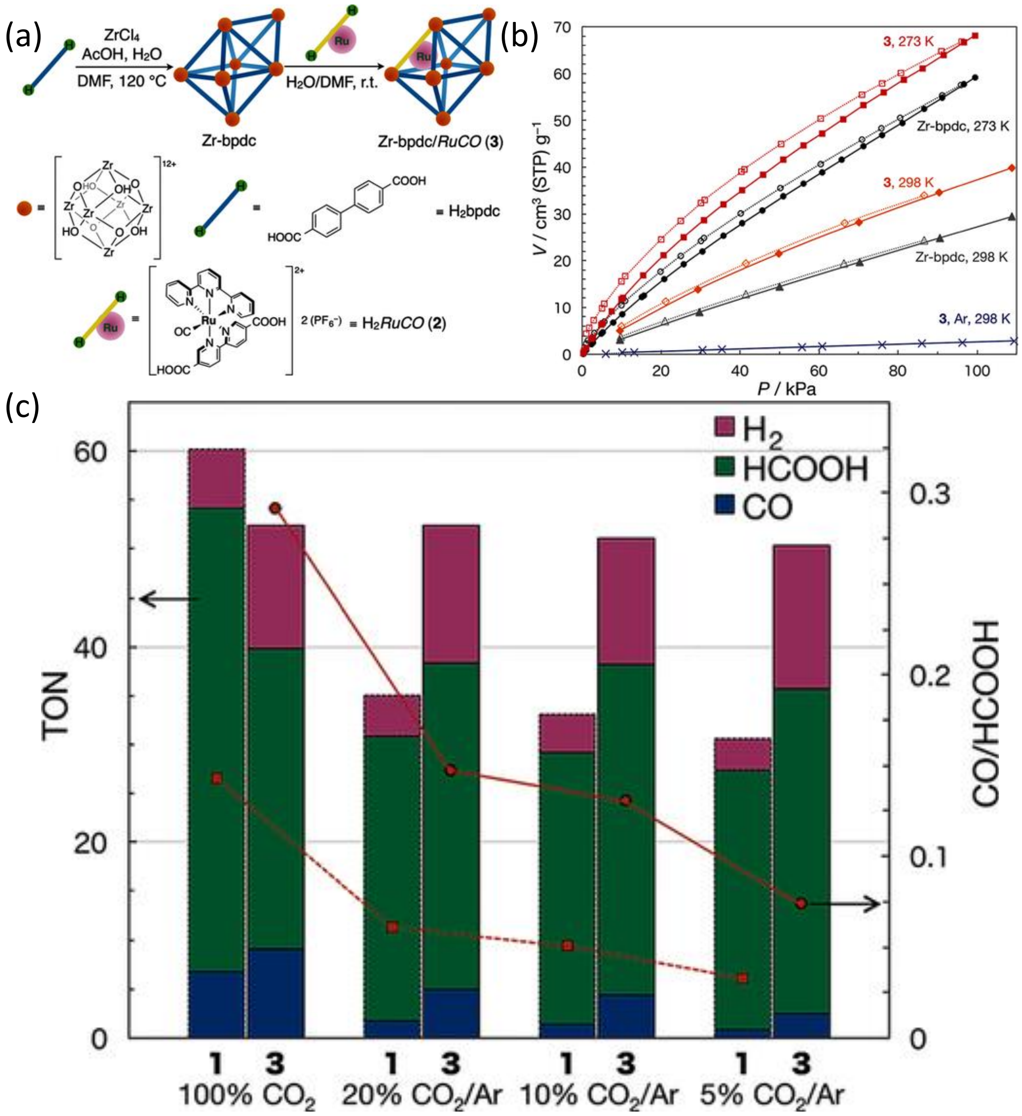

Figure 11: (a) Synthesis of UiO-67/RuCO by the PSE of H_2RuCO with bpdc in Zr-bpdc. (b) CO_2 and Ar adsorption isotherm profile collected at 273 and 298 K. (c) Photochemical CO_2 reduction of CO_2 with Ru^{II}–CO complex and UiO-67/RuCO. Reproduced with the permission from reference 111 with the permission from Willey Online Library.

One of the triggering factors for MOF-based CO_2 adsorption is recognizing or accessing the active site of the MOF known as open metal site (OMS) or unsaturated metal centre (UMC). The concept originated in the early 20's and 2005, HKUST-1 demonstrated an outstanding CO_2 storage capacity of 10 mmol/g under ambient temperature and above 40 bar pressure.[105] For Instance, a temperature-swing CO_2 adsorption experiments were performed in MOF-177 and MOF-74(Mg).[106] The latter one was marked by an outstanding selectivity (Selectivity factor 148.1) at a typical flue gas temperature. MOF-74(Mg) showed typically high CO_2 uptake capacity even more than previously most studied Zeolite NaX (SF 87.4) and further targeted for pre-/post- and natural gas separation.[107] On other hand, the competitive adsorption of water molecules over CO_2 restricts its application in the real domain. Therefore, hydrophobic and superhydrophobic frameworks are incorporated for practical CO_2 adsorption in presence of water.[108] Recently, several alkylamine functionalities have been covalently tethered to the linker of IRMOF-74-III predominantly for selective CO_2 capture under humid conditions (Figure 10).[109] Another very recent technology is adsorbing CO_2 from the air and generating a concentrated stream for industrial or in further sequestration. Few laboratories recently integrated such technology from lab to industrial scale production to control CO_2 level in a confined space like indoor, spacecraft and submarines.[110]

MOFs, MOF-derivatives and MOF-composites outperform other porous materials catalytic CO_2 conversion. To date, MOF performs in photocatalytic and electrocatalytic reduction, heterogeneous hydrogenation of CO_2 and conversion to organic products. One of the representative examples is found in a Zr-based MOF composite UiO-67-Ru^{II}. The post-synthetic exchange method was adapted for incorporating photoreactive Ru^{II}-CO ($[Ru^{II}(bpy)(terpy)(CO)](PF_6)_2$) complex into the pore of UiO-67.[111] The result revealed an exponential decrease in photocatalytic activity of the molecular catalyst with a reduction in CO_2 partial pressure (Figure 11). Similar results are extensively reported in recent times as the key to the successful implementation of MOFs as CO_2 adsorbents in their structural adaptability, interaction with the gaseous molecule and most importantly high CO_2 uptake chemical as well as mechanical stability even in presence of water.

1.3.2: Industrially important molecular separation

Hydrocarbon, as the name suggests, it is an organic compound that consists of only hydrogen and carbon. The majority of hydrocarbons are found in crude oil or petroleum gas and thus hydrocarbon separation is considered the most significant and complex industrial process. Adsorptive separation potentially fulfils the energy-efficient separation economy, saves 80% of utilized energy in comparison to conventional column-distillation technique.[112] Despite the variation in molecular geometry, there are five classes of hydrocarbons e.g., (a) alkane, (b) alkene, (c) alkyne, (d) cycloalkane and (e) arenes or aromatic hydrocarbons (Figure 12).

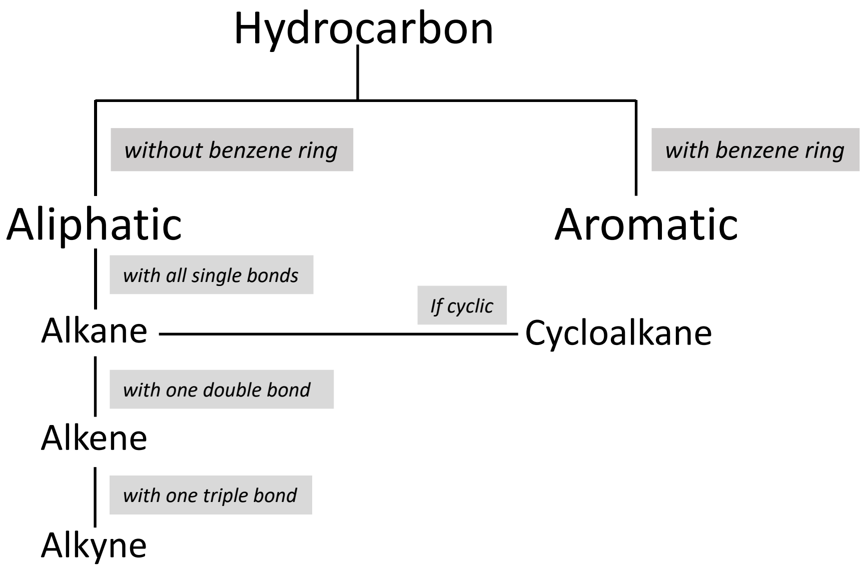

Figure 12: Classification of hydrocarbon and their inter-relation.

Hydrocarbons afford the most broadly used raw materials such as olefin, paraffin, alkyne, alkene and aromatic isomer for the industrial production of various polymers and chemicals.[113] Olefin/paraffin (e.g., C_2H_4/C_2H_6 and C_3H_6/C_3H_8) separation is known as the most energy-intensive process, accounts 0.3% of total global energy expenditure. In the early days, MIL and MOF-74 series attracted substantial attention for hydrocarbon storage and separation due to the presence of open metal sites.[114] MOF-74(Mg) exhibited higher binding affinity to both C_2H_4 and C_3H_6 compared to C_2H_6 and C_3H_8, respectively, introduced MOF as a potential material for olefin/paraffin separation.[115] One of the remarkable examples was demonstrated by Long *et al.* developed Fe_2(dobdc) MOF with unsaturated Fe(II) sites which showed a high ethylene/ethane separation factor, based on stronger interaction between unsaturated metal centre and π-electrons of C_2H_4.[116] In recent times, Chen *et al.* exposed that further oxygen modification of Fe_2(dobdc) i.e., Fe_2O_2(dobdc), showed a high C_2H_6 uptake (74.3 mL/g) with reverse selectivity concerning pristine one. The reported selectivity factor was nearly 4 with a high isosteric heat of adsorption (66.8 kJ/mol).[117] Further, Chen and his co-workers developed an energy-efficient and efficient synergistic sorbent separation strategy (SSST) by integrating three MOFs such as TIFSIX-2-Cu-i, Zn-atz-ipa and SIFSIX-3-Ni, with their own different favorable target molecules, obtain ultra-pure ethylene from the mixture of C_2H_2/CO_2/C_2H_4/C_2H_6.[118] In addition, other MOF based smart materials such

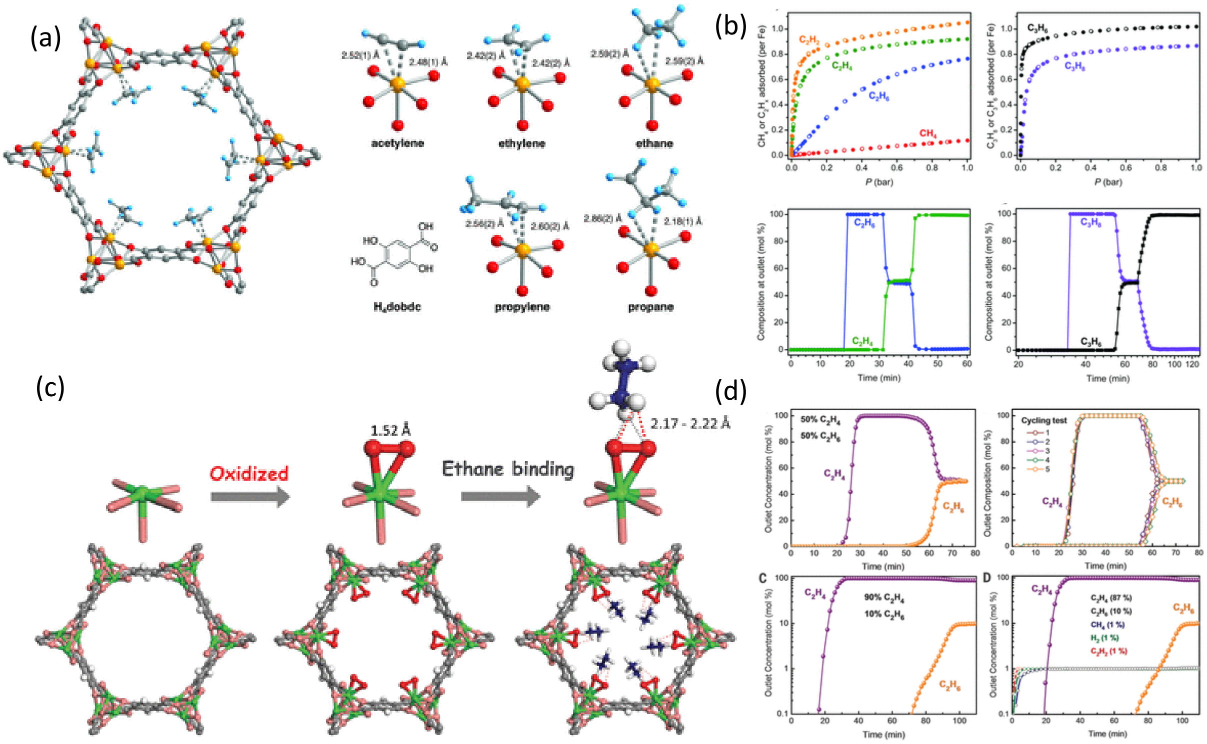

Figure 13: (a) A fragment of the solid-state structure of $Fe_2(dobdc)\cdot2C_2D_4$ (*left*) obtained by Neutron Powder Diffraction study. $H_4(dobdc)$ ligand and the first coordination spheres for the iron centres in the solid-state structures obtained upon treating $Fe_2(dobdc)$ with acetylene, ethylene, ethane, propylene, and propane (*right*). (c) The structure of $Fe_2(dobdc)$ (*left*), $Fe_2(O_2)(dobdc)$ (*middle*), and $Fe_2(O_2)(dobdc)–C_2D_6$ (*right*) revealed by NPD studies. Adsorption and dynamic breakthrough column experiment graph for activated (b) $Fe_2(dobdc)$ and (d) $Fe_2(O_2)(dobdc)$. Adapted from reference 116 and 117 with the permission from American Association for the Advancement of Science.

As thin-film, mixed matrix and stand-alone membranes are extensively studied for H_2/CO_2, N_2/CO_2, CO_2/CH_4 separation.[119] Gas-phase adsorption and separation is preferably studied by most of the MOF community, while isolation and purification of liquid mixtures such as chiral compounds, bio-based water-dispersible liquids and industrially important aromatic hydrocarbons are broadly studied in the recent decade. The most important structural isomer separation of this section is extracting each component from BTEX mixture. Benzene, toluene, ethylbenzene, and xylenes (ortho, meta and para) are important constituents in petroleum product e.g., gasoline or petrol.[120] They are highly important industrial substance, used in manufacturing adhesives, paint, rubber manufacturing units. First-row benchmark MOFs such as ZIFs, HKSUT-1, UiO-66, MIL and its derivatives are utilized for xylene separation.[121] Similarly, MOF outperforms many other classical molecular sieves for the molecular recognition from the mixture of benzene/toluene, benzene/cyclohexane, styrene/ethylbenzene, mesitylene derivatives and even more, while these alkyl-aromatics are connected through industrial synthetic procedure but having different size and functionality.[122]

1.3.3: Water stable MOF for several environmental applications

As mentioned earlier, the renewed structural understanding provides the platform to fabricate MOFs with high thermal, water and chemical stability. The last decade have witnessed the synthesis of new water stable MOFs, while there is a vast body of data of MOF performing as a heart of a protype utilized in nanotechnological device fabrication. Equipped with the idea of harvesting desert air, Yaghi and collaborators designed a proof-of-concept device by using low pressure water (low relative humidity) uptake characteristic of MOF-801 (Figure 14).[123] Following the path, a systematic on water capture-release kinetics was conducted by using MOF-303(Al), MOF-303/graphene, Aluminium fumarate, zeolite SAPO-34, and 13X as probe adsorbents for studying arid atmosphere water harvesting with the utilization of solar heating.[123-124] Further, MIL-101(Cr) was explored by integrating with hygroscopic salt or crosslinked polymer to study its maximum uptake capacity with steady release at 90% relative humidity.[125] MOF sorbents could well regulate the indoor humidity if these materials sharply adsorb beyond 65% relative humidity and release after 45% (45-65% RH; comfortable and healthy humidity limit for indoor environment advised by ASHRAE).[126] In addition, MOF could also be considered as the best choice for industrial cooling, drying or heating.

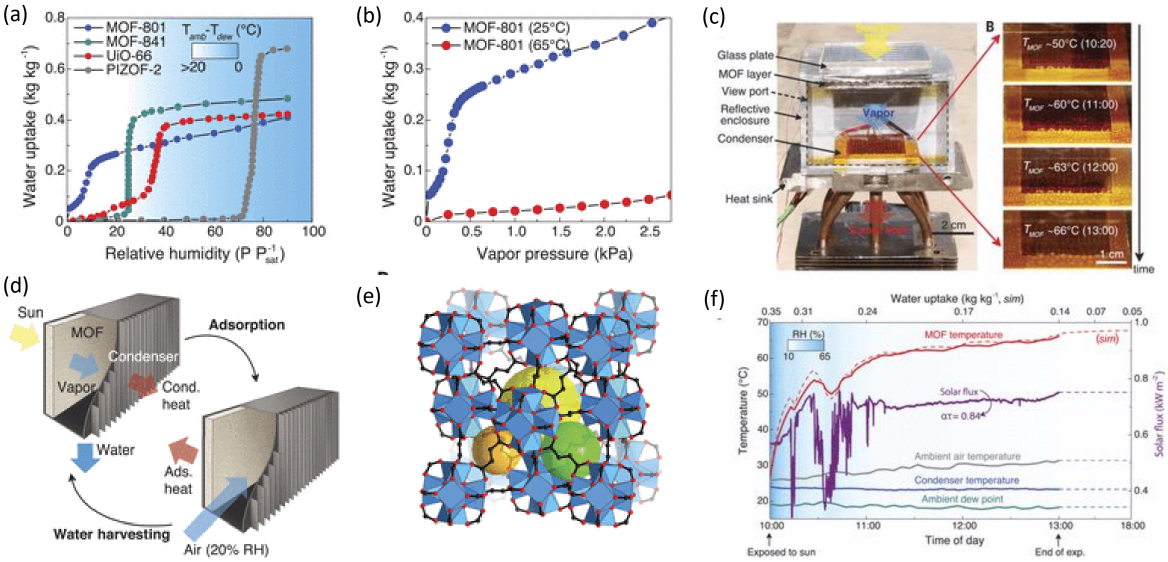

Figure 14: (a) Comparative water adsorption isotherm of water stable MOFs at 25 °C. (b) Water adsorption isotherm at varied temperatures. (c) Image of harvesting prototype. (d) Mechanism of solar-assisted water

harvesting scheme. (e) $Zr_6O_4(OH)_4(-COO)_{12}$ secondary building units are linked together with fumarates to form MOF-801. The yellow, orange and green spheres are defining different pore, while black, red and blue defines carbon, oxygen and Zr-polyhedra. (f) Representative parameter during water harvesting analysis. Reproduced from reference 123 with the permission from ©2017 American Association for the Advancement of Science.

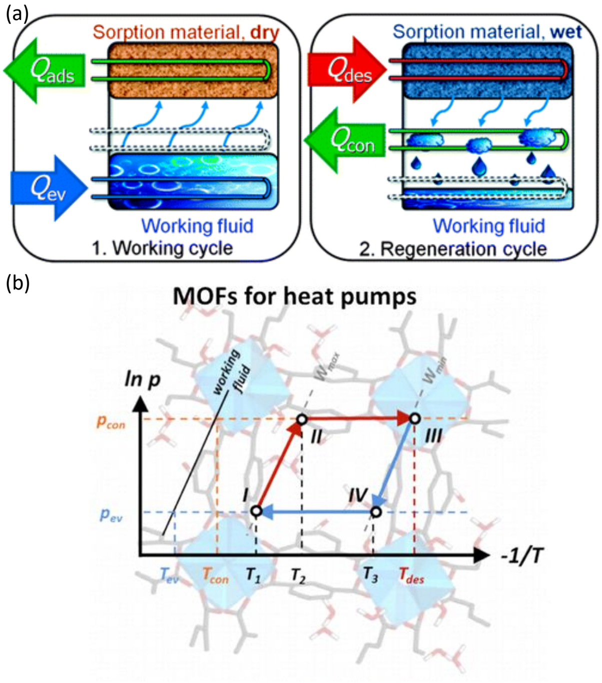

Figure 15: (a) Adsorption driven heat cycle with distinct adsorption and desorption stage. (b) Isosteric cycle diagram of an adsorption cycle. Reproduced from reference 127 with the permission from Royal Chemical Society ©2013.

The realization of an efficient adsorption-based heat pump or chiller, MOF has met all the criteria with high working capacity and a high coefficient of performance (CoP). Adsorptive heating or cooling system typically operates through a water adsorption-desorption mechanism (Figure 15). During adsorption, as working fluid (water) evaporates towards the adsorbent, heat (Q_{ev}) is dragged from the evaporator leading to a reduction in temperature enabling for cooling application. However, as adsorption is an exothermic process, heat (Q_{ads}) is released to the cooling fluid. Finally, when the adsorbent became saturated, regeneration is achieved through input heat (Q_{des}) which is further used to cool water of the condenser (Q_{con}).[127] Thus, this cycle can be used for heating and cooling, while the feasibility of the process is estimated by CoP. Lenzen *et al.* introduced a nanoscale MOF, CAU-23 ([Al(OH)($C_6H_2O_4S$)]), that possesses a high water adsorption capacity 0.37g/$g_{adsorbent}$ around 0.3 relative pressure with more than 5000 recyclability performance.[128] Interestingly, the required driving temperature is as low as 60 °C with a low cooling temperature of 10 °C, paving the path for more efficient waste heat utilization. Very recently, similar framework (KMF-1; $[Al(OH)(C_6H_3NO_4)]\cdot nH_2O$), demonstrated by combining computational assumption and experimental approaches, exhibited a S-shaped isotherm with best uptake (0.36 mL/mL), specific energy (263 kWh/m^3), heat storage (348 kWh/m^3) capacity as well as record high CoP (0.75 for heating, 1.74 for cooling).[129] Substantial studies were also reported for MOF and MOF-based membrane for heavy metal sensing, capture and many other primary and secondary technologies for water purification treatment.[130]

1.4: Conclusion and future outlook

Here, the chapter summarise the synthesis, structural chemistry and various targeted applications of MOF that substantially evolved since their original initiation is more than two decades ago. It complies the synthetic, structural and compositional evolution of MOF with optimized design strategy and diverse chemical structure. Nevertheless, like any other substance, all these systems have their intrinsic drawbacks. The following chapters summarize the collaboration of existing as well as novel synthesis technique and their applicability in storage, separation and water harvesting, bridged the gap between potential and practical applications. Therefore, the overall thesis is primarily based on three chapters. The first one demonstrates the novel synthesis strategy to combine microwave stimuli with system perturbation and mixed solvent approach to generate hierarchical porosity in a typical microporous framework. The study also ensures the structural bimodality by encapsulating nanoscale bio-molecule (VitB$_{12}$) or by supporting the growth of perovskite quantum dots in the mesoscopic void. In the next chapter, three different MOFs have been considered as potential materials for industrially important hydrocarbon separation through kinetic and thermodynamic preferences. Note that, both gas phase and liquid phase adsorption, separation and purification were studied for industrially important first row aromatic and aliphatic hydrocarbons. The last chapter mainly focused on the growth and stabilization of MOF nanoparticles by using one or more templates to enhance surface-to-volume ratio, uptake capacity and hydrothermal stability. These composites are utilized in direct water application studies by adsorbing airborne moisture under ambient or compressed air environments. Thus, a proof-of-concept MOF based water harvesting and high-pressure moisture trapping prototype were built to validate the viability of these approaches to provide fresh water under non-arid indoor conditions and dry-cool-clean air production to maintain sustainable indoor weather quality, correspondingly.

1.5: References

[1] a) H. Furukawa, K. E. Cordova, M. O'Keeffe and O. M. Yaghi, *Science* **2013**, *341*, 1230444; b) C. A. Trickett, A. Helal, B. A. Al-Maythalony, Z. H. Yamani, K. E. Cordova and O. M. Yaghi, *Nat. Rev. Mater.* **2017**, *2*, 17045; c) in *Copyright*, (Ed. S. K. Ghosh), Elsevier, **2019**, p. iv; d) M. Baci, M. A. Carreon, W. Chen, K. Dedecker, A. V. Desai, E. Dumas, S. Dutta, P. Falcaro, Y. Fang, O. K. Farha, M. Feng, S. K. Ghosh, A. J. Howarth, A. A. Kirchon, S. Kitagawa, A. Kumar, S. Laha, B. Lavédrine, S. Ma, Z. L. Magnuson, M. B. Majewski, T. K. Maji, S. Mukherjee, R. Ricco, S. Roy, P. Samanta, C. Serre, S. Sharma, V. K. Sharma, N. Steunou, M. J. Styles, Q. Wang, S. Wang, C. Xiao, L. Yang, M. J. Zaworotko, P. Zhang and H.-C. Zhou in List of Contributors, (Ed. S. K. Ghosh), Elsevier, **2019**, pp. xiii-xv.
[2] a) H.-C. J. Zhou and S. Kitagawa, *Chem. Soc. Rev.* **2014**, *43*, 5415-5418; b) *Chem.l Rev.* **2012**, *112*, 673-674; c) M. Eddaoudi, J. Kim, N. Rosi, D. Vodak, J. Wachter, M. O'Keeffe and O. M. Yaghi, **2002**, *295*, 469-472; d) H. Li, M. Eddaoudi, M. O'Keeffe and O. M. Yaghi, *Nature* **1999**, *402*, 276-279; e) D. J. Tranchemontagne, J. L. Mendoza-Cortés, M. O'Keeffe and O. M. Yaghi, *Chem. Soc. Rev.* **2009**, *38*, 1257-1283; f) J. Lee, O. K. Farha, J. Roberts, K. A. Scheidt, S. T. Nguyen and J. T. Hupp, *Chem. Soc. Rev.* **2009**, *38*, 1450-1459.
[3] a) H. Wang, Q.-L. Zhu, R. Zou and Q. Xu, *Chem* **2017**, *2*, 52-80; b) H. D. Lawson, S. P. Walton and C. Chan, *ACS Appl. Mater. Interfaces* **2021**, *13*, 7004-7020; c) J. Liu and C. Wöll, *Chem. Soc. Rev.* **2017**, *46*, 5730-5770; d) R. Haldar, S. Bhattacharyya and T. K. Maji, *J. Chem. Sci.* **2020**, *132*, 99; e) M. Ding, R. W. Flaig, H.-L. Jiang and O. M. Yaghi, *Chem. Soc. Rev.* **2019**, *48*, 2783-2828.
[4] M. Kondo, T. Yoshitomi, H. Matsuzaka, S. Kitagawa and K. Seki, *Angew. Chem., Int. Ed.* **1997**, *36*, 1725-1727.
[5] S. S.-Y. Chui, S. M.-F. Lo, J. P. H. Charmant, A. G. Orpen and I. D. Williams, *Science* **1999**, *283*, 1148-1150.
[6] H. Deng, S. Grunder, K. E. Cordova, C. Valente, H. Furukawa, M. Hmadeh, F. Gándara, A. C. Whalley, Z. Liu, S. Asahina, H. Kazumori, M. O'Keeffe, O. Terasaki, J. F. Stoddart and O. M. Yaghi, *Science* **2012**, *336*, 1018-1023.
[7] R. Banerjee, A. Phan, B. Wang, C. Knobler, H. Furukawa, M. O'Keeffe and O. M. Yaghi, *Science* **2008**, *319*, 939-943.
[8] a) S. Biswas, D. E. P. Vanpoucke, T. Verstraelen, M. Vandichel, S. Couck, K. Leus, Y.-Y. Liu, M. Waroquier, V. Van Speybroeck, J. F. M. Denayer and P. Van Der Voort, *J. Phys. Chem. C* **2013**, *117*, 22784-22796; b) G. Férey, C. Mellot-Draznieks, C. Serre, F. Millange, J. Dutour, S. Surblé and I. Margiolaki, *Science* **2005**, *309*, 2040-2042.
[9] Y.-B. Zhang, H.-L. Zhou, R.-B. Lin, C. Zhang, J.-B. Lin, J.-P. Zhang and X.-M. Chen, *Nat. Commun.* **2012**, *3*, 642.
[10] a) H. Furukawa, F. Gándara, Y.-B. Zhang, J. Jiang, W. L. Queen, M. R. Hudson and O. M. Yaghi, *J. Am. Chem. Soc.* **2014**, *136*, 4369-4381; b) J. H. Cavka, S. Jakobsen, U. Olsbye, N. Guillou, C. Lamberti, S. Bordiga and K. P. Lillerud, *J. Am. Chem. Soc.* **2008**, *130*, 13850-13851.
[11] W. Xuan, C. Zhu, Y. Liu and Y. Cui, *Chem. Soc. Rev.* **2012**, *41*, 1677-1695.

[12] I. M. Hönicke, I. Senkovska, V. Bon, I. A. Baburin, N. Bönisch, S. Raschke, J. D. Evans and S. Kaskel, *Angew. Chem., Int. Ed.* **2018**, *57*, 13780-13783.
[13] a) L. Feng, K.-Y. Wang, X.-L. Lv, T.-H. Yan and H.-C. Zhou, *Natl. Sci. Rev.* **2019**, *7*, 1743-1758; b) K. Shen, L. Zhang, X. Chen, L. Liu, D. Zhang, Y. Han, J. Chen, J. Long, R. Luque, Y. Li and B. Chen, *Science* **2018**, *359*, 206-210; c) S. Yuan, L. Zou, J.-S. Qin, J. Li, L. Huang, L. Feng, X. Wang, M. Bosch, A. Alsalme, T. Cagin and H.-C. Zhou, *Nat. Commun.* **2017**, *8*, 15356.
[14] K. P. Sonu, S. Laha, M. Eswaramoorthy and T. K. Maji in *Porous Materials: Recent Developments*, pp. 148-172.
[15] a) C. Liu, T. Li and N. L. Rosi, *J. Am. Chem.Soc.* **2012**, *134*, 18886-18888; b) V. Lykourinou, Y. Chen, X.-S. Wang, L. Meng, T. Hoang, L.-J. Ming, R. L. Musselman and S. Ma, *J. Am. Chem.Soc.* **2011**, *133*, 10382-10385.
[16] a) L.-B. Sun, J.-R. Li, J. Park and H.-C. Zhou, *J. Am. Chem.Soc.* **2012**, *134*, 126—129; b) *Chem. Commun.* **2011**, *47*, 7809–7811; c) L.-G. Qiu, T. Xu, Z.-Q. Li, W. Wang, Y. Wu, X. Jiang, X.-Y. Tian and L.-D. Zhang, *Angew. Chem. Int. Ed.* **2008**, *120*, 9629 –9633.
[17] J. Park, Z. U. Wang, L.-B. Sun, Y.-P. Chen and H.-C. Zhou, *J. Am. Chem.Soc.* **2012**, *134*, 20110-20116.
[18] S. Yang, X. Lin, W. Lewis, M. Suyetin, E. Bichoutskaia, J. E. Parker, C. C. Tang, D. R. Allan, P. J. Rizkallah, P. Hubberstey, N. R. Champness, K. Mark Thomas, A. J. Blake and M. Schröder, *Nat. Mater.* **2012**, *11*, 710-716.
[19] X.-Y. Yang, L.-H. Chen, Y. Li, J. C. Rooke, C. Sanchez and B.-L. Su, *Chem. Soc. Rev.* **2017**, *46*, 481-558.
[20] L. Feng, K.-Y. Wang, J. Willman and H.-C. Zhou, *ACS Cent. Sci.* **2020**, *6*, 359-367.
[21] a) B. Zhang, J. Zhang, C. Liu, X. Sang, L. Peng, X. Ma, T. Wu, B. Han and G. Yang, *RSC Adv.* **2015**, *5*, 37691–37696; b) R. Ramachandran, C. Zhao, D. Luo, K. Wang and F. Wang, *Electrochim. Acta* **2018**, *267*, 170-180; c) Y. Yue, Z.-A. Qiao, P. F. Fulvio, A. J. Binder, C. Tian, J. Chen, K. M. Nelson, X. Zhu and S. Dai, *J. Am. Chem. Soc.* **2013**, *135* 9572—9575.
[22] Y. Kim, TaoYang, G. Yun, M. B. Ghasemian, J. Koo, E. Lee, S. J. Cho and K. Kim, *Angew. Chem. Int. Ed.* **2015**, *54*, 13273 –13278.
[23] Y. Zhao, J. Zhang, B. Han, J. Song, J. Li and Q. Wang, *Angew. Chem. Int. Ed.* **2011**, *50*, 636-639.
[24] L. Peng, J. Zhang, Z. Xue, B. Han, X. Sang, C. Liu and G. Yang, *Nat. Commun.* **2014**, *5*, 4465.
[25] H. Guo, Y. Zhu, S. Wang, S. Su, L. Zhou and H. Zhang, *Chem. Mater.* **2012**, *24*, 444-450.
[26] D.-Y. Hong, Y. K. Hwang, C. Serre, G. Férey and J.-S. Chang, *Angew. Chem. Int. Ed.* **2009**, *19*, 1537-1552.
[27] Y. Yue, P. F. Fulvio and S. Dai, *Acc. Chem. Res.* **2015**, *48*, 3044—3052.
[28] a) Y. Yue, Z.-A. Qiao, P. F. Fulvio, A. J. Binder, C. Tian, J. Chen, K. M. Nelson, X. Zhu and S. Dai, *J. Am. Chem. Soc.* **2013**, *135*, 9572-9575; b) Y. Yue, A. J. Binder, R. Song, Y. Cui, J. Chen, D. K. Hensley and S. Dai, *Dalton Trans.* **2014**, *43*, 17893-17898.
[29] a) H.-Y. Li, S.-N. Zhao, S.-Q. Zang and J. Li, *Chem. Soc. Rev.* **2020**, *49*, 6364-6401; b) C. Y. Lee, O. K. Farha, B. J. Hong, A. A. Sarjeant, S. T. Nguyen and J. T. Hupp, *J. Am. Chem. Soc.* **2011**, *133*, 15858-15861; c) X.-f. Zhong and X. Sun, *Acta Pharmacol. Sin.* **2020**, *41*, 928-935; d) C. Wang, L. Wang, S. Tadepalli, J. J. Morrissey, E. D. Kharasch, R. R. Naik and S. Singamaneni, *ACS Sens.* **2018**, *3*, 342-351; e) Y. Zhang and B. Yan, *Nanoscale* **2019**, *11*, 22946-22953; f) D. Samanta, S. Roy, R. Sasmal, N. D. Saha, P. K R, R. Viswanatha, S. S. Agasti and T. K. Maji, *Angew. Chem. Int. Ed.* **2019**, *58*, 5008-5012.
[30] A. Carné, C. Carbonell, I. Imaz and D. Maspoch, *Chem. Soc. Rev.* **2011**, *40*, 291-305.
[31] S. Furukawa, J. Reboul, S. Diring, K. Sumida and S. Kitagawa, *Chem. Soc. Rev.* **2014**, *43*, 5700-5734.

[32] a) C. L. Ruiz-Zambrana, M. Malankowska and J. Coronas, *Dalton Trans.* **2020**, *49*, 15139-15148; b) K. A. S. Usman, J. W. Maina, S. Seyedin, M. T. Conato, L. M. Payawan, L. F. Dumée and J. M. Razal, *NPG Asia Mater.* **2020**, *12*, 58; c) F.-L. Li, P. Wang, X. Huang, D. J. Young, H.-F. Wang, P. Braunstein and J.-P. Lang, *Angew. Chem. Int. Ed.* **2019**, *58*, 7051-7056; d) N. Sikdar, M. Bhogra, Umesh V. Waghmare and T. K. Maji, *J. Mater. Chem. A* **2017**, *5*, 20959-20968.
[33] B. Liu, H. Shioyama, T. Akita and Q. Xu, *J. Am. Chem. Soc.* **2008**, *130*, 5390-5391.
[34] P. Pachfule, D. Shinde, M. Majumder and Q. Xu, *Nat. Chem.* **2016**, *8*, 718-724.
[35] a) Z. Liu, R. Ma, M. Osada, N. Iyi, Y. Ebina, K. Takada and T. Sasaki, *J. Am. Chem. Soc.* **2006**, *128*, 4872-4880; b) K. S. Novoselov, A. K. Geim, S. V. Morozov, D. Jiang, Y. Zhang, S. V. Dubonos, I. V. Grigorieva and A. A. Firsov, *Science* **2004**, *306*, 666-669; c) P.-Z. Li, Y. Maeda and Q. Xu, *Chem. Commun.* **2011**, *47*, 8436-8438.
[36] J. D. Evans, V. Bon, I. Senkovska, H.-C. Lee and S. Kaskel, *Nat. Commun.* **2020**, *11*, 2690.
[37] K. Susumu and K. Mitsuru, *Angew. Chem. Int. Ed.* **1998**, *71*, 1739-1753.
[38] R. Haldar, N. Sikdar and T. K. Maji, *Mater. Today* **2015**, *18*, 97-116.
[39] a) T. K. Maji, R. Matsuda and S. Kitagawa, *Nat. Mater.* **2007**, *6*, 142-148; b) P. Kanoo, R. Matsuda, M. Higuchi, S. Kitagawa and T. K. Maji, *Chem. Mater.* **2009**, *21*, 5860-5866; c) S. Kitagawa, R. Kitaura and S.-i. Noro, *Angew. Chem. Int. Ed.* **2004**, *43*, 2334-2375.
[40] S. Horike, S. Shimomura and S. Kitagawa, *Nat. Chem.* **2009**, *1*, 695-704.
[41] a) P. Nugent, Y. Belmabkhout, S. D. Burd, A. J. Cairns, R. Luebke, K. Forrest, T. Pham, S. Ma, B. Space, L. Wojtas, M. Eddaoudi and M. J. Zaworotko, *Nature* **2013**, *495*, 80-84; b) S. Ma, J. Eckert, P. M. Forster, J. W. Yoon, Y. K. Hwang, J.-S. Chang, C. D. Collier, J. B. Parise and H.-C. Zhou, *J. Am. Chem. Soc.* **2008**, *130*, 15896-15902; c) B. Kesanli, Y. Cui, M. R. Smith, E. W. Bittner, B. C. Bockrath and W. Lin, *Angew. Chem. Int. Ed.* **2005**, *44*, 72-75.
[42] A. Schneemann, V. Bon, I. Schwedler, I. Senkovska, S. Kaskel and R. A. Fischer, *Chem Soc. Rev.* **2014**, *43*, 6062-6096.
[43] H. Leclerc, T. Devic, S. Devautour-Vinot, P. Bazin, N. Audebrand, G. Férey, M. Daturi, A. Vimont and G. Clet, *J. Phys. Chem. C* **2011**, *115*, 19828-19840.
[44] F. Millange, C. Serre, N. Guillou, G. Férey and R. I. Walton, *Angew. Chem. Int. Ed.* **2008**, *47*, 4100-4105.
[45] C. Serre, F. Millange, C. Thouvenot, M. Noguès, G. Marsolier, D. Louër and G. Férey, *J. Am. Chem. Soc.* **2002**, *124*, 13519-13526.
[46] N. Sikdar, A. Hazra, D. Samanta, R. Haldar and T. K. Maji, *Angew. Chem. Int. Ed.* **2020**, *59*, 18479-18484.
[47] S. Surblé, C. Serre, C. Mellot-Draznieks, F. Millange and G. Férey, *Chem. Commun.* **2006**, 284-286.
[48] C. Mellot-Draznieks, C. Serre, S. Surblé, N. Audebrand and G. Férey, *J. Am. Chem. Soc.* **2005**, *127*, 16273-16278.
[49] a) D. N. Dybtsev, H. Chun and K. Kim, **2004**, *43*, 5033-5036; b) S. Pakhira, *RSC Adv.* **2019**, *9*, 38137-38147.
[50] T. K. Maji, M. Ohba and S. Kitagawa, *Inorg. Chem.* **2005**, *44*, 9225-9231.
[51] J. Liu, L. Chen, H. Cui, J. Zhang, L. Zhang and C.-Y. Su, *Chem. Soc. Rev.* **2014**, *43*, 6011-6061.
[52] S.-Y. Zhang, S. Jensen, K. Tan, L. Wojtas, M. Roveto, J. Cure, T. Thonhauser, Y. J. Chabal and M. J. Zaworotko, *J. Am. Chem. Soc.* **2018**, *140*, 12545-12552.
[53] G. B. Gardner, D. Venkataraman, J. S. Moore and S. Lee, *Nature* **1995**, *374*, 792-795.
[54] Z. Wang and S. M. Cohen, *J. Am. Chem. Soc.* **2007**, *129*, 12368-12369.
[55] S. M. Cohen, *Chem. Rev.* **2012**, *112*, 970-1000.

[56] S. Karmakar, S. Barman, F. A. Rahimi and T. K. Maji, *Energy Environ. Sci.* **2021**, *14*, 2429-2440.

[57] a) P. Falcaro, A. J. Hill, K. M. Nairn, J. Jasieniak, J. I. Mardel, T. J. Bastow, S. C. Mayo, M. Gimona, D. Gomez, H. J. Whitfield, R. Riccò, A. Patelli, B. Marmiroli, H. Amenitsch, T. Colson, L. Villanova and D. Buso, *Nat. Commun.* **2011**, *2*, 237; b) Q.-L. Zhu and Q. Xu, *Chem. Soc. Rev.* **2014**, *43*, 5468-5512; c) H. R. Moon, D.-W. Lim and M. P. Suh, *Chem. Soc. Rev.* **2013**, *42*, 1807-1824.

[58] H. Gu, C. Liu, J. Zhu, J. Gu, E. K. Wujcik, L. Shao, N. Wang, H. Wei, R. Scaffaro, J. Zhang and Z. Guo, *Advanced Composites and Hybrid Materials* **2018**, *1*, 1-5.

[59] A. Çalhan, S. Deniz, J. Romero and A. Hasanoğlu, *Korean J. Chem. Eng.* **2019**, *36*, 1489-1498.

[60] T.-H. Bae, J. S. Lee, W. Qiu, W. J. Koros, C. W. Jones and S. Nair, *Angew. Chem. Int. Ed.* **2010**, *49*, 9863-9866.

[61] T. Ben, C. Lu, C. Pei, S. Xu and S. Qiu, *Chem. Eur. J.* **2012**, *18*, 10250-10253.

[62] E. V. Perez, K. J. Balkus, J. P. Ferraris and I. H. Musselman, *J. Membr. Sci.* **2009**, *328*, 165-173.

[63] a) T. Uemura, S. Horike, K. Kitagawa, M. Mizuno, K. Endo, S. Bracco, A. Comotti, P. Sozzani, M. Nagaoka and S. Kitagawa, *J. Am. Chem. Soc.* **2008**, *130*, 6781-6788; b) T. Uemura, D. Hiramatsu, Y. Kubota, M. Takata and S. Kitagawa, *Angew. Chem. Int. Ed.* **2007**, *46*, 4987-4990; c) N. Yanai, T. Uemura, M. Ohba, Y. Kadowaki, M. Maesato, M. Takenaka, S. Nishitsuji, H. Hasegawa and S. Kitagawa, *Angew. Chem. Int. Ed.* **2008**, *47*, 9883-9886.

[64] B. Ghalei, K. Sakurai, Y. Kinoshita, K. Wakimoto, Ali P. Isfahani, Q. Song, K. Doitomi, S. Furukawa, H. Hirao, H. Kusuda, S. Kitagawa and E. Sivaniah, *Nat. Energy* **2017**, *2*, 17086.

[65] a) K. Xie, Q. Fu, P. A. Webley and G. G. Qiao, *Angew. Chem. Int. Ed.* **2018**, *57*, 8597-8602; b) H. T. Kwon and H.-K. Jeong, *J. Am. Chem. Soc.* **2013**, *135*, 10763-10768.

[66] a) W. Liang, L. Li, J. Hou, N. D. Shepherd, T. D. Bennett, D. M. D'Alessandro and V. Chen, *Chem. Sci.* **2018**, *9*, 3508-3516; b) X. Liu, N. K. Demir, Z. Wu and K. Li, *J. Am. Chem. Soc.* **2015**, *137*, 6999-7002.

[67] X. Li, Y. Liu, J. Wang, J. Gascon, J. Li and B. Van der Bruggen, *Chem. Soc. Rev.* **2017**, *46*, 7124-7144.

[68] D. T. Sun, N. Gasilova, S. Yang, E. Oveisi and W. L. Queen, *J. Am. Chem. Soc.* **2018**, *140*, 16697-16703.

[69] H. Liu, H. Zhu and S. Zhu, **2015**, *Macromol. Mater. Eng. 300*, 191-197.

[70] T. Uemura, S. Mochizuki and S. Kitagawa, *ACS Macro Lett.* **2015**, *4*, 788-791.

[71] a) W.-w. Zhan, Q. Kuang, J.-z. Zhou, X.-j. Kong, Z.-x. Xie and L.-s. Zheng, *J. Am. Chem. Soc.* **2013**, *135*, 1926-1933; b) F. Ke, L.-G. Qiu, Y.-P. Yuan, X. Jiang and J.-F. Zhu, *J. Mater. Chem.* **2012**, *22*, 9497-9500.

[72] a) R. Kumar, H.-T. Chen, J. L. V. Escoto, V. S. Y. Lin and M. Pruski, *Chem. Mater.* **2006**, *18*, 4319-4327; b) F. Hoffmann, M. Cornelius, J. Morell and M. Fröba, *Angew. Chem. Int. Ed.* **2006**, *45*, 3216-3251; c) I. I. Slowing, B. G. Trewyn, S. Giri and V. S.-Y. Lin, *Adv. Funct. Mater.* **2007**, *17*, 1225-1236.

[73] Z. Peng, **2004**, *43*, 930-935.

[74] H.-L. Jiang, B. Liu, Y.-Q. Lan, K. Kuratani, T. Akita, H. Shioyama, F. Zong and Q. Xu, *J. Am. Chem. Soc.* **2011**, *133*, 11854-11857.

[75] M. M. J. Treacy, T. W. Ebbesen and J. M. Gibson, *Nature* **1996**, *381*, 678-680.

[76] X. Huang, X. Qi, F. Boey and H. Zhang, *Chem. Soc. Rev.* **2012**, *41*, 666-686.

[77] R. Kumar, D. Raut, U. Ramamurty and C. N. R. Rao, *Angew. Chem. Int. Ed.* **2016**, *55*, 7857-7861.

[78] A. Chakraborty, P. Sutar, P. Yadav, M. Eswaramoorthy and T. K. Maji, *Inorg. Chem.* **2018**, *57*, 14480-14483.

[79] a) A. Chakraborty, A. Achari, M. Eswaramoorthy and T. K. Maji, *Chem. Commun.* **2016**, *52*, 11378-11381; b) A. Chakraborty, S. Roy, M. Eswaramoorthy and T. K. Maji, *J. Mater. Chem. A* **2017**, *5*, 8423-8430; c) A. Chakraborty, S. Laha, K. Kamali, C. Narayana, M. Eswaramoorthy and T. K. Maji, *Inorg. Chem.* **2017**, *56*, 9426-9435.

[80] R. Kumar, K. Jayaramulu, T. K. Maji and C. N. R. Rao, *Chem. Commun.* **2013**, *49*, 4947-4949.

[81] R. Kumar, K. Jayaramulu, T. K. Maji and C. N. R. Rao, *Dalton Trans.* **2014**, *43*, 7383-7386.

[82] a) J. Kim, S.-T. Yang, S. B. Choi, J. Sim, J. Kim and W.-S. Ahn, *J. Mater. Chem.* **2011**, *21*, 3070-3076; b) M. D. Allendorf, R. J. T. Houk, L. Andruszkiewicz, A. A. Talin, J. Pikarsky, A. Choudhury, K. A. Gall and P. J. Hesketh, *J. Am. Chem. Soc.* **2008**, *130*, 14404-14405.

[83] Y. E. Cheon and M. P. Suh, *Angew. Chem. Int. Ed.* **2009**, *48*, 2899-2903.

[84] C.-Y. Sun, S.-X. Liu, D.-D. Liang, K.-Z. Shao, Y.-H. Ren and Z.-M. Su, *J. Am. Chem. Soc.* **2009**, *131*, 1883-1888.

[85] a) C. Liu, L. Lin, Q. Sun, J. Wang, R. Huang, W. Chen, S. Li, J. Wan, J. Zou and C. Yu, *Chem. Sci.* **2020**, *11*, 3680-3686; b) H.-L. Tang, X.-J. Sun and F.-M. Zhang, *Dalton Trans.* **2020**, *49*, 12136-12144; c) T. Gadzikwa, O. K. Farha, C. D. Malliakas, M. G. Kanatzidis, J. T. Hupp and S. T. Nguyen, *J. Am. Chem. Soc.* **2009**, *131*, 13613-13615; d) Y. Chen, V. Lykourinou, C. Vetromile, T. Hoang, L.-J. Ming, R. W. Larsen and S. Ma, *J. Am. Chem. Soc.* **2012**, *134*, 13188-13191; e) D. Cunha, C. Gaudin, I. Colinet, P. Horcajada, G. Maurin and C. Serre, *J. Mater. Chem. B* **2013**, *1*, 1101-1108.

[86] a) M. Rubio-Martinez, C. Avci-Camur, A. W. Thornton, I. Imaz, D. Maspoch and M. R. Hill, *Chem. Soc. Rev.* **2017**, *46*, 3453-3480; b) N. Stock and S. Biswas, *Chem. Rev.* **2012**, *112*, 933-969.

[87] A. Rabenau, *Angew. Chem. Int. Ed.* **1985**, *24*, 1026-1040.

[88] a) J. Cravillon, S. Münzer, S.-J. Lohmeier, A. Feldhoff, K. Huber and M. Wiebcke, *Chem. Mater.* **2009**, *21*, 1410-1412; b) D. J. Tranchemontagne, J. R. Hunt and O. M. Yaghi, *Tetrahedron* **2008**, *64*, 8553-8557.

[89] a) M. Jian, H. Liu, T. Williams, J. Ma, H. Wang and X. Zhang, *Chem. Commun.* **2017**, *53*, 13161-13164; b) S. Bauer and N. Stock, *Angew. Chem. Int. Ed.* **2007**, *46*, 6857-6860.

[90] B. F. Hoskins and R. Robson, *J. Am. Chem. Soc.* **1990**, *112*, 1546-1554.

[91] F. Millange, R. El Osta, M. E. Medina and R. I. Walton, *CrystEngComm* **2011**, *13*, 103-108.

[92] a) E. Haque, N. A. Khan, J. H. Park and S. H. Jhung, *Chem. Eur. J.* **2010**, *16*, 1046-1052; b) T. Ahnfeldt, J. Moellmer, V. Guillerm, R. Staudt, C. Serre and N. Stock, *Chem. Eur. J.* **2011**, *17*, 6462-6468.

[93] J.-Y. Choi, J. Kim, S.-H. Jhung, H.-K. Kim, J.-S. Chang and K. Chae Hee, *Bull. Korean Chem. Soc.* **2006**, *27*, 1523-1524.

[94] Z. Ni and R. I. Masel, *J. Am. Chem. Soc.* **2006**, *128*, 12394-12395.

[95] C.-M. Lu, J. Liu, K. Xiao and A. T. Harris, *Chem. Eng. J.* **2010**, *156*, 465-470.

[96] M. Schlesinger, S. Schulze, M. Hietschold and M. Mehring, *Microporous Mesoporous Mater.* **2010**, *132*, 121-127.

[97] R. Ameloot, L. Pandey, M. V. d. Auweraer, L. Alaerts, B. F. Sels and D. E. De Vos, *Chem. Commun.* **2010**, *46*, 3735-3737.

[98] M. Klimakow, P. Klobes, A. F. Thünemann, K. Rademann and F. Emmerling, *Chem. Mater.* **2010**, *22*, 5216-5221.

[99] a) A. Pichon and S. L. James, *CrystEngComm* **2008**, *10*, 1839-1847; b) H. Yang, S. Orefuwa and A. Goudy, *Microporous Mesoporous Mater.* **2011**, *143*, 37-45.
[100] a) S. Bhattacharyya, D. Rambabu and T. K. Maji, *J. Mater. Chem. A* **2019**, *7*, 21106-21111; b) D. Rambabu, S. Bhattacharyya, T. Singh, C. M. L and T. K. Maji, *Inorg. Chem.* **2020**, *59*, 1436-1443.
[101] Q. Min Wang, D. Shen, M. Bülow, M. Ling Lau, S. Deng, F. R. Fitch, N. O. Lemcoff and J. Semanscin, *Microporou Mesoporous Mater.* **2002**, *55*, 217-230.
[102] J. L. Humphrey and G. E. Keller, **1997**.
[103] R. Monastersky, *Nature* **2013**, *497*, 13-14.
[104] a) S. Mukherjee, A. Kumar and M. J. Zaworotko in *2 - Metal-organic framework based carbon capture and purification technologies for clean environment*, (Ed. S. K. Ghosh), Elsevier, **2019**, pp. 5-61; b) J. Yu, L.-H. Xie, J.-R. Li, Y. Ma, J. M. Seminario and P. B. Balbuena, *Chem. Rev.* **2017**, *117*, 9674-9754.
[105] a) H. Li, C. E. Davis, T. L. Groy, D. G. Kelley and O. M. Yaghi, *J. Am. Chem. Soc.* **1998**, *120*, 2186-2187; b) A. R. Millward and O. M. Yaghi, *J. Am. Chem. Soc.* **2005**, *127*, 17998-17999.
[106] J. A. Mason, K. Sumida, Z. R. Herm, R. Krishna and J. R. Long, *Energy Environ. Sci.* **2011**, *4*, 3030-3040.
[107] a) W. Zhou, H. Wu and T. Yildirim, *J. Am. Chem. Soc.* **2008**, *130*, 15268-15269; b) S. R. Caskey, A. G. Wong-Foy and A. J. Matzger, *J. Am. Chem. Soc.* **2008**, *130*, 10870-10871.
[108] S. Roy, S. Laha and T. K. Maji in *10 - Potential of hydrophobic metal-organic framework-based materials for environmental applications*, (Ed. S. K. Ghosh), Elsevier, **2019**, pp. 319-354.
[109] a) R. W. Flaig, T. M. Osborn Popp, A. M. Fracaroli, E. A. Kapustin, M. J. Kalmutzki, R. M. Altamimi, F. Fathieh, J. A. Reimer and O. M. Yaghi, *J. Am. Chem. Soc.* **2017**, *139*, 12125-12128; b) A. M. Fracaroli, H. Furukawa, M. Suzuki, M. Dodd, S. Okajima, F. Gándara, J. A. Reimer and O. M. Yaghi, *J. Am. Chem. Soc.* **2014**, *136*, 8863-8866.
[110] a) M. M. Sadiq, M. P. Batten, X. Mulet, C. Freeman, K. Konstas, J. I. Mardel, J. Tanner, D. Ng, X. Wang, S. Howard, M. R. Hill and A. W. Thornton, *Adv. Sustain. Syst.* **2020**, *4*, 2000101; b) A. Kumar, D. G. Madden, M. Lusi, K.-J. Chen, E. A. Daniels, T. Curtin, J. J. Perry Iv and M. J. Zaworotko, *Angew. Chem. Int. Ed.* **2015**, *54*, 14372-14377.
[111] T. Kajiwara, M. Fujii, M. Tsujimoto, K. Kobayashi, M. Higuchi, K. Tanaka and S. Kitagawa, *Angew. Chem. Int. Ed.* **2016**, *55*, 2697-2700.
[112] D. S. Sholl and R. P. Lively, *Nature* **2016**, *532*, 435-437.
[113] J.-R. Li, R. J. Kuppler and H.-C. Zhou, *Chem. Soc. Rev.* **2009**, *38*, 1477-1504.
[114] a) N. L. Rosi, J. Kim, M. Eddaoudi, B. Chen, M. O'Keeffe and O. M. Yaghi, *J. Am. Chem. Soc.* **2005**, *127*, 1504-1518; b) P. D. C. Dietzel, Y. Morita, R. Blom and H. Fjellvåg, *Angew. Chem. Int. Ed.* **2005**, *44*, 6354-6358.
[115] Z. Bao, S. Alnemrat, L. Yu, I. Vasiliev, Q. Ren, X. Lu and S. Deng, *Langmuir* **2011**, *27*, 13554-13562.
[116] E. D. Bloch, W. L. Queen, R. Krishna, J. M. Zadrozny, C. M. Brown and J. R. Long, *Science* **2012**, *335*, 1606-1610.
[117] L. Li, R.-B. Lin, R. Krishna, H. Li, S. Xiang, H. Wu, J. Li, W. Zhou and B. Chen, *Science* **2018**, *362*, 443.
[118] K.-J. Chen, D. G. Madden, S. Mukherjee, T. Pham, K. A. Forrest, A. Kumar, B. Space, J. Kong, Q.-Y. Zhang and M. J. Zaworotko, *Science* **2019**, *366*, 241.
[119] a) S. Qiu, M. Xue and G. Zhu, *Chem. Soc. Rev.* **2014**, *43*, 6116-6140; b) Q. Qian, P. A. Asinger, M. J. Lee, G. Han, K. Mizrahi Rodriguez, S. Lin, F. M. Benedetti, A. X. Wu, W. S. Chi and Z. P. Smith, *Chem. Rev.* **2020**, *120*, 8161-8266.

[120] L. Mi, J. Sui, Y. Wu, G. Liang, Y. Zhang, Y. Pu, Y. Tian, S. Liu and L. Jiang, *Anal. Chem.* **2019**, *91*, 15804-15810.

[121] a) L. Alaerts, C. E. A. Kirschhock, M. Maes, M. A. van der Veen, V. Finsy, A. Depla, J. A. Martens, G. V. Baron, P. A. Jacobs, J. F. M. Denayer and D. E. De Vos, *Angew. Chem. Int. Ed.* **2007**, *46*, 4293-4297; b) L. Alaerts, M. Maes, L. Giebeler, P. A. Jacobs, J. A. Martens, J. F. M. Denayer, C. E. A. Kirschhock and D. E. De Vos, *J. Am. Chem. Soc.* **2008**, *130*, 14170-14178; c) M. A. Moreira, J. C. Santos, A. F. P. Ferreira, J. M. Loureiro, F. Ragon, P. Horcajada, K.-E. Shim, Y.-K. Hwang, U. H. Lee, J.-S. Chang, C. Serre and A. E. Rodrigues, *Langmuir* **2012**, *28*, 5715-5723.

[122] B. Van de Voorde, B. Bueken, J. Denayer and D. De Vos, *Chem. Soc. Rev.* **2014**, *43*, 5766-5788.

[123] H. Kim, S. Yang, S. R. Rao, S. Narayanan, E. A. Kapustin, H. Furukawa, A. S. Umans, O. M. Yaghi and E. N. Wang, *Science* **2017**, *356*, 430.

[124] a) F. Fathieh, M. J. Kalmutzki, E. A. Kapustin, P. J. Waller, J. Yang and O. M. Yaghi, *Sci. Adv.* **2018**, *4*, eaat3198; b) H. Kim, S. R. Rao, E. A. Kapustin, L. Zhao, S. Yang, O. M. Yaghi and E. N. Wang, *Nat. Commun.* **2018**, *9*, 1191; c) N. Hanikel, M. S. Prévot, F. Fathieh, E. A. Kapustin, H. Lyu, H. Wang, N. J. Diercks, T. G. Glover and O. M. Yaghi, *ACS Cent. Sci.* **2019**.

[125] a) A. Karmakar, P. G. M. Mileo, I. Bok, S. B. Peh, J. Zhang, H. Yuan, G. Maurin and D. Zhao, *Angew. Chem. Int. Ed.* **2020**, *59*, 11003-11009; b) J. Xu, T. Li, J. Chao, S. Wu, T. Yan, W. Li, B. Cao and R. Wang, *Angew. Chem. Int. Ed.* **2020**, *59*, 5202-5210; c) G. Yilmaz, F. L. Meng, W. Lu, J. Abed, C. K. N. Peh, M. Gao, E. H. Sargent and G. W. Ho, *Sci. Adv.* **2020**, *6*, eabc8605.

[126] a) D. Ma, P. Li, X. Duan, J. Li, P. Shao, Z. Lang, L. Bao, Y. Zhang, Z. Lin and B. Wang, *Angew. Chem. Int. Ed.* **2020**, *59*, 3905-3909; b) P. K. Tsobnang, E. Hastürk, D. Fröhlich, E. Wenger, P. Durand, J. L. Ngolui, C. Lecomte and C. Janiak, *Cryst. Growth Des.* **2019**, *19*, 2869-2880; c) R. G. AbdulHalim, P. M. Bhatt, Y. Belmabkhout, A. Shkurenko, K. Adil, L. J. Barbour and M. Eddaoudi, *J. Am. Chem. Soc.* **2017**, *139*, 10715-10722.

[127] a) M. F. de Lange, K. J. F. M. Verouden, T. J. H. Vlugt, J. Gascon and F. Kapteijn, *Chem. Rev.* **2015**, *115*, 12205-12250; b) X. Liu, X. Wang and F. Kapteijn, *Chem. Rev.* **2020**, *120*, 8303-8377.

[128] D. Lenzen, J. Zhao, S.-J. Ernst, M. Wahiduzzaman, A. Ken Inge, D. Fröhlich, H. Xu, H.-J. Bart, C. Janiak, S. Henninger, G. Maurin, X. Zou and N. Stock, *Nat. Commun.* **2019**, *10*, 3025.

[129] K. H. Cho, D. D. Borges, U. H. Lee, J. S. Lee, J. W. Yoon, S. J. Cho, J. Park, W. Lombardo, D. Moon, A. Sapienza, G. Maurin and J.-S. Chang, *Nat. Commun.* **2020**, *11*, 5112.

[130] a) B.-M. Jun, Y. A. J. Al-Hamadani, A. Son, C. M. Park, M. Jang, A. Jang, N. C. Kim and Y. Yoon, *Sep. Purif. Technol.* **2020**, *247*, 116947; b) M. Kadhom and B. Deng, *Appl. Mater. Today* **2018**, *11*, 219-230; c) V. Russo, M. Hmoudah, F. Broccoli, M. R. Iesce, O.-S. Jung and M. Di Serio, *Front. Chem. Eng.* **2020**, *2*, 15.

Chapter 2

MOFs with Hierarchical Porosity

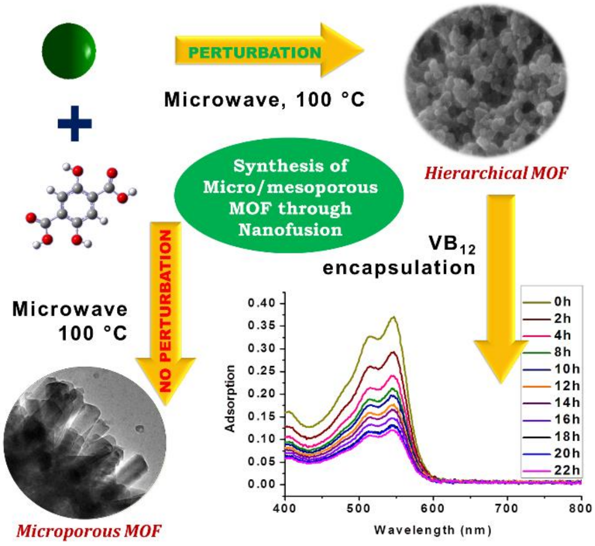

2.1: Synergistic Role of Microwave and Perturbation toward Synthesis of Hierarchical Porous MOFs with Tunable Porosity

A Manuscript based on this work has been published in Inorg. Chem. 2020, 59, 6, 3775.

Abstract

Creating hierarchical porosity in MOFs has attracted significant interest due to their immense potential in a wide range of applications from materials to life science. Herein, the work reports a unique methodology of combining perturbation-assisted nanofusion (PNF) with microwave (MW) stimuli to generate wide additional pores from (5-18) nm in the prototype MOF, Ni-MOF-74. An optimized combination of microwave exposure, perturbation in form of stirring, and solvent effect induce additional mesoscale porosity by fusion of MOF nanoparticles. The effect of microwave is realized by varying reaction time and medium using a range of solvents having different dielectric constants (DMSO, DMF, DMA, Acetone, EA, and THF). This chapter projects to generate a wide scale mesopore by fusion of nanoscale microporous MOF within a short reaction time by vigorous stirring, without using any template. This additional mesopore, thus generated, has been exploited by encapsulating 4.6 $\mu molg^{-1}$ of large bio-molecule Vitamin B_{12} (VB_{12}).

2.1.1: Introduction

Structural adaptation at the level of hierarchy is the key parameter for all-natural entities to exhibit exceptional robustness against environmental alterations with evolution.[1] An imitation of such natural functionalities in artificial domains can enhance their performance.[2] Hierarchically porous structures are constructed by multimodal interconnected pores with different lengths such as micro (<2 nm), meso (2-50 nm), and macropores (>50 nm). Recent times have witnessed significant developments for the synthesis of hierarchically porous metal-organic framework (MOF) materials having specific applications in catalysis,[3] separation,[4] biology,[5] and on several energy storage devices[6] based on higher storage capacity and increased mass transfer kinetics.[7] Most of the MOFs reported are microporous in nature; however, by increasing length of the linkers, several mesoporous MOFs have been synthesized and characterized.[8] But they often suffer from structural fragility and interpenetration.[8b, c, 9] Hierarchical MOFs with micro and mesoporosity show performances as a carrier for large dyes, drugs and different large biomolecules like proteins and enzymes.[10] Different approaches such as supramolecular or triblock copolymer surfactant assisted method,[11] microwave assisted synthesis,[12] solvent evaporation diffusion method,[13] and ionic liquid/ CO_2/ surfactant[14] systems have been demonstrated to synthesize hierarchically porous MOFs. Such MOFs are synthesized from microporous one via several routes of modification have drawbacks of small mesopores (~4-5 nm) with poor stability and require high temperature treatment to remove the surfactants.[11b, 15] The sporadic success of these methodologies of hierarchical MOFs has its own pros and cons and a universal straightforward synthetic method is yet to be developed. As a solution to this, one of the approaches in this regard is to treat the solvent as a template in order to generate hierarchy. One of the rarely attempted methods is perturbation assisted nanofusion (PNF), a method of fusing MOF nanoparticles with the benefit of strong stirring, which encourages the rate of particle condensation over crystallization leading to aggregation of these MOF nanoparticles towards the formation of mesopores.[16] In recent years, Yue et al. demonstrated PNF method in solvothermal conditions to prepare hierarchical IRMOF-3, Cu-BDC, and Cu-BTEC.[17] Later on, Dai and co-workers demonstrated a surfactant-free methodology for the room-temperature solvothermal synthesis of Zn-MOF-74 with mesopore exceeding 15 nm.[18]

This chapter unfolds a surfactant-free and fast methodology for the synthesis of hierarchical microporous-mesoporous MOF, HNi-MOF-74 (H stands for hierarchical) having the formula $[Ni_2(DHBDC).(guest)_n]$ (DHBDC= 2,5-dihydroxy-1,4-benzenedicarboxylate) with variable time by employing PNF in presence of microwave radiation using DMF: Water: EtOH (1/1/1) solvent mixture.[19] Microwave synthesis, at one stroke, reduces the reaction time as well as highlights the effect of solvent participation. The reaction time was varied to study the mechanism and the rate of mesopore formation with time. Interestingly, the product yield increases with time and finally, within 50 minutes of reaction time mesopore volume reaches its maxima with high surface area. The reaction in microwave mostly results from thermal effect originated from dipolar polarization of solvent as a consequence of dipole-dipole interaction between polar molecules and electromagnetic field. A series of solvents has been chosen with an ascending order of dielectric constants like ethyl acetate, THF, acetone, DMA and DMSO by replacing DMF from the solvent mixture used for the synthesis of HNi-MOF-74. The study reveals that increased solvent polarity micro/mesopore volume ratio also increases at a particular temperature. Furthermore, the meso-sized pore (~5-18 nm) in

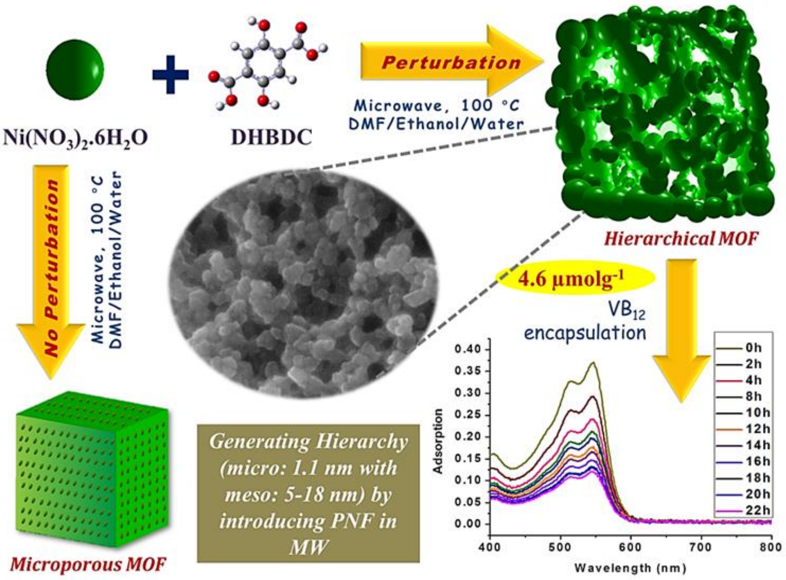

Scheme 1. Schematic representation of synthesis of HNi-MOF-74 and utilization of mesopore by encapsulating VB_{12}.

the MOF has been utilized by encapsulating nanosized Vitamin B_{12} (VB_{12}; 1.0× 1.6× 1.7 nm) (Scheme 1).[20] This work demonstrates an in-depth mechanistic study by creating hierarchical porosity in MOF-74 through a fast and facile route.

2.1.2: Experimental section

2.1.2.1: Materials

All the reagents and solvents were commercially available and used as obtained from commercial supplies without any further purification. $Ni(NO_3)_2.6H_2O$ and 2,5-dihydroxy-1,4-benzenedicarboxylic acid were obtained from Sigma Aldrich Chemical Co. N,N-dimethyl formamide (DMF), dimethyl sulphoxide (DMSO), ethyl acetate, dimethylacetamide (DMA), acetone and tetrahydrofuran (THF) were obtained from Spectrochem Pvt. Ltd (Mumbai, India).

2.1.2.2: Synthesis

Synthesis of HNi-MOF-74/t: To prepare Ni-MOF-74/50, 0.198g of $Ni(NO_3)_2.6H_2O$ (0.6811 mmol, 3.4 equiv) and 0.037g of 2,5-dihydroxy-1,4-benzenedicarboxylate (0.1968 mmol, 1 equiv) were dissolved in a 1:1:1 (v/v/v) combination of DMF (5.5 mL), ethanol (5.5 mL), water (5.5 mL) and stirred for 1 h. Then the reaction mixture is transferred to microwave reactor. The reaction mixture is heated to 100 °C in 20 min (a heating rate of 5 °C /min) and held at 100 °C for 40 minutes. The microwave power was controlled 850 W over the whole process with a constant 800 rpm stirring. Finally, it was collected in fresh DMF and washed subsequently with DMF and MeOH for 4 days.

A Similar method was followed to prepare all Ni-MOF-74-DMF/t where t (t stands for time in minutes) varies from 20, 30, 50, 60, and 70 minutes in order to cognize the role of perturbation (or stirring) in microwave.

Similarly, the analogous experiments to Ni-MOF-74-DMF/50 were performed under microwave at 850 W with 0 rpm stirring (i.e., without stirring) which revealed a typical type-I isotherm of microporous MOF and the compound was mentioned as Ni-MOF-74/50W (5).

Synthesis of HNi-MOF-74 by varying solvent polarity: A series of solvents have been chosen with increasing polarity, different dimensions and functional groups starting from Ethyl acetate to DMSO. $Ni(NO_3)_2.6H_2O$ (3.4 equiv.) and of 2,5-dihydroxy-1,4-benzenedicarboxylate (1 equiv.) was dissolved in a 1:1:1 (v/v/v) combination of DMSO (5.5 mL), ethanol (5.5 mL), water (5.5 mL) and stirred for 1 h. The rest of the synthesis methods are identical to the previous one and named this material as HNi-MOF-74-DMSO/50 (10). Similarly, 5.5 mL of DMA, Acetone, THF and ethyl acetate are used to prepare HNi-MOF-74-DMA/50, HNi-MOF-74-Acetone/50, HNi-MOF-74-THF/50, and HNi-MOF-74-EA/50 under identical conditions with 800 rpm stirring.

2.1.2.3: Physical measurements

Powder X-ray diffraction (PXRD) patterns were recorded on a Bruker D8 Discover instrument using Cu–Kα radiation Bruker D8 (40 kV, 30 MA). Thermo gravimetric analysis (TGA) was carried out (Mettler Toledo) in N_2 atmosphere (flow rate = 50 ml min^{-1}) in the temperature range 30 – 800 °C with 5 °C min^{-1} heating rate. UV–Vis spectra of samples were recorded on a Perkin Elmer Model Lambda 900 spectrophotometer. Infrared spectral studies were performed by making samples with KBr pellets using Bruker FTIR spectrometer in the region of 4000–400 cm^{-1}. The scanning electron microscopy images were obtained by using a Nova Nanosem 600 FEI field emission scanning electron microscope (FESEM) with an accelerating voltage of 10 kV. Energy dispersive analysis of X-rays (EDX) was carried out using the field emission scanning electron microscope. Transmission electron microscopy (TEM) images were taken with a JEOL JEM-3010 transmission electron microscope operating at 200 kV. The samples for FESEM and EDX were prepared by dispersing the sample in methanol then dropping the solution onto a piece of Silicon wafer. Similarly, for TEM, samples were prepared as previously mentioned method by drop-casting methanolic dispersion onto a carbon-coated grid. Reactions under microwave stimuli were carried by transferring reaction mixture in 30 mL wide-neck vials by using MONOWAVE 200 (Anton Paar Monowave Series; Serial Number: 81919734; Instrument Software Version: 4.10.9376.7) microwave reactor. Adsorption measurements were carried out using AUTOSORB IQ_2 and QUNATACHROME QUADRASORD-SI instruments for N_2 (77 K) and CO_2 (273 and 298 K). Approximately 100-150 mg samples were placed which had been prepared at 200 °C under a 1×10^{-1} Pa vacuum for about 12 h prior to each measurement of the isotherms. Ultrapure Helium gas at a certain pressure was allowed to diffuse into the sample cell for operating valve functions and dead volume measurement. The activated sample was placed into the sample cell (9 mm diameter), then the change of the pressure was monitored and the degree of adsorption was determined by the decrease in pressure at the equilibrium state. However, all the operations were computer controlled and instinctive. Water vapor adsorptions were carried out at 298 K using BELSORP AQUA 3 solvent vapor analyzer. The sample preparation and measurement principle in solvent vapor adsorption were analogous to gas adsorption measurement.

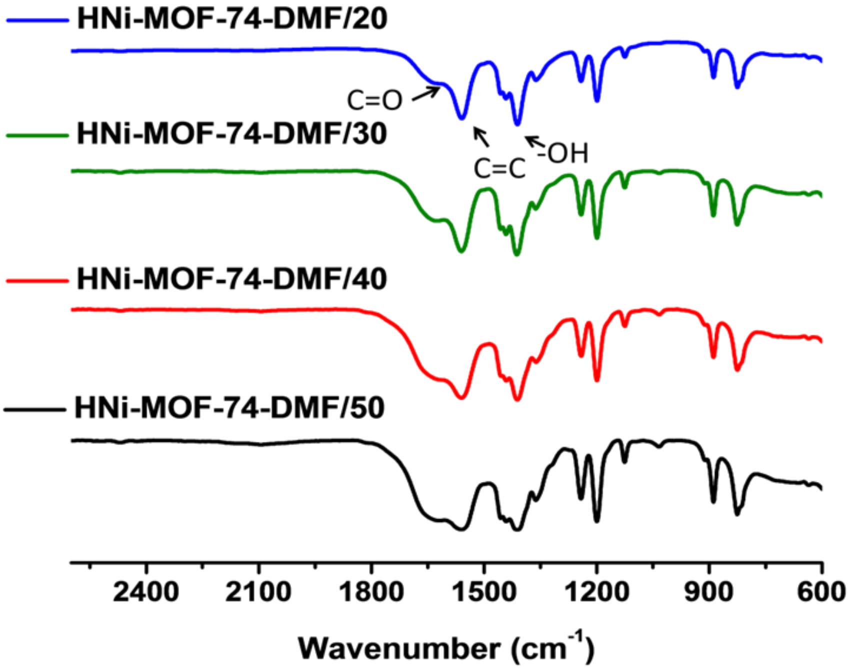

Figure 1: FT-IR spectra of HNi-MOF-74-DMF/t.

2.1.2.4: Analysis from gas adsorption isotherm

The surface area, pore volume and pore size distribution were calculated from the N_2 adsorption data of the corresponding samples using the ASiQwin software. The surface area was calculated using the Brunauer–Emmett–Teller (BET) theory, which is an extension from monolayer to multilayer adsorption. The BET equation is:

$$\frac{1}{v[\frac{P_0}{P}]}=\frac{C-1}{Cv_m}(P/P_0)+\frac{1}{Cv_m}$$

Where P and P_0 are the equilibrium and the saturation pressure of adsorbates at adsorption temperature, v is the adsorbed gas quantity, and v_m is the monolayer adsorbed gas quantity; C is the BET constant and can be expressed as:

$C = \exp((E_1-E_L)/RT)$

E_1 is the heat of adsorption for the first layer, and E_L is that for the second and higher layers. The BET equation is an adsorption isotherm and can be plotted as a straight line with 1/ [v(P_0/P)−1] on the y-axis and P/P_0 on the x-axis according to the experimental N_2 isotherms. The value of the slope and the y-intercept of the straight line can be used to calculate the monolayer adsorbed gas quantity (v_m) and the BET constant. The total surface area S_{total} and the specific surface area S_{BET} are given by:

$S_{total} = (v_m Ns)/v$

$S_{BET} = S_{total}/a$

Where N is the Avogadro number, s is the adsorption cross-section of the adsorbing species, V is the molar volume of the N_2 (adsorbed gas), and a is the mass of the solid adsorbent. The multi-point BET surface area was calculated for different samples using ASiQwin software in the P/P_0 range 0.05 to 0.30 approximately.

The total pore volume is calculated from the amount of vapor adsorbed at a relative pressure close to unity, by assuming that the pores are then filled with liquid adsorbate. The pore volume and pore size distributions were calculated using the Density Functional Theory (DFT), which can provide sorption and phase behavior of fluids in narrow pores on a molecular level. Indeed, the Non-Local Density Functional Theory (NLDFT) and Grand Canonical Monte Carlo simulation (GCMC) methods can describe the local fluid structure near curved solid walls accurately; the adsorption isotherms in model pores are determined from intermolecular potentials of the liquid-liquid and solid-liquid interactions. The relation between isotherms derived from the above approaches and the experimental isotherm on a porous solid can be interpreted in terms of a Generalized Adsorption Isotherm (GAI) equation:

$$N\left(\frac{P}{P_0}\right) = \int_{W_{min}}^{W_{max}} N(\frac{P}{P_0}, W) f(W) dW$$

Where, $N(P/P_0)$ = experimental adsorption isotherm data

W = pore width

$N(P/P_0,W)$ = isotherm on a single pore of width W

f(W) = pore size distribution function

The assumption which is reflected from the GAI equation is that the total isotherm consists of the number of individuals "single pore" isotherms multiplied by their relative distribution, f(W), over a range of pore sizes. The set of $N(P/P_0, W)$ isotherms (kernel) for a given system can be obtained by the DFT as indicated above. The pore size distribution can then be derived by solving the GAI equation numerically via a fast non-negative least square algorithm. The ASiQwin software has been used to calculate the pore size distribution using the NLDFT–N_2-carbon equilibrium transition kernel at 77 K based on a slit-pore model.

Determining t-plot: Statistical thickness: To determine micropore volume for a hierarchical system t-plot (volume *vs.* statistical thickness; *t*) is highly recommended. The *t* can be calculated independently by using the equation:

$$t(\text{Å}) = \frac{10^4 V_{liq}}{S_{BET}}$$

Using this equation, a V vs. t plot is constructed from t vs. P/P_0 data for a sample. The micropore surface areas can be calculated from the slopes and each successive interval calculation represents the area of all the micropores remaining unfilled. The calculations are continued until no further decrease in slope is found in the V *vs.* t plot, indicating that all the micropores have been filled.

2.1.3: Result and discussion

2.1.3.1: Impact of time and stirring to generate hierarchy under microwave

Microporous MOF-74 or CPO-27 series with the formula $[M_2(DHBDC)(guest)]$, $[M^{2+}$= Mg, Ni, Zn, Co, Fe; DHBDC= 2,5-dihydroxy-1,4-benzenedicarboxylate], have been extensively explored because of its high surface area and extraordinary performance of separating CO_2 from H_2 and N_2 or separation of light hydrocarbons in adsorptive process.[6c, 21] To understand the effect of microwave assisted synthetic method on porosity in the prototype microporous MOF, the adsorption behavior of the solvothermally prepared Ni-MOF-74 has been studied and related it with perturbation integrated microwave-assisted method for synthesizing hierarchically porous Ni-MOF-74 (Figure 2). The study revealed that the BET (Brunauer-Emmett-Teller) surface area is 1096 and 798 m^2/g for Ni-MOF-74-SOL and Ni-MOF-74-DMF/50W (where W stands for without perturbation) respectively, which exhibits a type-I adsorption profile, synthesized by the way of usual

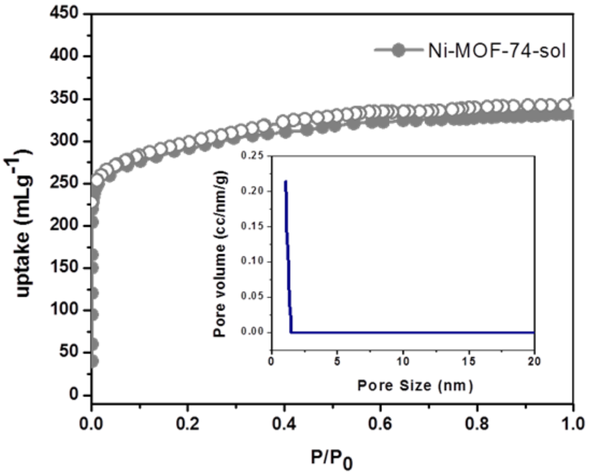

Figure 2: N$_2$ Adsorption Isotherm for solvothermally prepared Ni-MOF-74-SOL with pore size distribution derived through NLDFT method (inset).

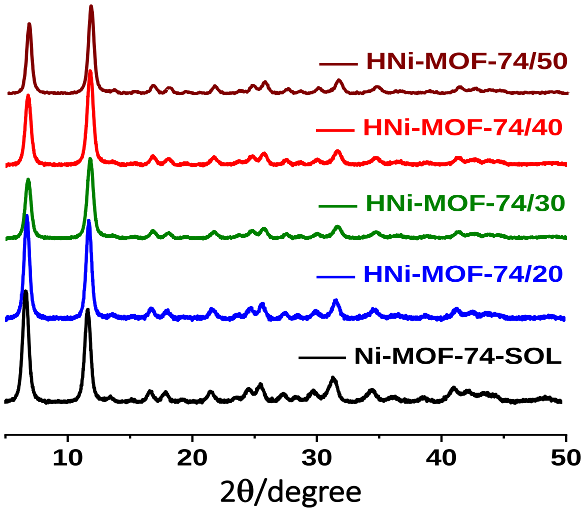

Figure 3: Powder XRD pattern of solvothermally prepared microporous Ni-MOF-74 (black) and of HNi-MOF-74/t prepared with different reaction times.

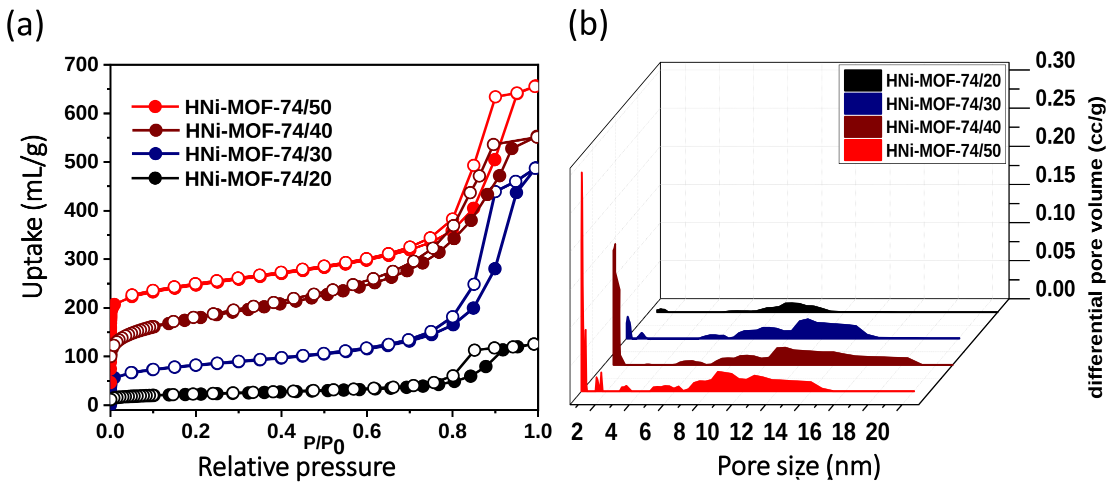

Figure 4: (a) N_2 adsorption isotherm of HNi-MOF-74-DMF/t (b) NLDFT pore size distribution of HNi-MOF-74-DMF/t.

solvothermal and microwave methods. The pore size calculation based on NLDFT method showed only micropore centered at 1.1 nm without any mesopore. Microwave-assisted method dramatically reduces the time with respect to solvothermally synthesized MOF-74. By keeping the reaction mixture 40 minutes (HNi-MOF-74-DMF/40) under microwave with the help of strong stirring, a hierarchical MOF with the surface area of 522 m^2/g (Figure 4) has been developed. The N_2 adsorption isotherm reveals an intermediate isotherm between type-I, which suggests the presence of microporosity and type-IV, which is related to mesoporosity with 0.369 micropore-to-mesopore volume ratio (V_{micro}/V_{meso}). To understand the time dependency for mesopore generation, additional three different hierarchical MOFs were synthesized by varying reaction time; t= 20, 30 and 50 minutes. Four MOFs were prepared as described in the experimental section and their PXRD patterns disclosed the presence of the pure phase of MOF-74 and compared with solvothermally prepared microporous Ni-MOF-74 (Figure 3). Figure 4a showed representative N_2 adsorption-desorption isotherm for HNi-MOF-74-DMF/20 (1), HNi-MOF-74-DMF/30 (2), HNi-MOF-74- DMF/40 (3), and HNi-MOF-74-DMF/50 (4). Prior to the adsorption measurement samples were activated at 200 °C under 10^{-1} Pa vacuum to remove the entrapped solvent molecules. In contrast to typical type-I isotherm of microporous Ni-MOF-74, type-IV isotherms with prominent hysteresis loops are observed for all HNi-MOF-74/t materials which are characteristic of large constricted mesopore (Figure 4a). The hysteresis at higher relative pressure and calculated pore size distributions by NLDFT method suggest the presence of additional mesopore along with

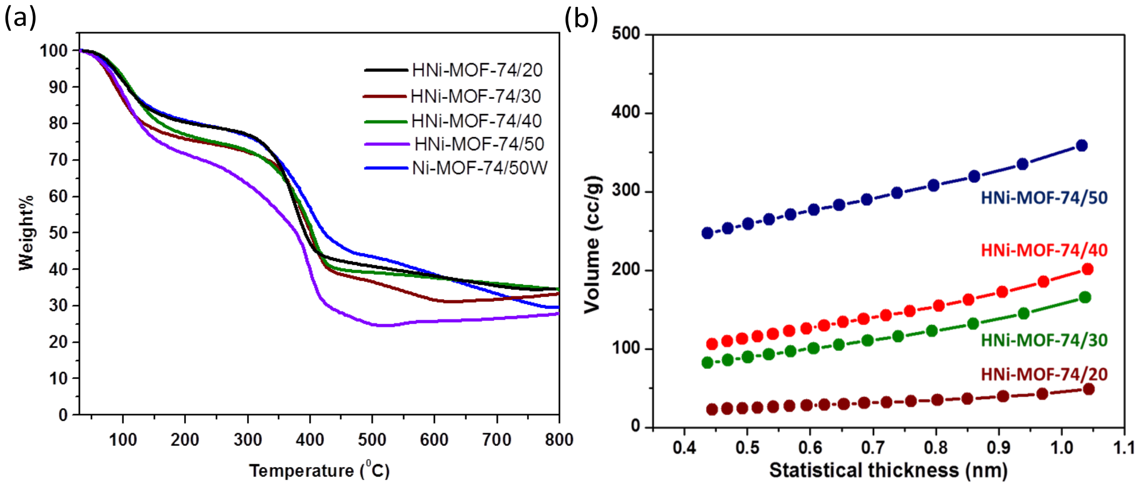

Figure 5: (a) TGA profile and (b) t-plot for all HNi-MOF-74/t calculated from N_2 adsorption isotherm in the P/P_0 range of 0.20 –0.50.

the characteristic micropore (1.1 nm) of MOF-74 in all the materials of HNi-MOF-74/t series (Figure 4b). The apparent surface areas were determined with the BET model in the range between P/P_0 ~0.05-0.30. The total pore volume was evaluated at $P/P_0 = 0.99$. BET surface area for 1, 2, 3 and 4 are 89, 265, 522, and 780 m^2/g that increase with time. Furthermore, N_2 adsorption capacity for 1, 2, 3 and 4 (12, 52, 123, 208 cm^3g^{-1} respectively) are observed for these mesostructured MOFs, even when the relative pressure (P/P_0) was as low as 0.008, suggesting the microporous contribution and it increases with increasing reaction time. Interestingly, the yield % (by assuming 100% conversation) was noticeably low for t = 20 and 30 (22% and 39%, respectively) whereas for t = 40 and 50 it was 51% and 67%. Probably, all these materials contain different amounts of non-crystalline material (especially at low reaction time) due to

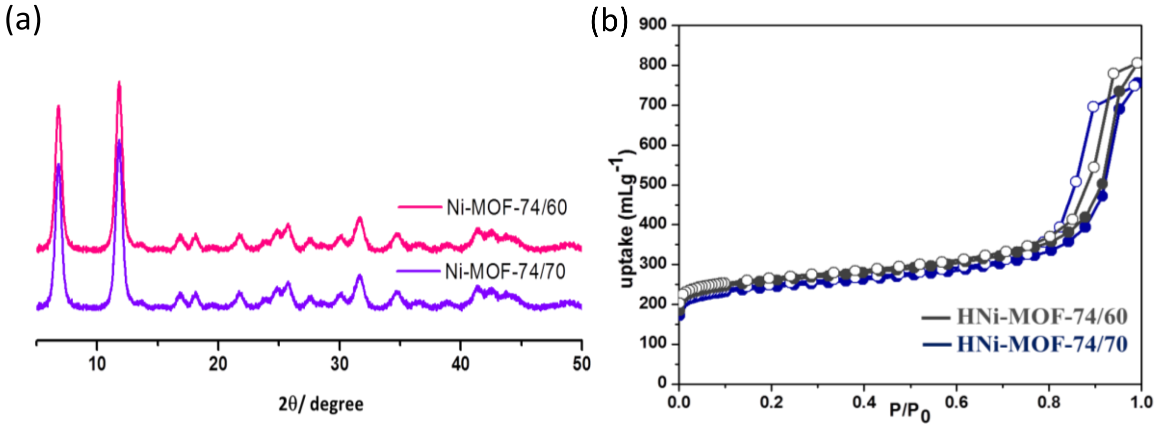

Figure 6: (a) PXRD pattern and (b) N_2 adsorption isotherm of HNi-MOF-74/60 and HNi-MOF-74/70.

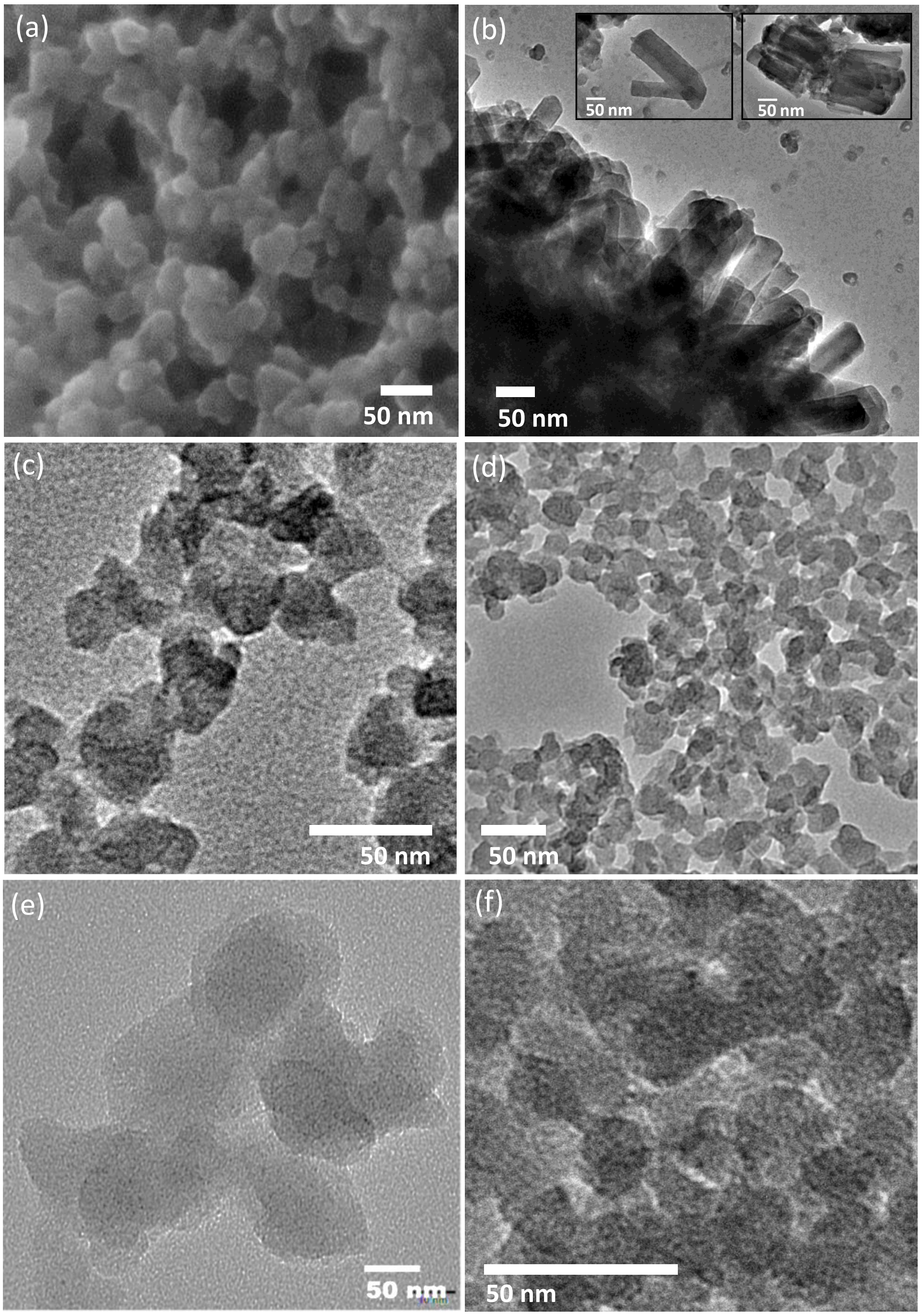

Figure 7: (a) FESEM image of Ni-MOF-74/50 (inset: high resolution), TEM images of (b) Ni-MOF-74-SOL, (c) Ni-MOF-74-DMF/50W, (d, e) Ni-MOF-74-DMF/50 and (f) Ni-MOF-74-DMSO/50.

incomplete reaction that leads to low surface areas. Furthermore, the presence of non-crystalline materials can be realized by TGA studies. Here the difference in weight loss has been observed, which leads to the diverse residual masses during decomposition (Figure 5a). At 50 minutes, the reaction condition is good enough to produce high surface area and this phenomenon is further supported by specific micropore volume (0.013, 0.053, 0.292, and 1.015 cm^3g^{-1} for 1 to 4 respectively) as realized from respective t-plots (Figure 5b). The total pore volume calculated from the adsorption isotherms for 1, 2, 3 and 4 are 0.22, 0.75, 1.083 and 1.842 cm^3g^{-1}. Furthermore, the micropore-mesopore volume ratio (V_{micro}/V_{meso}) enhanced from 0.061 to 1.27 suggests the gradual development of micro as well as mesopore (Table 1). Additionally, HNi-MOF-74 at 60 and

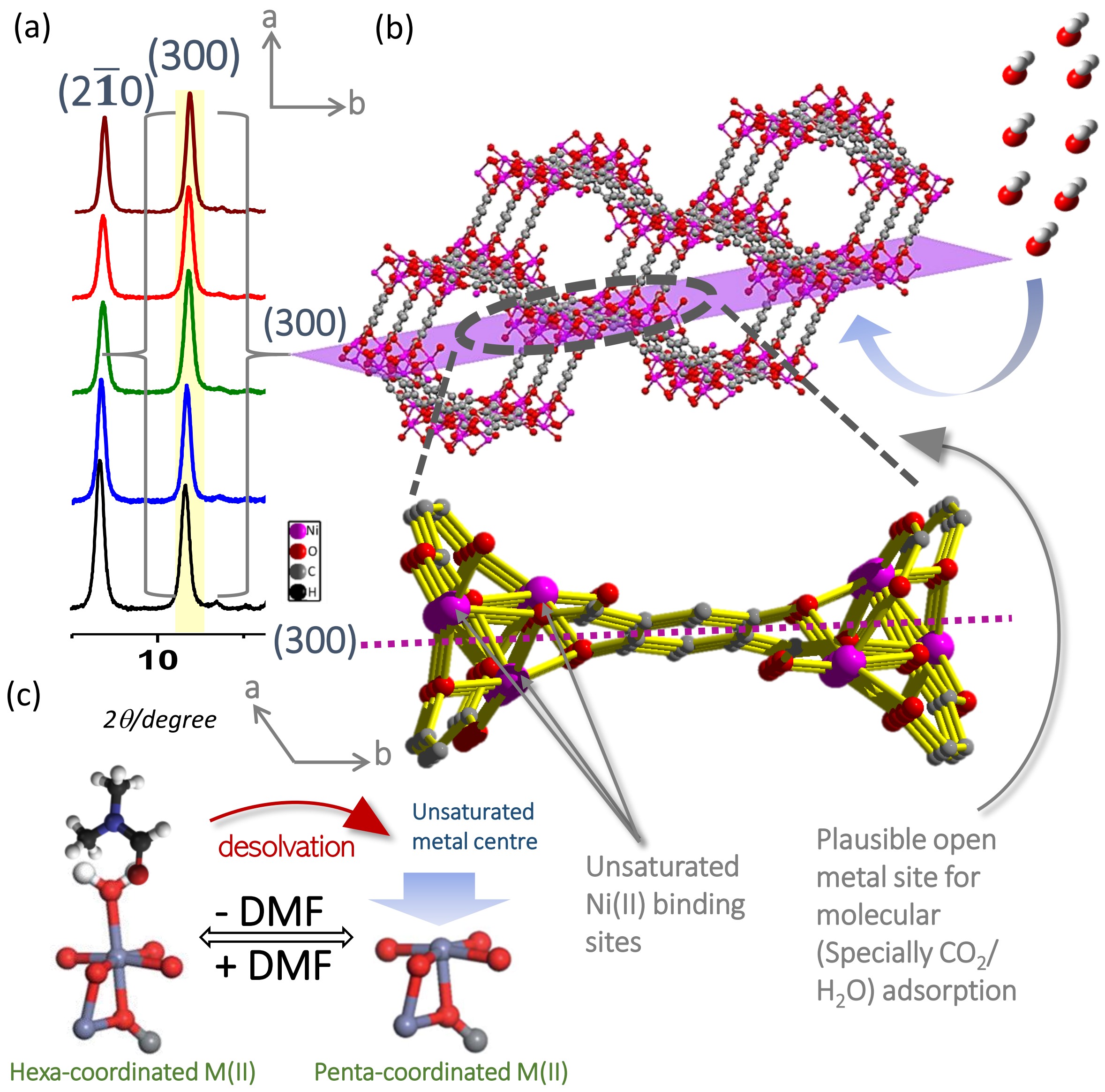

Figure 8: (a) Comparative PXRD pattern of Ni-MOF-74/t with highlighted peaks at 2θ = 6.8° and 11.9°; (b) Metal-ligand coordination environment at of Ni-MOF-74-SOL at (300) crystalline plane corresponding to peak at 2θ = 11.9°; (c) Schematic representation of change in metal coordination number due to solvent coordination to the bivalent metal ion.

70 minutes has been synthesized which revealed similar surface area to 4 indicating the complete formation of bimodal mesostructure at 50 minutes of reaction time (Figure 6). Pore size calculations were performed with the NLDFT method based on the adsorption isotherms (Figure 4b). The pore size expands remarkably from 7-11 nm for HNi-MOF-74/20 to 5-15 nm with increasing reaction time to 50 minutes. To understand the origin of mesopore FESEM (Field emission scanning electron microscopy) and TEM (transmission electron microscopy) microscopic studies have been performed and compared with non-perturbed one (Figure 7). FESEM study of 4 revealed irregular networks type morphology formed by fusing of spherical nanoparticles of diameter in the range of 20-50 nm (Figure 7a). This nanofusion of the nanocrystals resulted interparticle void space and corresponding mesopore formation. TEM image also supports the assembly of nanoparticles and network superstructure formation (Figure 7d, e). However, combining PNF in MW, bimodal hierarchical porosity can be achieved whereas microwave promotes formation of facile MOF nanoparticles and perturbation enables fusion of neonate nanoparticles to generate micro-mesostructured MOF. The results from adsorption and morphology studies have mostly explained the fusion of particles. But these studies were inadequate to explain whether nanofusion is guided by non-covalent surface assembly of such MOF crystals or by any other additional metal-ligand coordination. Recent demonstration explains that “nanofusion” is not a surface phenomenon but it encourages the nucleation of such MOF crystals by maximizing the surface between the two mixing phases and permitting multiple coordination between organic linkers and metal cations.[16] Interestingly, PXRD patterns of 1 to 4 showed that the intensity of $2\theta = 11.9°$ peak ((300) plane) gradually increases from compound 1 to 4 compared to $2\theta = 6.8°$ peak ($(2\bar{1}0)$ plane). This is in stark contrast of solvothermally prepared Ni-MOF-74 where the corresponding ($(2\bar{1}0)$ peak has higher intensity than (300) one. The increased intensity of the peak at $2\theta = 11.9°$, suggests the participation of additional molecule or the growth of the particle along the (300) plane (Figure 8a, b).[22] The octahedral geometry of Ni(II) (coordination number 6) in solvothermally prepared Ni-MOF-74 is satisfied by the coordinated DMF molecules (Figure 8c). In microwave condition with the help of strong perturbation, nanoparticles are fused by the Ni-DHBDC metal coordination on the surface without solvent participation. The nanofusion is driven by the metal-coordination between reactive unsaturated Ni sites and carboxylate or

hydroxy group of DHBDC linker positioned on the surface of the nanoparticles. This can be correlated as the (300) plane contains Ni-DMF species which is partially substituted by Ni-DHBDC coordination on the surface and the participation of such interaction gradually increased as the extent of nanofusion enhanced with time and corresponding intensity of the (300) plane.

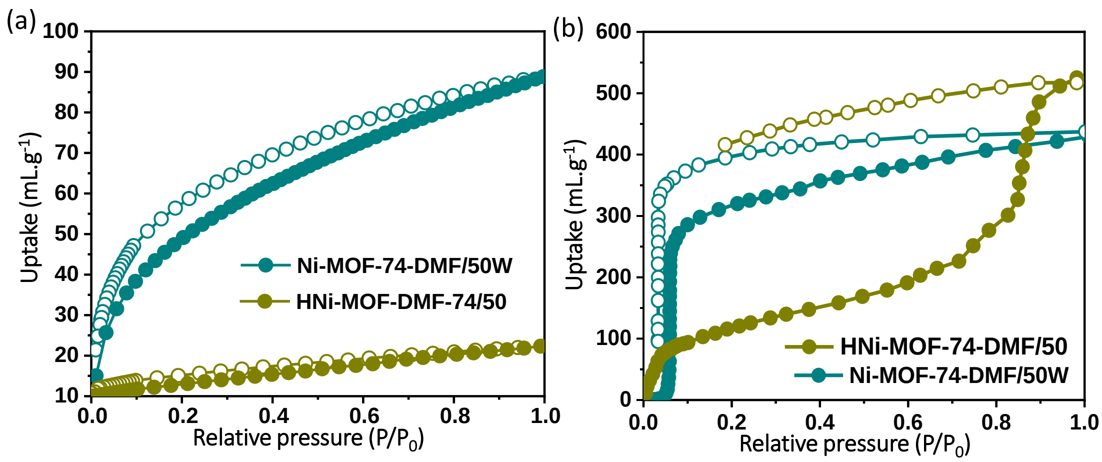

Figure 9: (a) CO_2 sorption isotherm for HNi-MOF-74-DMF/50 (yellow) and Ni-MOF-74-DMF/50W (cyan) at 298 K and (b) Water adsorption isotherm for HNi-MOF-74-DMF/50 (yellow) and Ni-MOF-74-DMF/50W (cyan) at 298 K.

To support the assumption, CO_2 and water vapor (at 298 K) adsorption have been performed with desolvated form of HNi-MOF-74-DMF/50 (4) and compared with the reported uptake values of solvothermally synthesized Ni-MOF-74.43,48 The CO_2 and water uptakes are 147 mL.g^{-1} and 615 mL.g^{-1}, respectively for Ni-MOF-74, which are significantly lower for HNi-MOF-74-DMF/50 and values are 14 mL.g^{-1} (CO_2) and 490 ml.g^{-1} (water). Higher uptake of CO_2 and water in MOF-74 (M= Mg, Ni, Co, Zn, Fe) series is

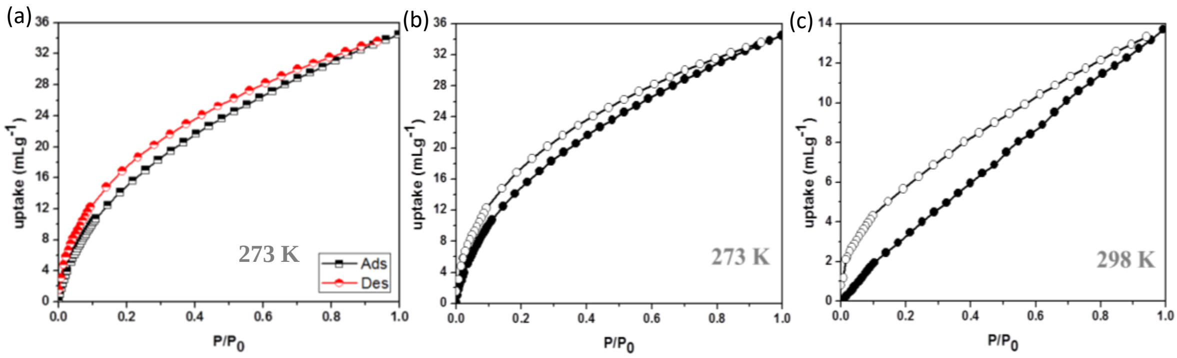

Figure 10: CO_2 adsorption isotherm of (a) HNi-MOF-74-DMF/50 (b, c) for HNi-MOF-74-DMSO/50 at 273 and 298 K, respectively.

correlated to the strong interaction between CO_2/ water with open metal sites formed on the pore surface after removal of DMF molecules. The nanofusion occurs along the crystallographic (300) plane (along M-DMF plane), which significantly reduces the density of solvent-bound metal centre in HNi-MOF-74-DMF/t. As a consequence, the number of unsaturated Ni sites also decreases which reduces the affinity for polar molecules like CO_2 or water towards pore to a great extent. Due to the shielding of active sites by nanofusion mechanism, the CO_2 uptake decreases abruptly (Figure 9a, 10). To execute the effect of perturbation, CO_2 and water vapor (at 298 K) adsorption have been performed with Ni-MOF-74-DMF/50W (89 mLg^{-1}) which is reasonably higher than HNi-MOF-74-DMF/50 (Figure 9). In addition, the water adsorption isotherm of HNi-MOF-74-DMF/50 (4) and Ni-MOF-74-DMF/50W (5) prominently defines the dissimilarity in pore geometry between these two materials (Figure 9b). The phenomenon of capillary condensation of water in large pores is well established. Adsorbed water molecule in mesopore acts as a nucleation site for the formation of larger water cluster and are preferentially accompanied by a hysteresis loop between adsorption and desorption profile with incomplete water release.[22] This is why, the material 5 exhibited a typical type-I isotherm whereas 4 shows a broad hysteresis with incomplete desorption.

2.1.3.2: Impact of solvent polarity

The mechanism of template-free hierarchical MOF synthesis is not well-established to date. It is believed that solvent participation holds the maximum importance over other

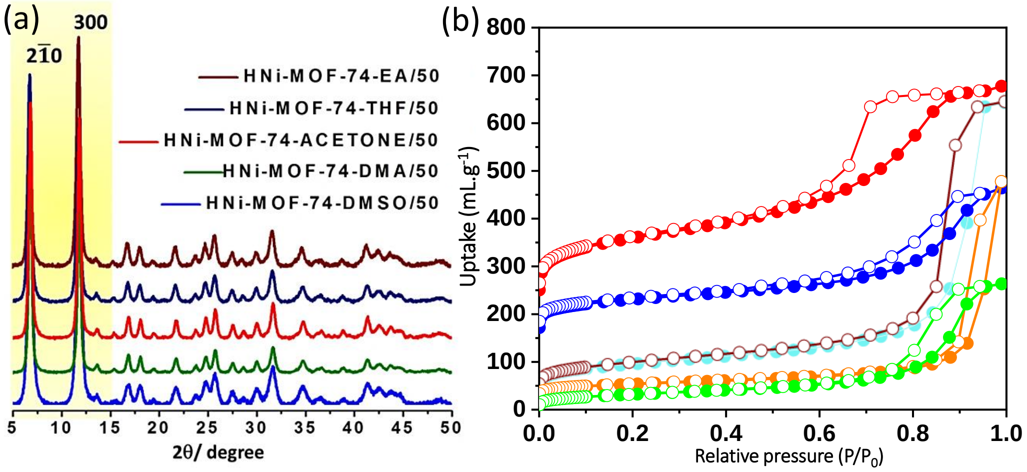

Figure 11: (a) PXRD pattern and (b) N_2 adsorption isotherm of HNi-MOF-74 at different solvent medium by substituting DMF at 77 K.

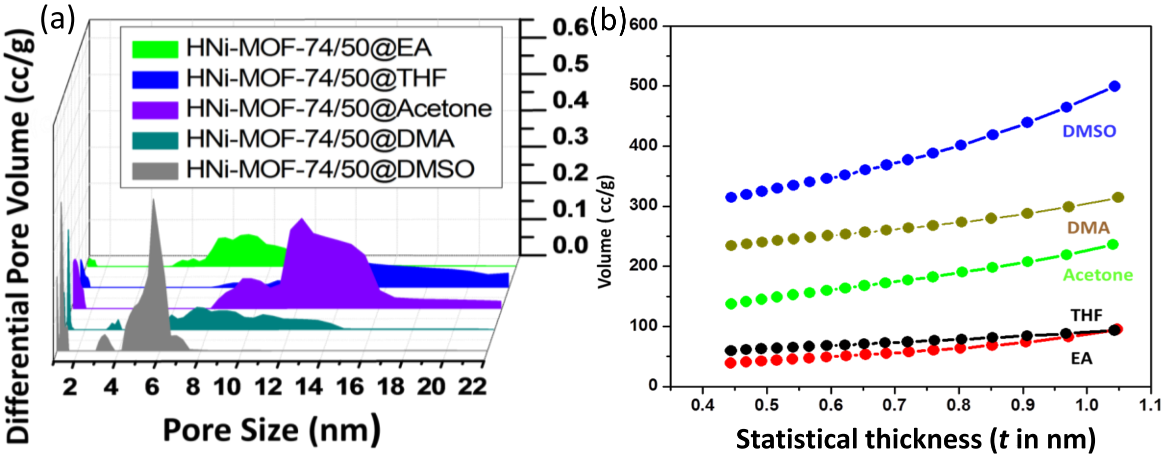

Figure 12: (a) NLDFT pore size distribution plot and (b) corresponding t-plot for HNi-MOF-74/50 synthesized by different solvent medium.

factors such as reaction time and ligand interaction towards the metal.[18] Previous reports on template-free MOF synthesis mostly highlight the presence of keto-functional group of DMF which is responsible for generating random mesopore by pore etching.[18] For a better understanding of solvent influence, microwave stimuli has been implemented where non-polar molecule is inserted to microwave radiation. This is why, to produce effective microwave adsorption, it has been shown that higher dielectric constant can be considered when solvents are submitted to microwave irradiation, as compared to conventional hydrothermal heating.[23] To understand the role of solvent molecule, DMF solvent was replaced, (dielectric constant 36) used for the synthesis of compound HNi-MOF-74-DMF/50 with different polarities such as ethyl acetate, THF, Acetone, DMA and DMSO having dielectric constant 6, 7, 20, 37 and 47, respectively. The well-correspondence of the powder X-ray diffraction (PXRD) patterns of HNi-MOF-74-EA/50 (6), HNi-MOF-74-THF/50 (7), HNi-MOF-74-ACETONE/50 (8), HNi-MOF-74-DMA/50 (9), HNi-MOF-74-DMSO/50 (10) approves the formation of materials with pure crystalline phase (Figure 11a). The N_2 adsorption isotherm has been measured for 6, 7, 8, 9 and 10. The increment in specific surface areas for 6, 7, 8 and 9 (which are 132, 190, 444, 749, and 1127 m^2g^{-1}, respectively) in the P/P_0 range of 0.05–0.30 is in good agreement with the increase in dielectric constant of corresponding solvent (Figure 11b). The BET surface area reaches to its maxima, 1127 m^2g^{-1}, when highly polar DMSO has been used as co-solvent. Similarly, all isotherms reveal dual porosity of such materials even after solvent substitution. Interestingly, the solvent polarity directly affects the

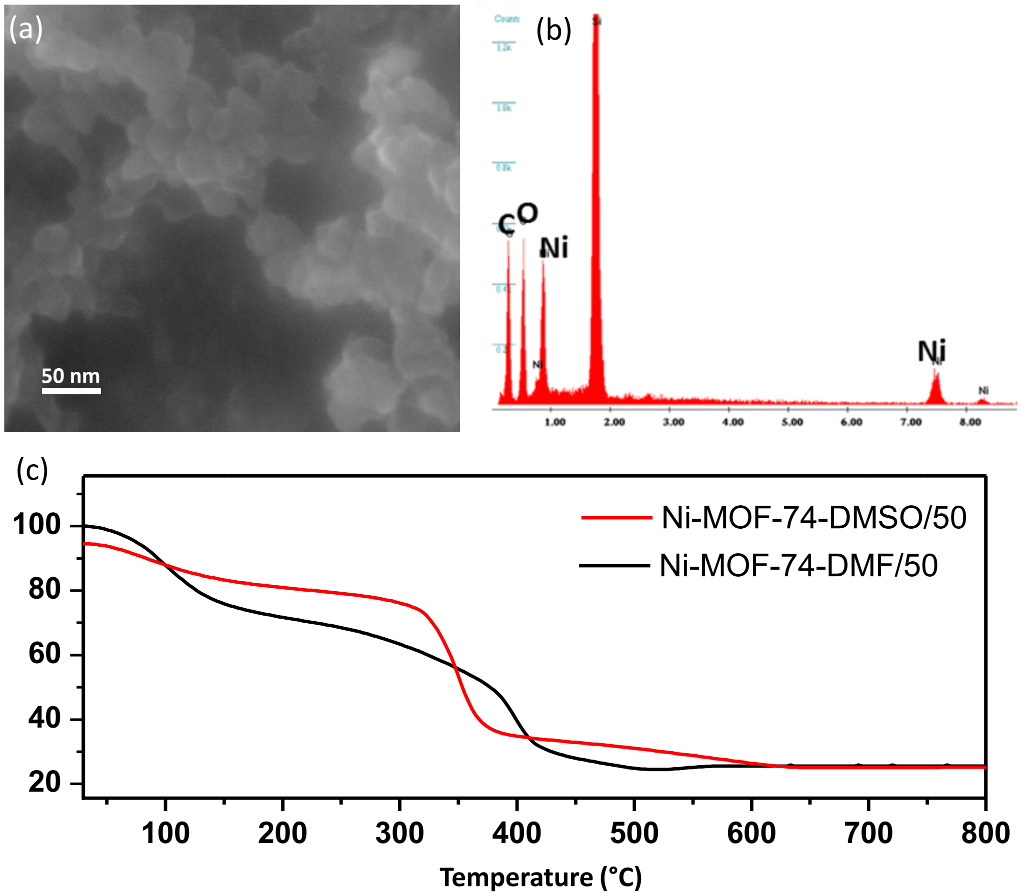

Figure 13: (a) FESEM, (b) EDX and (c) thermal stability study of HNi-MOF-74-DMSO/50.

surface area and resultant porosity. The calculated BET surface areas for HNi-MOF-74-DMF/50 (4) and HNi-MOF-74-DMA/50 (9) are 749 $m^2.g^{-1}$and 780 $m^2.g^{-1}$, respectively, where the dielectric constants of the solvents of DMF and DMA are similar (36 and 37 respectively); which suggests that solvent polarity directly affects the surface area. On an additional note, in spite of the absence of any keto-functional group in THF, 7 revealed the presence of dual porosity with $V_{micro}/V_{meso}= 0.14$. Accordingly, the V_{micro}/V_{meso} for 6 to 10 increases remarkably from 0.013 to 0.617 (Table 1). Figure 12 shows the pore size distribution and its gradual increment in volume at mesoscale region. Moreover, the enhancement in surface area suggests the accessibility of more N_2 molecules inside the pore whereas CO_2 adsorption is strongly guided by the availability of open metal sites. Interestingly, 10 showed an increment in surface area but the CO_2 adsorption (Figure 10) capacity stands similar to material 4. This observation strongly supports the proposal of nanofusion generated by additional metal-ligand covalent coordination. To further confirm the effect of solvent polarity, FESEM images were recorded for 10 to study the morphology. FESEM image of 10 shows the presence of analogous network morphology associated to 4, suggesting that the participation of solvent and its polarity to trigger the bimodal superstructure (Figure 13a, b). TGA analysis exhibited lower thermal stability due to the generation of mesopore. The gradual decrease in decomposition temperature with time further confirmed the augmentation in mesopore volume (Figure 13c).

Table 1: Calculated adsorption parameters for HNi-MOF-74 series obtained with the various solvent medium.

MOF	**Solvent (1:1:1=water/ethanol: x), x=**	**Reaction time (min)**	**Dielectric Constant**	**BET surface area (m^2/g)**	**Micropore volume (cm^3/g)**	**Mesopore volume (cm^3/g)**	**V_{micro}/V_{meso}**	**Total pore volume (cm^3/g)**	**Mesopore diameter (nm)**
1	DMF	20	36	89.15	0.013	0.211	0.061	0.224	7-11
2	DMF	30	36	265.58	0.053	0.701	0.075	0.754	5-14.5
3	DMF	40	36	522.57	0.292	0.792	0.369	1.083	4.5-19
4	DMF	50	36	780.67	1.015	0.827	1.27	1.842	3, 4.5-14.5
5	DMF	50	36	798.1	1.167	--	--	1.167	1.1
6	EA	50	6	132.9	0.01	0.73	0.013	0.74	4-14
7	THF	50	7	190.9	0.05	0.35	0.14	0.4	8-22
8	ACETONE	50	20	444.7	0.06	1.24	0.048	1.305	6-20
9	DMA	50	37	749.3	0.3	0.63	0.142	0.72	4-12
10	DMSO	50	47	1127.2	0.4	0.64	0.617	1.048	3.3-7

2.1.3.2: Utilization of mesopore by encapsulating VB_{12}

The formation of mesopore in HNi-MOF-74/50 is further supported by the encapsulation of larger nanosized molecule. Vitamin B_{12} (VB_{12}; 1.0× 1.6× 1.7 nm) has been chosen for

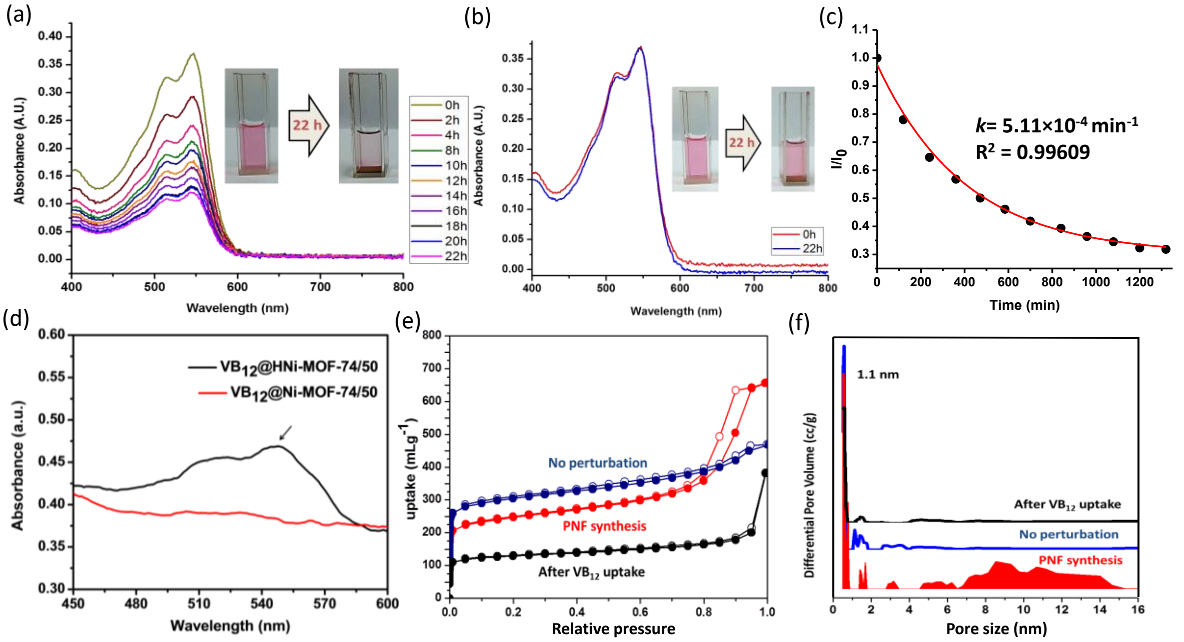

Figure 14: Time-dependent UV-Vis spectra of supernatant methanolic solutions of Vitamin B_{12} after introducing it with (a) HNi-MOF-74-DMF/50 and (b) Ni-MOF-74-DMF/50W. (c) fitting of the relative intensity change with time by utilizing monoexponential function. (d) UV-Vis spectra of methanolic solutions of VB_{12} encapsulated H-MOF and microporous MOF-74. Comparative (e) N_2 adsorption isotherm at 77K and (f) corresponding pore size distribution calculated by NLDFT method for HNi-MOF-74-DMF/50 (red), Ni-MOF-74-DMF/50W (blue) and VB_{12} encapsulated HNi-MOF-74-DMF/50 (black).

encapsulation which is too large to pass through the micropore of Ni-MOF-74 (1.1 nm), in order to investigate the presence of additional mesoporosity. The encapsulation study has been performed by immersing methanolic solution of VB_{12} (1.36×10^{-7} M; 0.185 mg in 50 μL) in methanolic dispersion of 4. The solution is filtered and UV spectra are measured in different time intervals to study the capture of VB_{12} by MOF. As seen in Figure 14a, a gradual decrease in the absorption band at 549 nm (S-band of VB_{12}) is observed and it was saturated after 22 h which suggests that about 4.6 $\mu molg^{-1}$ of VB_{12} can be encapsulated in MOF. The adsorption process follows the first-order kinetics with a rate constant value 5.11×10^{-4} min^{-1} (Figure 14c). The capture of VB_{12} from solution by MOF is further evident from N_2 adsorption isotherms. As observed from Figure 14e, a substantial decrease in N_2 uptake was observed for VB_{12}@4 compared to 4. Also, the pore size distribution profile exhibits only micropore distribution further emphasizing the capture of VB_{12} into the mesopores (Figure 14f). The VB_{12} capture has been also explored by using compound 5 in a similar method for 22 h, nonetheless, no changes in the absorption spectra are observed. These confirm the presence of mesopores in MOF and are essential for the capture of VB_{12} (Figure 14b).

2.1.4: Conclusion

In conclusion, a facile, rapid and one-pot template-free synthesis of micro/mesoporous MOF is presented by applying perturbation in form of stirring under the microwave. The effective reaction time was varied which changes the morphology as well as pore geometry. In addition, the solvent effect was further investigated and studied the adsorption behavior for the resulting series of materials. By adopting a simple synthetic strategy, a methodology has been developed where crystallinity, morphology, pore size and surface area can be tuned by optimizing solvent polarity and reaction time. In fact, the surface area attained by incorporating highly polar DMSO is highest in comparison to any reported hierarchical MOF derived from microporous one. The mesopores in the hierarchically porous MOFs have been exploited by encapsulating large biomolecule VB_{12}. Thus, our work demonstrates that PNF-assisted microwave synthesis of creating hierarchical superstructure showed superior effectivity which could not be achieved using traditional microporous Ni-MOF-74 and such materials can be further used to capture/delivering larger bio-molecules. Our strategy shows a simple and fast synthetic route to obtain hierarchical MOFs that would outweigh the traditional microporous MOF in terms of property and applications, such as the encapsulation and delivery of nanosized protein molecules.

2.1.5: References

[1] X.-Y. Yang, L.-H. Chen, Y. Li, J. C. Rooke, C. Sanchez and B.-L. Su, *Chem. Soc. Rev.* **2017**, *46*, 481-558.
[2] a) S. Furukawa, J. Reboul, S. Diring, K. Sumida and S. Kitagawa, *Chem. Soc. Rev.* **2014**, *43*, 5700-5734; b) A. Kirchon, L. Feng, H. F. Drake, E. A. Joseph and H.-C. Zhou, *Chem. Soc. Rev.* **2018**, *47*, 8611-8638.
[3] a) X. Chen, N. Wang, K. Shen, Y. Xie, Y. Tan and Y. Li, *ACS Appl.Mater. Interfaces* **2019**, *11*, 25976-25985; b) Z. Zhang, Y. Chen, S. He, J. Zhang, X. Xu, Y. Yang, F. Nosheen, F. Saleem, W. He and X. Wang, *Angew. Chem. Int. Ed.* **2014**, *53*, 12517-12521; c) L. Feng, Y. Wang, S. Yuan, K.-Y. Wang, J.-L. Li, G. S. Day, D. Qiu, L. Cheng, W.-M. Chen, S. T. Madrahimov and H.-C. Zhou, *ACS Catalysis* **2019**, *9*, 5111-5118.
[4] a) L. H. Wee, C. Wiktor, S. Turner, W. Vanderlinden, N. Janssens, S. R. Bajpe, K. Houthoofd, G. Van Tendeloo, S. De Feyter, C. E. A. Kirschhock and J. A. Martens, *J. Am. Chem. Soc.* **2012**, *134*, 10911-10919; b) X. Zhang, C. Y. Chuah, P. Dong, Y.-H. Cha, T.-H. Bae

and M.-K. Song, *ACS Appl.Mater. Interfaces* **2018**, *10*, 43316-43322; c) D. Kim, D. W. Kim, O. Buyukcakir, M.-K. Kim, K. Polychronopoulou and A. Coskun, *Adv. Funct. Mater.* **2017**, *27*, 1700706; d) X.-Y. Liu, F. Zhang, T.-W. Goh, Y. Li, Y.-C. Shao, L. Luo, W. Huang, Y.-T. Long, L.-Y. Chou and C.-K. Tsung, *Angew. Chem., Int. Ed* **2018**, *57*, 2110-2114.

[5] a) D. Wisser, F. M. Wisser, S. Raschke, N. Klein, M. Leistner, J. Grothe, E. Brunner and S. Kaskel, *Angew. Chem., Int. Ed* **2015**, *54*, 12588-12591; b) M. Tsotsalas, J. Liu, B. Tettmann, S. Grosjean, A. Shahnas, Z. Wang, C. Azucena, M. Addicoat, T. Heine, J. Lahann, J. Overhage, S. Bräse, H. Gliemann and C. Wöll, *J. Am. Chem. Soc.* **2014**, *136*, 8-11; c) B. Zhang, S. A. Davis, N. H. Mendelson and S. Mann, *Chem. Commun.* **2000**, 781-782; d) P. Li, Q. Chen, T. C. Wang, N. A. Vermeulen, B. L. Mehdi, A. Dohnalkova, N. D. Browning, D. Shen, R. Anderson, D. A. Gómez-Gualdrón, F. M. Cetin, J. Jagiello, A. M. Asiri, J. F. Stoddart and O. K. Farha, *Chem* **2018**, *4*, 1022-1034; e) Y. Luo, M. Ahmad, A. Schug and M. Tsotsalas, *Adv. Mater.* **2019**, *31*, 1901744.

[6] a) G. Srinivas, V. Krungleviciute, Z.-X. Guo and T. Yildirim, *Energy Environ. Sci.* **2014**, *7*, 335-342; b) S. J. Yang, T. Kim, J. H. Im, Y. S. Kim, K. Lee, H. Jung and C. R. Park, *Chem. Mater.* **2012**, *24*, 464-470; c) X. Cao, C. Tan, M. Sindoro and H. Zhang, *Chem. Soc. Rev.* **2017**, *46*, 2660-2677; d) S. Dutta, A. Bhaumik and K. C. W. Wu, *Energy Environ. Sci.* **2014**, *7*, 3574-3592.

[7] L.-G. Qiu, T. Xu, Z.-Q. Li, W. Wang, Y. Wu, X. Jiang, X.-Y. Tian and L.-D. Zhang, *Angew. Chem. Int. Ed.* **2008**, *47*, 9487-9491.

[8] a) H. Deng, S. Grunder, K. E. Cordova, C. Valente, H. Furukawa, M. Hmadeh, F. Gándara, A. C. Whalley, Z. Liu, S. Asahina, H. Kazumori, M. O'Keeffe, O. Terasaki, J. F. Stoddart and O. M. Yaghi, *Science* **2012**, *336*, 1018-1023; b) V. Lykourinou, Y. Chen, X.-S. Wang, L. Meng, T. Hoang, L.-J. Ming, R. L. Musselman and S. Ma, *J. Am. Chem. Soc.* **2011**, *133*, 10382-10385; c) C. Liu, T. Li and N. L. Rosi, *J. Am. Chem. Soc.* **2012**, *134*, 18886-18888.

[9] H. Deng, S. Grunder, K. E. Cordova, C. Valente, H. Furukawa, M. Hmadeh, F. Gándara, A. C. Whalley, Z. Liu, S. Asahina, H. Kazumori, M. O'Keeffe, O. Terasaki, J. F. Stoddart and O. M. Yaghi, *Science* **2012**, *336*, 1018-1023.

[10] a) P. Horcajada, T. Chalati, C. Serre, B. Gillet, C. Sebrie, T. Baati, J. F. Eubank, D. Heurtaux, P. Clayette, C. Kreuz, J.-S. Chang, Y. K. Hwang, V. Marsaud, P.-N. Bories, L. Cynober, S. Gil, G. Férey, P. Couvreur and R. Gref, *Nature Mater.* **2010**, *9*, 172-178; b) X. Gao, Y. Wang, G. Ji, R. Cui and Z. Liu, *CrystEngComm* **2018**, *20*, 1087-1093.

[11] a) T. Prasomsri, W. Jiao, S. Z. Weng and J. Garcia Martinez, *Chem. Commun.* **2015**, *51*, 8900-8911; b) M. Choi, H. S. Cho, R. Srivastava, C. Venkatesan, D.-H. Choi and R. Ryoo, *Nature Mater.* **2006**, *5*, 718.

[12] D.-Y. Hong, Y. K. Hwang, C. Serre, G. Férey and J.-S. Chang, *Adv. Funct. Mater.* **2009**, *19*, 1537-1552.

[13] L. Peng, J. Zhang, Z. Xue, B. Han, X. Sang, C. Liu and G. Yang, *Nature Commun.* **2014**, *5*, 4465.

[14] Y. Zhao, J. Zhang, B. Han, J. Song, J. Li and Q. Wang, *Angew. Chem., Int. Ed* **2011**, *50*, 636-639.

[15] a) L.-B. Sun, J.-R. Li, J. Park and H.-C. Zhou, *J. Am. Chem. Soc.* **2012**, *134*, 126-129; b) M.-H. Pham, G.-T. Vuong, F.-G. Fontaine and T.-O. Do, *Cryst. Growth & Des.* **2012**, *12*, 1008-1013.

[16] Y. Yue, P. F. Fulvio and S. Dai, *Acc. Chem. Res.* **2015**, *48*, 3044-3052.

[17] Y. Yue, A. J. Binder, R. Song, Y. Cui, J. Chen, D. K. Hensley and S. Dai, *Dalton Trans.* **2014**, *43*, 17893-17898.

[18] Y. Yue, Z.-A. Qiao, P. F. Fulvio, A. J. Binder, C. Tian, J. Chen, K. M. Nelson, X. Zhu and S. Dai, *J. Am. Chem. Soc.* **2013**, *135*, 9572-9575.
[19] a) X. Wu, Z. Bao, B. Yuan, J. Wang, Y. Sun, H. Luo and S. Deng, *Microporous Mesoporous Mater.* **2013**, *180*, 114-122; b) S. R. Caskey, A. G. Wong-Foy and A. J. Matzger, *J. Am. Chem. Soc.* **2008**, *130*, 10870-10871; c) N. L. Rosi, J. Kim, M. Eddaoudi, B. Chen, M. O'Keeffe and O. M. Yaghi, *J. Am. Chem. Soc.* **2005**, *127*, 1504-1518; d) T.-H. Bae and J. R. Long, *Energy Environ. Sci.* **2013**, *6*, 3565-3569.
[20] Y. Kim, T. Yang, G. Yun, M. B. Ghasemian, J. Koo, E. Lee, S. J. Cho and K. Kim, *Angew. Chem., Int. Ed* **2015**, *54*, 13273-13278.
[21] E. D. Bloch, W. L. Queen, R. Krishna, J. M. Zadrozny, C. M. Brown and J. R. Long, *Science* **2012**, *335*, 1606-1610.
[22] J. B. DeCoste, G. W. Peterson, B. J. Schindler, K. L. Killops, M. A. Browe and J. J. Mahle, *J. Mater. Chem. A* **2013**, *1*, 11922-11932.
[23] a) Z. Ni and R. I. Masel, *J. Am. Chem. Soc.* **2006**, *128*, 12394-12395; b) A. M. Rodríguez, P. Prieto, A. de la Hoz, Á. Díaz-Ortiz, D. R. Martín and J. I. García, *ChemistryOpen* **2015**, *4*, 308-317.

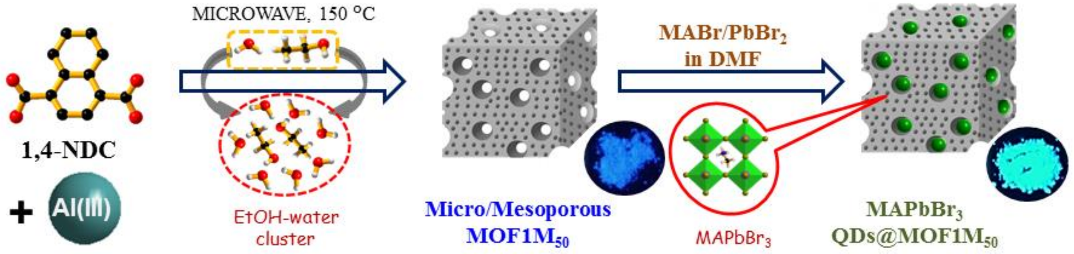

2.2: Modulating Hierarchical Micro/Mesoporosity by a Mixed Solvent Approach in Al-MOF: Stabilization of $MAPbBr_3$ Quantum Dots

A Manuscript based on this work has been published in Chem. Eur. J. 2020, 26, 14671.

Abstract

Various hierarchical micro/mesoporous MOFs based on ([Al(μ-OH)(1,4-NDC)]•H_2O) (MOF1) with tunable porosities (pore volume and surface area) have been synthesized by assembling Al(III) and 1,4-NDC (1,4-Naphthalenedicarboxylate) under microwave irradiation by varying ethanol/water solvent ratio. Water/ethanol mixture has played a crucial role in the mesopore generation in $MOF1M_{25}$, $MOF1M_{50}$, and $MOF1M_{75}$, which is achieved by in situ formation of water/ethanol clusters. By adjusting the ratio of water-ethanol, the particle size, surface area and micro/mesopore volume fraction of the MOFs is controlled. Furthermore, reaction time also plays a critical role in mesopore formation as realized by varying reaction time for the MOF with 50% ethanol ($MOF1M_{50}$). Additionally, hierarchical MOF ($MOF1M_{50}$) has been used as a template for the stabilization of $MAPbBr_3$ (MA = methylammonium) perovskite quantum dots (PQDs). $MAPbBr_3$ PQDs are grown inside $MOF1M_{50}$, where mesopores control the size of PQDs which leads to quantum confinement.

2.2.1: Introduction

The utilization of porous materials has infringed far beyond its typical applications in sorption [1] and separation [2] to bio-molecule encapsulation,[3] drug release,[4] sensing,[5] catalysis,[6] energy conversion [7] and storage devices.[8] Metal-organic frameworks (MOFs), comprising of metal nodes and organic linkers have appeared as fascinating materials, having tunable porosity, with pore diameters ranging from micro (< 2 nm) to meso (2-50 nm). Specifically, hierarchical micro/mesoporous MOFs are of great importance as bimodality in pore sizes, and geometry can accommodate diverse guest molecules of different sizes by fast mass transfer kinetics. Thus, hierarchical porosity in MOFs opens up the possibility of realizing advanced applications in separation, storage, catalysis, optoelectronics and energy storage/conversion.[9] To date, most of the reported MOFs are microporous, and augmentation of their pores to mesoscale range remains a formidable challenge. Several attempts have been made to introduce hierarchical porosity in MOFs, the first being ligand length extension[10] and template-assisted synthesis.[11] However, these methods are ridden with drawbacks like small mesopore formation, generation of interpenetrated structure, crystal phase collapse and poor stability upon template removal or high-temperature treatment.[10, 12] Recently, to circumvent these drawbacks, extensive efforts have been made to explore multiple routes in order to introduce structural bimodality within MOFs. By and large, such hierarchical MOFs, till now, have been modulated by using solvent as a medium, without the use of additional templates to trigger hierarchy. In fact, this solvent-induced method can be classified into two categories, namely, direct and indirect solvent contribution. Developing hierarchy via solvents or solvent adjustment method,[13] hydrolytic transformation route,[14] ionic liquid/supercritical CO_2 emulsion route,[15] or CO_2-expanded liquids as switchable solvents[16] are considered under the first category whereas the latter includes microwave influence,[17] perturbation assisted nano-fusion method[13c, 18] and acid-base adjustment routes.[19] While indirect solvent method predominantly induces random mesopore generation, direct solvent participation can confine the mesopore dimension and tune it depending on solvent size and functionality. Credibly, for the class of indirect solvent method, solvent acts as a second leading factor, whereas other modulators such as microwave irradiation, stirring during synthesis, metal-ligand additional coordination, and fusion of neonate nanoparticles play the crucial role to dictate mesopore size.[13, 18] Nevertheless, for the category of direct solvent method, the solvent is majorly responsible for generating mesoporosity, which is evident in the successful formation of well-ordered mesopores.[14-16] Such methods, as mentioned earlier, are mostly used to create mesoporosity and induce hierarchical porosity for specific applications. This creates the need for more sophisticated synthetic methods towards the formation of hierarchical micro/mesoporous MOFs, which can provide in-depth mechanistic understanding.

The formation of these hierarchical porous structures is of particular interest because they not only provide additional sorption properties, besides, the combination of micro and mesopores can also be exploited to grow and stabilize other molecular entities. In this context, hybrid organic-inorganic metal halide perovskite quantum dots (PQDs) are extremely relevant emergent materials, remarkable for their immense applications in solar cells, photovoltaics and photocatalysis.[20] The quantum confinement of such PQDs gives rise to unique optoelectronic properties, e.g., bandgap expansion, energy level quantization, and slower electron-phonon relaxation, upon restricting their sizes below their exciton Bohr radius. [20g]

Considering this approach, a solvent duo: water and ethanol have been employed to prepare a hierarchical micro/mesoporous MOF $[\{Al(\mu\text{-}OH)(1,4\text{-ndc})\}\cdot H_2O]$ (MOF1) (1,4-ndc = 1,4-naphthalenedicarboxylate), by introducing water-ethanol cluster with definite size. This particular MOF holds specific significance in this context since (i) it has a 3D robust structure with two different micropore channels of dimensions 7.7×7.7 Å^2 and 3.0×3.0 Å^2 [21] and (ii) it is non-porous with respect to N_2 in its pristine form. This work demonstrates the effect of microwave synthesis on nano/meso morphology of MOF1 with improved diffusion kinetics in its adsorption properties. With the combined impact of solvent-assisted method and microwave synthesis, a series of micro/mesoporous MOFs (MOF1M$_{25}$, MOF1M$_{50}$ and MOF1M$_{75}$) have been developed with tunable porosity by adjusting the water-ethanol solvent ratio and also by changing the reaction time (Scheme 1). The mesopores have been further exploited for growth and stabilization of $MAPbX_3$ PQDs with unique optoelectronic properties and added stability using a simplistic synthetic method.

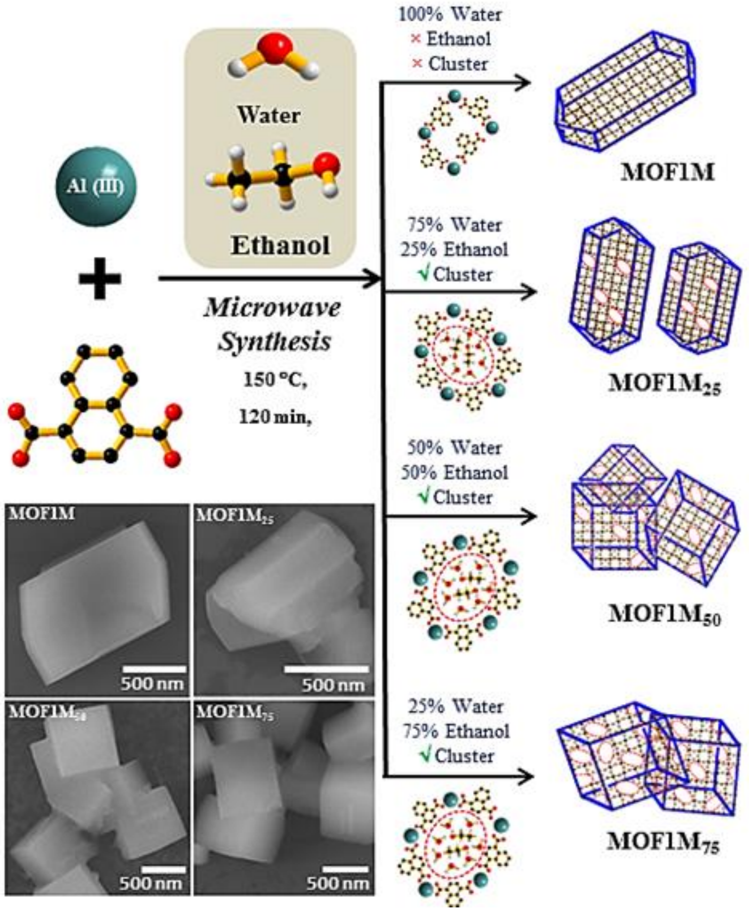

Scheme 1: Schematic illustration for the formation of micro/mesoporous MOFs (MOF1M, MOF1M$_{25}$, MOF1M$_{50}$ and MOF1M$_{75}$) and the effect of ethanol/ water solvents cluster on particle and pore size of the MOFs.

2.2.2: Experimental section

2.2.2.1: Materials

All the reagents employed are commercially available and used as provided without further purification. $Al(NO_3)_3·9H_2O$ has been obtained from Sigma-Aldrich. 1,4-naphthaledicarboxylic acid (1,4-H_2ndc) was obtained from Alfa Aesaer.

2.2.2.1: Synthesis

1,4-Naphthalenedicarboxylate (0.108 g, 0.5 mmol) and $Al(NO_3)_3·9H_2O$ (0.375 g, 1 mmol) were introduced in 30 mL wide-neck microwave vial, to this H_2O and EtOH (total 10 mL) were added, and further sonicated for 10 minutes. After that, the reaction vial was sealed and placed in MONOWAVE 200 microwave reactor. In microwave, the reaction mixture was heated to 150 °C (a heating rate of 6 °C /min) and held at same temperature from 120 minutes depending upon reaction condition (Table 1). The resulting solid white was filtered and washed with water repetitively and finally with ethanol and dried under vacuum. The PXRD pattern of the resulting MOFs reveals the formation of the pure crystalline phase of MOF1.

Table 1: Reaction condition of several MOF syntheses by altering mixed solvent concentration and reaction hold time in microwave.

Entry	Name	1,4-NDC: $Al(NO_3)_3 \cdot 9H_2O$ in mmol	H_2O: EtOH (total 10 ml)	Hold time at 150 °C in Microwave (in min)
1	MOF1M	0.5:1.0	10:0	120
2	MOF1M$_{25}$	0.5:1.0	7.5:2.5	120
3	MOF1M$_{50}$	0.5:1.0	5:5	120
4	MOF1M$_{75}$	0.5:1.0	2.5:7.5	120

Synthesis of $MAPbX_3$@ MOF1M$_{50}$: $PbBr_2$ (0.2 M, 0.073 g) was dissolved in 1 mL of N, N-dimethylformamide (DMF) and then 0.2 M (0.023 g) of CH_3NH_3Br was added with constant stirring. The precursor solution was heated at 80 °C for 1 h prior to impregnation. After one hour of heating, the precursor solution was added to 50 mg of MOF1M$_{50}$ powder in each 5 μL increments (total addition of 25 μL of precursor solution with a final concentration of 0.5 μL/mg) and vortexed for 30 minutes after every addition. Finally, the prepared composite was placed in oven at 100 °C for 1 h and washed subsequently with ethanol. The well-correspondence of the diffraction pattern of both MOF1M$_{50}$ and simulated $MAPbBr_3$ suggests the successful formation of QD@MOF composite.

2.2.2.3: Physical measurements

Microwave reactions were performed in the Monowave 200 microwave reactor from Anton Paar. Reactions under microwave stimuli were carried by transferring reaction mixture in 30 mL wide-neck vials by using MONOWAVE 200 (Anton Paar Monowave Series; Serial Number: 81919734; Instrument Software Version: 4.10.9376.7) microwave reactor. PL and UV-Vis spectra were recorded on Perkin-Elmer model LS 55 luminescence spectrometer and Perkin Elmer Lambda 900 UV-Vis spectrometer, respectively. Powder X-ray diffraction (PXRD) patterns were collected using a Bruker D8 Discover instrument using Cu-Kα radiation. Quantitative Phase Analysis (QPA) was performed by MAUD (Materials Analysis Using Diffraction) program. For multi-pattern fitting refinement cubic $MAPbBr_3$ and MOF1 CIF files are used. Morphological studies have been carried out using Leica-S440I Field Emission Scanning Electron Microscope (FESEM) by placing samples on a silicon wafer under high vacuum with an accelerating voltage of 100 kV. Transmission Electron Microscopy (TEM) analysis has been performed using JEOL JEM-2100 plus with an accelerating voltage at 200 kV. Energy dispersive spectroscopy (EDS) analysis was performed with an EDAX genesis instrument attached to the FESEM column.

2.2.2.4: Analysis from gas adsorption isotherm

Adsorption measurements were carried out using AUTOSORB IQ_2 and QUNATACHROME QUADRASORD-SI instruments at 77 K for N_2 and 273 K, 283 K, and 298 K for CO_2. The adsorbent samples (~100 mg) were placed which had been prepared at 150 °C under a 1×10^{-1} Pa vacuum for about 12 h prior to measurement of the isotherms. At a certain pressure, the ultrapure He was allowed to diffuse into the sample cell for operating valve functions and dead volume measurement. The activated sample was placed into the sample cell (9 mm diameter), then the change of the pressure was monitored and the degree of adsorption was calculated by the decrease in pressure at the equilibrium state. Nevertheless, all the operations were computer programmed and instinctive.

2.2.3: Result and discussion

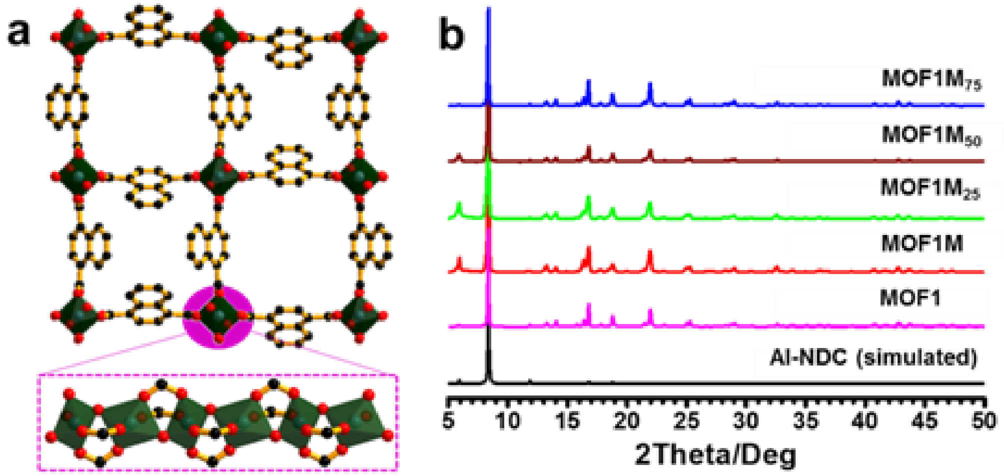

Figure 1: (a) View of 3D framework of MOF1 (below: showing 1D $\{Al(\mu\text{-}OH)(CO_2)_2\}_n$ chain) (b) PXRD patterns of MOF1, MOF1M, $MOF1M_{25}$, $MOF1M_{50}$ and $MOF1M_{75}$ compared with simulated pattern of MOF1.

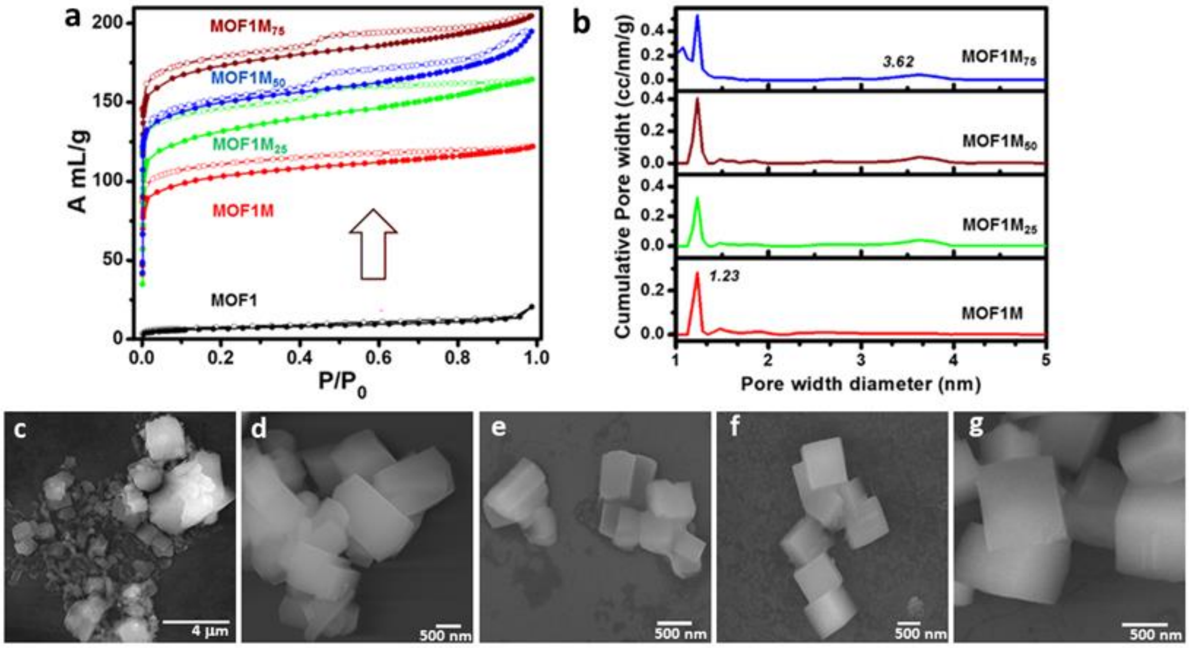

Figure 2: (a) N_2 adsorption/desorption isotherms of MOF1, MOF1M, MOF1M$_{25}$, MOF1M$_{50}$ and MOF1M$_{75}$ at 77 K, solid and open circles indicate adsorption and desorption, respectively. (b) Pore size distribution of MOF1M, MOF1M$_{25}$, MOF1M$_{50}$ and MOF1M$_{75}$. (c), (d), (e) (f) and (g) are FESEM images of MOF1, MOF1M, MOF1M$_{25}$, MOF1M$_{50}$ and MOF1M$_{75}$, respectively.

2.2.3.1: Synthesis and characterization of hierarchical MOF1M Series

{Al(μ-OH)(1,4-ndc)]·H_2O} (MOF1) is composed of infinite chains of corner-sharing octahedral $Al(OH)_2O_4$ crosslinked with 1,4 naphthanedicarboxylate (ndc) linkers forming two types of large and small channels with dimensions of 7.7 × 7.7 Å^2 and 3.0 × 3.0 Å^2 (Figure 1a).[21] It has been synthesized by conventional hydrothermal method (24 h, 180 °C) which revealed irregular morphologies. MOF1 showed non-porous nature with respect to N_2 sorption as realized by the negligible N_2 uptake at 77 K (Figure 2). In MOF synthesis, the microwave-assisted process has been used for producing small MOF nanoparticles and the process also dramatically reduces time as compared to the solvothermal method. [17,18b] The solvothermal synthesis of pristine MOF1 requires 24 hours.[21] However, in the microwave the synthesis of MOF1, designated as MOF1M, requires only 120 minutes. [13a,13b] The PXRD pattern of MOF1M proves that it is structurally identical to MOF1 and indicates its phase purity (Figure 1b). Interestingly,

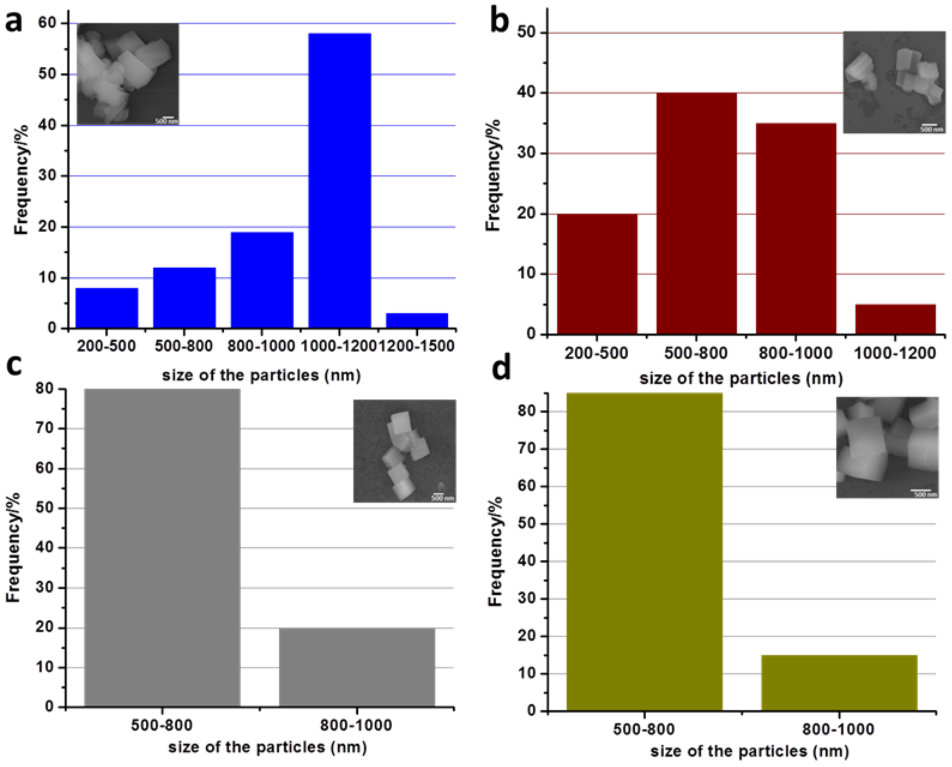

Figure 3: The size distribution histogram plot for (a) MOF1M, (b) $MOF1M_{25}$, (c) $MOF1M_{50}$, (d) $MOF1M_{75}$ with corresponding FESEM images.

N_2 adsorption (77K) for MOF1M showed typical type-I isotherm suggesting the microporous nature of the framework. The Brunauer-Emmett-Teller (BET) surface area and total pore volume were calculated to be 382 m^2/g and 0.18 cm^3g^{-1}, respectively. This dramatic enhancement in surface area in MOF1M compared to MOF1 can be attributed to the decrease in particle size as observed by field-emission scanning electron microscopic (FESEM) imaging. [2e, 2f] The pristine MOF1 showed irregular morphology with broad size distribution in micrometre range, whereas MOF1M shows elongated hexagon-shaped particles of 1 to 1.2 μm in length (Figure 2c, d). In microwave synthesis technique, MOF1M showed a significant reduction in particle size as compared to MOF1, which decreases the diffusion barrier for N_2 at mesoscale (Figure 2).

Since as observed that microwave synthesis decreases the particle sizes and enhances the surface area of the MOF1 significantly, the role of a solvent mixture is further explored for the generation of synthesis of mesoporous MOFs, which has been observed in a few previous reports.[13a-d,18] As believed, the synergistic effect of microwave and solvent mixture would lead to the generation of a nano/mesoscale hierarchical

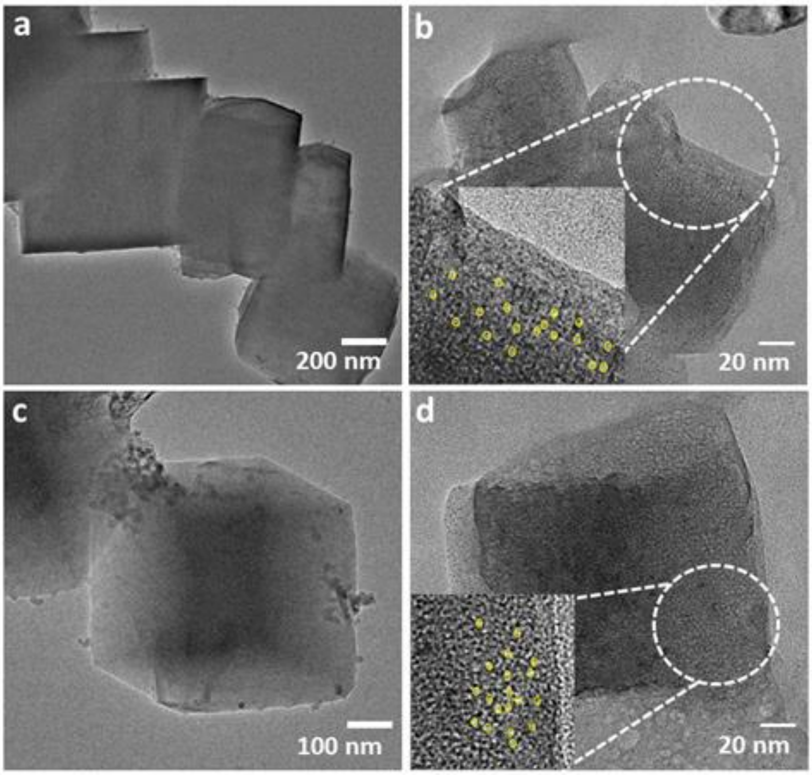

Figure 4: HRTEM images of MOF1M$_{50}$ (a, b) and MOF1M$_{75}$ (c, d). (*Inset:* Mesopore regions are spotted with yellow circles).

micro/mesoporous MOF.[13d] It has been reported that the introduction of ethanol in the reaction mixture containing metal salt and organic linker in aqueous solution, leads to the formation of water-ethanol clusters[22] that helped in crystallization and mesopore generation.[13a] With this in mind, different percentages of ethanol (25, 50 and 75%) to the reaction mixture was introduced that contains Al(III) salt, 1,4-ndc and water, which was then kept in a microwave reactor at 150 °C for 120 min that resulted in three different (MOF1M$_{25}$, MOF1M$_{50}$ and MOF1M$_{75}$) products. In all cases, the similarity of the PXRD patterns with the simulated PXRD pattern of MOF1 indicates towards the formation of identical structures (Figure 1).

The hierarchical MOFs were further characterized using various microscopic techniques. MOF1M$_{25}$, with 25% of ethanol in the reaction mixture, showed a mixture of elongated hexagonal and cubic particles broadly ranging from 500 nm to 1 μm as observed in FESEM imaging (Figure 2e, 3b). Further increase of EtOH percentage (50%) (MOF1M$_{50}$) in the reaction mixture yielded homogenous cubic particles of sizes in the range of 500-800 nm (Figure 2f, 3c). Similar morphology was also observed in the case of MOF1M$_{75}$

(with 75% of ethanol), where distribution of particles of 500-800 nm dimensions was identified all through (Figure 2g, 3d). Transmission electron microscopy (TEM) images were also captured for $MOF1M_{50}$ and $MOF1M_{75}$, which exhibited similar morphology and particle sizes, as observed in FESEM (Figure 4). Under HRTEM, mesopores of about ~3.5 to 4 nm dimensions were distinctly spotted over the $MOF1M_{50}$ and $MOF1M_{75}$ matrices (Figure 4a-d). Along with the TEM images further approve the existence of enhanced mesopore density and their widespread distribution over $MOF1M_{75}$ compared to $MOF1M_{50}$ (Figure 4b, d).

Table 2. BET surface area (S_{BET}), pore diameter and pore volume of the MOF synthesized in microwave varying with different ethanol/water ratios and reaction time. Micro and mesopore volumes are calculated from t-plot by considering P/P_0 from 0.2 to 0.7.

Sl. No.	Name	Surface area (m^2/g)	Pore width diameter (nm)	Micropore volume (cc/g)	Mesopore volume (cc/g)	Total Pore Volume (cc/g)
1	MOF1M	382	1.23	0.15	0.03	0.18
2	$MOF1M_{25}$	512	1.23, 3.62	0.20	0.05	0.25
3	$MOF1M_{50}$	682	1.23, 3.62	0.25	0.06	0.31
4	$MOF1M_{75}$	584	1.07, 1.23, 3.62	0.20	0.07	0.27

N_2 adsorption isotherms at 77 K showed a steady increase from $MOF1M_{25}$ to $MOF1M_{50}$ with increase of EtOH percentage, however, it decreases in the case of $MOF1M_{75}$ (Fig. 2a). All the three compounds exhibited a combination of typical type-I and type-IV isotherms for N_2 at 77 K. The steep uptake at low-pressure regions in all compounds suggested a high degree of microporosity in all the samples, whereas the H1 type broad hysteresis loop at higher relative pressures ($P/P_0 > 0.4$) implies capillary condensation of N_2 within the uniform mesopores. The BET surface areas for $MOF1M_{25}$, $MOF1M_{50}$ and $MOF1M_{75}$ are found to be 515, 682 and 584 m^2g^{-1}, respectively (Table 2). The pore size distributions for $MOF1M_{25}$, $MOF1M_{50}$ and $MOF1M_{75}$ obtained from the NLDFT method, and all these three samples showed mesopore with diameter 3.62 nm, in addition to micropore at 1.23 nm. With increasing the amount of EtOH, the number of cluster formation increased, as a consequence the mesopore volume increases in a regular array (0.05, 0.06, 0.07 cm^3g^{-1},

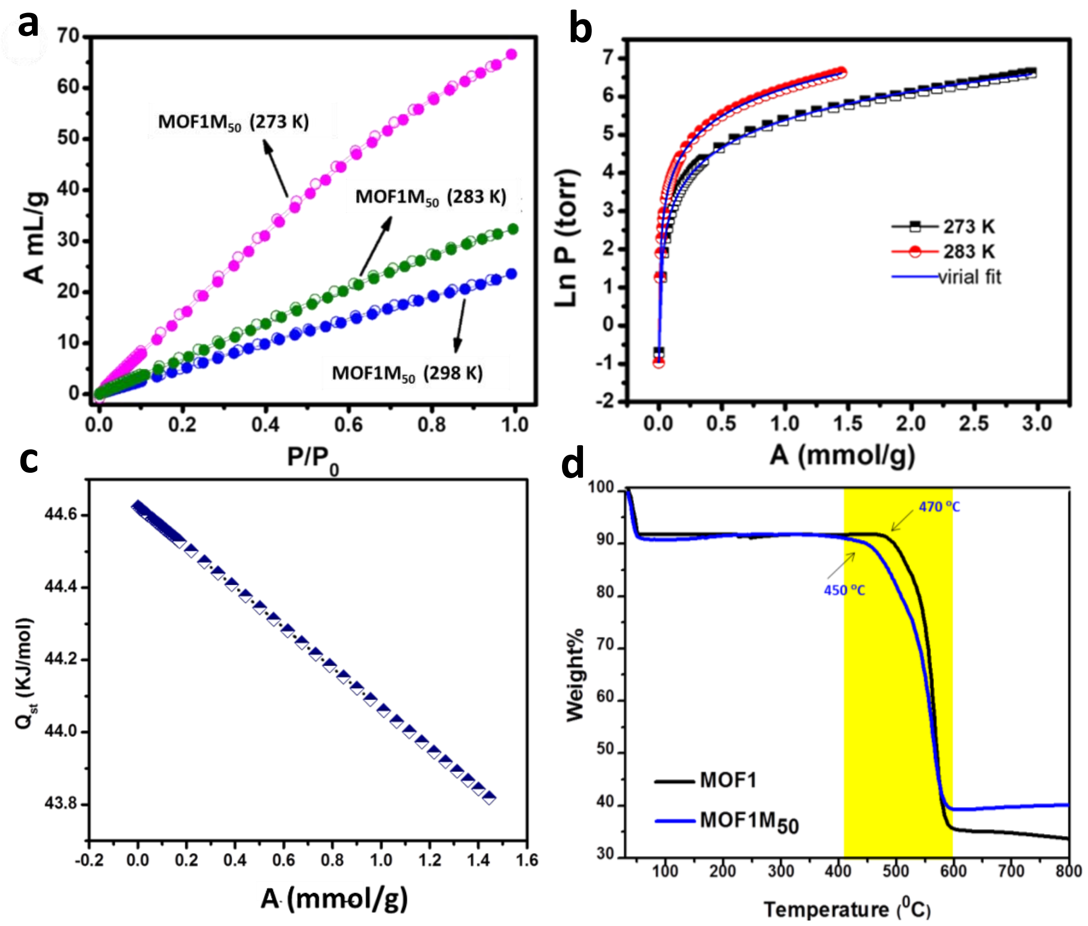

Figure 5: (a) CO$_2$ adsorption/desorption isotherms of MOF1M$_{50}$ at 298 K, 283 K, and 273 K, (b) Adsorption isotherms of CO$_2$ at 273 and 283 K were fitted in the virial equation, (c) from which the isosteric heat of adsorption (Q$_{st,f}$) for sample was calculated to be ~44.6 kJ.mol^{-1} at the zero coverage region. (d) Comparative TGA profile of MOF1M$_{50}$ with MOF1M.

respectively) (Figure 2b). However, in the case of MOF1M, only micropores were observed (Figure 2b, Table 2). The t-plot calculated in P/P$_0$ range of 0.2 to 0.7 generates the micro-to-mesopore volume ratio (V$_{micro/meso}$) for MOF1M$_{25}$, MOF1M$_{50}$ and MOF1M$_{75}$ are 4.0, 4.17 and 2.85 (Table 2). Hence, it can be inferred that while the presence of EtOH is definitely instrumental in generating the mesopores, and increasing the percentage of EtOH from 25 to 75% does not affect the mesopore diameter, (Figure 2e, Table 2) although mesopore volume is enhanced significantly. It is to be noted that, as the reaction was carried out under microwave, the particle size prominently decreased and was restricted to a particular morphology such as elongated hexagonal and cubic. Furthermore, with ethanol incorporation, particle size decreases and at 50% ethanol solvent environment it shows the minimum size with a homogeneous cubic morphology.

For cubic porous crystals, the surface area value is inversely proportional to the length of MOF crystal; S/ V α 1/a, where 'S', 'V' and 'a' are surface area, volume and length of the crystal.[23] This is why, MOF1M$_{50}$ exhibits maximum surface area with a minimum particle size as well as highest micro-to-mesopore volume ratio (V$_{\text{micro/meso}}$) of 4.17. These observations establish that the ratio of the solvents in the reaction mixture is instrumental in modulating the morphology and particle sizes in the MOF. In addition, the framework stability for MOF1M$_{50}$ remains intact and is almost similar to the pristine MOF, which is unlike all other hierarchical MOFs which lack stability owing to increased pore size and amplified pore volume (Figure 5d). The increment in surface area in MOF1M series compared to nonporous pristine MOF1 can be attributed to the reduction in diffusion barrier as a result of the successful formation of smaller particles under the microwave synthesis.[24] MOF1M$_{50}$ showed both the highest BET surface area as well as the maximum micropore volume that prompted us to explore the CO_2 capture studies at different temperatures. MOF1M$_{50}$ showed net uptake of 24 mL/g, 32 mL/g and 67 mL/g of CO_2 at 298 K, 283 K and 273 K at P =1 atm, respectively (Figure 5a). The adsorption isotherms of CO_2 at 273 and 283 K were fitted in the virial equation, from which the isosteric heat of adsorption ($Q_{st,f}$) was calculated to be ~44.6 kJmol^{-1} at the zero coverage region (Figure 5b, c).

2.2.3.2: Understanding the mechanism of mesopore formation

The evolution of small size particles was solely guided by microwave since MOF1M synthesized using only water as a solvent does not reveal any mesoporosity. The addition of ethanol as a co-solvent with water allows the hydrophobic alkyl group of ethanol to point away from the water molecule, forming micellar clusters through hydrogen bonding between water and the -OH moiety.[25b] These clusters act as template, allowing the nucleation and growth of MOF particles around them, thereby forming mesopores (Scheme 1). A wide range of experimental and theoretical studies have explained that when simple alcohol is mixed with water, the entropy of the randomly mixed molecules increases to a far lower extent than that expected for an ideal solution of a binary mixture.[25] The closer distance between water and ethanol molecules allows to form ice or clathrate-like structures through hydrogen bonding.[25b] In the microwave, as the reaction was carried far beyond ambient pressure (~10-15 bar), it reduces the entropy of the system by creating the possibility of more cluster formation. In addition, as it is believed, the dielectric heating also provides order in the orientation of polar and non-polar group in such a way that accelerates facile cluster formation under microwave condition. Upon increment of the EtOH content from 25% to 75%, the mesopore diameter remains the same, and there is an increment only in the mesopore number. This suggests that, under microwave with certain temperature and pressure (120 °C, 10-15 bar), a definite size of the water-ethanol cluster has formed with the formula of *(water)ₘ(ethanol)ₙ* where m and n are constant integers. As a consequence, with increasing ethanol concentration, a greater number of water-ethanol clusters of similar size have been formed, and mesopore volume increases correspondingly. [25c]

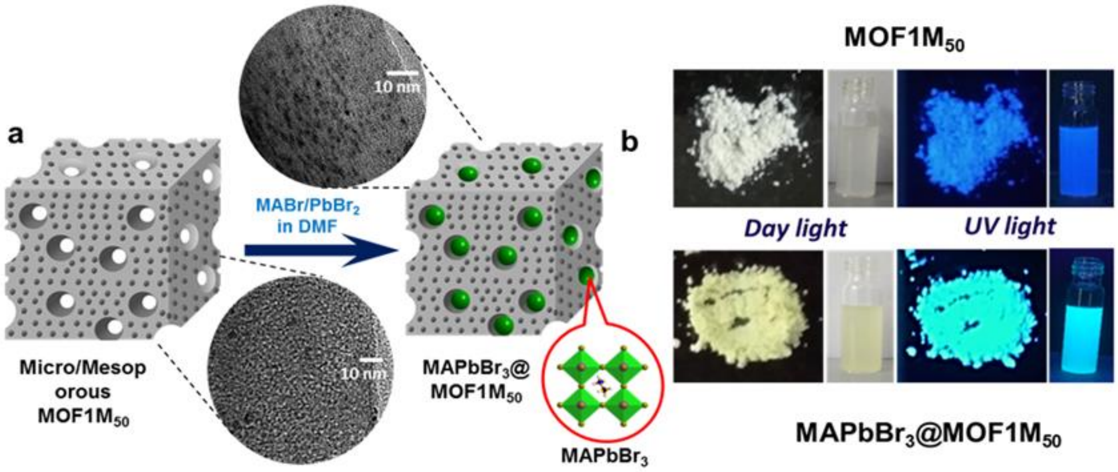

Figure 6. (a) Schematic representation for the formation of $MAPbBr_3$@MOF1M$_{50}$. (b) Photographs of solid state and EtOH dispersions for MOF1M$_{50}$ and $MAPbBr_3$@MOF1M$_{50}$ under day light and UV light.

2.2.3.3: Confinement of $MAPbBr_3$ perovskite quantum dots in MOF1M$_{50}$

The mesopores thus formed in MOF1M$_{50}$ can be used as templates for the growth and stabilization of important molecular entities for specific applications. The conventional methods for the synthesis of organic-inorganic hybrid perovskite quantum dots (PQDs), like $MAPbX_3$ (MA = Methylammonium, $CH_3NH_3^+$; X= Cl/Br/I), [26][20n][27] are all extremely tedious. In a template-based method, mesopores of MOF structure can house the PQD nanocrystals, thereby restricting their size and leading to quantum confinement effect. [20g, 28] Moreover, since the MOF acts as both a template and a size restrictor, this method will not depend on external capping agents or anti-solvents for its success. These advantages led us to attempt the growth and stabilization of $MAPbBr_3$ within the

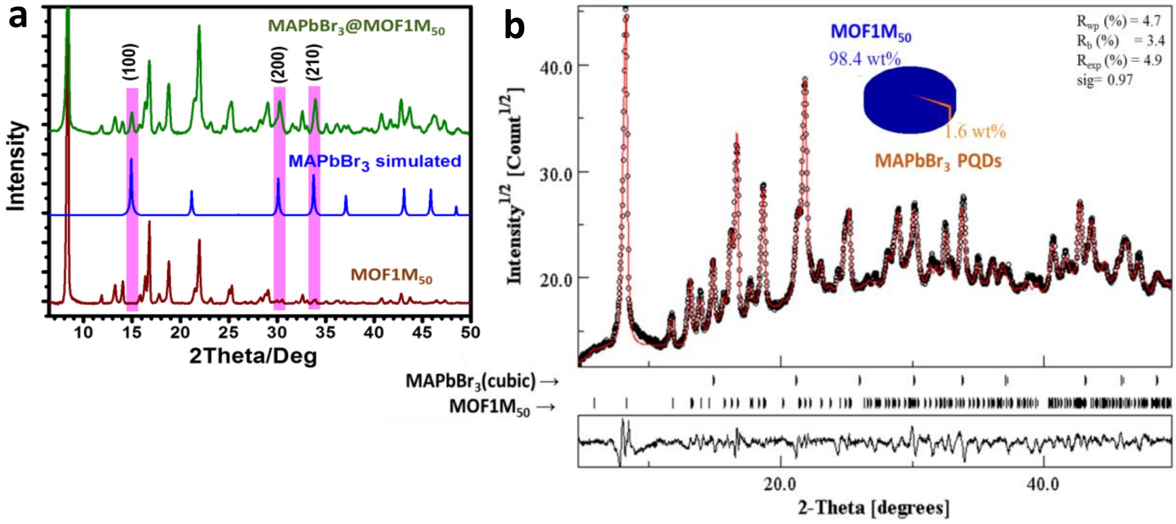

Figure 7: (a) PXRD comparison of MAPbBr$_3$@MOF1M$_{50}$ with simulated MAPbBr$_3$ and MOF1M$_{50}$. (b) Quantitative Phase Analysis (QPA) of MAPbBr$_3$@MOF1M$_{50}$ using MAUD program, showing the refinement for MAPbBr$_3$@MOF1M50 with the mixture phases of MOF1M$_{50}$ and cubic MAPbBr$_3$ and corresponding weight (%).

mesopores of MOF1M$_{50}$ (Figure 6a). The precursor solution mixture containing PbBr$_2$ and MABr were added to MOF1M$_{50}$ powders in 5 µL increments, each followed by vigorous vortex mixing to get a final concentration of 0.5 µL/mg. The resultant powder is dried at 100 °C and washed with ethanol to yield MAPbBr$_3$@MOF1M$_{50}$. PXRD pattern of MAPbBr$_3$@MOF1M$_{50}$ confirms the formation of MAPbBr$_3$ PQDs with the appearance of new peaks at $2\theta = 14.9$, 30.1 and 33.7°, which correspond to (100), (200) and (210) planes of MAPbBr$_3$, respectively (Figure 7). Furthermore, the quantitative phase analysis (QPA) obtained from the diffraction pattern has been calculated to investigate the weight percentage of MOF1M$_{50}$ and cubic MAPbBr$_3$ crystalline phases in MAPbBr$_3$@MOF1M$_{50}$.[29] The weight (%) is found to be 98.4(±2) and 1.6(±2) for MOF1M$_{50}$ and MAPbBr$_3$ PQDs, respectively (Figure 7b), which indicates the presence of cubic phase of MAPbBr$_3$ PQDs in MAPbBr$_3$@MOF1M$_{50}$. Moreover, N$_2$ adsorption isotherm at 77K for MAPbBr$_3$@MOF1M$_{50}$ showed a significant decrease as compared to MOF1M$_{50}$, indicating pore blocking by the PQDs (Figure 8a). In NLDFT pore size distribution graph, the peak corresponding to the mesopores of 3.62 nm diameter is almost vanished, suggesting the growth of the PQDs on these mesopores (Figure 8b). Under TEM, the PQDs of diameters 3-4 nm were found to be distributed over the MOF matrix, implying that their size has

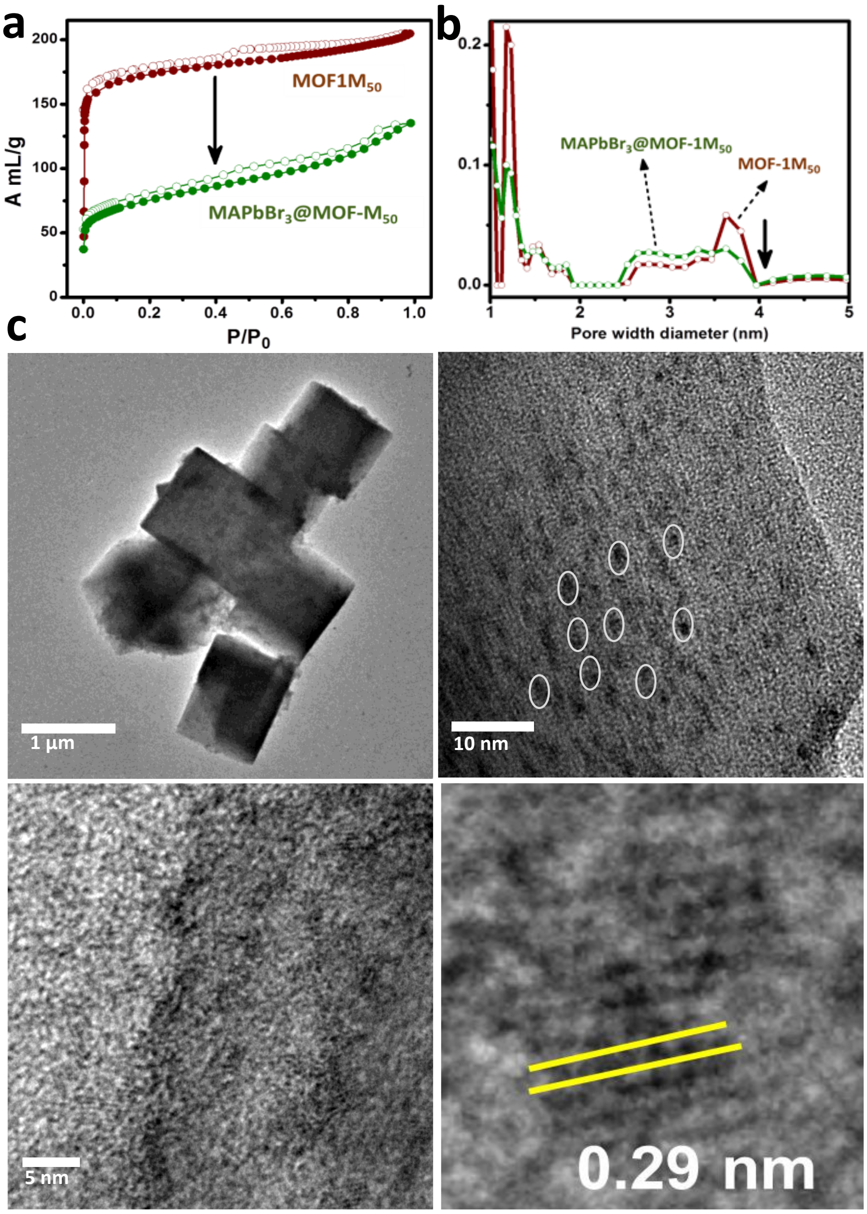

Figure 8: (a) N_2 uptake comparison of $MOF1M_{50}$ with $MAPbBr_3@MOF1M_{50}$ at 77 K. solid and open circles are indicating adsorption and desorption respectively. (b) Pore size distribution comparison of $MOF1M_{50}$ with $MAPbBr_3@MOF1M_{50}$. (c) TEM images of $MAPbBr_3@MOF1M_{50}$.

been restricted by the mesopores (Figure 8c). HRTEM showed that the PQDs have lattice fringes of width 0.29 nm corresponding to (100) plane of $MAPbBr_3$ QDs. For comparison, $MAPbBr_3$ PQDs with an average size of 3.3 nm were synthesized via a reported method, and the corresponding HRTEM images were obtained (Figure 8c, bottom right), and it showed similar lattice fringes. [20n] $MOF1M_{50}$ showed a white color under ambient light and a blue emission under a UV lamp. In contrast, $MAPbBr_3@MOF1M_{50}$ is yellow under

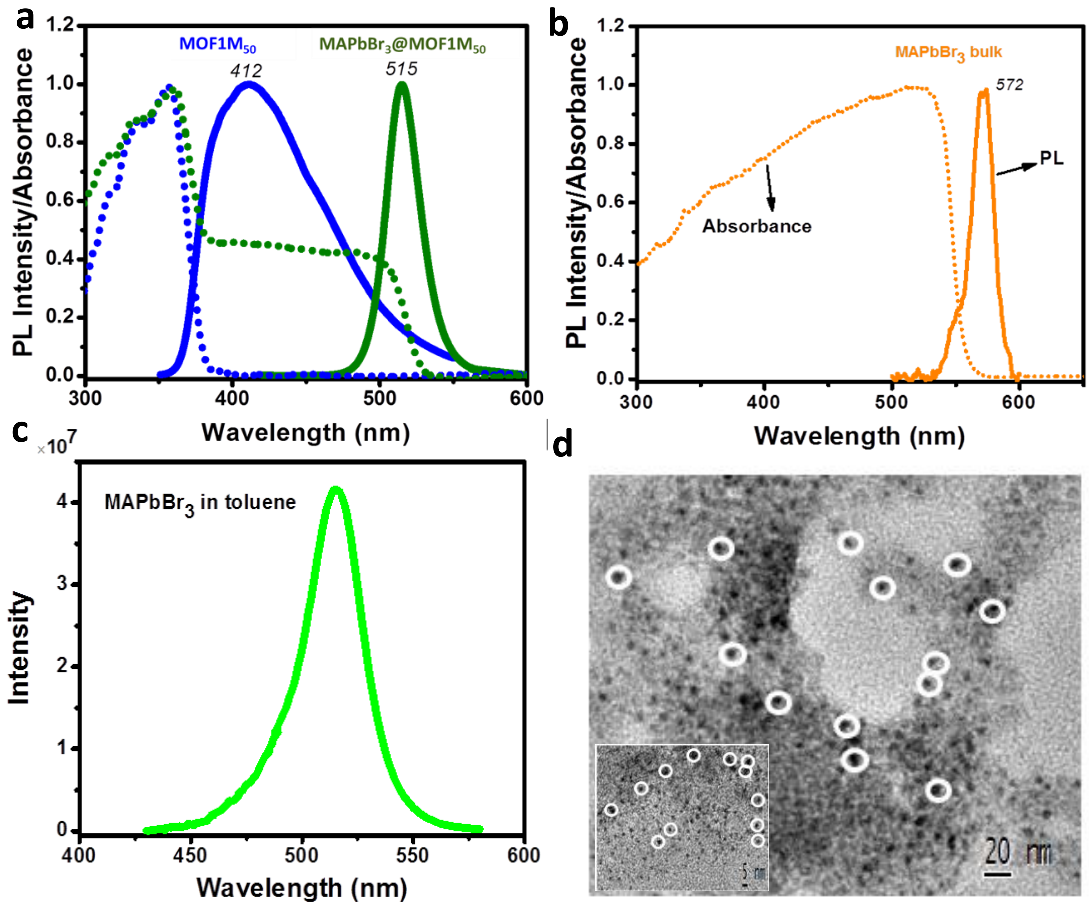

Figure 9: (a) UV-Vis (dotted line) and photoluminescence (solid line) spectra for pristine micro/mesoporous MOF; MOF1M$_{50}$ (λ_{ex} at 340 nm) and MAPbBr$_3$@MOF1M$_{50}$ (λ_{ex} at 400 nm). (b) UV-Vis (dotted line) and photoluminescence (solid line) spectra for bulk MAPbBr$_3$. (c) PL spectrum of MAPbBr$_3$ QDs in toluene upon excitation of 365 nm. (d) TEM images of MAPbBr$_3$ QDs (*inset:* high resolution).

ambient light and exhibited a bright green emission under UV light, indicating the formation of PQDs (Figure 6b). The photophysical properties of this composite were further studied in detail. MOF1M$_{50}$ showed an absorption band at 357 nm and an emission band at 412 nm (λ_{ex} 340 nm) (Figure 9a). In addition to the absorption band of the MOF1M$_{50}$, in the UV-vis spectrum of MAPbBr$_3$@MOF1M$_{50}$, a broadband was identified tailing till 535 nm, corresponding to the MAPbBr$_3$ PQDs. MAPbBr$_3$@MOF1M$_{50}$ showed an emission maximum at 515 nm upon being excited at 400 nm (Figure 9a). Both the PL and UV bands corresponding to MAPbBr$_3$ in MAPbBr$_3$@MOF1M$_{50}$ showed a blue shift from the bulk MAPbBr$_3$, thereby clearly showing quantum confinement (Figure 9b). [20g, 28a] Malgras *et al.* [20g, 28a] Zhang *et al.* [30] and D. Zhang *et al.* [31] reported the PL bands

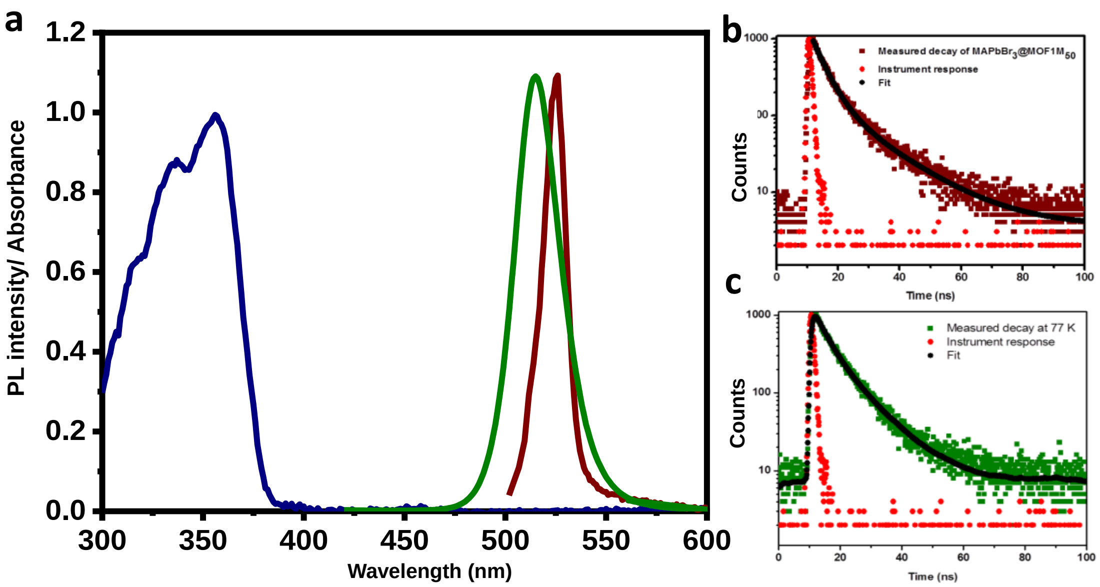

Figure 10: (a)Photoluminescence and UV-vis (blue) spectral comparison of $MAPbBr_3@MOF1M_{50}$ at 298 K and 77 K (λ_{ex} at 400 nm), and corresponding lifetime measurements of $MAPbBr_3@MOF1M_{50}$ at (b) 298 and (c) 77 K.

of confined $MAPbBr_3$ PQDs in mesoporous silica and MOF situated in between 473 nm to 527 nm based on their increasing crystal size.[20a-d, 20g, 20k, 28a] The emission of $MAPbBr_3@MOF1M_{50}$ composite is in the same range, which establishes the confinement of the PQDs within the mesopores. The separately synthesized $MAPbBr_3$ PQDs of 3.3 nm diameter showed emission maximum at 515 nm in toluene upon excitation of 365 nm, indicating that the emission in $MAPbBr_3@MOF1M_{50}$ at 515 nm corresponds to the $MAPbBr_3$ PQDs confined within the mesopores (Figure 9c). The absolute quantum yield (QY) is observed to be 6.77% for $MAPbBr_3@MOF1M_{50}$. The time-resolved PL spectrum of $MAPbBr_3@MOF1M_{50}$ showed a tri-exponential decay with an average lifetime of 8.17 ns (Figure 10, Table 3). The shorter lifetime could be the consequence of dominant surface trapping as the crystal size decreases.[20g] In addition, PL at 77 K was further measured by keeping the sample under a dewar filled with liquid nitrogen. A red-shifted emission was observed with maxima at 525 nm upon excitation at 400 nm at 77 K (Figure 10a). In general, the temperature dependency i.e., the semiconductor energy gap, is influenced by electron-phonon interaction and thermal expansion of the lattice.[32] At low temperature, due to thermal shrinkage of quantum dot lattice, the energy gap between the valence band maxima and conduction band minima decreases as a consequence of increased phonon-electron interaction. Thereby, PL spectra was red-shifted and average exciton lifetime increased from 8.17 (298 K) to 9.12 (77 K) ns (Figure 10, Table 3).

Table 3: PL lifetime details.

Sample	Average Lifetime (ns)	PL Quantum Yield (Φ) %
$MAPbBr_3$@MOF1M$_{50}$; Ex. 400, Em. 515; 298 K	8.17	6.77
$MAPbBr_3$@MOF1M$_{50}$; Ex. 400, Em. 515; 77 K	9.12	--

2.2.4: Conclusion

In a nutshell, this chapter has successfully demonstrated synthesis and characterization of a series of micro/mesoporous hierarchical MOFs of by assembling Al(III) and 1,4-ndc by changing the ratio water-ethanol solvent system or time under microwave heating. Water-EtOH clusters facilitate the formation of mesopores, and the increasing amount of EtOH promotes the mesopore volume. Furthermore, the change in the solvent mixture composition also modulates the morphology and particle sizes. As a matter of course, this is a contemporary approach to generate hierarchical MOFs with integral stability which can be adapted for developing MOFs for specific as well as comprehensive applications. Additionally, MOF1M$_{50}$ micro/mesoporous MOF was used for the confinement of $MAPbBr_3$ PQDs within its mesopores. These results may help in the synthesis of perovskite QDs in mesoporous MOF as a template in a simple route for further optoelectronic applications. Overall, this is a simple and effective method for the synthesis of hierarchical MOFs that can open the vista for several specific applications.

2.2.5: References

[1] (a) G. Srinivas, V. Krungleviciute, Z.-X. Guo, T. Yildirim, *Energy Environ.Sci.* **2014**, *7*, 335-342; (b) H. Furukawa, N. Ko, Y. B. Go, N. Aratani, S. B. Choi, E. Choi, A. Ö. Yazaydin, R. Q. Snurr, M. O'Keeffe, J. Kim, O. M. Yaghi, *Science* **2010**, *329*, 424-428; (c) J. J. Goings, S. M. Ohlsen, K. M. Blaisdell, D. P. Schofield, *J. Phys. Chem. A* **2014**, *118*, 7411-7417; (d) S. Ma, D. Sun, J. M. Simmons, C. D. Collier, D. Yuan, H.-C. Zhou, *J. Am. Chem. Soc.* **2008**, *130*, 1012-1016.
[2] (a)T. Rodenas, I. Luz, G. Prieto, B. Seoane, H. Miro, A. Corma, F. Kapteijn, F. X. Llabrés i Xamena, J. Gascon, *Nat. Mater.* **2015**, *14*, 48-55; (b) T.-Y. Ma, H. Li, A.-N. Tang, Z.-Y. Yuan,

Small **2011**, *7*, 1827-1837; (c) N. Sikdar, S. Bonakala, R. Haldar, S. Balasubramanian, T. K. Maji, *Chem. Eur. J.* **2016**, *22*, 6059-6070; (d) S. Bhattacharyya, A. Chakraborty, A. Hazra, T. K. Maji, *ACS Omega* **2018**, *3*, 2018-2026; (e) A. Chakraborty, A. Achari, M. Eswaramoorthy, T. K. Maji, *Chem. Commun.* **2016**, *52*, 11378-11381; (f) A. Chakraborty, S. Roy, M. Eswaramoorthy, T. K. Maji, *J. Mater. Chem. A* **2017**, *5*, 8423-8430.

[3] Y. Chen, V. Lykourinou, C. Vetromile, T. Hoang, L.-J. Ming, R. W. Larsen, S. Ma, *J. Am. Chem. Soc.* **2012**, *134*, 13188–13191.

[4] (a) K. M. L. Taylor-Pashow, J. D. Rocca, Z. Xie, S. Tran, W. Lin, *J. Am. Chem. Soc.* **2009**, *131*, 14261–14263; (b) W. J. Rieter, K. M. Pott, K. M. L. Taylor, W. Lin, *J. Am. Chem. Soc.* **2008**, *130*, 11584–11585; (c) D. Samanta, S. Roy, R. Sasmal, N. D. Saha, P. K R, R. Viswanatha, S. S. Agasti, T. K. Maji, *Angew. Chem. Int. Ed.* **2019**, *58*, 5008-5012.

[5] L. E. Kreno, K. Leong, O. K. Farha, M. Allendorf, R. P. V. Duyne, J. T. Hupp, *Chem. Rev.* **2012**, *112*, 1105–1125.

[6] J. Lee, O. K. Farha, J. Roberts, K. A. Scheidt, S. T. Nguyen, J. T. Hupp, *Chem. Soc. Rev.* **2009**, *38*, 1450-1459.

[7] (a) G. Hasegawa, K. Kanamori, T. Kiyomura, H. Kurata, K. Nakanishi, T. Abe, *Adv. Energy Mater.* **2014**, *5*; (b) J. H. Pikul, H. Gang Zhang, J. Cho, P. V. Braun, W. P. King, *Nat. Commun.* **2013**, *4*, 1732; (c) N. Sikdar, B. Konkena, J. Masa, W. Schuhmann, T. K. Maji, *Chem. Eur. J.* **2017**, *23*, 18049-18056.

[8] (a) Z. Zhao, G. Liu, B. Li, L. Guo, C. Fei, Y. Wang, L. Lv, X. Liu, J. Tian, G. Cao, *J. Mater. Chem. A* **2015**, *3*, 11320-11329; (b) T. Singh, C. Das, N. Bothra, N. Sikdar, S. Das, S. K. Pati, T. K. Maji, *Inorg. Chem.* **2020**, *59*, 3160-3170.

[9] (a) X.-Y. Yang, L.-H. Chen, Y. Li, J. C. Rooke, C. Sanchez, B.-L. Su, *Chem. Soc. Rev.* **2017**, *46*, 481-558; (b) S. He, Y. Chen, Z. Zhang, B. Ni, W. He, X. Wang, *Chem. Sci.* **2016**, *7*, 7101-7105.

[10] (a) C. Liu, T. Li, N. L. Rosi, *J. Am. Chem. Soc.* **2012**, *134*, 18886-18888; (b) V. Lykourinou, Y. Chen, X.-S. Wang, L. Meng, T. Hoang, L.-J. Ming, R. L. Musselman, S. Ma, *J. Am. Chem. Soc.* **2011**, *133*, 10382-10385.

[11] (a) L.-B. Sun, J.-R. Li, J. Park, H.-C. Zhou, *J. Am. Chem. Soc.* **2012**, *134*, 126−129; (b) *Chem. Commun.* **2011**, *47*, 7809–7811; (c) L.-G. Qiu, T. Xu, Z.-Q. Li, W. Wang, Y. Wu, X. Jiang, X.-Y. Tian, L.-D. Zhang, *Angew. Chem.* **2008**, *120*, 9629 –9633; (d) K. Jayaramulu, K. S. Krishna, S. J. George, M. Eswaramoorthy, T. K. Maji, *Chem. Commun.* **2013**, *49*, 3937-3939.

[12] S. Yang, X. Lin, W. Lewis, M. Suyetin, E. Bichoutskaia, J. E. Parker, C. C. Tang, D. R. Allan, P. J. Rizkallah, P. Hubberstey, N. R. Champness, K. Mark Thomas, A. J. Blake, M. Schröder, *Nat. Mater.* **2012**, *11*, 710-716.

[13] (a) B. Zhang, J. Zhang, C. Liu, X. Sang, L. Peng, X. Ma, T. Wu, B. Han, G. Yang, *RSC Adv.* **2015**, *5*, 37691–37696; (b) R. Ramachandran, C. Zhao, D. Luo, K. Wang, F. Wang, *Electrochim. Acta* **2018**, *267*, 170-180; (c) Y. Yue, Z.-A. Qiao, P. F. Fulvio, A. J. Binder, C. Tian, J. Chen, K. M. Nelson, X. Zhu, S. Dai, *J. Am. Chem. Soc.* **2013**, *135* 9572−9575.

[14] Y. Kim, TaoYang, G. Yun, M. B. Ghasemian, J. Koo, E. Lee, S. J. Cho, K. Kim, *Angew. Chem. Int. Ed.* **2015**, *54*, 13273 –13278.

[15] Y. Zhao, J. Zhang, B. Han, J. Song, J. Li, Q. Wang, *Angew. Chem. Int. Ed.* **2011**, *50*, 636-639.

[16] L. Peng, J. Zhang, Z. Xue, B. Han, X. Sang, C. Liu, G. Yang, *Nat. Commun.* **2014**, *5*, 4465.

[17] D.-Y. Hong, Y. K. Hwang, C. Serre, G. Férey, J.-S. Chang, *Adv. Funct. Mater.* **2009**, *19*, 1537-1552.

[18] (a) Y. Yue, P. F. Fulvio, S. Dai, *Acc. Chem. Res.* **2015**, *48*, 3044−3052; (b) S. Laha, A. Chakraborty, T. K. Maji, *Inorg. Chem.* **2020**, *59*, 3775-3782.

[19] H. Guo, Y. Zhu, S. Wang, S. Su, L. Zhou, H. Zhang, *Chem. Mater.* **2012**, *24*, 444-450.

[20] (a) J. Cho, Y.-H. Choi, T. E. O'Loughlin, L. D. Jesus, S. Banerjee, *Chem. Mater.* **2016**, *28*, 6909−6916; (b) J. A. Sichert, Y. Tong, N. Mutz, M. Vollmer, S. Fischer, K. Z. Milowska, R. G. Cortadella, B. Nickel, C. Cardenas-Daw, J. K. Stolarczyk, A. S. Urban, J. Feldmann, *Nano Lett.* **2015**, *15*, 6521−6527; (c) J. Choi, H. C. Woo, X. Huang, W.-G. Jung, B.-J. Kim, S.-W. Jeon, S.-Y. Yim, J.-S. Lee, C.-L. Lee, *Nanoscale* **2018**; (d) W. Deng, H. Fang, X. Jin, X. Zhang, X. Zhang, J. Jie, *J. Mater. Chem. C* **2018** *6*, 4831-4841; (e) Y. Hassan, Y. Song, R. D. Pensack, A. I. Abdelrahman, Y. Kobayashi, M. A. Winnik, G. D. Scholes, *Adv. Mater.* **2016**, *28*, 566–573; (f) A. Kojima, K. Teshima, Y. Shirai, T. Miyasaka, *J. Am. Chem. Soc.* **2009**, *131*, 6050–6051; (g) V. Malgras, S. Tominaka, J. W. Ryan, J. Henzie, T. Takei, K. Ohara, Y. Yamauchi, *J. Am. Chem. Soc.* **2016**, *138*, 13874−13881; (h) X. Jin, X. Zhang, H. Fang, W. Deng, X. Xu, J. Jie, X. Zhang, *Adv. Funct. Mater.* **2018**, *28*, 1705189; (i) G. Li, F. W. R. Rivarola, N. J. L. K. Davis, S. Bai, T. C. Jellicoe, F. d. l. Peña, S. Hou, C. Ducati, F. Gao, R. H. Friend, N. C. Greenham, Z.-K. Tan, *Adv. Mater.* **2016**, *28*, 3528–3534; (j) J. Burschka, N. Pellet, S.-J. Moon, R. Humphry-Baker, P. Gao, M. K. Nazeeruddin, M. Gra¨tzel, *Nature* **2013**, *499*, 316-319; (k) L. Polavarapu, B. Nickel, J. Feldmann, A. S. Urban, *Adv. Energy Mater.* **2017**, *7*, 1700267; (l) H.-S. Kim, C.-R. Lee, J.-H. Im, K.-B. Lee, h. Moehl, A. Marchioro, S.-J. Moon, R. Humphry-Baker, J.-H. Yum, J. E. Moser, M. Gra¨tzel, N.-G. Park, *Sci. Rep.* **2012**, *2*, 591; (m)Y. Wei, X. Deng, Z. Xie, X. Cai, S. Liang, P. a. Ma, Z. Hou, Z. Cheng, J. Lin, *Adv. Funct. Mater.* **2017**, *27*, 1703535; (n) F. Zhang, H. Zhong, C. Chen, X.-g. Wu, X. Hu, H. Huang, J. Han, B. Zou, Y. Dong, *ACS Nano* **2015**, *9*, 4533–4542; (o) V. K. Ravi, N. Singhal, A. Nag, *J. Mater. Chem. A* **2018**, *6*, 21666-21675.

[21] A. Comotti, S. Bracco, P. Sozzani, S. Horike, R. Matsuda, J. Chen, M. Takata, Y. Kubota, S. Kitagawa, *J. Am. Chem. Soc.* **2008**, *130*, 13664–13672.

[22] (a) S. Dixit, J. Crain, W. C. K. Poon, J. L. Finney, A. K. Soper, *Nature* **2002**, *416*, 829-832; (b) E. J. W. Wensink, A. C. Hoffmann, P. J. v. Maaren, D. v. d. Spoel, *J. Chem. Phys.* **2003**, *119*, 7308-7317; (c) A. Wakisaka, K. Matsuura, *J. Mol. Liq.* **2006**, *129*, 25–32.

[23] S. Diring, S. Furukawa, Y. Takashima, T. Tsuruoka, S. Kitagawa, *Chem. Mater.* **2010**, *22*, 4531-4538.

[24] N. Sikdar, M. Bhogra, Umesh V. Waghmare, T. K. Maji, *J. Mater. Chem. A* **2017**, *5*, 20959-20968.

[25] (a) E. J. W. Wensink, A. C. Hoffmann, P. J. v. Maaren, D. v. d. Spoel, *J. Chem. Phys.* **2003**, *119*, 7308-7317; (b) S. Dixit, J. Crain, W. C. K. Poon, J. L. Finney, A. K. Soper, *Nature* **2002**, *416*, 829-832; (c) A. Wakisaka, K. Matsuura, *J. Mol. Liq.* **2006**, *129*, 25-32.

[26] M. C. Weidman, A. J. Goodman, W. A. Tisdale, *Chem. Mater.* **2017**, *29*, 5019−5030.

[27] H. Huang, F. Zhao, L. Liu, F. Zhang, X.-g. Wu, L. Shi, B. Zou, Q. Pei, H. Zhong, *ACS Appl. Mater. Interfaces* **2015**, *7*, 28128–28133.

[28] (a) V. Malgras, J. Henzie, T. Takeia, Y. Yamauchi, *Chem. Commun.* **2017**, *53*, 2359--2362; (b) S. Bhattacharyya, D. Rambabu, T. K. Maji, *J. Mater. Chem. A* **2019**, *7*, 21106-21111; (c) D. Rambabu, S. Bhattacharyya, T. Singh, C. M. L, T. K. Maji, *Inorg. Chem.* **2020**, *59*, 1436-1443; (d) Z. Chen, Z.-G. Gu, W.-Q. Fu, F. Wang, J. Zhang, *ACS Appl. Mater. Interfaces* **2016**, 8, 28737–28742.

[29] L. Lutterotti, *Nucl. Instrum. Methods Phys. Res B* **2010**, *268*, 334-340.

[30] C. Zhang, B. Wang, W. Li, S. Huang, L. Kong, Z. Li, L. Li, *Nat. Commun.* **2017**, *8*, 1138.

[31] D. Zhang, Y. Xu, Q. Liu, Z. Xia, *Inorg. Chem.* **2018**, *57*, 4613-4619.

[32] (a) H. C. Woo, J. W. Choi, J. Shin, S.-H. Chin, M. H. Ann, C.-L. Lee, *J. Phys. Chem. Lett.* **2018**, *9*, 4066-4074; (b) S. M. Lee, C. J. Moon, H. Lim, Y. Lee, M. Y. Choi, J. Bang, *J. Phys. Chem. C* **2017**, *121*, 26054-26062.

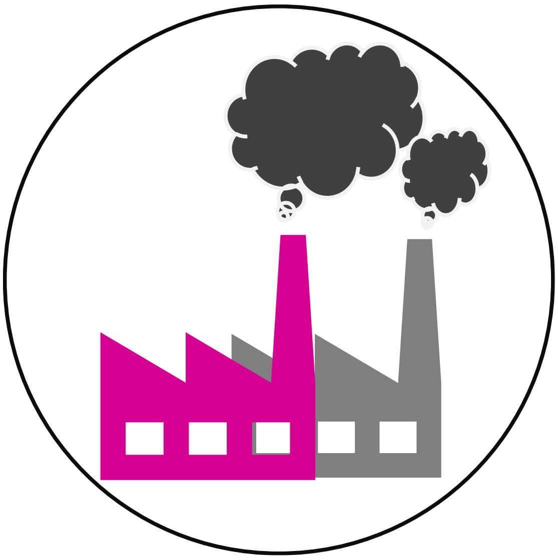

Chapter 3

Hydrocarbon Capture, Separation and Purification

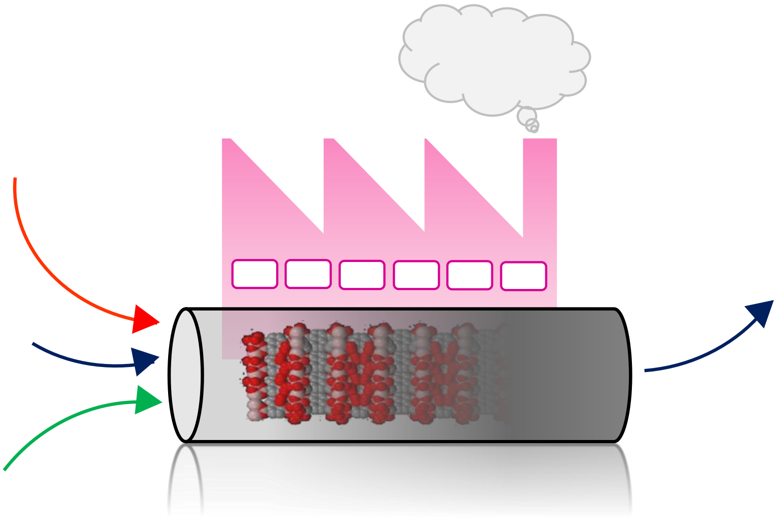

3.1: Highly Selective Multicomponent Hydrocarbon Separation with a Tailor-made Al-MOF

Manuscript under preparation

Abstract

Light hydrocarbon separation is considered one of the most industrially challenging and desired chemical separation processes as they are highly essential in polymer and chemical industries. Among them, separating ethylene (C_2H_4) from ethane (C_2H_6) and acetylene (C_2H_2) from carbon dioxide (CO_2) is of paramount importance and poses significant difficulty. Here, the Al-MOF (Al(μ-OH)(1,4-ndc)]·H_2O) (MOF1) with hierarchical porosity has been synthesized by adjusting reaction time in the microwave by keeping constant solvent concentration (1:1 Water/EtOH duo) to understand the effect of time on mesoporosity generation. The best surface area is achieved with a tailored reaction time of 15 minutes, showing high uptake capacity for all hydrocarbons with an order of $C_2H_2>C_2H_6>CO_2>C_2H_4>CH_4$ under ambient conditions. The material performs outstanding separation of ethylene (C_2H_4) not only for a binary mixture (C_2H_4/C_2H_6) but also for a quaternary combination ($C_2H_4/C_2H_6/C_2H_2/CO_2$ and $C_2H_4/C_2H_6/C_2H_2/CH_4$) of varying concentrations. The detailed separation/purification mechanism was unveiled by gas sorption isotherms, computational simulation, mixed-gas adsorption estimation, selectivity calculation, real-time dynamic column and membrane breakthrough experiments.

3.1.1: Introduction

Purification and separation of chemical mixtures extract 15% of total industrial energy consumption and are expected to be three times more in next twenty years as demand increases sharply in chemical industries.[1] At present, industry performs separation by utilizing two major classical techniques either *via* cryogenic distillation or solvent extraction process.[2] However, all these separation technologies are impaired by high energy penalties and adsorptive separation using porous material is more environment friendly, effortless and energy-inexpensive that would compensate 80% of total energy expenditure.[3] The separation of several bulk chemical commodities involving light hydrocarbons (methane, ethane, ethylene, acetylene, etc.), which are the kernel of much industrial manufacturing, is one of the most critically challenging as a consequence of the comparable shape and volatilities of these molecules.[4] Among them, ethylene (C_2H_4) is most commercially significant as it has been exceeded a global production of 200 million tonnes.[5] Conventionally, ethylene is obtained through steam cracking and thermal decomposition of ethane (C_2H_6), in which a certain amount of ethane co-exists and needs to be removed to produce polymer grade (99.9%+ purity) ethylene, broadly utilized in polymer, fiber and chemical industries.[6] In addition, being acquired as a by-product in petroleum refining, C_2H_6 is also refined on an industrial scale from natural gas (CH_4 ~70-90%, CO_2 ~0-10%, C_2H_6 and C_2H_4 ~1-15%).[7] Moreover, as an outcome of similar physicochemical properties, it is complex to separate C_2H_6, C_2H_4, CO_2, C_2H_2 and CH_4 (Table 1) through a one-step purification technique.[4b]

Methane (CH_4), cornerstone of natural gas, has attracted immense attention as an alternative to conventional petroleum-based fuel.[8] Commercial natural gas contains approximately 3-5% of ethane, 0.2-0.5% of propane and 0.5-2% of carbon dioxide as impurities.[9] Isolating methane from carbon dioxide (CO_2) is one of the prime industrial separations as it reduces per unit energy expenditure and prevents corrosion of the pipeline by removing major acid contains.[10] Ethane (C_2H_6) comes after methane as second largest component in which separation of ethane and methane is required. On the other hand, extracted pure ethane could be further utilized as a mother precursor for ethylene preparation by steam cracking strategy.[11] Acetylene (C_2H_2) is a major feedstock for polymer, polyester, plastic and chemical industries for synthesizing essential organic compounds including acrylic acid derivatives, α-ethynyl alcohols and vinyl compounds.[12] C_2H_2 is mainly produced by the cracking or partial combustion method, co-existing with spin-offs such as methane and carbon dioxide.[12a] Purification of C_2H_2 is enormously challenging essentially to that of carbon dioxide in terms of similarities in shape (C_2H_2, 3.32 × 3.34 × 5.7 Å^3; CO_2; 3.18 × 3.33 × 5.36 Å^3), boiling point (189.3 K for C_2H_2 and 194.7 K for CO_2) and physical properties (polarizability for C_2H_2 and CO_2 are 19.5 and 33.3-39.3, respectively).[13]

In the last two decades, great endeavors have been dedicated to designing metal-organic frameworks (MOFs) as promising sorbents for various gas separation ranging from the simple N_2/CO_2 or H_2/CO_2 to most challenging ones such as alkane/alkene, olefin/paraffin by modulating surface area, pore geometry, supramolecular interactions and considering adsorbate-adsorbent interaction dictated by thermodynamic and kinetic preferences. To avail preferential selectivity of MOFs, few strategies have been generally adopted; (i) tunning pore size/shapes, (ii) introducing functional organic linker to generate strong binding sites, (iii) decorating pore environment for favored polarity and (iv) enhancing open metal sites' (OMSs) density for coordinating unsaturated hydrocarbons.[14] Indeed, different MOFs with their exclusive features have been explored for selective adsorption of CH_4/CO_2,[15] CH_4/C_2H_6,[15a, 16] C_2H_2/CO_2,[17] C_2H_2/C_2H_4,[18] and C_2H_4/C_2H_6.[11, 19] The task became further complicated when CO_2 is also an impurity with other C_2 gas mixtures such as C_2H_2, C_2H_4 and C_2H_6. Compared to other similar-sized C_2H_4, CO_2; C_2H_6 exhibited less polarity (dipolar moment) while polar adsorbents are usually selective to previous gases. Lu and his team revealed selective adsorption of ethane (86 cm^{3}g^{-1} at 298 K) and acetylene from a ternary mixture of $C_2H_2/C_2H_6/C_2H_4$ (0.5:0.5:99, v/v/v) by a single-step breakthrough operation.[20] In 2019, Chen *et al.* pioneered the concept of SSST (synergistic sorbent separation technology) to enable ultrapure C_2H_4 from the ternary and quaternary mixture by using tandem packets of three benchmark MOFs.[1b] In this aspect, constructing a single MOF by rational utilization of non-polar functional group with high uptake capacity and optimized pore size/shape is still highly desirable from the viewpoint of multi-component gas adsorption and separation.

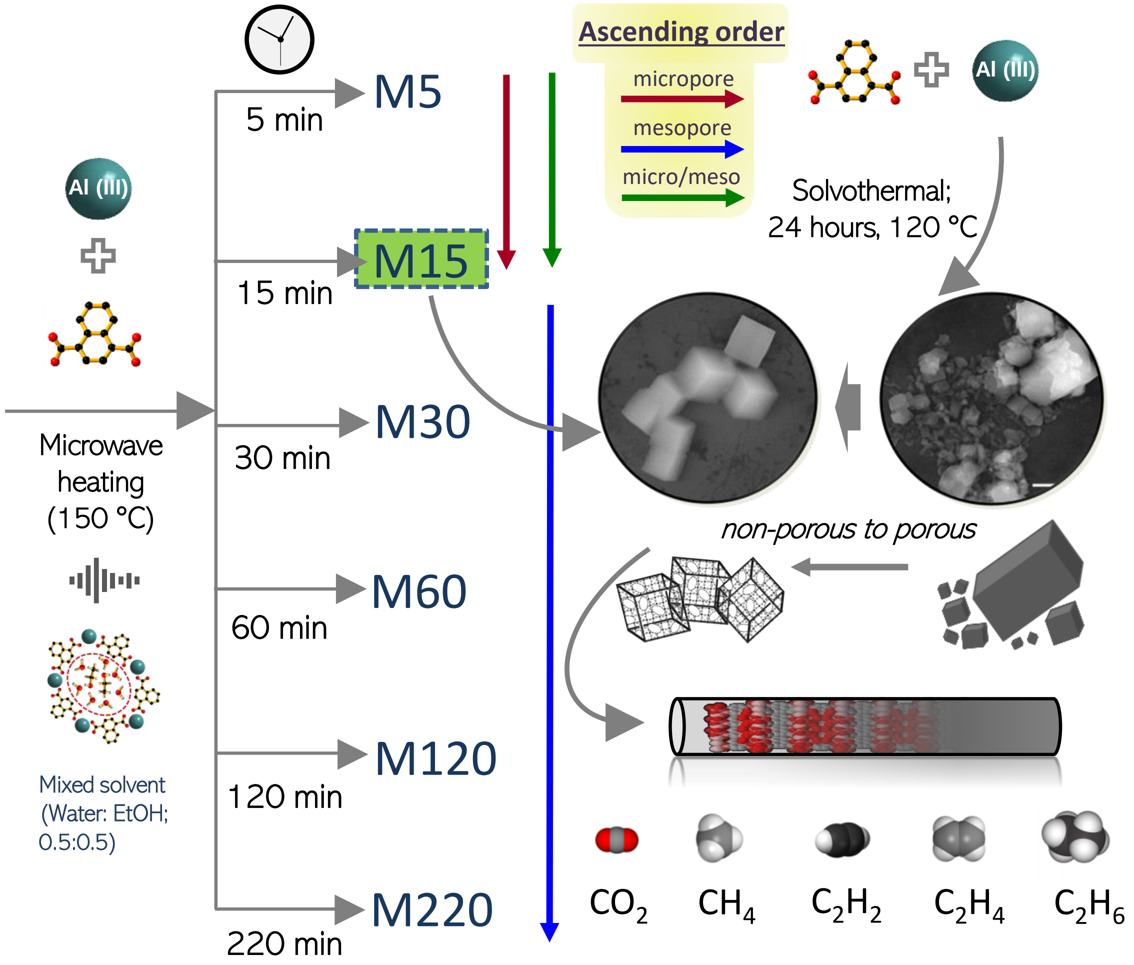

Scheme 1: Schematic representation of tailor-made hierarchical Al-MOF under microwave by tuning reaction time. 'M' stands for microwave and the best material, M15 has been chosen for detailed hydrocarbon sorption and separation studies.

The synthesis and characterization of various micro/mesoporous MOFs (Al(μ-OH)(1,4-ndc)]·H_2O) (MOF1) have been reported in the previous chapter under microwave irradiation by introducing water-ethanol solvent cluster.[21] The microwave heating enables fast nucleation that helps the formation of smaller particle sizes with increased surface-to-volume ratio. The particular MOF1 holds high thermal and chemical stability with a 3D robust structure counting two different micropore channels of dimensions 3.0×3.0 Å^2 and 7.7×7.7 Å^2.[22] In continuation to the previous chapter, this investigation unfolds the impact of reaction time (*t*) in tunning particle size and porosity of Al-MOF by keeping all other reaction conditions intact. The products are labeled as M5, M15, M30, M60, M120 and M220 as the respective reaction times (*t*) are 5, 15, 30, 120, and 220 minutes. M15 showed the maximum surface area with highest micro-mesopore volume ratio. Further characterization and versatile C_2 sorption and separation performance from the binary (CO_2/CH_4, CH_4/C_2H_6, C_2H_2/CO_2, and C_2H_4/C_2H_6) and quaternary ($CO_2/C_2H_2/C_2H_4/C_2H_6$ and $CH_4/C_2H_2/C_2H_4/C_2H_6$) gas mixtures have been performed for M15 with collaborative understanding from density functional theory and stepwise dynamic breakthrough separation. In addition, a successful H_2/CO_2 and CO_2/CH_4 separation by fabricating mixed matrix membrane through blending MOF with polysulfone has been also reported in this chapter (Scheme 1).

Table 1: Physical parameters of selected gas and vapor adsorbate.[4b, 23]

	Molecular dimension (Å)			Boiling point (K)	Polarizability×10^{25} cm^3	Dipole moment×10^{18} esu cm	Quadruple moment×10^{26} esu cm^2
	x	y	z				
CO_2	3.18	3.33	5.36	216.55	29.11	0.109	4.3
CH_4	3.63	3.98	3.98	111.66	25.93	--	--
C_2H_2	3.32	3.34	5.76	188.40	33.3-39.3	--	--
C_2H_4	3.28	4.18	4.84	169.42	42.52	--	1.5
C_2H_6	3.81	4.08	4.82	184.55	44.3-44.7	0.366	0.65

3.1.2: Experimental section

3.1.2.1: Materials

All the reagents employed are commercially available and used as provided without further purification. $Al(NO_3)_3{\cdot}9H_2O$ and polysufone (M_w ~35,000; transparent pallet) have been obtained from Sigma-Aldrich. 1,4-naphthaledicarboxylic acid (1,4-H_2ndc) was obtained from Alfa Aeser.

3.1.2.2: Synthesis

1,4-Naphthalenedicarboxylate (0.108 g, 0.5 mmol) and $Al(NO_3)_3{\cdot}9H_2O$ (0.375 g, 1 mmol) were introduced in 30 ml wide-neck microwave vial, to this H_2O and EtOH (5 mL each) were added, and further sonicated for 10 minutes. After that, the reaction vial was sealed and placed in MONOWAVE 200 microwave reactor. In microwave, the reaction mixture was heated to 150 °C (a heating rate of 6 °C /min) and held at same temperature from 5 to 220 minutes. The resulting solid white was filtered and washed with water repetitively and finally with ethanol and dried under vacuum. Six different materials were synthesized by using same metal and linker ratio but altering reaction hold time (5-220 minutes). Products are labeled as M5, M15, M30, M60, M120 and M220 as the respective reaction times are 5, 15, 30, 120, and 220 minutes. The PXRD pattern of the resulting MOFs reveals the formation of the pure crystalline phase as indexed with the simulated pattern of the parent framework (Figure 2).

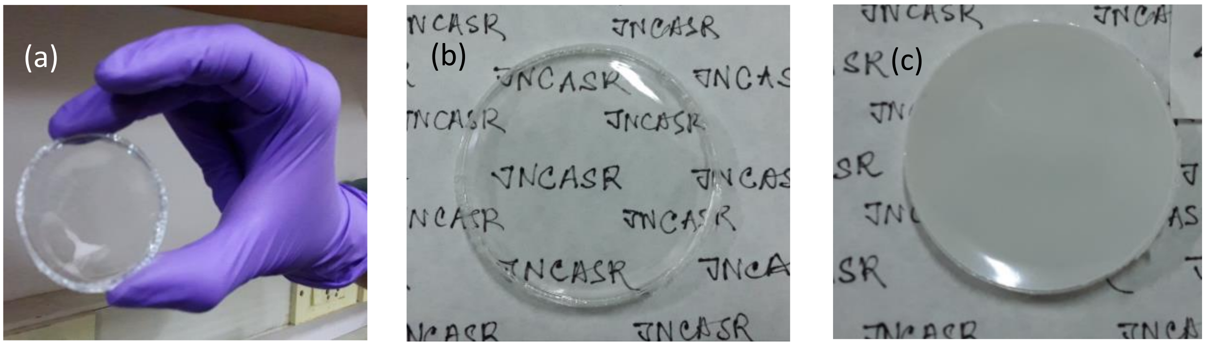

Figure 1: Photograph of standalone polysulfone (a, b) and (c) MOF@PSF mixed matrix membrane.

Membrane fabrication: MOF@PSF mixed matrix membrane have been synthesized by solution casting method. M15 powders (0.034 g) were dispersed in 25 mL DCM (dicholoromethane) and the mixture was ultrasonicated. The PSF (0.4 g; polysulfone) was added to the suspension and stirred for another 5 days. An incipient film was cast with the solution on a glass plate using a 'doctor's knife' by using low boiling point solvent DCM to fabricate film through solvent evaporation. Finally, after 24 hrs, the membrane formed on the glass plate was removed carefully and dried at room temperature in the air. The size of stand-alone membranes is further adjusted according to the customized set-up and dimensions are mentioned in Table 3.

3.1.2.3: Physical measurements

The powder XRD pattern of the compounds has been recorded by using Cu-Kα radiation (Bruker D8 Discover; 40 kV, 30 mA). The PXRD pattern (Figure 1) of the resulting MOFs of varied reaction conditions (5,15, 30, 60, 120, 220 minutes) reveals the formation of the pure crystalline phase of (Al(μ-OH)(1,4-ndc)]·H_2O). Morphological studies have been carried out using Lica-S440I Field Emission Scanning Electron Microscope (FESEM) by placing samples on a silicon wafer under high vacuum with an accelerating voltage of 100 kV.

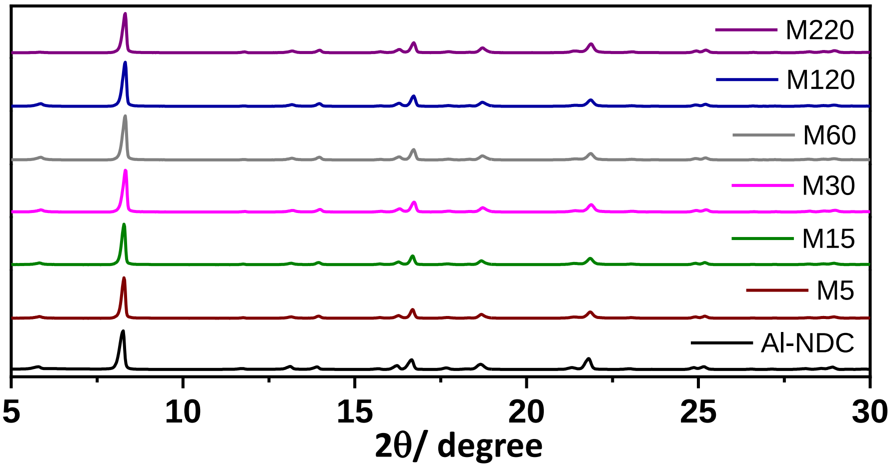

Figure 2: PXRD patterns of Al-NDC synthesized through microwave (M5, M15, M30, M60, M120 and M220) reactor by varying reaction time.

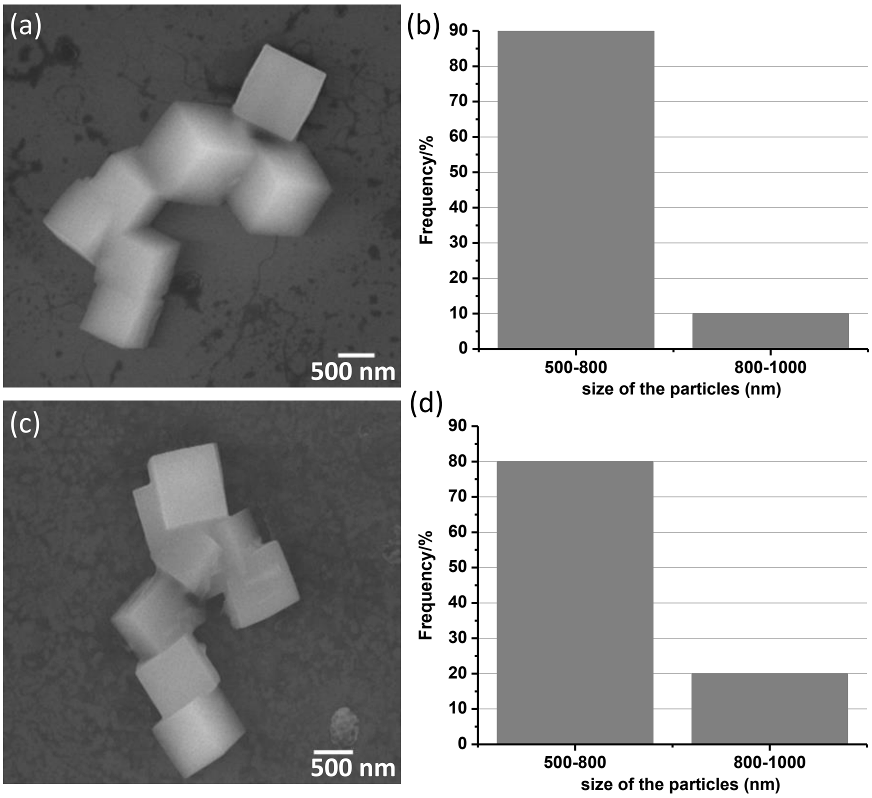

Figure 3: FESEM images and corresponding size distribution histogram of M15 (a, b) and M120 (c, d).

3.1.2.4: Adsorption details

The adsorption isotherms of hydrocarbons (CH_4, C_2H_2, C_2H_4 and C_2H_6) including CO_2 and N_2 (at 77 K) of M15 have been measured using QUADRASORB-SI analyzer and AUTOSORB IQ_2 instrument at 273 and 298 K. The surface area, pore volume and pore size distribution were calculated from the N_2 adsorption data (measured at 77 K) of the corresponding samples using the ASiQwin software. All the compounds have been activated at 150 °C under 1×10^{-1} Pa vacuum for about 16 h prior to measurement of the isotherms. All the gases used for adsorption measurement are of scientific/research grade with 99.999% purity. Dead volume is measured with helium gas. The surface area was calculated using the Brunauer–Emmett–Teller (BET) theory, which is an extension from monolayer to multilayer adsorption. The total pore volume is calculated from the amount of vapor adsorbed at a relative pressure close to unity, by assuming that the pores are then filled with a liquid adsorbate. The pore volume and pore size distributions were calculated using the Density Functional Theory (DFT), which can provide the sorption and phase behaviour of fluids in narrow pores on a molecular level. Indeed, the Non-Local Density Functional Theory (NLDFT) and Grand Canonical Monte Carlo simulation (GCMC) methods can describe the local fluid-structure near curved solid walls accurately; the adsorption isotherms in model pores are determined from intermolecular potentials of the liquid-liquid and solid-liquid interactions. The relation between isotherms derived from the above approaches and the experimental isotherm on a porous solid can be understood by GAI (Generalized Adsorption Isotherm) equation.

$$N\left(\frac{P}{P_0}\right) = \int_{W_{min}}^{W_{max}} N(\frac{P}{P_0}, W) f(W) dW$$

Where, $N(P/P_0)$ = experimental adsorption isotherm data,

W = pore width, $N(P/P_0, W)$ = isotherm on a single pore of width W,

f(W) = pore size distribution function.

The assumption which is reflected from the GAI equation is that the total isotherm consists of a number of individuals “single pore” isotherms multiplied by their relative distribution, f(W), over a range of pore sizes. The set of $N(P/P_0, W)$ isotherms (kernel) for a given system can be obtained by the DFT as indicated above. The pore size distribution can then be derived by solving the GAI equation numerically via a fast non-negative least square algorithm. The ASiQwin software has been used to calculate the pore size distribution using the NLDFT–N_2-carbon equilibrium transition kernel at 77 K based on a slit-pore model. The Water adsorption was at 293 K at vapor state by using BELSORP-aqua analyzer. All operations were automatic and software controlled.

3.1.2.4.1: Heat of adsorption

The virial expression of the following type has been used to fit the combined single component isotherm at 273 and 298 K.

$$\ln(P) = \ln(A) + \frac{1}{T}\sum_{i=0}^{m} a_i A^i + \sum_{i=0}^{n} b_i A^i \qquad \text{(eq. 1)}$$

P is the pressure expressed in torr, A is the amount adsorbed in mmol/g, T is the temperature in K, a_i and b_i are virial coefficients, and m, n represents the number of coefficients required to adequately describe the isotherms (eq. 1). The value of m and n was gradually increased until the contribution of extra added a and b coefficients were negligible towards the final fit. The values of the virial coefficient a_i were taken to calculate the isosteric heat of adsorption using the following expression.

$$Q_{st} = -R\sum_{i=0}^{m} a_i A^i + \sum_{i=0}^{n} b_i A^i \qquad \text{(eq. 2)}$$

Q_{st} is the coverage-dependent isosteric heat of adsorption and R is the universal gas constant.

3.1.2.5: Computational details

The adsorption sites were determined using the 'Adsorption Locator' implemented in the Materials studio[24] software. A 1x1x2 supercell of Al-NDC was used to locate CO_2, CH_4, C_2H_2, C_2H_4, and C_2H_6 within the framework. Both the framework and the adsorbate were assumed to be rigid. Only site-site non-bonded interaction contribution to the total potential energy was considered. Lennard-Jones parameters were taken from the Universal Force-field (UFF)[25], and the partial charges on the atoms were assigned using the charge equilibration (Q_{Eq})[26] method.

The two lowest energy atomic configurations for each adsorbate molecule located in the small and large pores of the framework system obtained using the method mentioned above was used as the initial configuration for Geometry optimization using Density Functional Theory (DFT). PBE[27] exchange-correlation functional with Grimme's D3[28] dispersion correction method was employed in all our calculations. Calculations were performed using Quickstep[29] module implemented in the CP2K[30] software package with core and valence electrons represented by GTH[29] pseudopotentials and TZ2VP-MOLOPT[31] basis sets. Default settings were used for SCF convergence and geometry optimization.

On determining the optimized geometry, the binding energy (BE) was calculated using the following expression:

$$BE_{adsorbate} = E_{framework+adsorbate} - (E_{framework} + E_{adsorbate})$$

Where, $E_{framework+adsorbate}$, $E_{framework}$, and $E_{adsorbate}$ denote the energy of the framework-adsorbate, the framework, the adsorbate, respectively.

IAST selectivity and two-component mixed adsorption were estimated from the Langmuir-Freundlich model.

$$q = q_s\left(\frac{bp^t}{1+bp^t}\right) \qquad \text{(eq. 3)}$$

Table 2: The estimated factors of considerations are as followed

	Temperature (K)	n_s (mol/kg)	b(Pa-t)	t
CO_2	293	537.83	5.01e-7	1.05
CH_4	293	298.00	4.25e-8	1.22
C_2H_2	293	96.24	4.4e-6	1.14
C_2H_4	293	38.82	3.22e-6	1.21
C_2H_6	293	62.07	2.17e-6	1.26

3.1.2.6: Separation studies

3.1.2.6.1: Stepwise dynamic breakthrough separation

Stepwise dynamic breakthrough separation (SDBS) minutely differs from usual breakthrough operation as it involves complete desorption of both the gas mixtures from the packed column by making the material regenerated for subsequent experiments with

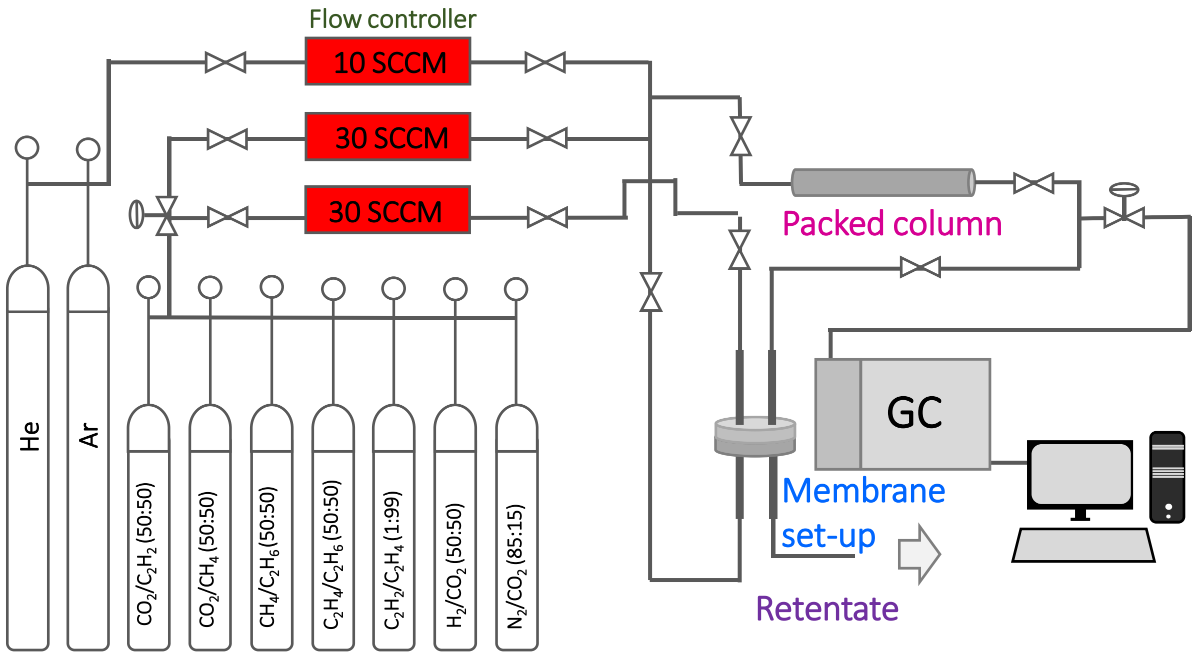

Figure 4: Schematic representation of custom-made separation (breakthrough/membrane) arrangement.

ultrahigh purification of each commodity. The material was first activated prior to loading in the column and further after loading it was further regenerated by continuous flowing of carrier gas for 1 h. The SDBS of the M15 (~1.048 g) for CO_2/CH_4, CH_4/CO_2, C_2H_2/CO_2, C_2H_4/C_2H_6 gas mixtures were analyzed by using packed column of 16.5 cm length and 0.3 cm diameter. The continuous flow was regulated by mass flow controller by using Helium as a carrier gas with a total flow of 2.2-2.9 mL/min (Figure 4). Further breakthrough separation was performed by using quaternary gas mixtures as $CO_2/C_2H_2/C_2H_4/C_2H_6$ (0.25:0.25:0.25:0.25; v/v/v/v) and $CH_4/C_2H_2/C_2H_4/C_2H_6$ (0.12:0.1:0.75:0.12; v/v/v/v). Likewise, He used as a carrier gas contributes 85% of total concentration with a flow of 3.32-3.36 mL/min. The relative percentage of outlet gas was analyzed by gas chromatography (Agilent 7890 B).

3.1.2.6.2: Mixed matrix membrane separation

Gas permeation and separation were carried out in a custom-made cell under ambient conditions (Figure 3). Similarly, as mentioned above, accurate gas flow was sustained through mass flow controllers (HORIBA-STEC). Pure feed gases, H_2 and CO_2 were used with a flow of 10-12 mLmin^{-1}. Gas mixtures, H_2/CO_2, CO_2/CH_4 were kept constant at a similar flow rate as maintained for individual feed. On the other hand, N_2 was used as sweep gas and flow was kept constant at 6 mLmin^{-1}. The eluent gas concentrations were analyzed through gas chromatographs fitted with packed/capillary molecular sieve columns for H_2, CO_2 and CH_4 separation and permeation.

The single gas permeation was calculated as;

$$P_A = \frac{x_{P_A} f t}{x_{P_{N_2}} . A(P_F x_{F_A} - P_P x_{P_A})} \qquad \text{(eqn. 4)}$$

Where P_A= Permeability of gas A. x_{FA}, x_{PA} are the mole fraction of gas A in feed and permeate stream; xP_{N_2}, mole fraction of sweep gas. P_F, P_P are the pressure in the feed and permeate stream, respectively.

A = area of the membrane, t = thickness of the membrane, f = flow rate of the sweep gas.

The binary gas mixtures, the permeation values were calculated as;

$$P_1(Barrer) = \frac{x_1 f t 10^{10}}{[1-(x_1+x_2).A.(P_1 x_1^F - P_2 x_2^F)]} \qquad \text{(eqn. 5)}$$

Where P_1= Permeability of gas 1 in Barrer, x_1, x_2 are the mole fraction of gas 1 and 2 in permeate stream, x_1^F mole fraction of gas 1 in the feed stream, x_2^F mole fraction of gas 2 in feed stream. P_1, P_2 are the pressure in feed and permeate side, correspondingly.

A is the, t is the thickness of the membrane and f is the flow rate of the sweep gas ($mL.min^{-1}$). Finally, the separation factor of selectivity is calculated as;

$$\alpha = (\frac{P_1}{P_2}) \text{ or } (\frac{P_A}{P_B}) \qquad \text{(eqn. 6)}$$

3.1.4: Result and discussion

3.1.4.1: Adsorption studies

In our previous chapter (2.2), a series of hierarchical micro/mesoporous MOFs by assembling Al(III) and 1,4-naphthalenedicarboxylate *via* modulation of solvent fraction under microwave heating has been reported. By adjusting the ratio of the solvent duo, water and ethanol; particle size, micro/mesopore volume ratio and overall surface area of the MOFs were controlled.[21] In this chapter, in order to understand the effect of reaction time on porosity, six (five more) different reactions were carried out in a 50:50 water/ethanol mixture changing reaction times of 5, 15, 30, 60, 120 and 220 min, which yielded M5, M15, M30, M60, M120 and M220, correspondingly. The parent material

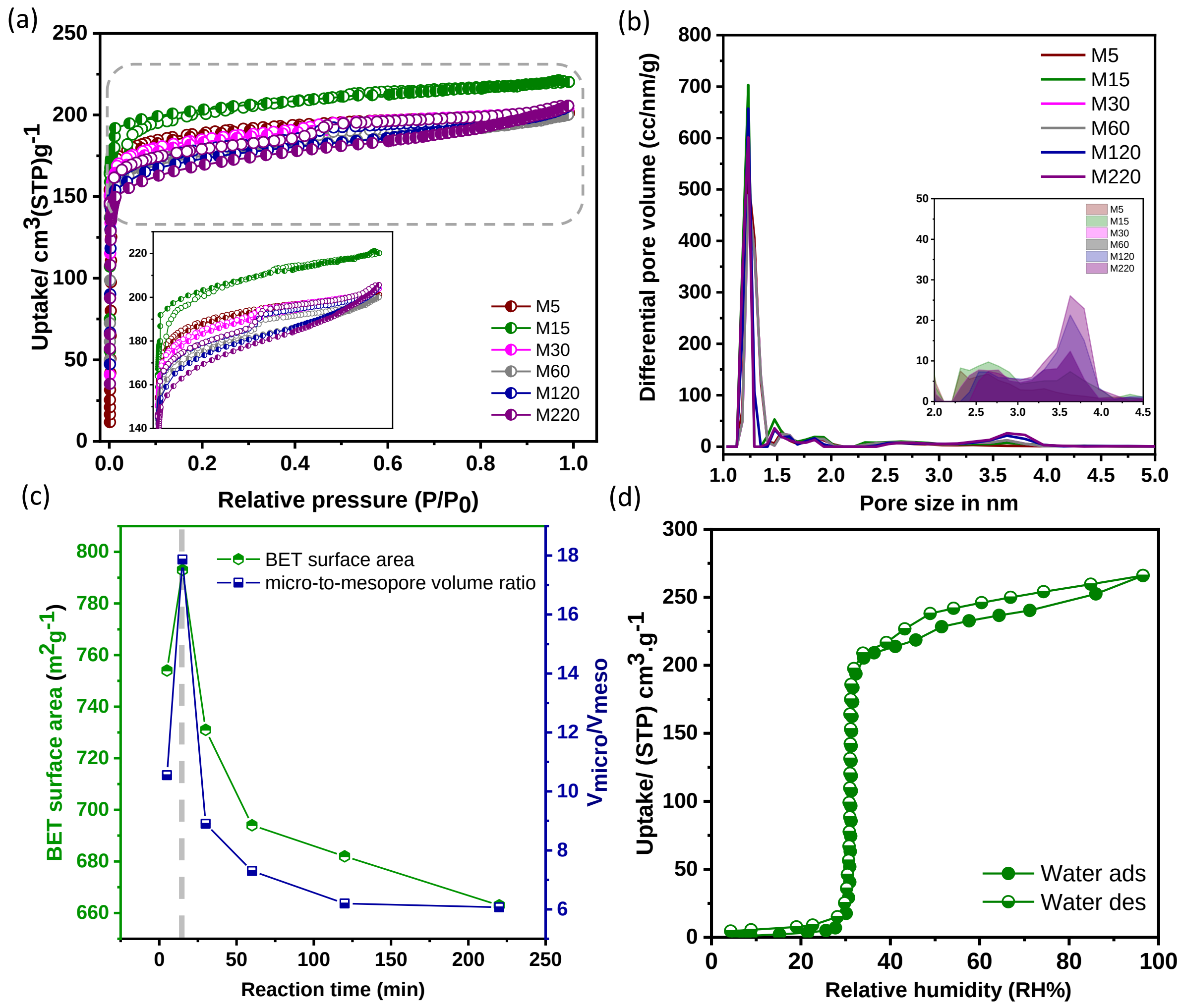

Figure 5: (a) N_2 adsorption isotherm of M5, M15, M30, M60, M120 and M220 at 77 K (*inset*: Zoom because of high adsorption region leads to saturation), (b) Corresponding pore size distribution plot calculated through NLDFT method (*inset*: differential pore volume at mesopore region), (c) A plot of reaction time with BET surface area and micro-to-mesopore volume ratio of all the products. (d) Water adsorption isotherm at 293 K for M15.

behaves non-porous towards N_2 adsorption.[22] However, the synthetic modification by introducing fast nucleation through microwave heating and water/ethanol mixed solvent approach has been observed an improvement in structural porosity by rising high surface-to-volume ratio based on particle downsizing (Scheme 1, Figure 3). N_2 adsorption experiments were performed at 77 K to establish permanent porosity and M5/15/30/60/120/220 exhibited predominantly type-I isotherm with BET surface areas was calculated to be 759, 793, 731, 694, 682 and 664 m^{2}g^{-1}, respectively (Figure 5a). Isotherm for M5 and M15 exhibits characteristic type-I profile corresponding to microporous nature whereas M30-220 exhibited mesopore formation by showing a

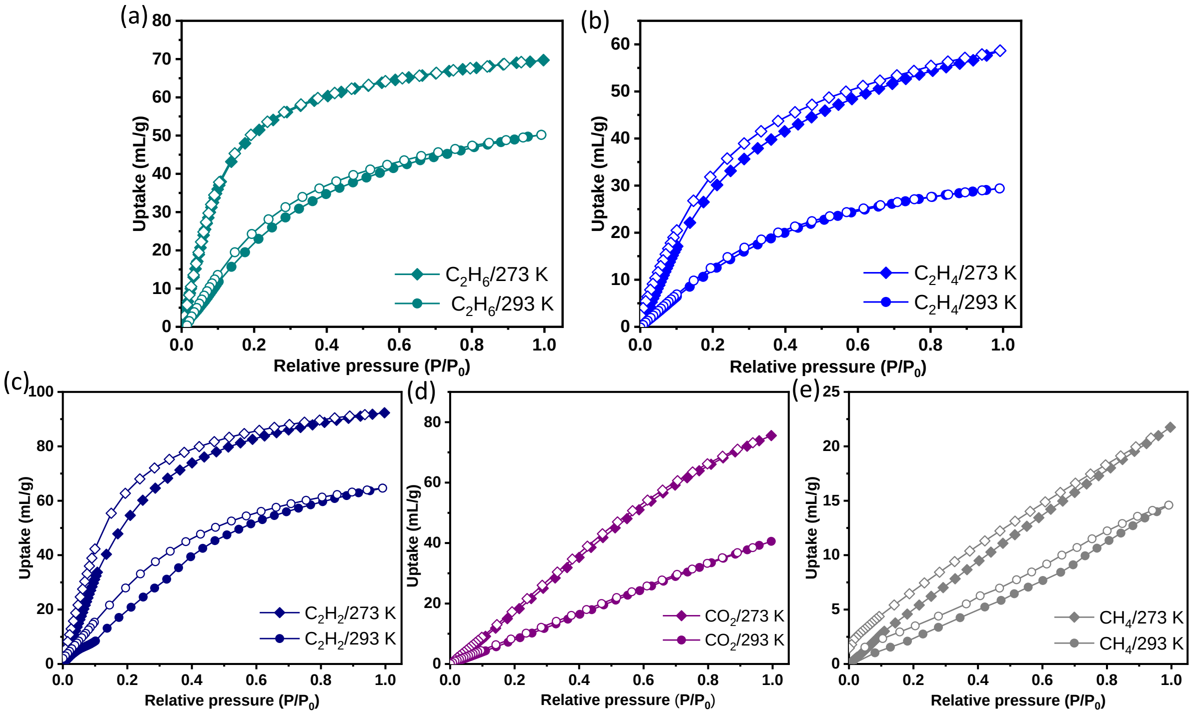

Figure 6: Single-component adsorption-desorption of (a) C_2H_6, (b) C_2H_4, (c) C_2H_2, (d) CO_2, (e) CH_4 for M15 measured at two different temperatures, 273 and 293 K at 1 bar relative pressure.

combination of type-I and type-IV. NLDFT model-based pore size distribution analysis reveals the formation of mesopore around 3.6 nm with a gradual decrease in surface area and corresponding micro-to-mesopore volume ratio for post-30 min reaction time (Figure 5b, c). There are few reports of low polarity or hydrophobic MOFs[11, 32] are reported with such a high surface area including structural rigidity, desirable pore aperture, facile reaction condition, fascinating thermal and chemical stabilities with excellent moisture robustness.[33] Thus, a remarkable high surface area with exclusive microporosity (centred at 1.2 nm) of M15 (hydrophobic pore, evidenced from water adsorption, Figure 5d) prompted us to investigate its light hydrocarbon adsorption and separation properties.

Single component adsorption-desorption isotherms for CO_2, CH_4, C_2H_2, C_2H_4, and C_2H_6 were obtained from activated M15 at 293 and 273 K. As shown in Figure 6, according to their adsorption profile up to 1 bar relative pressure follows the array C_2H_2>C_2H_6>CO_2>C_2H_4>CH_4 with saturation uptake values of 64 (2.85 $mmolg^{-1}$), 50 (2.23 $mmolg^{-1}$), 40 (1.785 $mmolg^{-1}$), 29 (1.29 $mmolg^{-1}$) and 14 (0.625 $mmolg^{-1}$) mLg^{-1} (or cm^3g^{-1}) at 293 K, respectively. The isosteric heat of adsorption (Q_{st}) was estimated using the Clausius-Clapeyron equation by fitting the isotherms at 293 and 273 K to the

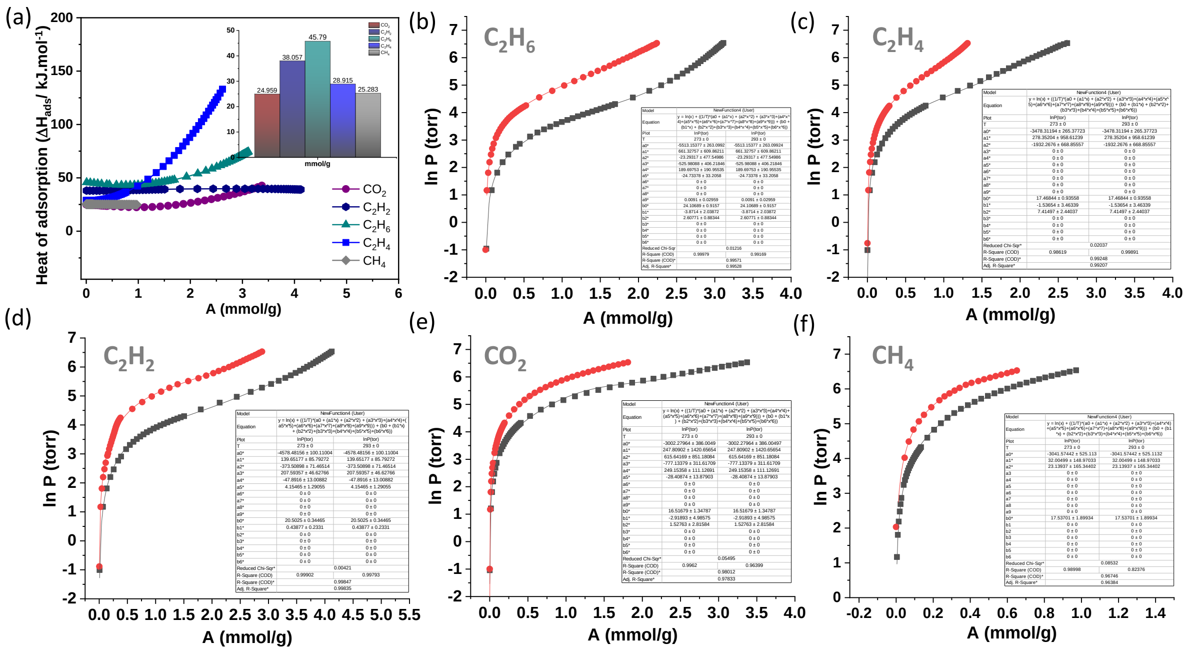

Figure 7: Isosteric heat of adsorption (Q_{st}) at (a) various loading amounts (near-zero loading values are in inset), Adsorption isotherms of (b) C_2H_6, (c) C_2H_4, (d) C_2H_2, (e) CO_2 and (f) CH_4 at 273 and 293 K were fitted in the virial equation.

eqn. 1 and 2 (Figure 7). The order of resultant Q_{st} at near-zero coverage is C_2H_6 (45.79 $kJmol^{-1}$)> C_2H_2 (38.05 $kJmol^{-1}$)> C_2H_4 (28.91 $kJmol^{-1}$)> CH_4 (25.28 $kJmol^{-1}$) ≈ CO_2 (24.95 $kJ.mol^{-1}$). The relatively higher Q_{st} values for C_2H_6 and C_2H_2 attribute efficient adsorbate-adsorbent interaction as the smaller channel surfaces are innately enriched with aromatic rings may hold the potential for enabling preferential sorption through multiple interactions. Notably, the coverage-dependent adsorption enthalpy for CH_4, CO_2 and C_2H_2 does not vary substantially with loading suggesting uniformity in binding sites. On the other hand, for C_2H_6 and C_2H_4 the binding enthalpy gradually increases across the range of loading amounts of both gases, which is congruent with their variation in polarizability, quadrupole moment and sorption isotherm. Henceforth, for C_2H_6 and C_2H_4 molecules, their binding interactions with the inert surface rely on variation inefficient interaction sites, which may vary sensitively as adsorbate-adsorbate interaction overtakes by adsorbate-adsorbent interaction at relatively high- pressure region as a consequence of possible encapsulation in larger pore.[34] The comparative selectivity understanding of C_2H_6 vs. C_2H_4, C_2H_2 vs. CO_2 and C_2H_2 vs. C_2H_4 with representative porous materials has been reported in Figure 8. As documented in Table 1, ethane-ethylene separation is extremely challenging because of comparable physical properties. C_2H_4 (1.5×10^{-26} esu

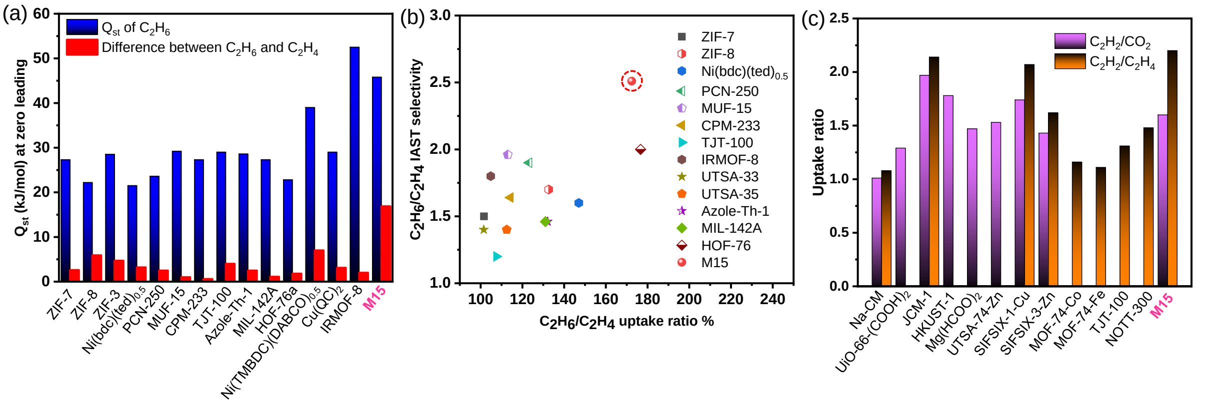

Figure 8: (a) Comparison of the isosteric heat (Q_{st}) of C_2H_6 and C_2H_4 with (b) the comparison of selectivity and volumetric C_2H_6/C_2H_4 uptake ratio % among representative porous materials. (c) The similar comparative diagram of the volumetric uptake ratio of C_2H_2/CO_2 and C_2H_2/C_2H_4 among representative hydrocarbon sorbent materials.

cm^2) shows higher quadrupole moment over C_2H_6 (0.65×10^{-26} esu cm^2), while fabricating C_2H_4-selective MOFs are quite straightforward, for example, by incorporating unsaturated metal site or hydrogen-bonding acceptor to stimulate the selectivity.[35] Achieving reverse phenomena, by enabling preferential sorption of C_2H_6 over C_2H_4 is a bit difficult as well as it can simplify the separation process by selectively release pure C_2H_4 from downstream outlet.[4a, 36] On similar note, separating C_2H_2/CO_2 is equally complex as a consequence of cognate molecular dimension (C_2H_2: 3.32 ×3.34 × 5.7 Å^3 and CO_2: 3.18 × 3.33 × 5.36 Å^3) and boiling points (C_2H_2, 189.3 K; CO_2, 194.7 K). The resultant generous uptake ratio of C_2H_6 over C_2H_4 and C_2H_2 over CO_2 is not only motivating us to inspect practical utility but also improve the understanding of hydrocarbon binding equations with such porous materials.

3.1.4.2: Theoretical studies

To gain better insight into the adsorption affinities of diverse C_2H_6, C_2H_4, C_2H_2, CO_2 and CH_4 gas molecules inside M15, the preferential host-guest interaction and binding energy (ΔE) was estimated by density functional theory optimization. From computational exercise, the lowest energy atomic configuration by considering each individual molecule in small and large pores of the framework has been visualized and the obtained binding energy values clearly indicate small pore as a primary house for guest accommodation at zero-coverage loading (M15 versus single guest interaction; Figure 9). On determining the optimized geometry, the binding energy (BE) was calculated using the following expression: $BE_{adsorbate} = E_{framework+adsorbate} - (E_{framework} + E_{adsorbate})$. Where, $E_{framework+adsorbate}$, $E_{framework}$, and $E_{adsorbate}$ denote the energy of the framework-adsorbate, the framework, the adsorbate, respectively. The adsorption site (smaller pore) was found to have higher binding energy values for both C_2H_6 (12.10 kcal/mol) and C_2H_4 (11.3 kcal/mol). As visualized in Figure 10, every single C_2H_6 or C_2H_4 molecule can produce six or four C-H···π interactions between C-H and benzene ring of the linker.

However, smaller kinetic diameter of C_2H_4 validating (3.03-3.06 Å) strong C-H···π binding associations over C_2H_6 (3.52-3.58 Å), but the greater number of hydrogen atoms in the latter induces more van der Waals (vdW) interactions. This provided a stronger preference for ethane over ethylene. The obtained static binding energy (ΔE) for C_2H_2, CO_2, CH_4 are 10.29, 9.25 and 9.02 kcal/mol. The interaction patterns are fully consistent with adsorption enthalpy calculated from the experimental single-component adsorption isotherm. In CO_2@M15, the guest locates exactly centre to the pore by forming π···π interaction (3.98 Å) with C···O distance in the range of 3.44<C···O<4.0 Å (Figure 10e).

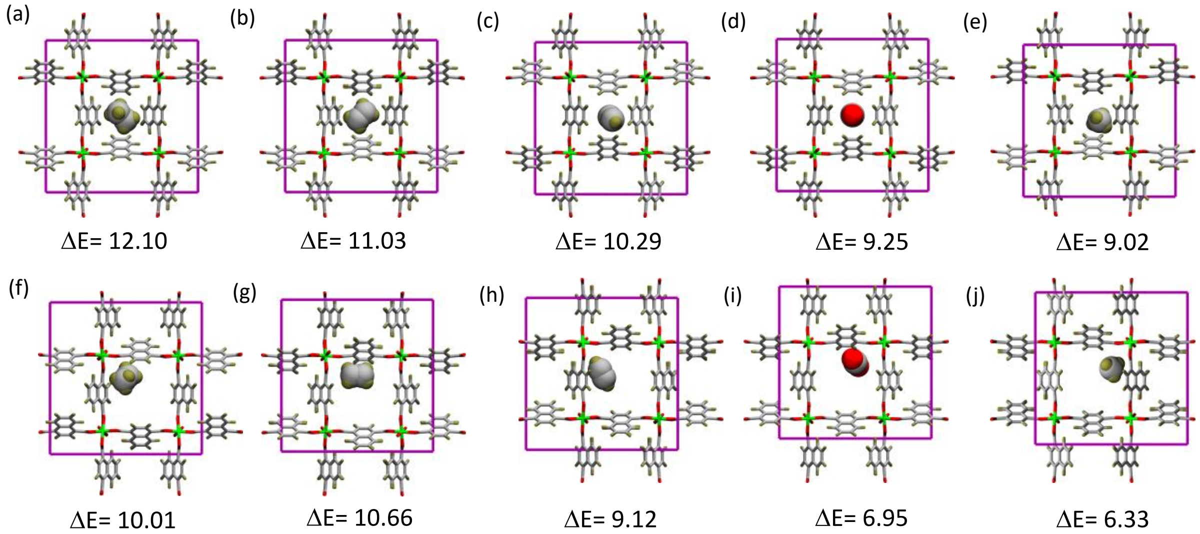

Figure 9: Calculated binding energy (ΔE in $kcal.mol^{-1}$) of the preferential C_2H_6 (a, f), C_2H_4 (b, g), C_2H_2 (c, h), CO_2 (d, i) and CH_4 (e, j) adsorption sites through vdW interactions by considering small (a-e) and large pore (f-j) as a primary binding site, respectively.

Indeed, the theoretical model of C_2H_2 adsorbed pore resulting beneficial π···π interaction along strong C-H···π hydrogen bonding interaction with a distance ranging from 3.47 to 3.76 Å. The vdW interactions between linearly inclined C_2H_2 with aromatic rings and additional C-H···π synergy is more noteworthy than the interaction between CO_2 with

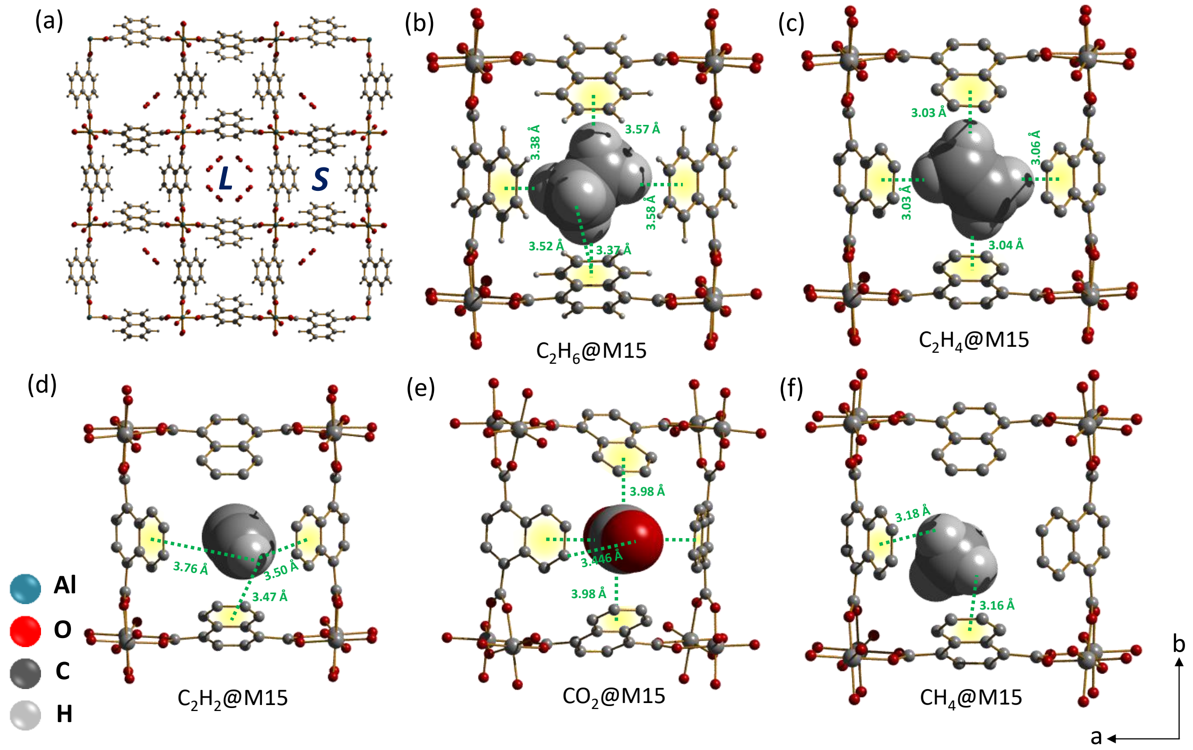

Figure 10: (a) Crystal structure of parent MOF with smaller and larger pore designation as '*S*' and '*L*'. Preferential adsorption sites for (b) C_2H_6, (c) C_2H_4, (d) C_2H_2, (e) CO_2 and (f) CH_4 in M15 as obtained by computational simulations (Al cyan, O red, C dark grey, H light grey).

host's binding sites. This host-guest interaction also reflects in previously mentioned binding energy, isosteric heat of adsorption and single-component adsorption isotherms that determines beneficial adsorption of C_2H_6 over C_2H_4 and C_2H_2 over CO_2. CH_4 showed the least preference (9.02 kcal/mol) to the pore associated through a few C-H⋯π interaction (Figure 10f).

Next, to estimate adsorption selectivity and mixed component adsorption isotherm, ideal adsorption solution theory (IAST)[37] was employed by using the equimolar composition of gasses having a similar size and physical properties. As shown in Figure 11a, and b, the adsorption selectivity for C_2H_6/C_2H_4 and C_2H_2/CO_2 at a pressure 100 kPa was calculated to be 2.59 and 2.54, respectively. The calculated bi-component equimolar hydrocarbon adsorption isotherms are shown in Figure 11 by fitting single-component experimental adsorption isotherm in Langmuir-Freundlich model. For, C_2H_6/C_2H_4 the mixed adsorption at 100 kPa for C_2H_6 and C_2H_4 are 41 and 29 mL/g, respectively, whereas for C_2H_2/CO_2 combination the individual saturation uptakes are 44 and 17 mL/g. The selectivity value raises with increasing gas pressure for ethane/ethylene that confirms

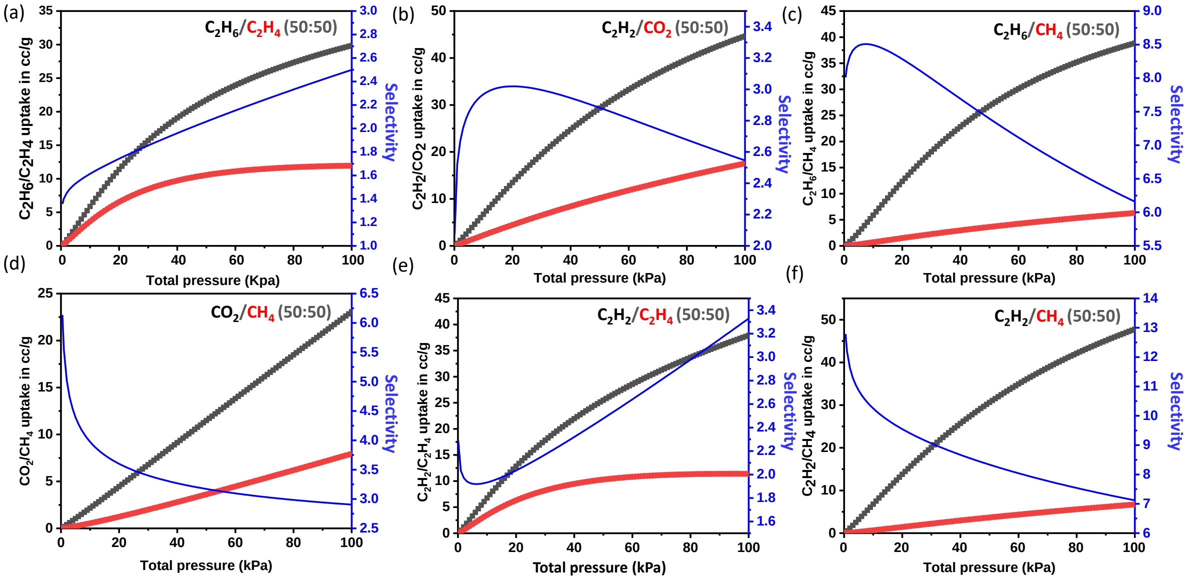

Figure 11: Predicted mixture adsorption isotherm and IAST selectivity of M15 for (a) C_2H_6/C_2H_4, (b) C_2H_2/CO_2, (c) C_2H_6/CH_4, (d) CO_2/CH_4, (e) C_2H_2/C_2H_4, and (f) C_2H_2/CH_4 at 293 K from 0.5 to 100 kPa total gas pressure.

the real separation ability of M15 under practical conditions. For C_2H_2/CO_2, the selectivity factor reaches maxima (3.018) at 20 kPa and further dropped with increasing loading pressure. For other equimolar mixtures selectivity of C_2H_6 over CH_4, CO_2 over CH_4, C_2H_2 over C_2H_4, and C_2H_2 over CH_4 are 6.15, 2.9, 3.32 and 7.12, respectively at 100 kPa under ambient temperature (293 K). As per the documented literature report, M15 should be the first MOF showing such high selectivity in the range of 2 to 8 for all light hydrocarbon mixtures at ambient conditions (100 kPa and 293 K).

3.1.4.3: Column and membrane breakthrough separation

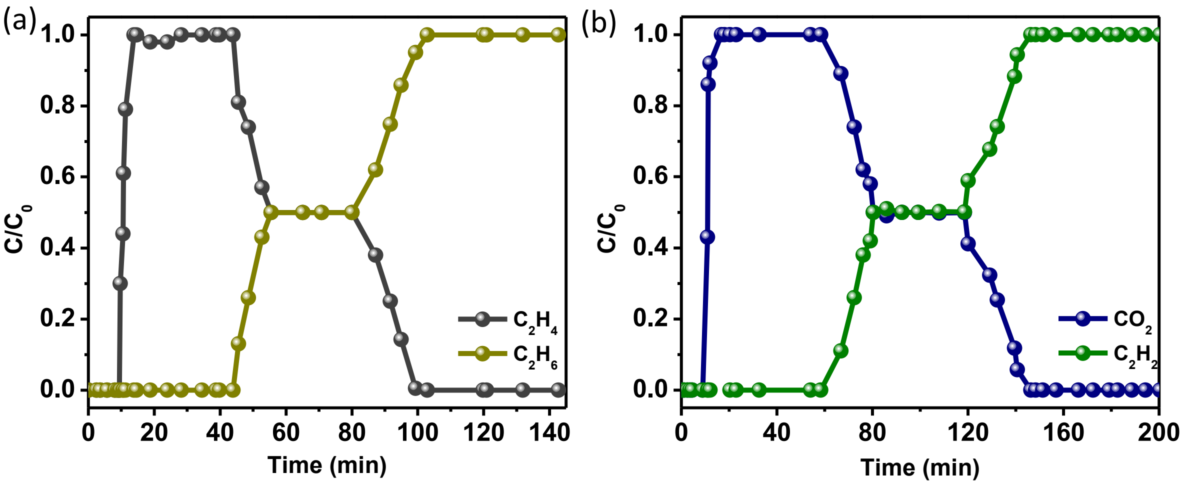

Figure 12: Experimental column breakthrough curves for equimolar (a) C_2H_6/C_2H_4 and (b) C_2H_2/CO_2 gas mixtures.

As motivated by selectivity estimation, a series of practical breakthrough experiments were carried out on M15 for bi-component and quaternary-component gas mixtures. As shown in Figure 12, C_2H_6/C_2H_4 mixture was streamed through a packed column of activated adsorbent with the rate of 2.8 mL/min at 298 K. C_2H_4 can be detected first from the outlet gas runoff during initial purges, resulting in desirable polymer grade purity for more than 40 minutes, while no C_2H_6 was found. Approximately around 45 minutes, as adsorbent became saturated in the dynamic equimolar flow, C_2H_6 reaches its breakthrough point as detected from in outlet downstream. Perceptibly, the C_2H_6 selective M15 allowed early release of pure C_2H_4, significantly simplifies the purification of these petrochemicals. However, as soon as the outlet stream reaches to equimolar proportion, by closing the feed flow and only allowing carrier gas the absorbed amount of C_2H_6 could be removed by making the column regenerated for subsequent separations. Thereafter, similar process was followed for the equimolar mixture of C_2H_2/CO_2, CO_2/CH_4 and C_2H_6/CH_4. For C_2H_2/CO_2, CO_2 appears in the outlet flow as early as 10 minutes, while it took almost 6.5 times longer for C_2H_2 to reach its breakthrough point, reveals excellent separation performance for C_2H_2 from CO_2. In contrast, for CO_2/CH_4 and C_2H_6/CH_4, C_2H_6 broke through the bed at 40 min, while for CO_2 it is 16 min as both of them showed efficient adsorption over weakly interacted CH_4 (Figure 13). Note that, all breakthrough time intervals were tested multiple times through the process of subsequent regeneration and found comparable by showing the excellent renewability of the material.

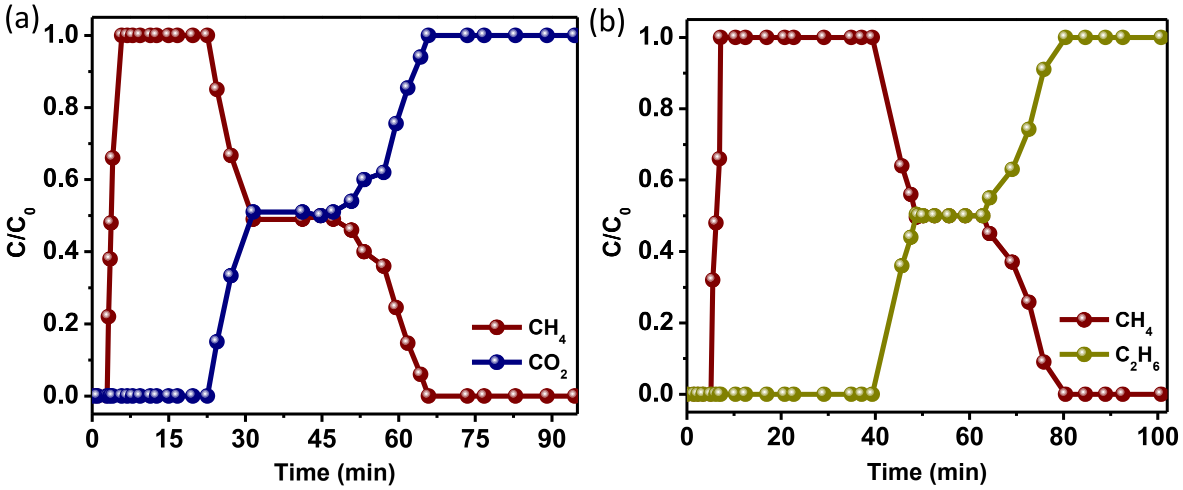

Figure 13: Experimental column breakthrough curves for equimolar (a) CO_2/CH_4 and (b) C_2H_6/CH_4 gas mixtures.

Further studies for M15@PSF mixed matrix membrane also exhibit preferential permeation of H_2 over CO_2 and CH_4 over CO_2. Membrane fabrication and data collection are elaborately described in the experimental section. Arguably, H_2 purification from CO_2 is highly demanded its direct fuel cell applications and MMM's selectivity for such case is calculated to be 2.86 with a permeability of each gas are 1253 and 438, respectively (Table 3). For CO_2/CH_4, the obtained selectivity value is 0.9.

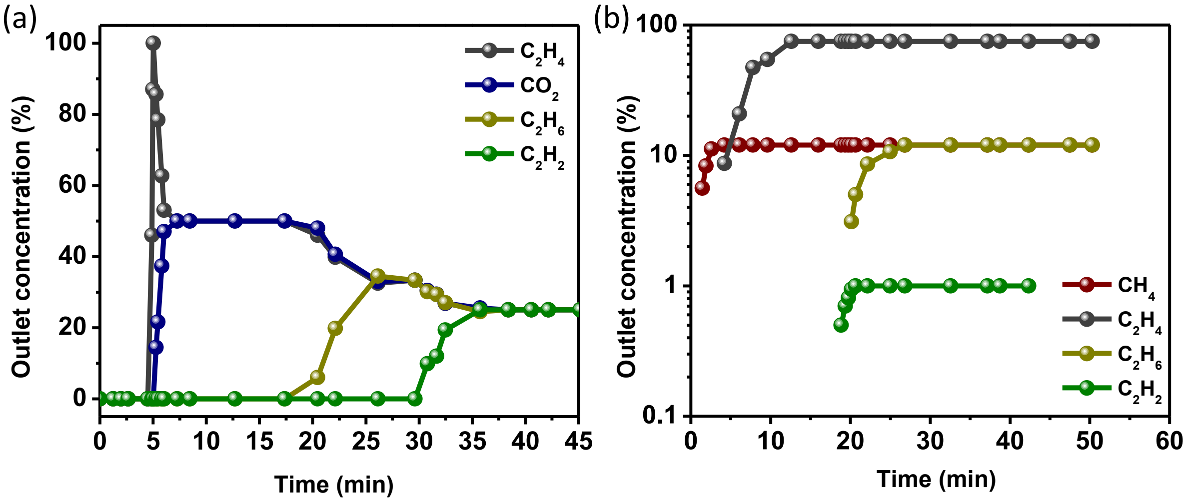

Figure 14: Quaternary mixture separation of (a) $C_2H_6/C_2H_4/C_2H_2/CO_2$ (0.25:0.25:0.25:0.25) and (b) $C_2H_4/C_2H_6/CH_4/C_2H_2$ (0.75:0.12:0.12:0.01).

Table 3: Selectivity of M15@PSF mixed matrix membrane

	H_2/CO_2	CH_4/CO_2	Radius (cm)	Thickness (mm)
M15@PSF	2.86	0.9	4	0.11

The separation capacity of M15 was further tested using an equimolar $C_2H_6/C_2H_4/CO_2/C_2H_2$ mixture. A sharp and pure separation of all four gases was observed with an early release of C_2H_4, with no evidence of CO_2, C_2H_2 or C_2H_6 in the first 5 minutes. Such flawless separation of C_2H_4 with a polymer grade purity (99.9%+) only through a single breakthrough separation is rarely found in the literature (Figure 14a). Moreover, the traditional C_2H_4 production also co-exists with other by-products mainly C_2H_6 with a trace amount of CH_4 and C_2H_2. So, this material was further investigated for the separation from a quaternary mixture of $C_2H_4/C_2H_6/CH_4/C_2H_2$ (0.75/0.12/0.12/0.01). As shown in Figure 14b, highly efficient separation of even trace amount (1%) of C_2H_2 was achieved by passing the mixture over a packed column of activated M15. All the practical separation measurements are well consistent with experimental and simulated adsorption isotherm, selectivity and binding interactions.

3.1.5: Conclusion

In conclusion, the chapter reveals a robust Al-based metal-organic framework in a continuation to the previous chapter by adjusting reaction duration under microwave to achieve exclusive microporosity with high surface area. The forgoing results showed that the material (Al(μ-OH)(1,4-ndc)]·H_2O; MOF1) possesses not only extraordinary chemical and thermal stability but also exhibits exceptional sorption and selectivity performance of a tailor-made MOF (M15). It unveiled remarkable preferential interactions with C_2H_6 over C_2H_4 and C_2H_2 over CO_2, considered as the most delicate combinations for separation in petroleum industries. The key to selectivity, as found, is a combination of multiple van der Waals interactions and the suitable channel-like pores to match with different light hydrocarbons. At one end, single and mixed-gas adsorption, selectivity estimation, step-wise dynamic breakthrough separation from bi- and quaternary-component mixtures unfolds extraordinary separation potency of such material. On the other hand, the study also reveals the specific affinity of each hydrocarbon as a consequence of thermodynamic and kinetic preferences to the adsorbent as supported by binding energy estimation and molecular level visualization thorough DFT calculation.

3.1.6: References

[1] a) D. S. Sholl and R. P. Lively, *Nature* **2016**, *532*, 435-437; b) K.-J. Chen, D. G. Madden, S. Mukherjee, T. Pham, K. A. Forrest, A. Kumar, B. Space, J. Kong, Q.-Y. Zhang and M. J. Zaworotko, *Science* **2019**, *366*, 241.
[2] N. A. Khan, Z. Hasan and S. H. Jhung, *Chem. Euro. J.* **2014**, *20*, 376-380.
[3] U. Wagner and H. M. Weitz, *Ind. Eng. Chem.* **1970**, *62*, 43-48.
[4] a) R. Krishna, *ACS Omega* **2020**, *5*, 16987-17004; b) L. Yang, S. Qian, X. Wang, X. Cui, B. Chen and H. Xing, *Chem. Soc. Rev.* **2020**, *49*, 5359-5406.
[5] a) I. Amghizar, L. A. Vandewalle, K. M. Van Geem and G. B. Marin, *Engineering* **2017**, *3*, 171-178; b) in *Front Matter*, (Ed. J. G. Speight), Gulf Professional Publishing, Boston, **2011**, p. iii.
[6] a) A. van Miltenburg, J. Gascon, W. Zhu, F. Kapteijn and J. A. Moulijn, *Adsorption* **2008**, *14*, 309-321; b) L. Li, R.-B. Lin, R. Krishna, H. Li, S. Xiang, H. Wu, J. Li, W. Zhou and B. Chen, *Science* **2018**, *362*, 443.
[7] R. W. Baker, *Ind. Eng. Chem. Res.* **2002**, *41*, 1393-1411.
[8] a) Y. Peng, V. Krungleviciute, I. Eryazici, J. T. Hupp, O. K. Farha and T. Yildirim, *J. Am. Chem. Soc.* **2013**, *135*, 11887-11894; b) B. Li, H.-M. Wen, W. Zhou, Jeff Q. Xu and B. Chen, *Chem* **2016**, *1*, 557-580.

[9] T. Rodenas, M. van Dalen, E. García-Pérez, P. Serra-Crespo, B. Zornoza, F. Kapteijn and J. Gascon, *Adv. Func. Mater.* **2014**, *24*, 249-256.

[10] Y. Liu, G. Liu, C. Zhang, W. Qiu, S. Yi, V. Chernikova, Z. Chen, Y. Belmabkhout, O. Shekhah, M. Eddaoudi and W. Koros, *Adv. Sci.* **2018**, *5*, 1800982.

[11] P.-Q. Liao, W.-X. Zhang, J.-P. Zhang and X.-M. Chen, *Nat. Commun.* **2015**, *6*, 8697.

[12] a) A. Granada, S. B. Karra and S. M. Senkan, *Ind. Eng. Chem. Res.* **1987**, *26*, 1901-1905; b) D. A. Plattner, Y. Li and K. N. Houk, p.

[13] R. Matsuda, R. Kitaura, S. Kitagawa, Y. Kubota, R. V. Belosludov, T. C. Kobayashi, H. Sakamoto, T. Chiba, M. Takata, Y. Kawazoe and Y. Mita, *Nature* **2005**, *436*, 238-241.

[14] a) V. Guillerm, Ł. J. Weseliński, Y. Belmabkhout, A. J. Cairns, V. D'Elia, Ł. Wojtas, K. Adil and M. Eddaoudi, *Nat. Chem.* **2014**, *6*, 673-680; b) B. R. Barnett, S. T. Parker, M. V. Paley, M. I. Gonzalez, N. Biggins, J. Oktawiec and J. R. Long, *J. Am. Chem. Soc.* **2019**, *141*, 18325-18333; c) R.-B. Lin, L. Li, H.-L. Zhou, H. Wu, C. He, S. Li, R. Krishna, J. Li, W. Zhou and B. Chen, *Nat. Mater.* **2018**, *17*, 1128-1133.

[15] a) N. Sikdar, S. Bonakala, R. Haldar, S. Balasubramanian and T. K. Maji, *Chem. Euro. J.* **2016**, *22*, 6059-6070; b) A. Chakraborty, S. Roy, M. Eswaramoorthy and T. K. Maji, *J. Mater. Chem. A* **2017**, *5*, 8423-8430; c) A. Chakraborty, A. Achari, M. Eswaramoorthy and T. K. Maji, *Chem. Commun.* **2016**, *52*, 11378-11381.

[16] a) Y. K. Ponraj and B. Borah, *J. Mol. Graph.* **2020**, *97*, 107574; b) Y. He, Z. Zhang, S. Xiang, F. R. Fronczek, R. Krishna and B. Chen, *Chem. Euro. J.* **2012**, *18*, 613-619.

[17] a) W. Fan, S. Yuan, W. Wang, L. Feng, X. Liu, X. Zhang, X. Wang, Z. Kang, F. Dai, D. Yuan, D. Sun and H.-C. Zhou, *J. Am. Chem. Soc.* **2020**, *142*, 8728-8737; b) A. Luna-Triguero, J. M. Vicent-Luna, R. M. Madero-Castro, P. Gómez-Álvarez and S. Calero, *ACS Appl. Mater. Interfaces* **2019**, *11*, 31499-31507; c) J. Lee, C. Y. Chuah, J. Kim, Y. Kim, N. Ko, Y. Seo, K. Kim, T. H. Bae and E. Lee, *Angew. Chem. Int. Ed.* **2018**, *57*, 7869-7873.

[18] a) A. Hazra, S. Jana, S. Bonakala, S. Balasubramanian and T. K. Maji, *Chem. Commun.* **2017**, *53*, 4907-4910; b) A. Hazra, A. Jain, M. S. Deenadayalan, S. A. Adalikwu and T. K. Maji, *Inorg. Chem.* **2020**, *59*, 9055-9064; c) S. Bhattacharyya, A. Chakraborty, A. Hazra and T. K. Maji, *ACS Omega* **2018**, *3*, 2018-2026.

[19] a) H. Yang, Y. Wang, R. Krishna, X. Jia, Y. Wang, A. N. Hong, C. Dang, H. E. Castillo, X. Bu and P. Feng, *J. Am. Chem. Soc.* **2020**, *142*, 2222-2227; b) R.-B. Lin, H. Wu, L. Li, X.-L. Tang, Z. Li, J. Gao, H. Cui, W. Zhou and B. Chen, *J. Am. Chem. Soc.* **2018**, *140*, 12940-12946.

[20] H.-G. Hao, Y.-F. Zhao, D.-M. Chen, J.-M. Yu, K. Tan, S. Ma, Y. Chabal, Z.-M. Zhang, J.-M. Dou, Z.-H. Xiao, G. Day, H.-C. Zhou and T.-B. Lu, *Angew. Chem. Int. Ed.* **2018**, *57*, 16067-16071.

[21] S. Laha, D. Rambabu, S. Bhattacharyya and T. K. Maji, *Chem. Euro. J.* **2020**, *26*, 14671-14678.

[22] A. Comotti, S. Bracco, P. Sozzani, S. Horike, R. Matsuda, J. Chen, M. Takata, Y. Kubota and S. Kitagawa, *J. Am. Chem. Soc.* **2008**, *130*, 13664-13672.

[23] J.-R. Li, R. J. Kuppler and H.-C. Zhou, *Chem. Soc. Rev.* **2009**, *38*, 1477-1504.

[24] D. S. J. S. D. D. S. Biovia, **2020**.

[25] A. K. Rappe, C. J. Casewit, K. S. Colwell, W. A. Goddard and W. M. Skiff, *J. Am. Chem. Soc.* **1992**, *114*, 10024-10035.

[26] A. K. Rappe and W. A. Goddard, *J. Phys. Chem.* **1991**, *95*, 3358-3363.

[27] J. P. Perdew, K. Burke and M. Ernzerhof, *Phys. Rev. Lett.* **1996**, *77*, 3865-3868.

[28] a) S. Grimme, S. Ehrlich and L. Goerigk, *J. Comput. Chem.* **2011**, *32*, 1456-1465; b) S. Grimme, J. Antony, S. Ehrlich and H. Krieg, **2010**, *132*, 154104.

[29] J. VandeVondele, M. Krack, F. Mohamed, M. Parrinello, T. Chassaing and J. Hutter, *Comput Phys. Commun.* **2005**, *167*, 103-128.

[30] J. Hutter, M. Iannuzzi, F. Schiffmann and J. VandeVondele, *WIREs Comput. Mol. Sci.* **2014**, *4*, 15-25.
[31] M. Krack, *Theor. Chem. Acc.* **2005**, *114*, 145-152.
[32] a) C. Gücüyener, J. van den Bergh, J. Gascon and F. Kapteijn, *J. Am. Chem. Soc.* **2010**, *132*, 17704-17706; b) X. Zhang, J.-X. Wang, L. Li, J. Pei, R. Krishna, H. Wu, W. Zhou, G. Qian, B. Chen and B. Li, *Angew. Chem. Int. Ed.* **2021**, *60*, 10304-10310.
[33] a) M. Sarker, H. J. An, D. K. Yoo and S. H. Jhung, *Chem. Eng. J.* **2018**, *338*, 107-116; b) E. V. Alexandrov, A. V. Goltsev, R. A. Eremin and V. A. Blatov, *J. Phys. Chem. C* **2019**, *123*, 24651-24658; c) X. Liu, X. Wang and F. Kapteijn, *Chem. Rev.* **2020**, *120*, 8303-8377; d) Y. Hu, Y. Chen, Y. Liu, W. Li, M. Zhu, P. Hu, H. Jin and Y. Li, *Micropor. Mesopor. Mater.* **2018**, *270*, 67-74.
[34] a) S. Sircar and D. V. Cao, *Chem. Eng.Technol.* **2002**, *25*, 945-948; b) W. Fan and A. Chakraborty, *Micropor. Mesopor. Mater.* **2018**, *260*, 201-207.
[35] a) B. Li, Y. Zhang, R. Krishna, K. Yao, Y. Han, Z. Wu, D. Ma, Z. Shi, T. Pham, B. Space, J. Liu, P. K. Thallapally, J. Liu, M. Chrzanowski and S. Ma, *J. Am. Chem. Soc.* **2014**, *136*, 8654-8660; b) S. Yang, A. J. Ramirez-Cuesta, R. Newby, V. Garcia-Sakai, P. Manuel, S. K. Callear, S. I. Campbell, C. C. Tang and M. Schröder, *Nat. Chem.* **2015**, *7*, 121-129.
[36] J. Pires, M. L. Pinto and V. K. Saini, *ACS Appl. Mater. Interfaces* **2014**, *6*, 12093-12099.
[37] A. L. Myers and J. M. Prausnitz, *AIChE Journal* **1965**, *11*, 121-127.

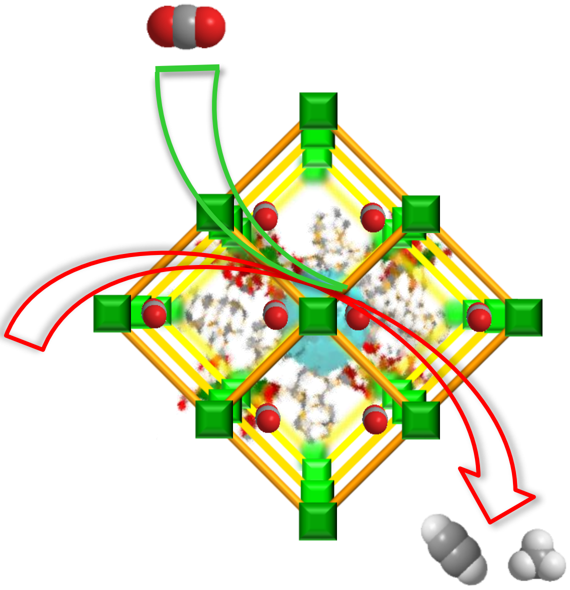

3.2: An Adsorbate Biased Dynamic 3D Porous Framework for Inverse CO_2 Sieving over C_2H_2.

Manuscript under preparation

Abstract

Separating carbon dioxide (CO_2) from acetylene (C_2H_2) is one of the most critically important and complex industrial separations due to similarities in physicochemical properties and molecular dimensions. The chapter reports a novel Ni-based three-dimensional $\{[Ni_4(\mu_3\text{-}OH)_2(\mu\text{-}H_2O)_2(1,4\text{-ndc})_3](3H_2O)\}_n$ (1,4-H_2ndc = 1,4-naphthalenedicarboxylic acid) framework contains one-dimensional pore channel (3.05×3.57 Å^2), well-matched with the molecular size of CO_2 and C_2H_2, decorated with unsaturated metal center and pendant oxygen atoms. The framework is dynamic in nature and shows multistep gate opening type CO_2 adsorption at 195, 273 and 298 K, but not for C_2H_2. The structural transformation from non-porous to porous upon adsorption of polar molecules (CO_2, H_2O), clearly evident from adsorption isotherm, demonstrates remarkable selectivity for CO_2 over other non-polar hydrocarbons (C_2H_2, CH_4). Temperature and pressure dependent adsorption study, dynamic breakthrough experiments elucidate rarely attempted CO_2 selectivity over C_2H_2 which is further corroborated by crystallographic analysis, selectivity approximation and adsorbate-adsorbent bond enthalpy estimation.

3.2.1: Introduction

Acetylene (C_2H_2), an important monomeric organic feedstock in chemical as well as polymer industries and is extensively used as a fuel in welding apparatus.[1] Commonly, C_2H_2 is prepared through partial combustion of methane or cracking of hydrocarbons. Thus, ultra-pure C_2H_2 production is required for the manufacture of industrial chemicals, but, impurities such as carbon dioxide (CO_2) and methane (CH_4) often coexist in reactor products.[2] Undoubtedly, the purification of C_2H_2 from irresistible CO_2 impurities is considered as one of the utmost challenging tasks due to the similarities in molecular dimensions (C_2H_2: 3.32 ×3.34 × 5.7 $Å^3$ and CO_2: 3.18 × 3.33 × 5.36 $Å^3$).[3] The present purification technology needs to operate under cryogenic temperatures and high pressures and this makes the separation more critical because of analogous boiling points (C_2H_2, 189.3 K; CO_2, 194.7 K).[2c, 4] Hence, aforesaid classical techniques for gas separation, such as solvent extraction or cryogenic distillation, are costly, inefficient, and extremely energy-consuming. In this context, adsorptive separation through porous materials attracts great interest as it is more environment-friendly, energy-inexpensive, afford much lower cost and thus it is considered as a next generation separation technology.

As benefited from delicate control over pore accessibility and pore environment, metal-organic frameworks (MOFs) show great aptitude in the realm of gas storage and separation.[5] Fatefully, most of the reported MOFs determine very similar binding affinity for both C_2H_2 and CO_2, whereas a few of them reveals partial separation but exclusive separation is hardly reported.[6] In those few successful reports, pores are typically designed to preferentially adsorb C_2H_2 over CO_2 by utilizing the hydrophobic pore environment, acid-base interaction with the binding site and introducing linkers with highly polarizable π-electrons.[7] However, in each case, the blowdown step requires an additional deep vacuum for ultrapure C_2H_2 recovery due to its strong binding to the pore.[8] Thus, by enabling inverse selectivity i.e., favored CO_2 adsorption over C_2H_2 could neglect the co-current blowdown step and make the overall separation process more facile and energy-inexpensive. On that note, Yang *et al.* first reported preferential adsorption of CO_2 over C_2H_2 by incorporating both pendant carboxyl and pyridyl groups in the channels.[9] Recently, Kitagawa and co-workers demonstrated selective adsorption of CO_2 using a flexible PCP driven by CH-π and π-π interactions but also delimits considerable C_2H_2 uptake of 86.2 $mL.g^{-1}$ STP at 195 K.[10] Therefore, it is desirable to design a flexible material that will offer some specific sites to bind CO_2 molecules exclusively and reject C_2H_2.

In particular, compared to the rigid frameworks, there has been a growing interest in the flexible or dynamic framework (3rd generation and four-dimensional MOFs) that changes their structures in response to external stimuli, manifests high molecular selectivity and recognition hallmark.[11] Principally, this structural dynamic arises due to (i) host-lattice transformation (shape responsive fitting of a guest in a shrinkable host),[12] (ii) crystal-to-crystal sliding,[13] (iii) adjustable pore void (contraction and expansion of framework)[14] and (iii) porous to non-porous switch over with abrupt gate opening or step-wise adsorption phenomenon.[15] Such structural adaptability with gated adsorption-desorption towards a specific adsorbate requires a better understanding of sorption mechanism and associated structural modifications, as the difference in physical parameters of the hydrocarbons is extremely delicate.

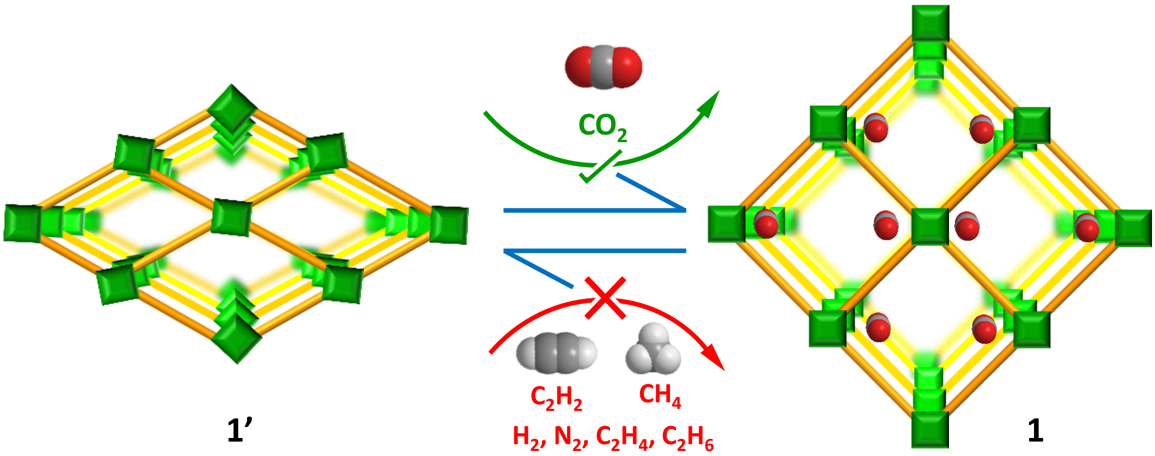

Figure 1: Schematic representation dynamic MOF for its preferential CO_2 adsorption.

It has been sought to design and synthesize such a novel three-dimensional metal-organic framework embodied by $\{[Ni_4(\mu_3\text{-}OH)_2(\mu\text{-}H_2O)_2(1,4\text{-}ndc)_3](3H_2O)\}_n$ (1,4-H_2ndc = 1,4-naphthalenedicarboxylic acid) (**1**). The accessible 1D pore channel with high polarity and aperture size of near 3.3 Å, enabling preferential CO_2 binding in the confined pore. Temperature-dependent and in situ powder X-ray diffraction studies during the vapor adsorption isotherm collectively provide better insight into structural dynamicity

(Figure 1). The desolvated **1** (**1'**) shows a gate opening type multistep adsorption profile for CO_2 at 195, 273, and 298 K, leading to appreciable selective adsorption of CO_2 over C_2H_2 and CH_4 at ambient temperature (298 K) by verifying the mechanism of adsorptive biasness. Dynamic breakthrough measurements are carried out to disclose experimental separation execution.

3.2.2: Experimental section

3.2.2.1: Materials

All the reagents employed are commercially available and used as provided without further purification. $Ni(NO_3)_2.6H_2O$ has been obtained from Spectrochem. 1,4-naphthaledicarboxylic acid (1,4-H_2ndc) was obtained from Alfa Aeser.

3.2.2.2: Synthesis

A mixture containing $Ni(NO_3)_2{\cdot}6H_2O$ (0.5 mmol, 0.145 g), 1,4-H_2ndc (0.5 mmol, 0.108 g) and KOH (1.0 mmol, 0.056 g) is suspended in teflon bomb containing 10 mL water and stirred for 30 mins. The solution was then heated at 180 °C for a period of 10 days. The dark green colored block-shaped crystals of **1** were then collected and further washed in water for several times. Yield: 80 % (with respect to metal). Anal. Calc. for $C_{36}O_{19}Ni_4H_{18}$ C: 43.711; H: 1.83; Found C: 44.98; H: 2.01. FT-IR (KBr pellet, 4000–400 cm^{-1}): 3444 (br), 1610 (s), 1590 (w), 1412 (s).

3.2.2.3: Physical measurements

Elemental analyses are carried out using a Thermo Fischer Flash 2000 Elemental Analyzer. FT-IR spectra are recorded on a Bruker IFS 66v/S spectrophotometer using KBr pellets in the region 4000-400 cm^{-1}. Thermogravimetric analyses (TGA) are carried out (Metler Toledo) in nitrogen atmosphere in the temperature range of 30–700 °C (heating rate 5 °C min^{-1}). The powder XRD pattern of the compounds has been recorded by using Cu-Kα radiation (Bruker D8 Discover; 40 kV, 30 mA). The patterns have been agreed with those calculated from single crystal structure determination.

3.2.2.4: X-ray crystallography

X-ray single-crystal structure data of **1** has been collected on a Bruker Smart-CCD diffractometer equipped with a normal focus, 2.4 kW sealed tube X-ray source with graphite monochromated Mo-Kα radiation (λ= 0.71073 Å) operating at 50 kV and 30 mA. The program SAINT[16] is used for the integration of diffraction profiles and absorption correction was made with SADABS[17] program. All the structures are solved by SIR92[18] and refined by full-matrix least-squares method using SHELXL-97.[19] All the hydrogen atoms are fixed by HFIX and placed in ideal positions. Potential solvent accessible area or void space is calculated using the PLATON multipurpose crystallographic software. All the crystallographic and structure refinement data of **1** are summarized in Table 2. Selected bond lengths and angles for **1** are given in Table 2-3, respectively. All calculations were carried out using SHELXS 97,[20] PLATON,[21] and WinGX system, Ver 1.80.05.

3.2.2.5: Adsorption details

The adsorption isotherms of CO_2 (at 195, 273 and 298 K), N_2 (at 77 and 298 K), CH_4, C_2H_2, C_2H_4 and C_2H_6 (at 298 and 273 K) of **1'** have been measured using AUTOSORB IQ2 instrument. The compound **1** has been activated at 195 °C under 1×10^{-1} Pa vacuum for about 16 h prior to measurement of the isotherms. All the gases used for adsorption measurement are of scientific/research grade with 99.999% purity. Dead volume is measured with helium gas. The adsorbates are passed into the sample cells, and then the change of the pressure is monitored and the degree of adsorption is determined by the decrease in pressure at the equilibrium state. All operations are software defined and automatic.

The adsorption isotherms of different solvents (MeOH at 293 K and H_2O at 298 K) for **1′** are measured in the vapor state by using a BELSORP-aqua3 volumetric adsorption instrument from BEL, Japan. All the samples of about ~100 mg are prepared by adopting a similar procedure mentioned earlier prior to measurement of the isotherms. The solvent molecules used to generate the vapor are degassed fully by repeated evacuation. Dead volume is measured with Helium gas. The adsorbate was placed into the sample cell, then the change of the pressure is monitored, and the degree of adsorption is determined by the decrease in pressure at the equilibrium state.

3.2.2.5.1: IAST selectivity

Ideal adsorbed solution theory (IAST) was used to predict selectivity in binary mixture adsorption of H_2/CO_2 (1:1, v/v), N_2/CO_2 (0.85/0.15, v/v), CO_2/CH_4 (1:1, v/v) and CO_2/C_2H_2 (1:1, v/v) from the experimental single-gas adsorption isotherm by fitting it into single-site Langmuir-Freundlich equation (eq. 3). The binary adsorption of A and B, according to IAST these two equations are to be followed;

$$yP_t = xP_a \qquad \text{(eq. 1)}$$

$$(1-y)P_t = (1-x).P_b \qquad \text{(eq. 2)}$$

where x and y denote the molar fraction of A in the adsorbed phase and the molar fraction of A in the bulk phase, respectively. P_t is the total gas pressure; P_a and P_b are the pressure of components A and B at the same spreading pressure as that of the mixture, respectively. The equation used to fit the single component gas mixture is as follows;

$$y = y_o(ln\frac{BP^n}{1+BP^n}) \qquad \text{(eq. 3)}$$

Therefore, the molar fraction of A in the adsorbed phase can be obtained from the following equation:

$$y_{0,a}\ln\left(1+\frac{B_aP_t^{n1}y}{x}\right) - y_{0,b}\ln\left(1+\frac{B_bP_t^{n2}(1-y)}{(1-x)}\right) = 0 \qquad \text{(eq. 4)}$$

Where $Y_{0,\ a}$, B_a and n_1 are the Langmuir-Freundlich fitting parameters of adsorption equilibrium of pure A, $Y_{0,\ b}$, B_b and n_2 are Langmuir-Freundlich parameters of adsorption equilibrium of pure B.

The unknown x in Eq. (4) has been solved by MATLAB (Version 7.14.0.739 (R2012a)) for fixed P_t and y values. Then calculated the predicted adsorption selectivity, which is defined as;

$$S = \frac{x_1/y_1}{x_2/y_2} \qquad \text{(eq. 5)}$$

Where, x_i and y_i are the mole fractions of component i (i = 1, 2; A, B) in the adsorbed and bulk phases, respectively. The IAST calculations were carried out for equimolar gas phase mixtures.

3.2.2.5.2: Heat of adsorption

The virial expression of the following type has been used to fit the combined single component isotherm at 273 and 298 K.

$$\ln(P) = \ln(A) + \frac{1}{T}\sum_{i=0}^{m} a_i A^i + \sum_{i=0}^{n} b_i A^i \qquad \text{(eq. 6)}$$

P is the pressure expressed in torr, A is the amount adsorbed in mmol/g, T is the temperature in K, a_i and b_i are virial coefficients, and m, n represents the number of coefficients required to adequately describe the isotherms (eq. 6). The value of m and n was gradually increased until the contribution of extra added a and b coefficients were negligible towards the final fit. The values of the virial coefficient a_i were taken to calculate the isosteric heat of adsorption using the following expression.

$$Q_{st} = -R\sum_{i=0}^{m} a_i A^i + \sum_{i=0}^{n} b_i A^i \qquad \text{(eq. 7)}$$

Q_{st} is the coverage dependent isosteric heat of adsorption and R is the universal gas constant.

3.2.2.6: Dynamic breakthrough separation experiments

The real-time adsorption-based separation and purification process of **1'** for H_2/CO_2 (1:1, v/v), N_2/CO_2 (0.85/0.15, v/v), CO_2/CH_4 (1:1, v/v) and CO_2/C_2H_2 (1:1, v/v) gas mixture was analyzed by using packed column of 12.4 cm (~1.65 g of powdered **1**) length and 0.3 cm diameter. The sample was first activated at 195 °C for 12 h prior to loading in column and after loading it was further regenerated by the continuous flowing of carrier gas for 1 h. The continuous flow was regulated by mass flow controller by using Helium as a carrier gas for N_2/CO_2, CO_2/CH_4 and CO_2/C_2H_2 and Argon for H_2/CO_2, respectively. For N_2/CO_2 and H_2/CO_2 dynamic breakthrough separation was performed and for other hydrocarbon mixtures, stepwise dynamic breakthrough separations were performed to exclusively separate each isomer with polymer grade purity and consecutive sample regeneration (Table 1).

The total flow rate and corresponding breakthrough times are as follows;

Table 1: Experimental dynamic	Conc. (A: B)	Flow rate (total) in mL.min^{-1}	Carrier gas	Outlet time (for gas A) in sec	Outlet time for (gas B) in sec

breakthrough details. Feed gas mixture (A: B)					
H_2/CO_2	(0.5:0.5)	2.2	Ar	8	232
N_2/CO_2	(0.85:0.15)	2.2	He	4	272
CO_2/CH_4	(0.5:0.5)	2.8	He	85	298
CO_2/C_2H_2	(0.5:0.5)	2.8	He	98	345

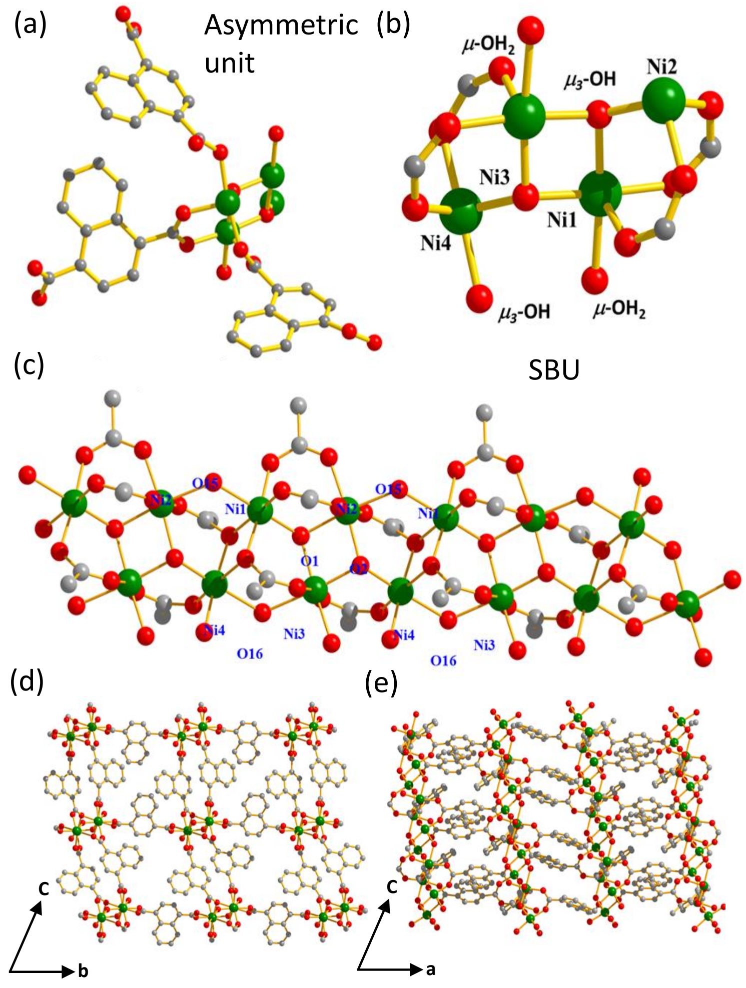

Figure 1: (a) Asymmetric unit of 1 (b) secondary building unit of 1 (c) Ni-O chain showing the bridging water and hydroxyl groups; O1, O2 is the μ_3-OH group and O15, O16 are two μ-OH_2 groups. Crystal structure view of structure 1 along (d) a direction and (e) b direction.

3.2.4: Result and discussion

3.2.4.1: Crystal structure description of $\{[Ni_4(\mu_3\text{-}OH)_2(\mu\text{-}H_2O)_2(1,4\text{-ndc})_3](3H_2O)\}_n$ (**1**)

The reaction of 1,4-H_2ndc with Nickel in water under basic pH yielded dark green colour block shape crystals of **1**. Single crystal X-ray diffraction reveals that **1** crystalizes in triclinic $P\bar{1}$ space group. The asymmetric unit comprises of four Ni^{2+} ions, three 1,4-ndc ligands, two μ_3-OH groups, two μ-OH_2 and three crystal-line water molecules (Figure 1a, b). The square grid type three dimensional is formed by the chains of fused Ni(II) octahedral units and 1,4-ndc as illustrated in figure 1d, e. Four independent Ni(II) atoms are assembled into a two parallel Ni-O-Ni chains. One is comprised of Ni1, Ni2, are connected with μ_3-OH group, μ-OH_2 and μ-O from carboxylate ligands. On other hand, Ni3, Ni4 are connected with carboxylate group by *syn-syn* mode interaction (Figure 1b-c). Thus, in the parallel chains, each Ni1 and Ni3 are associated with three different carboxylate oxygen atoms and individual Ni2 and Ni4 is attached with the one μ_3-OH, μ-OH_2, two μ-O and two carboxylates from four different linkers forming distorted NiO_6 octahedron to make four alternate triangular arrays. The intrachain Ni1-Ni2 separation distances are 3.289 Å (*syn–syn* bridging), 3.821 Å (μ-OH_2 bridging) and for Ni3–Ni4 it is 3.325 Å and 3.786 Å, respectively. The Ni-O distances with 1,4-ndc oxygen atoms, and μ_3-OH are all comparable and in the range of 1.975 (2)-2.221(3) Å. The O-Ni-O cis angles lie in the range of 79.72(11)-102.49(11)° and the transoid angles are in the range of 166.90(11)-176.37(11)° showing the degree of deviation from the ideal octahedron. The bond angle varies for the same in the window of 81.41(10)-176.36(11)°. The dicarboxylate 1,4-ndc diverge from the chain and connect to the Ni(II) atom of the adjacent chains, leading to a 3D framework with two alternative square shaped channels along *a*-axis. Each pore contains guest water molecules (4 in the large, 2 in the small pore) and the removal of guests might cause structural shrinkage as these interactions would disappear. Excluding the guest molecules, 1 has undulating wide and narrow channels (9.8% void space) along the *a*-axis with an aperture size of 3.05×3.57 Å^2, which contests well with the molecular dimension of CO_2 and C_2H_2, underlying size sieving of this particular combination.

Table 2: Crystal data and refinement parameters of **1**.

Parameters	**1**
Empirical formula	$C_{36}O_{19}Ni_4H_{18}$
Formula weight	1001
Crystal system	Triclinic
Space group	$P\bar{1}$
a, Å	7.1062(14)
b, Å	13.604(3)
c, Å	20.640(4)
α, deg	98.860(10)
β, deg	95.760(9)
γ, deg	101.554(8)
V, Å^3	1913.7(7)
Z	2
T, K	293
μ, mm^{-1}	2.019
D_{calcd}, g/cm^3	1.717
$F(000)$	996
Reflections[$I>2\sigma(I)$]	5651
Total reflections	25279
Unique reflections	6730
λ(Mo-Kα)	0.71073
R_{int}	0.032
GOF on F^2	1.16
$R_1[I>2\sigma(I)]^a$	0.0362

R_w[all data]^b	0.1336

^{a} $R = \Sigma||F_o| - |F_c||/\Sigma|F_o|$. ^{b} $R_w = [\Sigma(w(F_o^2 - F_c^2)^2)/\ \Sigma(w(F_o^2)^2)]^{1/2}$

Table 3: Selected bond lengths (Å) of 1.

O1-Ni2	1.975(2)	O1-Ni1	2.017(3)	O1-Ni3	2.027(2)	O2-Ni4	1.991(2)
O2-Ni1	2.017(2)	O2-Ni3	2.047(3)	O3-Ni2	2.038(3)	O4-Ni1	2.039(3)
O5-Ni3	2.069(3)	O6-Ni4	2.033(3)	O7-Ni2	2.068(3)	O7-Ni4	2.107(3)
O8-Ni1	2.052(3)	O9-Ni4	2.012(3)	O10-Ni3	2.033(3)	O11-Ni2	1.993(3)
O12-Ni1	2.062(3)	O13-Ni3	2.042(3)	O14-Ni4	2.100(3)	O14-Ni2	2.145(3)
O15-Ni2	2.195(3)	O15-Ni1	2.221(3)	O16-Ni4	2.167(3)	O16-Ni3	2.196(3)
Ni1-O8	2.052(3)	Ni2-O14	2.145(3)	Ni2-O15	2.195(3)	Ni3-O13	2.042(3)
Ni4-O14	2.100(3)	Ni4-O7	2.107(3)	Ni4-O16	2.167(3)		

Table 4: Selected bond angles (°) of 1.

O1-Ni1-O2	82.39(10)	O1-Ni1-O4	94.07(10)	O2-Ni1-O4	176.36(11)
O1-Ni1-O8	91.45(10)	O2-Ni1-O8	92.84(10)	O4-Ni1-O8	86.41(11)
O1-Ni1-O12	101.62(11)	O2-Ni1-O12	89.92(11)	O4-Ni1-O12	91.61(11)
O8-Ni1-O12	166.90(12)	O1-Ni1-O15	175.70(10)	O2-Ni1-O15	93.55(10)
O4-Ni1-O15	89.97(11)	O8-Ni1-O15	87.32(10)	O12-Ni1-O15	79.72(10)
O1-Ni2-O11	102.50(11)	O1-Ni2-O3	91.03(11)	O11-Ni2-O3	92.63(11)
O1-Ni2-O7	86.14(10)	O11-Ni2-O7	167.24(10)	O3-Ni2-O7	96.62(11)
O1-Ni2-O14	93.82(10)	O11-Ni2-O14	86.89(11)	O3-Ni2-O14	175.13(10)
O7-Ni2-O14	83.15(10)	O1-Ni2-O15	172.91(10)	O11-Ni2-O15	84.30(11)
O3-Ni2-O15	86.62(11)	O7-Ni2-O15	87.48(10)	O14-Ni2-O15	88.50(10)
O1-Ni3-O10	86.75(10)	O1-Ni3-O13	92.24(10)	O10-Ni3-O13	169.97(11)
O1-Ni3-O2	81.41(10)	O10-Ni3-O2	99.46(11)	O13-Ni3-O2	90.25(11)
O1-Ni3-O5	174.28(11)	O10-Ni3-O5	95.82(11)	O13-Ni3-O5	86.12(11)
O2-Ni3-O5	93.11(10)	O1-Ni3-O16	93.31(10)	O10-Ni3-16	82.97(11)
O13-Ni3-O16	87.13(11)	O2-Ni3-O16	174.01(10)	O5-Ni3-O16	92.08(10)
O2-Ni4-O9	101.52(11)	O2-Ni4-O6	89.89(10)	O9-Ni4-O6	93.92(12)

O2-Ni4-O14	85.88(10)	O9-Ni4-O14	168.37(11)	O6-Ni4-O14	95.06(10)
O2-Ni4-O7	93.90(10)	O9-Ni4-O7	87.21(11)	O6-Ni4-O7	175.75(10)
O14-Ni4-O7	83.30(10)	O2-Ni4-O16	173.57(10)	O9-Ni4-O16	84.31(11)
O6-Ni4-O16	86.98(11)	O14-Ni4-O16	88.80(10)	O7-Ni4-O16	89.05(10)

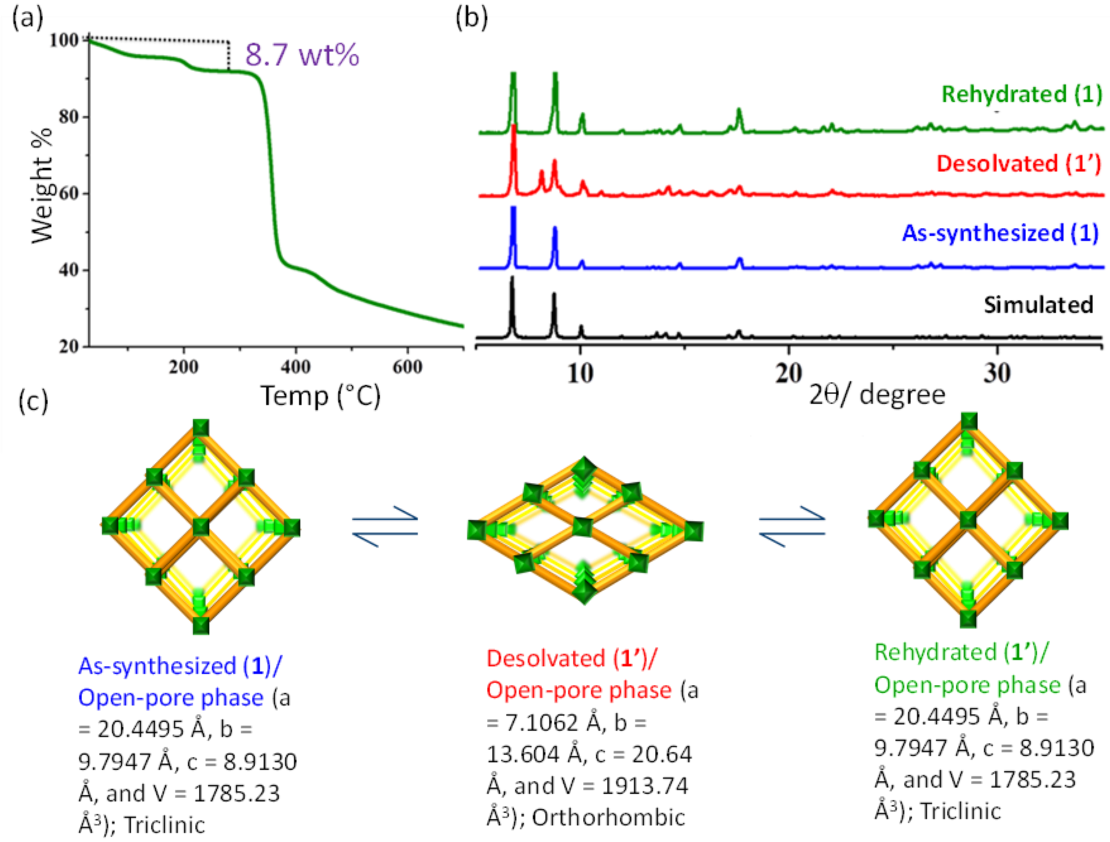

Figure 2: (a) TGA curves for **1** in the temperature range 30−650 °C (b) PXRD pattern of 1 recorded at different states: (I) simulated (II) as-synthesized (III) desolvated 1'(IV) rehydrated phase of 1 with cell parameter values that revel structural shrinkage upon activation.

3.2.4.2: Powder X-ray and TGA analysis

The PXRD pattern of as-synthesized **1** shows high crystallinity, and well correspondence with simulated pattern indicates is purity in bulk phase and further supported by thermogravimetric analysis. TGA of **1** revealed the loss of three water molecules at 127 °C with a weight loss of 5.34%, consistent with the calculated value (5.7%) and this phase is tenable up to 225 °C. At 225-280 °C, further weight loss (expt. 3.4%, cald. 3.8%) was accomplished due to the release of two bridging water molecules and the dehydrated framework is stable till 330 °C (Figure 2a). After complete dehydration, **1** shrink from triclinic to orthorhombic **1'** (call parameters of a = 20.4495 Å, b = 9.7947 Å, c = 8.9130

Å, and V = 1785.23 Å^3) with approximately 6.7% reduction in cell volume, suggests overall contraction to denser phase indexed by TOPAS programme.[22] Further rehydration of 1’ (exposed to water vapor for 48 h), revives the as-synthesized phase as exposed from the exact resemblances in diffraction pattern (Figure 2b, c).

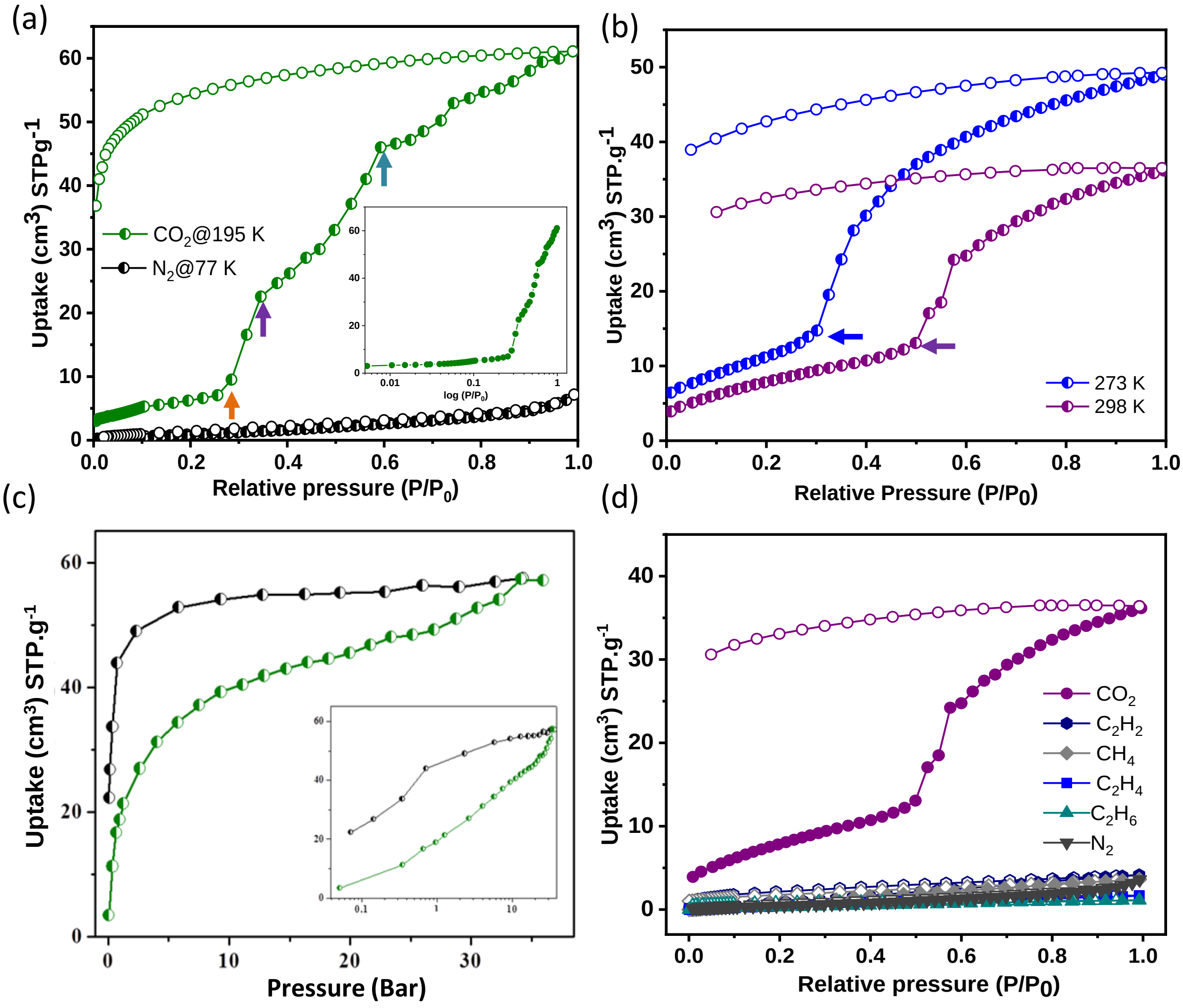

Figure 3: (a) N_2 and CO_2 adsorption isotherm of **1’** at 77 and 195 K (Inset; log curve for clear understanding of close-to-open phase transition). (b) CO_2 adsorption isotherm of **1’** at 273 and 298 K, respectively, reports shifting in gate opening pressure upon changing measurement temperature. (c) High-pressure CO_2 adsorption isotherm at 273 and 298 K (inset). (d) All hydrocarbon (CH_4, C_2H_2, C_2H_4, C_2H_6) adsorption isotherm including CO_2 and N_2 at ambient temperature (298 K).

3.2.4.3: Adsorption studies

The gas adsorption properties were studied with respect to N_2 at 77 K and CO_2 at 195 K (Figure 3a). No significant N_2 adsorption is observed indicating non-porous nature of the framework which could be correlated to the structural change upon dehydration. On the contrary, **1'** unveiled a gate opening type multistep CO_2 adsorption (195 K) profile with a total uptake of 61 cm^3g^{-1} (11.9 wt % and 2.47 molecules/formula unit), the gated CO2 uptake could be credited to the smaller kinetic diameter (3.3 Å for CO_2; 3.64 Å for N_2) and the quadrupolar nature of CO_2, which facilitate interaction with the pore surface decorated with unsaturated Ni(II) sites and oxygen atoms from the bridging -OH and carboxyl groups. The adsorption isotherm showed negligible CO_2 uptake up to $P/P_0 \sim 0.25$ the abrupt increase in uptake is noticed and finally saturates at $P/P_0 = 0.99$. The non-coincidence with the adsorption isotherm with a broad hysteresis as appeared in desorption profile suggesting strong confinement of CO_2 molecules inside the pore. CO_2 adsorption isotherms were also measured at 273 and 298 K. The total uptake capacities are 49 (9.8 wt% and 2.02 molecules/formula unit, at 273 K) and 37 (7.8 wt% and 1.62 molecules/formula unit, at 298 K) cm^3g^{-1}. The threshold gate opening pressure shifted to 0.25 to 0.5 at 273 and 298 K, respectively (Figure 3b). The gate opening pressure increases with rise in measurement temperature. The isosteric heat of adsorption (Q_{st}) for CO_2 is calculated with the adsorption isotherms at 273 and 298 K by utilizing the Clausius–Clapeyron equation, and it reveals high value of 42.35 kJ/mol, which reflects strong adsorbate-adsorbent interaction (Figure 4a). The value sharply increases at the high loading pressure of CO_2 suggests structural expansion from non-porous to porous phase. Such non-porous to porous transition is further evidenced by high-pressure CO_2 adsorption isotherm (Figure 3c). As measurement performed beyond 1.0 bar, adsorption profile exhibits type-I isotherm with a total uptake capacity of 57 cm^3g^{-1} and 56 cm^3g^{-1} at 273 and 298 K, respectively.

Such dynamic pore chemistry and pore geometry associated with suitable pore aperture (3.05×3.57 Å^2) insisted us to evaluate the sorption performance of **1'** for other small light hydrocarbons (CH_4, C_2H_2, C_2H_4, C_2H_6) under ambient condition (Figure 3d). C_2H_2 has a rod-shaped anisotropic linear geometry similar to CO_2 with acidic hydrogen at both ends, expected **1'** to be a good adsorbent for C_2H_2 too. Surprisingly, **1'** adsorbs negligible amounts of C_2H_2 and CH_4 (4.1 and 3.6 cm^3g^{-1}, respectively), which is significantly less compared to CO_2 uptake under similar conditions. This is not well enough to transform non-porous to porous phase, and possibly this can be attributed to the low dipole and

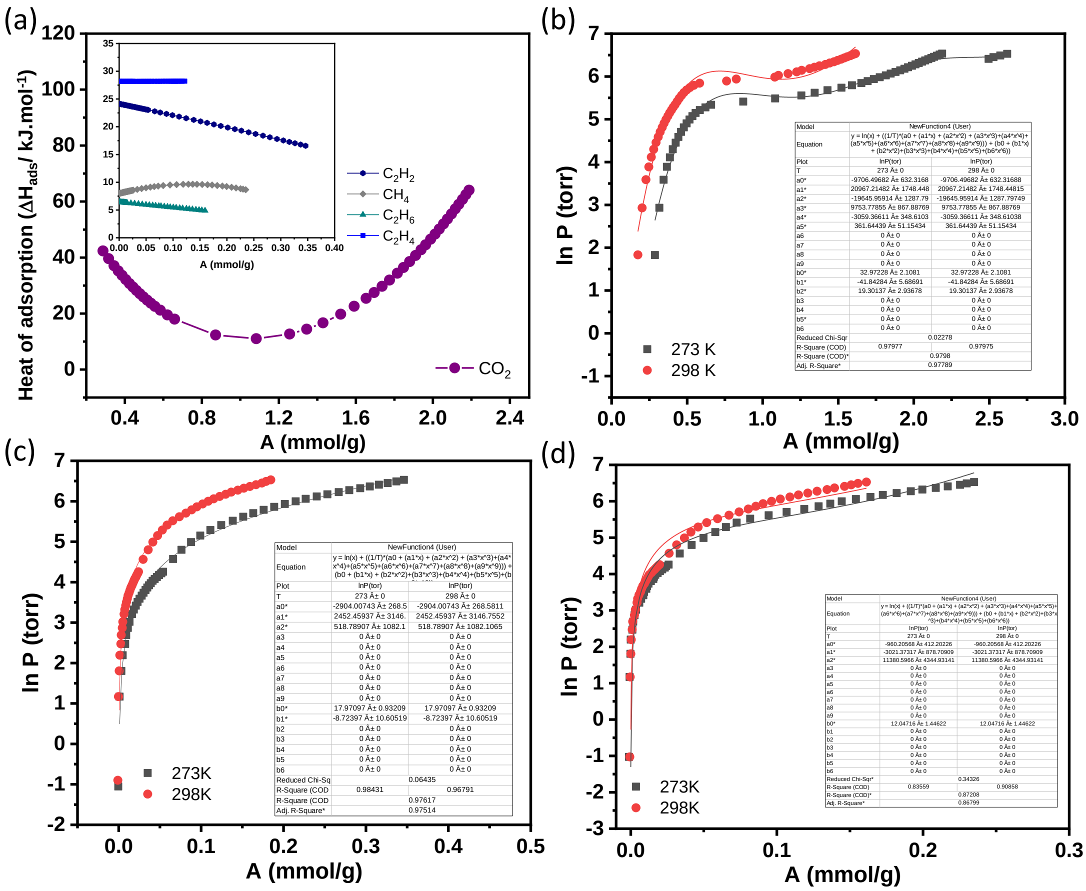

Model	NewFunction4 (User)	
Equation	y = ln(x) + ((1/T)*(a0 + (a1*x) + (a2*x^2) + (a3*x^3)+(a4*x^4)+(a5*x^5)+(a6*x^6)+(a7*x^7)+(a8*x^8)+(a9*x^9))) + (b0 + (b1*x) + (b2*x^2)+(b3*x^3)+(b4*x^4)+(b5*x^5)+(b6*x^6))	
Plot	lnP(tor)	lnP(tor)
T	273 Â± 0	298 Â± 0
a0*	-9706.49682 Â± 632.3168	-9706.49682 Â± 632.31688
a1*	20967.21482 Â± 1748.448	20967.21482 Â± 1748.44815
a2*	-19645.95914 Â± 1287.79	-19645.95914 Â± 1287.79749
a3*	9753.77855 Â± 867.88769	9753.77855 Â± 867.88769
a4*	-3059.36611 Â± 348.6103	-3059.36611 Â± 348.61038
a5*	361.64439 Â± 51.15434	361.64439 Â± 51.15434
a6	0 Â± 0	0 Â± 0
a7	0 Â± 0	0 Â± 0
a8	0 Â± 0	0 Â± 0
a9	0 Â± 0	0 Â± 0
b0*	32.97228 Â± 2.1081	32.97228 Â± 2.1081
b1*	-41.84284 Â± 5.68691	-41.84284 Â± 5.68691
b2*	19.30137 Â± 2.93678	19.30137 Â± 2.93678
b3	0 Â± 0	0 Â± 0
b4	0 Â± 0	0 Â± 0
b5*	0 Â± 0	0 Â± 0
b6	0 Â± 0	0 Â± 0
Reduced Chi-Sqr	0.02278	
R-Square (COD)	0.97977	0.97975
R-Square (COD)*	0.9798	
Adj. R-Square*	0.97789	

Model	NewFunction4 (User)	
Equation	y = ln(x) + ((1/T)*(a0 + (a1*x) + (a2*x^2) + (a3*x^3)+(a4*x^4)+(a5*x^5)+(a6*x^6)+(a7*x^7)+(a8*x^8)+(a9*x^9))) + (b0 + (b1*x) + (b2*x^2)+(b3*x^3)+(b4*x^4)+(b5*x^5)+(b	
Plot	lnP(tor)	lnP(tor)
T	273 Â± 0	298 Â± 0
a0*	-2904.00743 Â± 268.5	-2904.00743 Â± 268.5811
a1*	2452.45937 Â± 3146.	2452.45937 Â± 3146.7552
a2*	518.78907 Â± 1082.1	518.78907 Â± 1082.1065
a3	0 Â± 0	0 Â± 0
a4	0 Â± 0	0 Â± 0
a5	0 Â± 0	0 Â± 0
a6	0 Â± 0	0 Â± 0
a7	0 Â± 0	0 Â± 0
a8	0 Â± 0	0 Â± 0
a9	0 Â± 0	0 Â± 0
b0*	17.97097 Â± 0.93209	17.97097 Â± 0.93209
b1*	-8.72397 Â± 10.60519	-8.72397 Â± 10.60519
b2	0 Â± 0	0 Â± 0
b3	0 Â± 0	0 Â± 0
b4	0 Â± 0	0 Â± 0
b5	0 Â± 0	0 Â± 0
b6	0 Â± 0	0 Â± 0
Reduced Chi-Sq	0.06435	
R-Square (COD	0.98431	0.96791
R-Square (COD	0.97617	
Adj. R-Square*	0.97514	

Model	NewFunction4 (User)	
Equation	y = ln(x) + ((1/T)*(a0 + (a1*x) + (a2*x^2) + (a3*x^3)+(a4*x^4)+(a5*x^5)+(a6*x^6)+(a7*x^7)+(a8*x^8)+(a9*x^9))) + (b0 + (b1*x) + (b2*x^2)+(b3*x^3)+(b4*x^4)+(b5*x^5)+(b6*x^6))	
Plot	lnP(tor)	lnP(tor)
T	273 Â± 0	298 Â± 0
a0*	-960.20568 Â± 412.20226	-960.20568 Â± 412.20226
a1*	-3021.37317 Â± 878.70909	-3021.37317 Â± 878.70909
a2*	11380.5966 Â± 4344.93141	11380.5966 Â± 4344.93141
a3	0 Â± 0	0 Â± 0
a4	0 Â± 0	0 Â± 0
a5	0 Â± 0	0 Â± 0
a6	0 Â± 0	0 Â± 0
a7	0 Â± 0	0 Â± 0
a8	0 Â± 0	0 Â± 0
a9	0 Â± 0	0 Â± 0
b0*	12.04716 Â± 1.44622	12.04716 Â± 1.44622
b1	0 Â± 0	0 Â± 0
b2	0 Â± 0	0 Â± 0
b3	0 Â± 0	0 Â± 0
b4	0 Â± 0	0 Â± 0
b5	0 Â± 0	0 Â± 0
b6	0 Â± 0	0 Â± 0
Reduced Chi-Sqr*	0.34326	
R-Square (COD)	0.83559	0.90858
R-Square (COD)*	0.87208	
Adj. R-Square*	0.86799	

Figure 4: (a) Gas adsorption enthalpies at various gas (CH_4, C_2H_2, C_2H_4, C_2H_6) loading concentrations. Virial fitting of the CO_2 (b), C_2H_2 (c), and CH_4 (d)for **1'**.

quadrupole moment of these gases and also unfavourable pore geometry of **1'**. However, for C_2H_4 (4.16 Å) and C_2H_6 (4.44 Å) adsorption was extremely ruled out because of the size mismatch between pore aperture and their kinetic diameters. The isosteric heat of adsorption was calculated based on the adsorption isotherm at 273 and 298 K. The heat of adsorption at zero coverage for C_2H_2 (24.1 kJ/mol), C_2H_6 (6.46 kJ/mol), C_2H_4 (28.15 kJ/mol) and CH_4 (7.95 kJ/mol) does not show any appreciable change with loading, corresponding exclusive mechanism of CO_2 discriminatory gate effect to the pore over all other hydrocarbons (Figure 4). Electrostatic interaction between pore and adsorbate gas molecules are known to play critical roles for preferential molecular sieving.[23] To better understand the nature of pore surface, solvent vapour (water and methanol at 298 K) adsorption has been carried out with activated **1** (**1'**). Strikingly, the water vapour (kinetic diameter 2.64 Å) adsorption

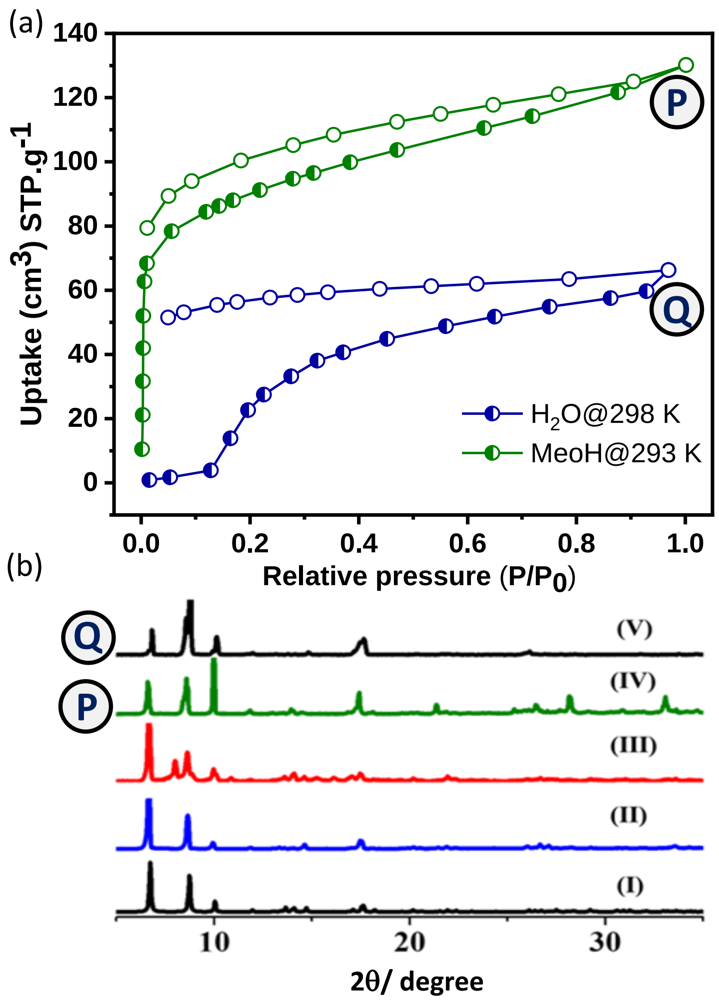

Figure 5: (a) Vapor adsorption isotherm of H_2O and MeOH at 298 and 293 K, respectively. (b) The powder XRD patterns are recorded at adsorption point P, Q and further indexed and compared with other reference patterns. (b) **1** recorded at different states: (I) simulated (II) **1** (III) **1’** (IV) **1’** at P and (V) **1’** at Q, represents the complete pore filling after adsorbing water and methanol molecules.

isotherm of **1’** showed characteristic type-I profile with saturation uptake of 128 cm^3g^{-1} (5.1 molecules/formula unit; Figure 5a). The steep uptake at a relatively low-pressure region suggests strong interaction of water molecules with the pore carved with unsaturated Ni(II) centers and oxygen atoms of the OH and OCO groups from the ndc-ligand. As expected, pore shows less affinity towards methanol molecules revealed a distinct gate opening type profile due to its larger size (3.62 Å) and less polar compare to H_2O. This could be further reinforced βE_0 values as obtained from D-R equation[24] (Dubinin-Radushkevitch equation) that reveals the adsorbate-adsorbent interactions,

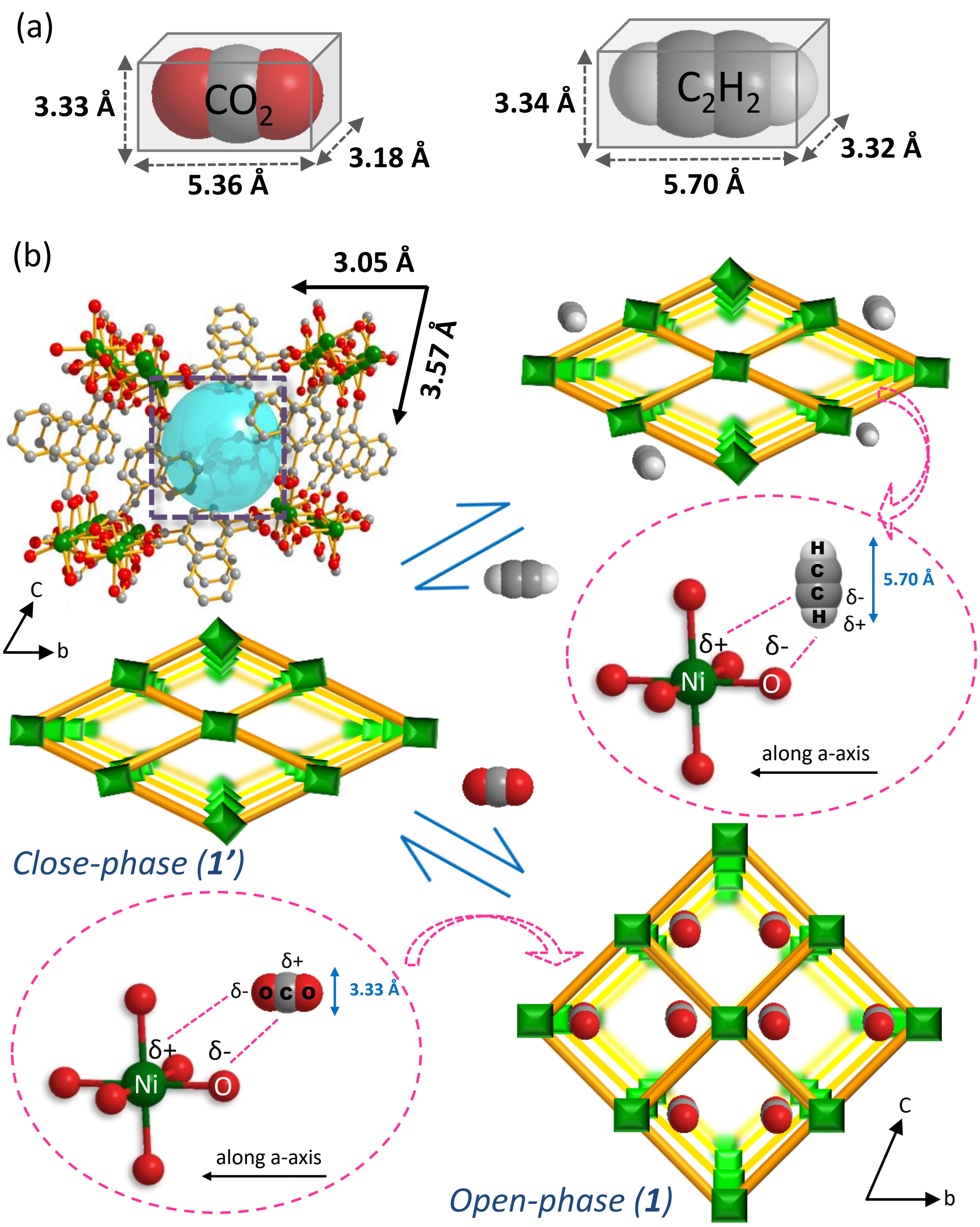

Figure 6: (a) Molecular dimensions of CO_2 and C_2H_2. (b) Schematic CO_2 biased adsorption mechanism with a visualization of close-to-open phase transition induced through electrostatic interaction between **1** and CO_2 in the pore under ambient condition.

which are found to be 7.8 and 2.5 $kJmol^{-1}$ for H_2O and CH_3OH, respectively. To better understand the porosity switchover upon guest loading, PXRD measurements of the samples were collected at points P and Q, during H_2O and CH_3OH vapor adsorption, respectively. The pattern indexed at these points matches well with the diffraction patterns of as-synthesized (**1**) structure, suggesting the expansion of the framework from activated phase (**1′**) to the original state (**1**, open-pore phase) to accommodate guest molecules (Figure 5b). Adsorption isotherm, structural analysis from crystallography study undoubtedly corroborating hydrophilic pore surface biased for polar molecules such as water and carbon dioxide. Comparing CO_2 with N_2, H_2, and CH_4, except CO_2, all have zero quadruple and dipole moments. Whereas C_2H_2, C_2H_4 and C_2H_6 have relatively less polarizability but the values are non-zero integers.[25] C_2H_6 and C_2H_4 possess higher kinetic diameters but a large deviation in adsorption between CO_2 and C_2H_2 is extremely surprising as they have comparable molecular quadrupole moment but in the opposite direction (C_2H_2, 20.5×10^{-40} C m^2; CO_2, -13.4×10^{-40} C m^2).[26] As illustrated in Figure 6, it has been speculated, the electrostatic potential generated by the unsaturated Ni(II) center interacts with the oxygen atom, and the negative electrostatic potential generated in the pendant oxygen atom of the ligand induces C atom of the CO_2 molecule to primarily bind in a head-on orientation inside the pore, resulting in the non-porous to porous transformation (Figure 6). For C_2H_2, due to inverse polarizability, it has to bind in a lateral fashion that forbids its entrance due to larger size (5.7 Å) along z direction. Thus, for CO_2, it shows discriminatory gate opening sorption isotherm in the open pore phase and then further stabilized by strong host-guest interactions.

3.2.4.4: Adsorptive separation based on dynamic breakthrough measurement

Next, to anticipate the potential of **1'** in the separation of industrially important H_2/CO_2, N_2/CO_2, CO_2/CH_4 and CO_2/C_2H_2 gas mixtures, the calculation was performed by adopting the ideal adsorbed solution theory (IAST) after fitting isotherms to the dual-site Langmuir−Freundlich equation at ambient temperature (298 K). As shown in figure 7a, the adsorption selectivity for challenging gas mixtures as CO_2/CH_4 and CO_2/C_2H_2 at 110 kPa and 298 K were calculated to be 1.32 and 1.51, respectively. The value is comparable with other accounted values and the uptake ratio is reasonably higher (around 9) comparable to few other literature reports at saturated gas pressure.[7a, 9-10, 27] The real-time breakthrough separation by using similar binary compositions by passing the mixture through a packed column of **1'** with 2.2-2.8 ml/min flow rate. Figure 7a, b shows that **1'** can achieve efficient separation of H_2/CO_2 (0.5:0.5, v/v) and N_2/CO_2 (0.85:0.15, v/v) mixtures. For CO_2/CH_4 and CO_2/C_2H_2, stepwise dynamic breakthrough separation

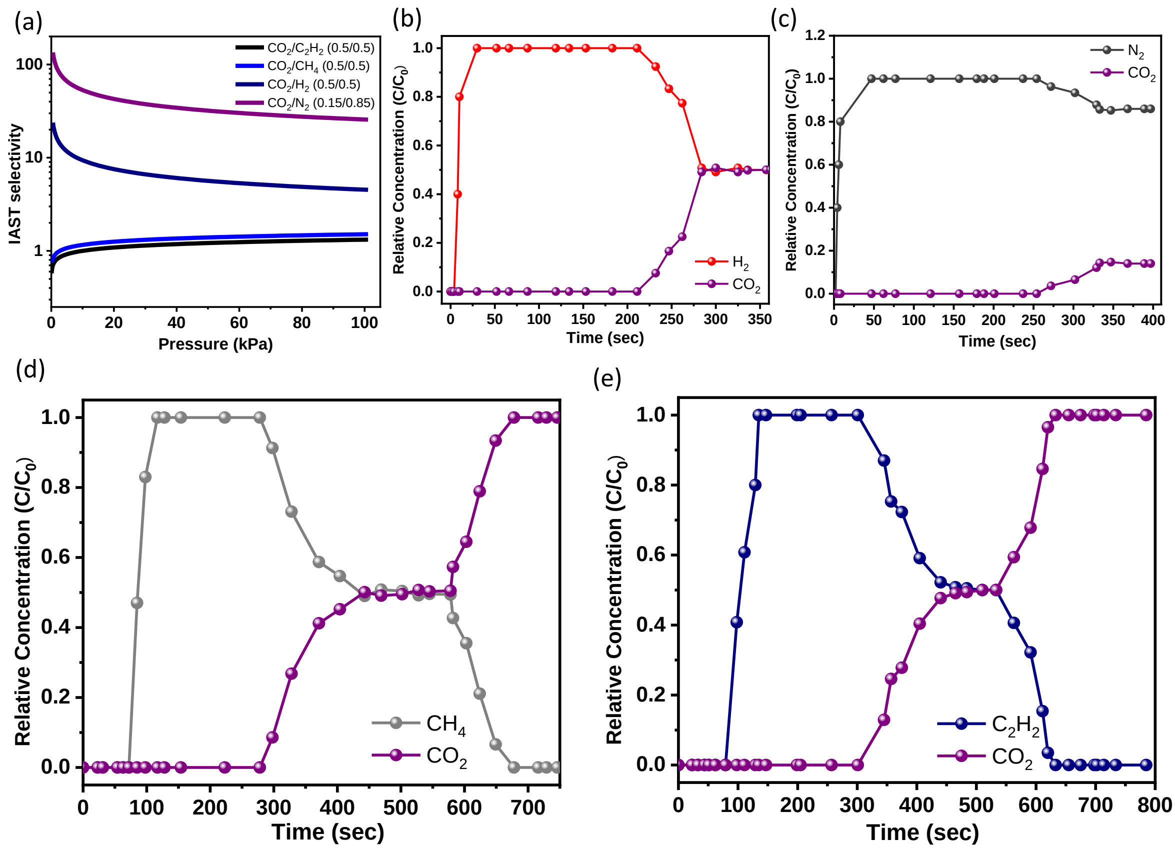

Figure 7: (a) IAST selectivity approximation and (b-e) experimental dynamic breakthrough separation under ambient condition.

was performed where CH_4 and C_2H_2 were first eluted and quickly approached polymer-grade without detectable CO_2 (Figure 7c, d). CO_2 was retained in the packed column for three times longer until the material reached its saturated uptake. Upon saturation, CO_2 broke through and corresponding outlet gas mixtures quickly reached equimolar proportions. Thereafter, by stopping feed mixtures and flowing a purge of carrier gas (He here) through the packed column the retained amount of CO_2 could be removed with high purity by making the column regenerated for subsequent separations. Most of the reported frameworks are selective towards C_2H_2 and as a result polymer-grade C_2H_2 can be only eluted in the downstream desorption phase of fixed bed adsorptive operation. The ability of **1'** towards selective adsorption of CO_2 is a paramount advantage of this dynamic framework as pure C_2H_2 can be produced during the adsorption phase, ending the separation easier and more cost-effective.

3.2.5: Conclusion

In conclusion, a novel three-dimensional Ni-based framework has been synthesized, characterized and studied for separating industrially important gas mixtures with similar size and physical properties. Compared to conventional approaches of size-selective molecular sieving and supramolecular interaction, such a dynamic 'soft' framework with the narrow one-dimensional pore space could exhibit better separation efficacy. In this case, the framework exhibits multistep gate opening behavior exclusively for one component due to differences in size, polarizability and alignment in the pore governed by electrostatic interactions. Such discriminatory sorption of CO_2 makes this framework highly selective from its spin-off components in particular C_2H_2 and CH_4. The practical feasibility of this framework is further tested under continuous flowing conditions by using CO_2/C_2H_2 and CO_2/CH_4 gas mixtures at ambient temperature. Therefore, these results will provide a new strategy for designing and utilizing a dynamic flexible porous framework for biased CO_2 capture and an inverse separation from the most important industrial analog C_2H_2.

3.2.6: References

[1] P. J. Stang and F. Diederich, *Modern acetylene chemistry*, John Wiley & Sons, **2008**, p.
[2] a) J.-W. Zhang, M.-C. Hu, S.-N. Li, Y.-C. Jiang, P. Qu and Q.-G. Zhai, *Chem. Commun.* **2018**, *54*, 2012-2015; b) Y. Ye, Z. Ma, R.-B. Lin, R. Krishna, W. Zhou, Q. Lin, Z. Zhang, S. Xiang and B. Chen, *J. Am. Chem. Soc.* **2019**, *141*, 4130-4136; c) R. Matsuda, R. Kitaura, S. Kitagawa, Y. Kubota, R. V. Belosludov, T. C. Kobayashi, H. Sakamoto, T. Chiba, M. Takata, Y. Kawazoe and Y. Mita, *Nature* **2005**, *436*, 238-241.
[3] C. R. Reid and K. M. Thomas, *Langmuir* **1999**, *15*, 3206-3218.
[4] M. Bühl and G. Wipff, *ChemPhysChem* **2011**, *12*, 3095-3105.
[5] a) S. Roy, A. Chakraborty and T. K. Maji, *Coord. Chem. Rev.* **2014**, *273-274*, 139-164; b) H. Li, K. Wang, Y. Sun, C. T. Lollar, J. Li and H.-C. Zhou, *Mater. Today* **2018**, *21*, 108-121; c) A. Hazra, A. Jain, M. S. Deenadayalan, S. A. Adalikwu and T. K. Maji, *Inorg. Chem.* **2020**, *59*, 9055-9064; d) A. Chakraborty, S. Roy, M. Eswaramoorthy and T. K. Maji, *J. Mater. Chem. A* **2017**, *5*, 8423-8430; e) A. Hazra, S. Jana, S. Bonakala, S. Balasubramanian and T. K. Maji, *Chem. Commun.* **2017**, *53*, 4907-4910; f) R. Haldar, N. Sikdar and T. K. Maji, *Mater. Today* **2015**, *18*, 97-116.
[6] a) J.-P. Zhang and X.-M. Chen, *J. Am. Chem. Soc.* **2009**, *131*, 5516-5521; b) K.-J. Chen, Hayley S. Scott, David G. Madden, T. Pham, A. Kumar, A. Bajpai, M. Lusi, Katherine A. Forrest, B. Space, John J. Perry and Michael J. Zaworotko, *Chem* **2016**, *1*, 753-765.
[7] a) R.-B. Lin, L. Li, H. Wu, H. Arman, B. Li, R.-G. Lin, W. Zhou and B. Chen, *J. Am. Chem. Soc.* **2017**, *139*, 8022-8028; b) A. Luna-Triguero, J. M. Vicent-Luna, R. M. Madero-Castro, P. Gómez-Álvarez and S. Calero, *ACS Appl.Mater. Interfaces* **2019**, *11*, 31499-31507; c) W. Fan, S. Yuan, W. Wang, L. Feng, X. Liu, X. Zhang, X. Wang, Z. Kang, F. Dai, D. Yuan, D. Sun and H.-C. Zhou, *J. Am. Chem. Soc.* **2020**, *142*, 8728-8737; d) H.-G. Hao, Y.-F. Zhao, D.-M.

Chen, J.-M. Yu, K. Tan, S. Ma, Y. Chabal, Z.-M. Zhang, J.-M. Dou, Z.-H. Xiao, G. Day, H.-C. Zhou and T.-B. Lu, *Angew. Chem., Int. Ed.* **2018**, *57*, 16067-16071.
[8] R. Krishna, *ACS Omega* **2020**, *5*, 16987-17004.
[9] W. Yang, A. J. Davies, X. Lin, M. Suyetin, R. Matsuda, A. J. Blake, C. Wilson, W. Lewis, J. E. Parker, C. C. Tang, M. W. George, P. Hubberstey, S. Kitagawa, H. Sakamoto, E. Bichoutskaia, N. R. Champness, S. Yang and M. Schröder, *Chem. Sci.* **2012**, *3*, 2993-2999.
[10] M. L. Foo, R. Matsuda, Y. Hijikata, R. Krishna, H. Sato, S. Horike, A. Hori, J. Duan, Y. Sato, Y. Kubota, M. Takata and S. Kitagawa, *J. Am. Chem. Soc.* **2016**, *138*, 3022-3030.
[11] a) S. Krause, N. Hosono and S. Kitagawa, *Angew. Chem., Int. Ed.* **2020**, *59*, 15325-15341; b) A. Schneemann, V. Bon, I. Schwedler, I. Senkovska, S. Kaskel and R. A. Fischer, *Chem. Soc. Rev.* **2014**, *43*, 6062-6096; c) T. K. Maji, R. Matsuda and S. Kitagawa, *Nat. Mater.* **2007**, *6*, 142-148; d) J. D. Evans, V. Bon, I. Senkovska, H.-C. Lee and S. Kaskel, *Nat. Commun.* **2020**, *11*, 2690.
[12] a) Y. Takashima, V. M. Martínez, S. Furukawa, M. Kondo, S. Shimomura, H. Uehara, M. Nakahama, K. Sugimoto and S. Kitagawa, *Nature Commun.* **2011**, *2*, 168; b) T. K. Maji, K. Uemura, H.-C. Chang, R. Matsuda and S. Kitagawa, *Angew. Chem., Int. Ed.* **2004**, *43*, 3269-3272.
[13] a) K. Biradha and M. Fujita, *Angew. Chem. Int. Ed.* **2002**, *41*, 3392-3395; b) K. Biradha, Y. Hongo and M. Fujita, *Angew. Chem. Int. Ed.* **2002**, *41*, 3395-3398.
[14] N. Nijem, H. Wu, P. Canepa, A. Marti, K. J. Balkus, T. Thonhauser, J. Li and Y. J. Chabal, *J. Am. Chem. Soc.* **2012**, *134*, 15201-15204.
[15] a) Q.-Y. Yang, P. Lama, S. Sen, M. Lusi, K.-J. Chen, W.-Y. Gao, M. Shivanna, T. Pham, N. Hosono, S. Kusaka, J. J. Perry Iv, S. Ma, B. Space, L. J. Barbour, S. Kitagawa and M. J. Zaworotko, *Angew. Chem., Int. Ed.* **2018**, *57*, 5684-5689; b) S. Nandi, P. De Luna, R. Maity, D. Chakraborty, T. Daff, T. Burns, T. K. Woo and R. Vaidhyanathan, *Mater. Horiz.* **2019**, *6*, 1883-1891.
[16] SMART (V 5.628), SAINT (V 6.45a), XPREP, SHELXTL; Bruker AXS Inc. Madison, Wisconsin, USA. **2004**.
[17] G. M. Sheldrick, Siemens Area Detector Absorption Correction Program, University of Götingen, Götingen, Germany,**1994**.
[18] A. Altomare, G. Cascarano, C. Giacovazzo and A. Guagliardi, *J. Appl. Crystallogr.* **1993**, *26*, 343-350.
[19] G. M. Sheldrick, SHELXL-97, Program for Crystal Structure Solution and Refinement; University of Götingen, Götingen, Germany, **1997**.
[20] G. M. Sheldrick, SHELXS 97, Program for the Solution of Crystal Structure, University Götingen, Germany, **1997**.
[21] A. Spek, *J. Appl. Crystallogr.* **2003**, *36*, 7-13.
[22] M. M. Dubinin, *Chem. Rev.* **1960**, *60*, 235-241.
[23] M. Chen, S. Chen, W. Chen, B. E. G. Lucier, Y. Zhang, A. Zheng and Y. Huang, *Chem. Mater.* **2018**, *30*, 3613-3617.
[24] N. D. Hutson and R. T. Yang, *Adsorption* **1997**, *3*, 189-195.
[25] J.-R. Li, R. J. Kuppler and H.-C. Zhou, *Chem. Soc. Rev.* **2009**, *38*, 1477-1504.
[26] J. M. Junquera-Hernández, J. Sánchez-Marín and D. Maynau, *Chem. Phys. Lett.* **2002**, *359*, 343-348.
[27] a) J. Lee, C. Y. Chuah, J. Kim, Y. Kim, N. Ko, Y. Seo, K. Kim, T. H. Bae and E. Lee, *Angew. Chem., Int. Ed.* **2018**, *57*, 7869-7873; b) Y. Du, Y. Chen, Y. Wang, C. He, J. Yang, L. Li and J. Li, *Sep. Purif. Technol.* **2021**, *256*, 117749.

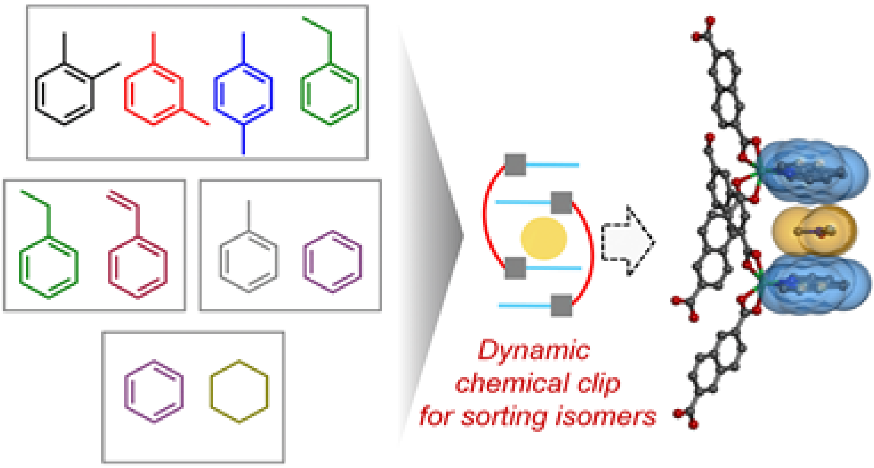

3.3: A Dynamic Chemical Clip in Supramolecular Framework for Sorting Alkylaromatic Isomers using Thermodynamic and Kinetic Preferences

A Manuscript based on this work has been published in Angew. Chem. Int. Ed., 2021, 60, 2.

Abstract

Adsorptive chemical separation is at the forefront of future technologies, to be used in chemical and petrochemical industries. In this process, a porous adsorbent selectively allows a single component from a mixture of three or more chemical components to be adsorbed or permeate. To separate the remaining unsorted chemical mixture, a different type of adsorbent is required. A unique adsorbent which can recognize and separate each of the chemicals from a mixture of three or more components is the necessity for the next generation porous materials. This chapter demonstrates a “dynamic chemical clip” in a supramolecular framework capable of thermodynamic and kinetics-based chemical separation. The dynamic space, featuring strong preference for aromatic guests through π-π and C-H···π interactions and adaptability, can recognize the individual chemical isomers from mixtures (such as C_8 alkylaromatic isomers, benzene, toluene and styrene) and separate those based on thermodynamic and kinetic factors. The liquid-phase high selectivity and separation of the aromatic isomers are possible by the adaptability of the “chemical clip”, thus elucidates the prime factors in a combinatorial approach, involving crystallographic evidence and detail computational studies.

3.3.1: Introduction

The energy-efficient chemical separation method is the most urgent technology at the current time. The conventional distillation process cannot be considered as a sustainable route for chemical and petrochemical industries in the near future, as concerns over fuel-energy resource, environmental and economic factors are at the extreme stage.[1] Alternative solution, like adsorption-based separation is a potential route, but far from being mature enough. In this process, a porous material (adsorbent) excludes or includes an adsorbate selectively; thus, it can separate a mixture of two or more chemical components with an estimated ~ 80% reduction of energy consumption compared to the distillation column method.[2] A careful consideration of the physical (size, shape, polarity) and chemical nature (acidic/basic, protic/aprotic) A convenient approach is to design a material with fixed pore dimension, so that size or shape-based exclusion or selection is rendered.[3] Consecutively, pore surfaces of the adsorbent can be functionalized for preferential exclusion or inclusion.[3c] Evidently, these bestow a wide prospect for new porous material design and fabrication, thus realizing targeted material for important chemical separation.

The number of industrially important chemicals is fairly large. A certain category of those having very similar physical properties poses a substantial challenge for straightforward separation.[2] For example, benzene derivatives (BTEX: benzene (Benz), toluene (Tol), ethylbenzene (Eb) and xylenes) which are the primary source of polymers, fibres and fuels; in particular C_8 alkylaromatic isomers (xylenes and ethylbenzene).[4] For all these to separate from their corresponding sources (chemical mixtures), the amount of energy consumed by distillation process is astonishingly high.[2, 4] An advancement in these chemical separation process is considered as important as “to change the world”.

Considering the precisely balanced size, shape, and functionality requirements[4] for separation of benzene derivatives, the design principle of the porous structure should be precise and straightforward. In this regard, crystalline porous coordination polymers (PCPs)[5] are high-surface area materials,[6] possessing structural order with intrinsic and adjustable porosity.[7] Reticular synthesis strategy[8] has been extremely successful with

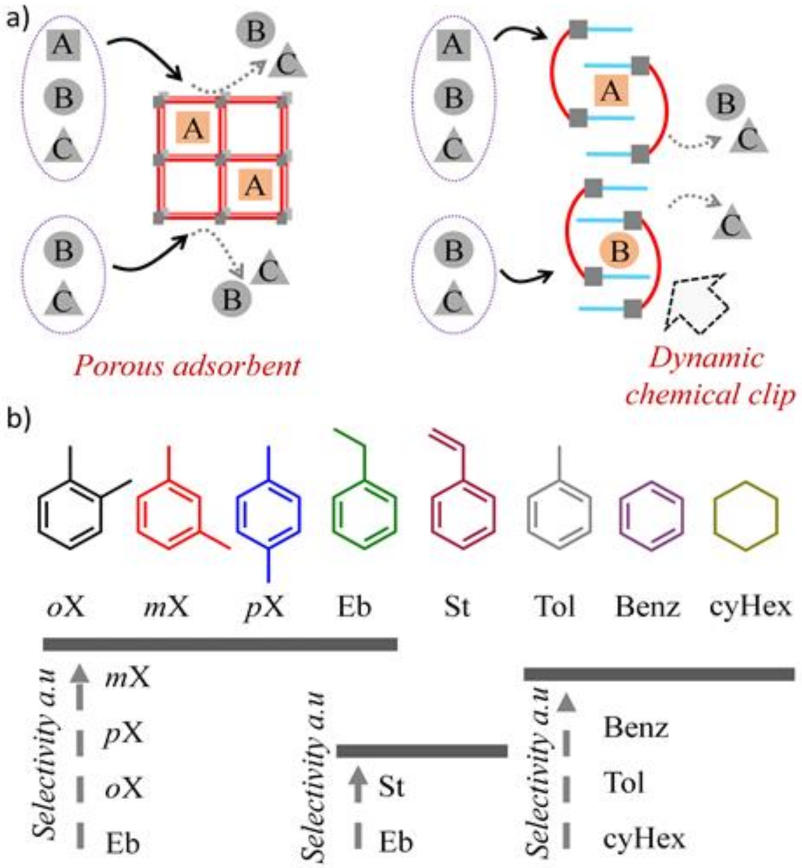

Scheme 1: (a) A schematic illustration of the “dynamic chemical clip” for separation of individual chemical isomers (A, B and C), in comparison to the conventional porous adsorbents; (b) Chemical isomers sorted by the dynamic chemical clipping process (a.u = arbitrary unit).

PCPs to design tailor-made chemical space.[9] Hence, critical adsorption-based separation can be best achieved by employing PCP as an adsorbent. This is represented obviously with the number of available PCPs for separation, mostly by size-exclusion or specific adsorbate-adsorbent interactions.[10] With a fitting pore size and functionality of a PCP, one of the adsorbates among A, B and C can be separated from the mixture of A+B+C (Scheme 1a). However, often it fails to separate the individual components. In this chapter, it has been demonstrated that the stringent pore size/shape/functionality may not be the indispensable elements to realize excellent separation performance, but dynamic and adaptable porous coordination polymer can be remarkably efficient to separate each component of adsorbate mixture (Scheme 1a). Here, this chapter reports dynamic chemical clip for the chemical separation. The “chemical clip” term defines the geometry of the dynamic nanospace in a flexible supramolecular framework created by a one-dimensional CP, as shown in scheme 1a. The chemical adsorption site and diffusion parameter, i.e., the thermodynamic and kinetic factors, respectively, are finely controlled by the dynamic framework leading to surprising selectivity of the chemical isomers.

In response to physical stimuli and inclusion or exclusion of guest from the pores, substantial structural change can be observed for dynamic or soft PCPs; i.e. the 3rd generation and four-dimensional-PCPs.[11] This structural dynamics (reversible or irreversible), unavailable in the conventional porous materials such as zeolite, porous carbon, can be instrumental towards chemical selectivity.[12] Scheme 1a illustrates the difference between a conventional porous adsorbent and a dynamic adsorbent. This chapter unfolds the utilization of the coordination polymer, a chemical space (functional pore) can be designed to be adaptable towards guest molecules, in the present case alkylaromatics (Scheme 1b). The structural adaptability and adsorption selectivity (thermodynamic and kinetic) towards the chemical isomers enormously vary, although the difference in the physical parameters of the isomers (C_8 isomers) are very subtle (Table 1).

Table 1: Physical properties (boiling point, kinetic diameter, polarizability and dipole moment) of the adsorbates.[3c, 13]

Alkylaromatics	Boiling point (°C)	Kinetic diameter (Å)	Polarizability $\times 10^{25}$/ cm^3 (σ)	Dipole moment (D)
ortho-xylene	144.44	6.8	141-149	0.64
meta-xylene	139.19	6.8	142	0.37
para-xylene	138.38	5.8	137-149	0.10
ethyl benzene	136.21	5.8	142	0.59
styrene	145.2	5.8	145	0.13
benzene	80.1	5.349-5.85	100-107.4	0
toluene	110.6	5.25	118-123	0.36
cyclohexane	80.8	6.0	108.7-110	0

The “dynamic chemical clip” equipped coordination polymer is capable of sorting individual alkylaromatics (Scheme 1b) from their mixtures. An assembly of 1D coordination polymer, [Zn(*o*-phen)(2,6-ndc)·DMF][14] (**1**; *o*-phen = 9,10-phenantholine, 2,6-ndc = 2,6-naphthalenedicarboxylate, DMF = N,N'-dimethylformamide) resulted in dynamic nanospace with optimal potential to house aromatic isomers or molecules with different binding energies. The interplay of the thermodynamic and kinetic process resulted in an exclusive selectivity towards meta-xylene (*m*X) isomer among the C_8

isomers, unveiled by crystallographic and theoretical analyses. The current finding surpasses the previously studied PCPs[4, 10d, 15] by demonstrating high selectivity towards each component of the C_8 isomers and elucidating the isomer-binding sites by single-crystal structure determination (Table 2). Experimental and theoretical determination of separation efficiency unequivocally established the advantages of the dynamic PCP. Its far-reaching competency is revealed by selectivity/separation of the other BTEX chemical (styrene (St)/ethylbenzene (Eb); toluene (Tol)/benzene (Benz); benzene (Benz)/cyclohexane (cyHex)), as illustrated in the Scheme 1b.

Table 2: Porous material showing selective adsorption of solvent molecules in liquid/ vapor Phase.

Sl No.	Material	Selective isomer	Mixture contains	Involved mechanism	Separation technique
1	HKUST-1[15e]	*m*X	Xylene, Benz, Tol	Size selectivity and guest-adsorbent interaction	GC[a]
2	SOS@HKUST-1[15f]	*m*X	*o*X, *p*X, *m*X	Guest-guest interaction	Adsorptive separation, HPLC[b]
3	Mg-CUK-1[15g]	*p*X	*o*X, *p*X, *m*X	Host-guest force and Guest-guest stacking	^{1}H-NMR
4	MIL-47[15h]	*p*X	*o*X, *p*X, *m*X, EB	Host-guest interaction	Breakthrough and pulse gas chromatography
5	Ce(HTCPB) Nd(HTCPB)[15a]	*p*X	*o*X, *p*X, *m*X	Shape selective	GCMC[c]
6	(R,R)-(−)-2,3-dimethoxy-1,1,4,4-tetraphenylbutane-1,4-diol[15i]	*p*X	*o*X, *p*X, *m*X, EB	Size selective	GC
7	silicalite-1[15j]	*p*X	*o*X and *p*X	Size exclusion	Membrane based
8	CMS[15k]	*p*X	*o*X and *p*X	Size exclusion	Membrane based
9	MAF-6[15l]	*o*X	*o*X, *p*X, *m*X,	Size and shape exclusion	Computation modelling
10	CD-MOF[15m]	*o*X	*o*X, *p*X, *m*X, EB	Shape recognition	Breakthrough separation, HPLC, and GCMC
11	$Ni(NCS)_2(PPP)_4$[15n]	*o*X	*o*X, *p*X, *m*X	Host-guest interaction	Selective sorption and GC

12	RHO-ZMOF[15o] ZIF-67	*o*X	*o*X, *p*X, *m*X	Shape selective	Selective sorption, GC, DFT[d]
13	Dyna MOF-100[15p]	St	St/Eb	Host-guest interaction	GC, Breakthrough and pulse chromatographic simulation
14	MIL-47, 53 (Al)[15q]	St	St./Eb	Host-guest interaction	Liquid phase batch adsorption
15	Pillar[6]arene[15r]	St	St/Eb	Host-guest interaction	Molecular simulation
16	MAF-41[10d]	St	ST/Tol, ST/ Bz, EB/ST and EB/ST/Tol/Bz	Host-guest interaction and size-selective molecular sieving	GC, GCMC, DFT
20	$Cd(abppt)_2.(ClO_4)_2$[15s]	Benz, Tol	Benz/Tol/*o, m, p*- xylene	Size and shape exclusion	Adsorptive separation, ^{1}H-NMR

[a]Gas Chromatography, [b]high-performance liquid chromatography, [c]Grand Canonical Monte Carlo, [d]Density Functional Theory

3.3.2: Experimental section

3.3.2.1: Materials

All the reagents employed were commercially available and used as provided. Metal salt was obtained from Spectrochem, 2,6-naphthalene dicarboxylic acid, 1,10-phenanthroline, ortho/meta/para-xylenes, styrene, ethylbenzene, toluene, benzene and cyclohexane were obtained from Sigma Aldrich chemicals.

3.3.2.2: Synthesis

Synthesis of **1**[14] was carried out according to the previously reported methodology. 2,6-naphthalenedicarboxylic acid (0.022 g, 0.1 mmol) and ortho-phenanthroline (0.020 g, 0.1 mmol) were dissolved in 5 mL of dimethyl formamide and mixed well. 0.030 g (0.1 mmol) of $Zn(NO_3)_2·6H_2O$ was added to the ligand solution and sonicated before the sealed glass vial was kept in an oven at 120 °C for 36 h. Crystals of 1 were isolated and washed with fresh DMF before the powder X-ray diffraction measurement to check the phase purity.

Desolvated **1** or **1a** was prepared by heating 1 at 170 °C for 12 h under reduced pressure of 1×10^{-1} Pa. Yield of 1: 78 %; Anal. Calcd. for $C_{27}H_{21}N_3O_5Zn$: C, 60.91; H, 3.94; N, 7.89.

Found C, 61.31; H, 4.13; N, 7.56. FT-IR (KBr pellet, 4000-400 cm^{-1}): 3069(w), 2932(w), 1675(s), 1602(s), 1560(m), 1415(s), 1190(s), 1080(s), 930(s), 853(s), 793(s), 727(s), 645(s).

Syntheses of [Zn(ndc)(*o*-phen)]·ortho-xylene)] (*o*X@1), [Zn(ndc)(*o*-phen)]·meta-xylene)] (*m*X@1), [Zn(ndc)(*o*-phen)]·para-xylene)] (*p*X@1), [Zn(ndc)(*o*-phen)]·styrene)] (St@1) and [Zn(ndc)(*o*-phen)]·toluene)][14] (Tol@1).

2,6-naphthalenedicarboxylic acid (0.022 g, 0.1 mmol) and orthophenanthroline (0.02 g, 0.1 mmol) were dissolved in 5 mL of dimethyl formamide (DMF) and mixed well. 0.030 g (0.1 mmol) of $Zn(NO_3)_2 \cdot 6H_2O$ was added to the ligand solution and sonicated for 10 min. 1 mL of ortho-xylene was added to this clear solution before the sealed glass vial was kept in an oven at 120 °C for 36 h. Good quality light yellow color crystals were isolated and washed with fresh DMF before taking for single-crystal X-ray diffraction measurement.

The other PCPs were also synthesized following similar methodology except ortho-xylene was replaced by meta-xylene, para-xylene, styrene and toluene[14] respectively. Yield of *o*X@1: 69%; Anal. Calcd. for $C_{32}H_{24}N_2O_4Zn$: C, 67.67; H, 4.61; N, 6.93. Found C, 65.77; H, 4.11; N, 7.21. FT-IR (KBr pellet, 4000-400 cm^{-1}): 3084(w), 2930(w), 1672(s), 1610(s), 1517(m), 1495(m), 1190(s), 1143(s), 1110(s), 930(s), 849(s), 806(s), 726(s), 645(s). Yield of *m*X@1: 73%; Anal. Calcd. for $C_{32}H_{24}N_2O_4Zn$: C, 66.82; H, 4.32; N, 7.11. Found C, 66.45; H, 4.78; N, 7.54. FT-IR (KBr pellet, 4000-400 cm^{-1}) 3071(w), 2935(w), 1612(m), 1486(m), 1250(m), 1191(s) 1096(w), 1040(w), 932(s), 776(s), 680(s). Yield of *p*X@1: 74%; Anal. Calcd. for $C_{32}H_{24}N_2O_4Zn$: C, 68.34; H, 4.22; N, 7.31. Found C, 67.94; H, 4.13; N, 7.48. FT-IR (KBr pellet, 4000-400 cm^{-1}) 3066(w), 2928(m), 1671(s), 1515(m), 1457(s), 1120(s), 1045(s), 932(s), 850(s), 795(s), 645(s). Yield of St@1: 67%; Anal. Calcd. for $C_{32}H_{22}ZnN_2O_4Zn$: C, 66.97; H, 4.78; N, 7.76. Found C, 67.22; H, 4.51; N, 7.97. FT-IR (KBr pellet, 4000-400 cm^{-1}) 3082(w), 2930(w), 1820(m), 1632(m), 1492(s), 1192 (s), 1087(s), 992(s), 910(s), 775(s), 698(s), 645(s). Yield of Tol@1: 70%; Anal. Calcd. for $C_{31}H_{22}ZnN_2O_4Zn$: C, 68.54; H, 4.77; N, 7.19. Found C, 67.48; H, 4.89; N, 7.24. FT-IR (KBr pellet, 4000-400 cm^{-1}) 3051(w), 2933(w), 1678(s), 1590(s), 1494(s), 1187(m), 1099(m), 932(s), 853(s), 797(s), 641(m).

3.3.2.3: X-ray single-crystal diffraction

Suitable single crystals of *o*X@1, *m*X@1, *p*X@1 and St@1 were mounted on a thin glass fiber. X-ray crystallographic data of such crystals were collected on a Bruker Smart-CCD diffractometer equipped with a normal focus, 2.4 kW sealed tube X-ray source with graphite monochromated Mo-Kα radiation ($\lambda = 0.71073$ Å) operating at 50 kV and 30 mA. The program SAINT[16] was used for integration of diffraction profiles, and absorption correction was made with SADABS[17] program. Structures were solved by SIR 92[18] and refined by the full-matrix least-squares method using SHELXL-97.[19] All hydrogen atoms were fixed in ideal positions by HFIX command. In addition, non-hydrogen atoms were refined anisotropically. All crystallographic and structure refinement data are summarized in Table 3. All calculations were carried out using SHELXL 97, PLATON,[20] SHELXS 97[21] and X-Seed Ver 4.[22] The crystal structures can be obtained from CCDC number 2044677-2044680.

3.3.2.4: Physical measurements

NMR spectra were obtained with a Bruker AVANCE 400 (400 MHz) Fourier transform NMR spectrometer with chemical shifts reported in parts per million (ppm). Thermogravimetric analyses (TGA) were carried out (Metler Toledo) in N_2 atmosphere in the temperature range 40-400 °C (heating rate = 5 °C min^{-1}). FT-IR spectra were recorded on a Bruker IFS 66v/S spectrophotometer using KBr pellets in the region 4000-400 cm^{-1}.

3.3.2.4: Adsorption and separation studies

Adsorption isotherms and kinetics of xylene vapors at 298 K were measured for the desolvated **1** (**1a**) by using a BELSORP-aqua-3 analyzer. A sample of about ~ 100 mg was prepared by heating at 170 °C for about 12 h under vacuum (1×10^{-1} Pa) prior to measurement of the isotherms. The solvent molecules used to generate the vapor was degassed fully by repeated evacuation. Dead volume was measured with helium gas. The adsorbate was placed into the sample tube, then the change of the pressure was monitored and the degree of adsorption was determined by the decrease in pressure at the equilibrium state. All operations were computer controlled and automatic.

In a fixed-bed column separation experiment, a glass pipette was filled with **1a** (~2.5-inch length) as shown below and 1:1:1:1 mixture of C_8 isomers was eluted in hexane (3 ml) at once. The use of hexane is important for the easy flow through the fixed-bed column and the choice is based on following criteria: i) the dilution solvent should not be adsorbed by the adsorbent, ii) miscibility with the adsorbates, iii) low-boiling so that activation of the adsorbent is easy. 7 fractions at 5, 10, 15, 20, 25, 30 and 45 min were collected to determine the isomer percentages by GC.

3.3.2.4.1: Selectivity study and related calculations

About 100 mg of activated sample was immersed in a solution mixture in equimolar C_8 alkylaromatics (0.5 mL of each isomer with 3 mL of hexane) at room temperature for 2 days. The saturated samples were filtered and subsequently washed in hexane and dried under ambient condition (25 °C) to remove isomers adhered to the surface of the sample. After that, approximately 5 mg of sample dissolved in HCl/d_6-DMSO were analyzed by ^{1}H-NMR.

Selectivity factor between two species '*a*' and '*b*' is defined as;

$$S_{ab} = \frac{x_a y_b}{x_b y_a}$$

Where, *x* and *y* represent the mole fraction of the species in adsorbed and liquid phase, respectively. For equimolar binary mixture, S_{ab} can be simplified as;

$$S_{ab} = \frac{x_a}{x_b}$$

This ratio can be derived from the integrated area ratio of corresponding methyl group of *o*X/*p*X, *o*X/*m*X and *m*X/*p*X binary mixtures. For xylene isomers (same molecular weight and 1:1 mixture), the selectivity factor is defined as;

$$S_{ab} = \frac{q_a}{q_b}$$

Where, q is the relatively integrated area of corresponding methyl groups of xylene isomers (including 6 H).

$S_{pX/oX} = 5.17/0.08 = 64.62$

Considering a relatively integrated area for *p*X ~5.17 and *o*X ~0.08 by integrating peak positions at 2.25 and 2.21 ppm, respectively. The preferential absorption for *p*X over *o*X is 0.86/formula (5.17/6; including 6 H).

$S_{m\mathrm{X}/o\mathrm{X}}$ = 5.46/0.07= 78.0 (by integrating peak positions at 2.27 and 2.21 ppm; *m*X selectivity 0.91/formula).

$S_{m\mathrm{X}/p\mathrm{X}}$ = 5.41/0.09= 60.11 (by integrating peak positions at 2.27 and 2.25 ppm; *m*X selectivity 0.90/formula).

The preferential selectivity of *m*X from the mixture of 4-components (*m*X, *p*X, *o*X and Eb) is calculated by considering the corresponding relative integrated area of each component. For the equimolar quaternary phase, the selectivity factor can be simplified as;

$$S_{\mathrm{a}} = \frac{3(q_a)/6}{\frac{1}{6}q_b + \frac{1}{6}q_c + \frac{1}{2}q_d}$$

Where, q_a, q_b, q_c and q_d are the integrated area of corresponding methyl groups of xylene isomers (considering 6H) and methylene group of ethylbenzene (considering 2 H).

$$S_{m\mathrm{X}/(o\mathrm{X}+p\mathrm{X}+\mathrm{Eb})} = \frac{3\left(\frac{5.43}{6}\right)}{\left(\frac{0.11}{6}\right)+\left(\frac{0.06}{6}\right)+\left(\frac{0.03}{3}\right)} = 2.715/(0.018+0.01+0.01) = 71.44$$

The preferential absorption for *m*X from 4-component mixture is 0.905/formula (5.43/6). Likewise, the calculated relative selectivity for other binary mixture is;

$$S_{\mathrm{St/Eb}} = \frac{2q_e}{q_f} = (2\times0.63)/0.02 = 63$$

$$S_{\mathrm{Benz/cyHex}} = \frac{2q_g}{q_h} = (2\times3.85)/0.04 = 192.5$$

$$S_{\mathrm{Benz/Tol}} = \frac{q_g}{2q_i} = 3.70/(2\times0.04) = 46.25$$

Where, q_e, q_f, q_g, q_h and q_i are the integrated area of corresponding hydrogen of St (1 H), Eb (2 H), Benz (6 H), Tol (3 H) and cyHex (12 H), respectively.

3.3.3: Computational details

Periodic Density Functional Theory (DFT) calculations were performed using the CP2K package (https://www.cp2k.org/)[23] which uses hybrid Gaussian and plane wave density functional scheme.[24] To obtain the positions of the constituent atoms at the minimum potential energy, First, the lattice parameters were varied in small steps (using in-house code) beginning with experimentally determined parameters, the set of lattice parameters which yields the lowest energy (also calculated using CP2K) was selected. Then a Geometry optimization was performed using CP2K with the lattice parameters determined in the previous step. The optimized coordinates were considered for all the binding energy calculations.

All the calculations were carried using the QUICKSTEP module of CP2K.[25] The core electrons of the atoms were represented by norm-conserving pseudopotentials of Goedecker-Teter-Hutter (GTH)[26] and the valence electrons by the Double-ζ Valence Potential (DZVP) basis set[27] optimized for molecules. PBE exchange-correlation functional with empirical van der Waals correction prescribed by Grimme (DFT-D3)[28] was used. The electron density was represented using an energy cutoff of 280 Ry, and the Realspace cutoff was chosen to be 40 Ry. The criterion for geometry optimization was the RMS force on atoms was less than $4.5e^{-5}$ along with Max force on any atom less than $3.0e^{-4}$.

The PCP crystal structures encapsulating xylenes, styrene, and toluene guests were determined in this work. Optimizations were performed with 2x2x1 replications for mX and oX@1, and 2x1x1 replications were used for the remaining, respectively. The optimized crystal structures were used to calculate total energies of (i) PCP + guests, (ii) PCP, and (iii) guests alone. Binding energy ΔE was calculated using $\Delta E = E(PCP+Guest) - E(PCP) - nxE(Guest)$. The optimized cell parameters and the Binding energies per guest molecule are reported in Table 4. Note that PCP means a guest removed PCP, without any change in the structure.

CP2K input: Cell lengths (@r_a@, @r_b@ & @r_c@) and angles (@r_alpha@ @r_beta@ @r_gamma@) in the following input file for a given initial configuration were varied using a shell script and was then supplied to CP2K as input for geometry optimization. The set of parameters that yielded the minimum energy at the end of geometry optimization was taken as the optimized cell parameters. On obtaining the optimized cell parameters and atomic positions using the above script. The following script was used to calculate the energy of the system (one SCF cycle in DFT) for the framework, the guests and the combined system. In addition to calculating single-point energies for the calculation of binding energies, the electron densities were also stored for the calculation of electron density difference maps.

3.3.3.1: Electron Density Difference Map

The electron density difference maps were calculated to delineate the interactions between xylene isomers with the PCP. These were performed on the structures which were optimized using PBE-D3 method in CP2K. The electron density difference was calculated using the relation,

$$\Delta\rho = \rho(\text{PCP-guest}) - \rho(\text{PCP}) - \rho(\text{guest})$$

Where $\Delta\rho$, ρ(framework-guest), ρ(framework) and ρ(guest) are the electron density difference of the system, total electron density of the framework containing the guests, individual electron density of the framework and isolated guests respectively.

Plane wave-based codes such as CPMD or CP2K do not handle hybrid exchange-correlation functionals efficiently. Thus, although the B3LYP or M06 functionals have been shown to well account for dispersion interactions, these are not implemented in periodic DFT codes. Thus, Gaussian calculations have been employed to estimate the guest-PCP interaction strength. Unfortunately, periodic calculations cannot be carried out with such an approach. However, one can identify regions of the framework which are proximal to the adsorbed guests and can consider such a fragment, and terminate it sensibly with hydrogen atoms. It should then be possible to obtain binding energies of the adsorbate with this fragment and also identify various interactions contributing to it. Iso-surfaces of increased and decreased Electron density differences for PCP encapsulating the guests are shown in Figure 9.

3.3.3.2: Osmotic Framework Adsorbed Solution Theory (OFAST)

Osmotic ensemble appropriately describes adsorption of gas molecules in the flexible nanoporous materials.[29] In the osmotic ensemble, four parameters i) chemical potential of adsorbed gas (μ), ii) temperature (T), iii) number of molecules of nanoporous framework (N_f), and iv) mechanical constraint on the system (which is external pressure P in this case), are kept fixed and number of adsorbed gas molecules (N) can change according to the fixed four parameters.

Single component OFAST: For adsorption of a gas i in the α phase of a flexible framework, the thermodynamic potential (Ω_{os}^{α}) in the osmotic ensemble (Ω_{os}^{α}) can be written as,[30]

$$\Omega_{os}^{\alpha}(T,P,\mu_i) = F^{\alpha} + PV^{\alpha} - \mu_i N_i\,, \qquad \text{(eq.1)}$$

where, F^{α} is the Helmholtz free energy of the empty PCP in phase α, V^{α} is the of the volume of the framework in phase α, N_i is the total molar uptake of gas i in framework, and μ_i is the chemical potential of gas i in adsorbed phase. Eq. 1 can be simplified using the fundamental relation of chemical potential and approximating molar volume of gas using ideal gas law ($V_m(p) = RT/p$), which results in,[29]

$$\Omega_{os}^{\alpha} = F^{\alpha} + PV^{\alpha} - RT\int_0^P \frac{n_i^{\alpha}(p,T)}{p}\,dp\,, \qquad \text{(eq.2)}$$

where, R is the gas constant and $n_i^{\alpha}(T,p)$ is the adsorption isotherm of gas i in phase α of the framework. For another phase β of the framework similar equation can be written as,

$$\Omega_{os}^{\beta} = F^{\beta} + PV^{\beta} - RT\int_0^P \frac{n_i^{\beta}(p,T)}{p}\,dp\,. \qquad \text{(eq.3)}$$

The pressure of gas molecules which induces transition of framework from phase α to β is referred as transition pressure (P_{Trans}). At P_{Trans}, both phases have equal thermodynamic potential (i.e. $\Omega_{os}^{\alpha} = \Omega_{os}^{\beta}$), which results in (using eq. 2, 3),

$$\Delta F = RT\left[\int_0^{P_{Trans}} \frac{n_i^{\alpha}(p,T)}{p}\,dp + \int_0^{P_{Trans}} \frac{n_i^{\beta}(p,T)}{p}\,dp\right] - P\Delta \mathrm{V}, \qquad \text{(eq.4)}$$

where, $\Delta F = F^{\beta} - F^{\alpha}$ and $\Delta V = V^{\beta} - V^{\alpha}$. In our case, there is no adsorption in the α phase (or phase before gate opening pressure) and $P\Delta\mathrm{V}$ factor is negligible, therefore,

$$\Delta F = RT\left[\int_0^{P_{Trans}} \frac{n_i^{\beta}(p,T)}{p}\,dp\right]. \qquad \text{(eq.5)}$$

Langmuir-Freundlich adsorption isotherm model ($n = n_s \frac{bp^t}{1+bp^t}$) was used to fit experimental adsorption isotherm in β phase (or phase after gate opening pressure). Using this model in eq. 5, as obtained,

$$\Delta F = RT\left[\frac{n_s}{t} log\left(1 + bP_{Trans}{}^{t}\right)\right]. \qquad \text{(eq.6)}$$

For each guest molecule, used eq. 6 has been used to calculate free energy change in structural transition of framework. All the values are reported in Table 5.

Multi-component OFAST: For a mixture of m type of guests in the α phase of a flexible adsorbent, the thermodynamic potential (Ω_{os}^{α}) in the osmotic ensemble can be written as,[30]

$$\begin{aligned}\Omega_{os}^{\alpha} &= F^{\alpha} + PV^{\alpha} - RT\sum_{i=1}^{m}\int_0^P \frac{n_i^{\alpha}(p,T)}{p}dp \\ &= F^{\alpha} + PV^{\alpha} - RT\int_0^P \frac{n_{total}^{\alpha}(p,T)}{p}dp\,,\end{aligned} \qquad \text{(eq.7)}$$

where, $n_i^{\alpha}(T,p)$ is the co-adsorption isotherm of guest i in phase α of the adsorbent and n_{total}^{α} is the total amount of guest uptake. Similarly, for phase β

$$\begin{aligned}\Omega_{os}^{\beta} &= F^{\beta} + PV^{\beta} - RT\sum_{i=1}^{m}\int_0^P \frac{n_i^{\beta}(p,T)}{p}dp \\ &= F^{\beta} + PV^{\beta} - RT\int_0^P \frac{n_{total}^{\beta}(p,T)}{p}dp\,,\end{aligned} \qquad \text{(eq.8)}$$

Subtracting eq.7 and 8 results in,

$$\Delta\Omega = \Delta F + P\Delta V - RT\int_0^P \frac{n_{total}^{\beta}(p,T) - n_{total}^{\alpha}(p,T)}{p}dp. \qquad \text{(eq.9)}$$

where, $\Delta\Omega = \Omega_{os}^{\beta} - \Omega_{os}^{\alpha}$. In eq.9, neglecting $P\Delta V$ and considering no adsorption in α phase results in (eq.10)

$$\Delta\Omega = \Delta F - RT\int_0^P \frac{n_{total}^{\beta}(p,T)}{p}dp.$$

The stable phase of a framework (among α and β phases) at a given p, T, and gas composition is the phase with lowest osmotic potential. Therefore, eq.10 is utilized to identify stable phase of the framework and computed mixture selectivity using ideal adsorbed solution theory (IAST)[8] in that phase.

For the Zn-NDC MOF, different type of guests has different values of ΔF. For such MOFs, Couck et al.[31] proposed use of mole fraction of adsorbed guest phases to estimate framework ΔF for guest mixture. In the present work, similar approach has been used with a slight variation and estimated mixture ΔF using,

$$\Delta F = \sum_{i=1}^{m} x_i \Delta F_i, \tag{eq.11}$$

where, x_i is the mole fraction ($\sum x_i = 1$) of i^{th} adsorbed guests in the β phase of PCP (as there is no adsorption in α phase), calculated using IAST.

3.3.4: Result and discussion

3.3.4.1: Structural dynamicity

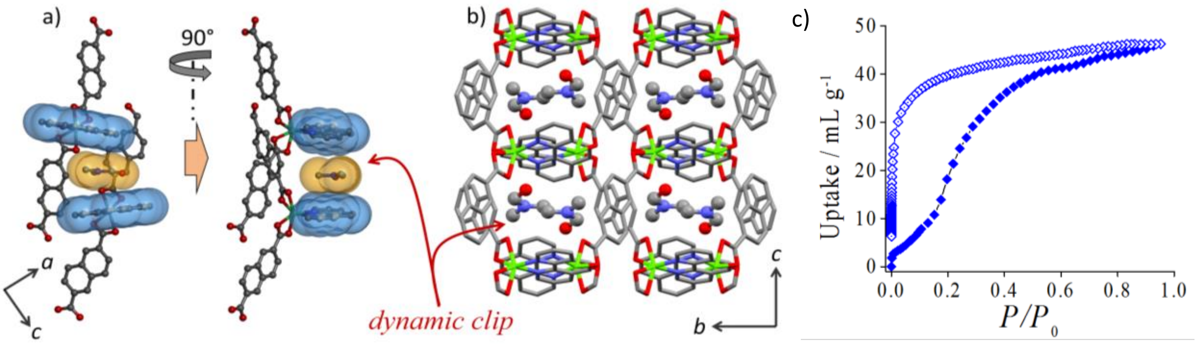

Figure 1: (a) View of the sandwiched nanospace created by *o*-phen from the neighboring 1D polymer filled by DMF; (b) 1D channels in **1** filled with guest DMF (shown in ball and stick model). (c) CO_2 adsorption-desorption profile of **1a** at 195 K.

As a dynamic adsorbent, a 1D coordination polymer formed by continuous linkage of 2,6-ndc and Zn(II)-*o*-phen units have been choosen.[14] The *o*-phen chelating linker constricts the growth to 1D, but also allows to extend the structure in 3D through C-H⋯π and C-H⋯O hydrogen bonding interactions. In this supramolecular polymer 1, a sandwiched space is created between two *o*-phen rings from neighboring 1D polymers, referred as a "chemical clip", as demonstrated in Figure 1a. In 1 the void space is occupied by guest DMF. The nanospace length between the o-phen is 7.428-9.260 Å in **1**. This is suitable for a flat aromatic guest molecule to fit in and remains tightly clipped by π-π interaction with the *o*-phen. View along the *a*-axis shows the 1D channel accommodating the guest DMF in 1 (Figure 1b). The optimal spacing between the *o*-phen units, as realized, is suitable for aromatic amines and toluene, and the nanospace has affinity towards small aromatic molecules.[14] The dynamic nature of the framework was confirmed by stepwise adsorption of CO_2 (Figure 1c) and subsequent structural change. It was revealed that removal of the guest DMF from the nanospace rearranges the structure in a closely packed material (**1a**, ~21.3% reduction in cell volume compared to the parent structure 1).[14] This is understandably to stabilize the 3D framework by close contact interactions in the absence of void filling guest. Filling up of the nanospace with guests like aromatic amines or CO_2 regenerates the porous structure, similar to **1**, as indicated by the previous in situ PXRD experiments coupled with CO_2 adsorption.[14] With these compelling pieces of evidence of structural dynamics and the intrinsic affinity for aromatic guests to encapsulate through the π-π and C-H···π interactions, it is postulated that guest DMF removed **1** or **1a** to be an efficient aromatic isomers adsorbent. The work pursued to demonstrate that the "chemical clip" created by two *o*-phen units is dynamic in nature, and can be selective towards the specific aromatic isomers.

3.3.4.2: Adsorption and diffusion kinetics

In the following, the work reveals the capability of framework towards the efficient separation of i) C_8 isomers, ii) St/Eb, iii) Benz/Tol and iv) Benz/cyHex. The wide spectrum of selectivity will establish the adaptability of the clip, not possible to achieve by a rigid/semirigid conventional porous material. First, the C_8 isomers selectivity was performed in **1a**. For this, single-component vapor adsorption, vapor diffusion kinetics, liquid-phase separation by fixed-bed column chromatography and batch experiments were carried out in detail. Single-component vapor adsorption isotherms recorded at 298 K revealed that **1a** could adsorb xylenes, while Eb is not adsorbed (Figure 2a, c). The saturation uptake amounts for *o*X, *m*X and *p*X are 3.33, 4.13 and 3.87 mmol/g,

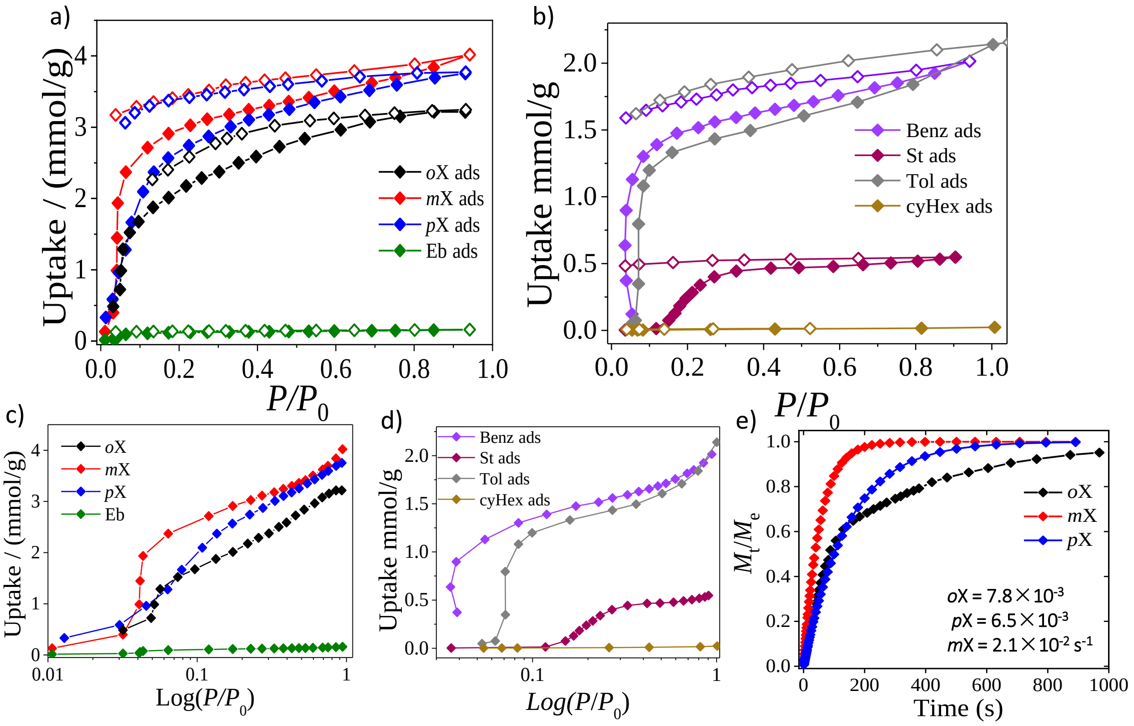

Figure 2: (a, b) Single-component alkylaromatic vapor adsorption isotherm and (c, d) corresponding log curve. (e) Kinetic vapor adsorption isotherm of **1a**.

respectively. This indicated that in **1a**, 92% of the void space created by the *o*-phen units are occupied by *m*X, while the occupation % of *o*X and *p*X is lower. In addition to this difference, the vapor uptake profiles exhibit distinct gate-opening type[12a, b] adsorption (Figure 2c), confirming the dynamic nature of the host. The higher and steeper uptake for *m*X at low partial vapor pressure compared to *o*X or *p*X indicated that **1a** has a higher thermodynamic and kinetic affinity towards *m*X. No adsorption of Eb by **1a** is not surprising considering that the ethyl group of Eb (i) requires larger space and (ii) induces nonaromatic interaction. Any such distinct feature is absent among the xylenes, but surprisingly the adsorption isotherms indicated prominent differences. To comprehend the differences in xylene-adsorbent kinetic interaction, the single-component diffusion kinetics measurement [32] of the xylenes (at 298 K) in their vapor phase was further carried out (Figure 2e). The plot of M_t/M_e vs time (t), where M_t is the mass uptake at time t, M_e is the mass uptake at equilibrium, revealed a mass diffusion order as *m*X>*p*X>*o*X. Using a linear driving force mass transfer model (LDF)[32], as realized, at the low vapor pressure of P/P_0 ~ 0.07, i.e. when xylene-host interaction is the only determining parameter, the kinetic rate constant (*k*) of *m*X is one order of magnitude larger than the other two (*o*X = 7.8×10^{-3}, *p*X = 6.5×10^{-3} and *m*X = 2.1×10^{-2} s^{-1}). This revelation is surprising, considering the fact that *m*X is an intermediate isomer with respect to size/shape/physical parameters [3c, 4] (Table 1). Next, the vapor adsorption profiles of the remaining BTEX-related chemicals were performed. Figure 2b and d illustrate the single-component vapor adsorption profiles of those. For Benz and Tol, **1a** exhibits commensurate adsorption of 1 molecule/formula wt. (2.01 and 2.13 mmol/g, respectively) and for St 0.55 mmol/g. Nonaromatic cyHex is not adsorbed by **1a**. Note, for Benz and Tol, at the very low vapor pressure of $P/P_0 \sim 0.05$ and for St at $P/P_0 \sim 0.12$ a distinct gate opening feature is observed. This is in accordance with the dynamic nature of **1a**. These results indicate that St/Eb and Benz/cyHex separation could be easily achieved.

3.3.4.3: Sorting through breakthrough and batch experiments

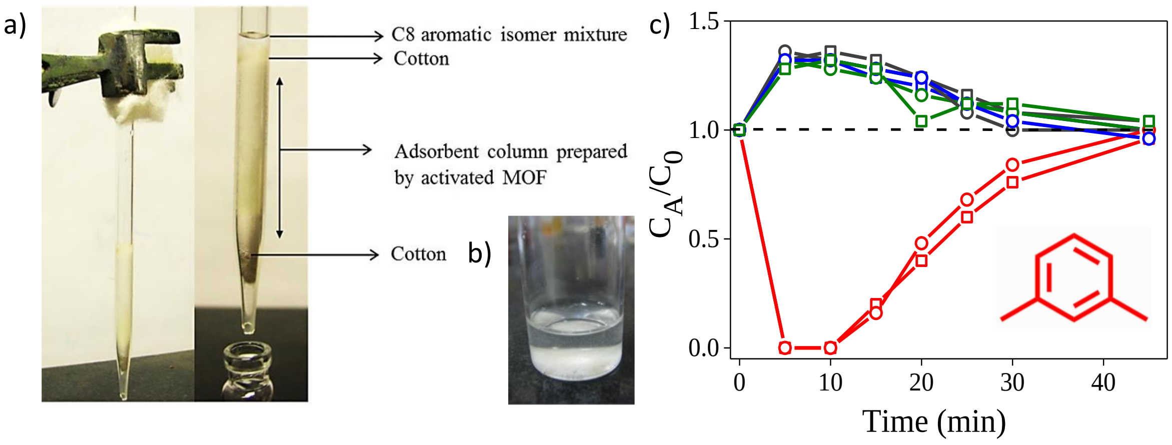

Figure 3: (a) Breakthrough and (b) batch reaction experimental set-up with (c) breakthrough experiment for C_8 isomers: retention times of C_8 isomers, black: oX, red: mX, blue: pX, green: Eb; empty square and circle symbols represent two independent experiments.

Realizing the unique affinity of **1a** towards *m*X, its separation ability from the mixture of C_8 isomers have been tested. While the non-inclusion of Eb from the mixture is evident, as observed, exclusive selectivity for *m*X, by a fixed-bed breakthrough column experiment (Figure 3a). The eluent containing 1:1:1:1 (v/v) mixture of C_8 isomers is eluted through a fixed-bed column of **1a** at ambient condition, as illustrated in Figure 3c.

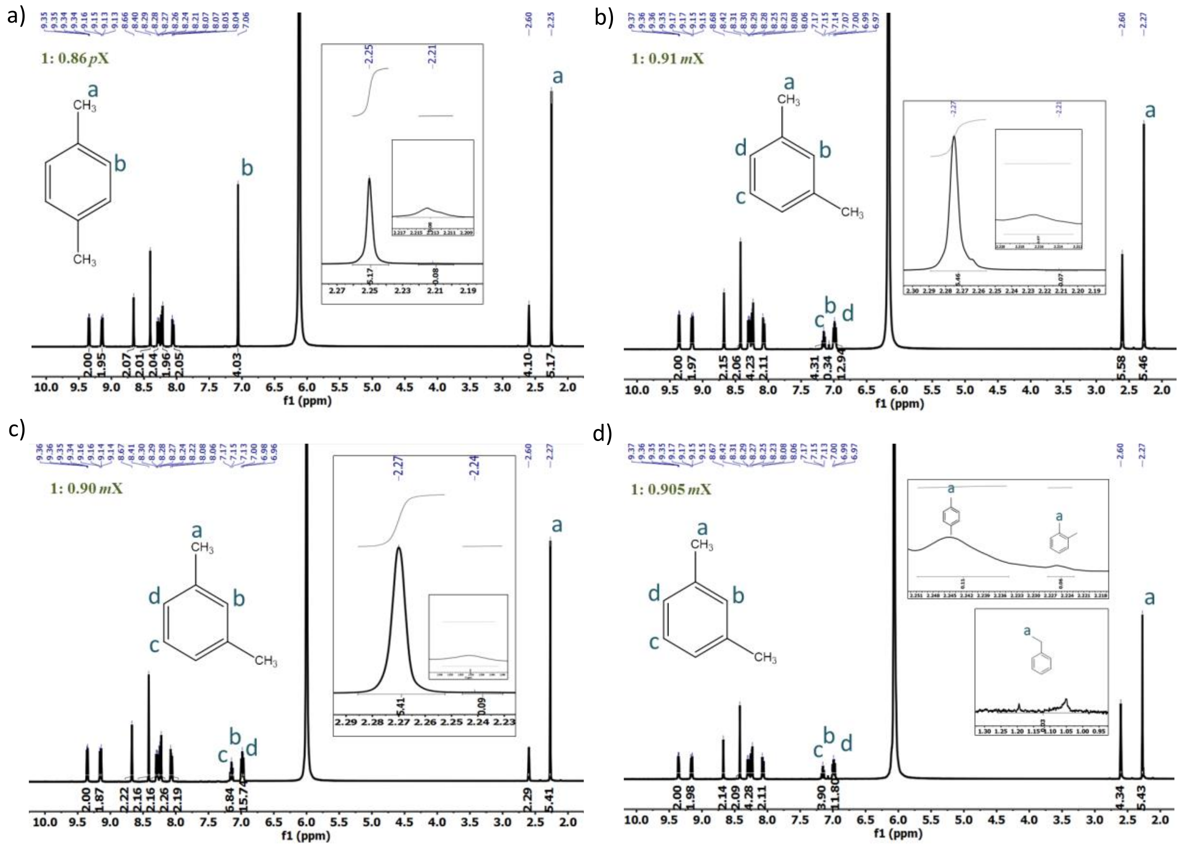

Figure 4: ^{1}H-NMR spectrum of the digested adsorbent (**1a**) after from the batch experiment carried out for 1:1 mixture of (a) *p*X and *o*X, (b) *m*X and *o*X, (c) *m*X and *p*X and (d) 4-component C_8 mixture (1:1:1:1).

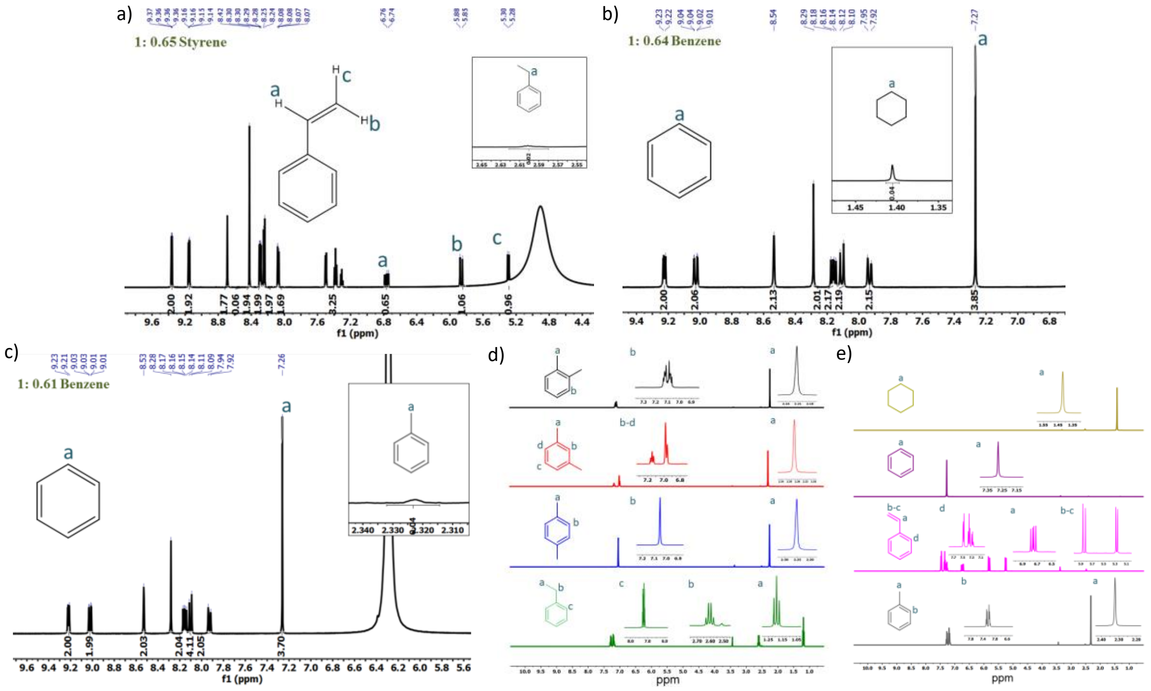

Figure 5: ^{1}H-NMR spectrum of the digested adsorbent (**1a**) after from the batch experiment carried out for 1:1 mixture of (a) St and Eb, (b) Benz and cyHex, (c) Benz and Tol, and only guest isomers (d) *o*X, *m*X, *p*X, EB, (e) cycHex, Benz, St and Tol, respectively.

Fractions of the eluent are collected in a different time interval and analyzed by gas chromatography experiment to realize ~ 10 min of breakthrough-time for *m*X. The other isomers are immediately excluded by **1a**, supporting the exclusive selectivity towards *m*X. This experimental finding established the separation capability of **1a** in a multicomponent mixture of C_8 isomers. To establish the selectivity preferences quantitatively, selectivity tests using a 4-component C_8 mixture (1:1:1:1) and 2-component mixtures of *o*X/*m*X, and *o*X/*p*X and *m*X/*p*X (experimental set-up; Figure 3b) were carried out. Such selectivity study is not possible in a fixed-bed column, as in this process only the most kinetically selective isomer is adsorbed in the column. Whereas in the batch experiment, adsorption process is equilibrated by thermodynamic preferences. Hence, the batch experiments by utilizing ^{1}H-NMR as a characterization tool the amounts of adsorbed isomers by **1a** could be determined quantitatively (Figure 4). The results revealed that **1a** preferentially adsorbs *m*X; ~ 0.92/formula from the 4-component mixture, and from *o*X/*m*X and *m*X/*p*X binary mixtures. By comparing the integral peak area in ^{1}H-NMR, the calculated selectivity towards *m*X in the 4-component mixture was found to be $S_{mX/(oX+pX+Eb)} = 71.4\pm2.8$, and in the case of 2-component mixtures $S_{mX/oX} = 78.5\pm3.6$; $S_{mX/pX} = 60.1\pm3.4$. Among the *p*X and *o*X, **1a** selectively adsorbed *p*X ($S_{pX/oX} = 64.6\pm3.7$; 0.84 *p*X/formula). This confirms a selectivity order of *m*X>*p*X>*o*X, which is the same as observed in the vapor diffusion kinetics measurement.

Quantitative estimation by ^{1}H-NMR, similar to the case of xylenes, revealed that **1a** selectively adsorbs 0.64 St/formula over Eb and 0.64 Benz/formula over cyHex from their binary (1:1) mixtures (Figure 5b-c). The estimated selectivities are $S_{St/Eb} = 63\pm2.7$ and $S_{Benz/cyHex} = 192.5\pm8.6$. In the case of Benz/Tol, although the total uptake amounts are nearly the same, low-pressure uptake of Benz vapor is steeper than Tol vapor. This difference made a substantial impact, as **1a** selectively adsorbed 0.61 Benz/formula over Tol from a binary (1:1) mixture with a selectivity of $S_{Benz/Tol} = 46.2\pm1.8$ (Figure 5). This result, in the same line with xylene selectivities, again stressing the fact that **1a** recognizes the isomers, using its adaptable and dynamic chemical clipping process. A summary of the estimated isomer selectivities is listed in Figure 2g. Following the experimental evidence, as pursued to elucidate the determining factors of the intriguing selectivity. Note that (i) for St/Eb separation, incompatibility of the bulky aliphatic ethyl-group in Eb with the "dynamic clip" is the primary factor; (ii) for Benz/Tol

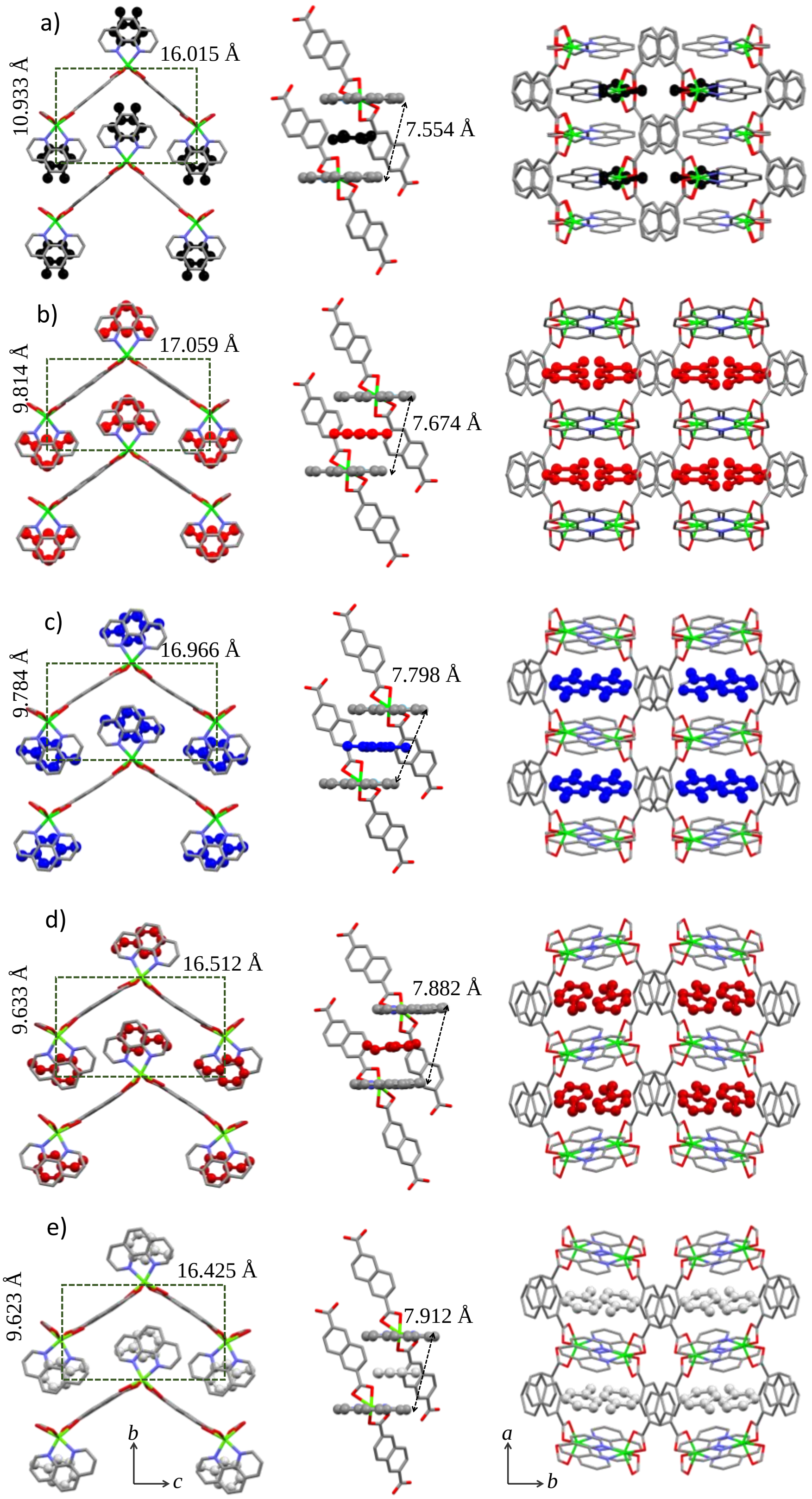

Figure 6: Spatial geometries of the encapsulated (a-e) xylenes, styrene and toluene; left to right: view along *a*-axis showing methyl-group orientations, view of the "dynamic chemical space" with inter-*o*-phen distances, view along *c*-axis showing the 1D channel view occupied by the adsorbates.

Table 3: Crystal structure refinement parameters of encapsulated ortho-xylene, para-xylene, meta-xylene and styrene.

Empirical formula	$C_{32}H_{24}ZnN_2O_4$ (*o*X@1)	$C_{32}H_{24}ZnN_2O_4$ (*m*X@1)	$C_{32}H_{24}ZnN_2O_4$ (*p*X@1)	$C_{32}H_{22}ZnN_2O_4$ (St@1)
M_r	1130.84	565.92	565.92	563.91
crystal System	Orthorhombic	Monoclinic	Monoclinic	Monoclinic
space group	*Pbcn* (No. 60)	*P*2/c (No. 7)	$P2_1/c$ (No. 14)	$P2_1/c$ (No. 14)
a (Å)	7.554(5)	7.674(3)	7.798(5)	7.8816(7)
b (Å)	21.865(5)	9.814(5)	19.568(5)	19.2650(16)
c (Å)	16.015(4)	17.059(5)	16.966(5)	16.5121(14)
α (deg)	90	90	90	90
β (deg)	90	90.727(5)	90.805(5)	92.489
γ (deg)	90	90	90	90
V (Å^3)	2645(14)	1284.7(9)	2588.6(19)	2504.8(40)
Z	2	2	4	4
T (K)	293	100	293	273
D_c (g cm^{-3})	1.420	1.463	1.452	1.498
μ (mm^{-1})	0.969	0.999	0.991	1.024
F(000)	1166	586	1168	1164
θ_{max} (deg)	28.292	28.366	28.0	25.0
λ (Mo Kα)(Å)	0.71073	0.71073	0.71073	0.71073
tot. data	37191	20686	39250	63942
unique data, R_{int}	3281, 0.058	3218, 0.042	5877, 0.089	4403, 0.172
data [$I > 2\sigma(I)$]	2248	2482	2780	3188
R^a,	0.0486	0.0353	0.0436	0.0925
R_w^b	0.1664	0.1059	0.924	0.2760
GOF	1.062	1.005	0.845	1.25

$^aR = \Sigma||Fo| - |Fc||/\Sigma|Fo|$. $^bR_w = [\Sigma w(Fo^2 - Fc^2)^2/ \Sigma w(Fo^2)^2]^{1/2}$

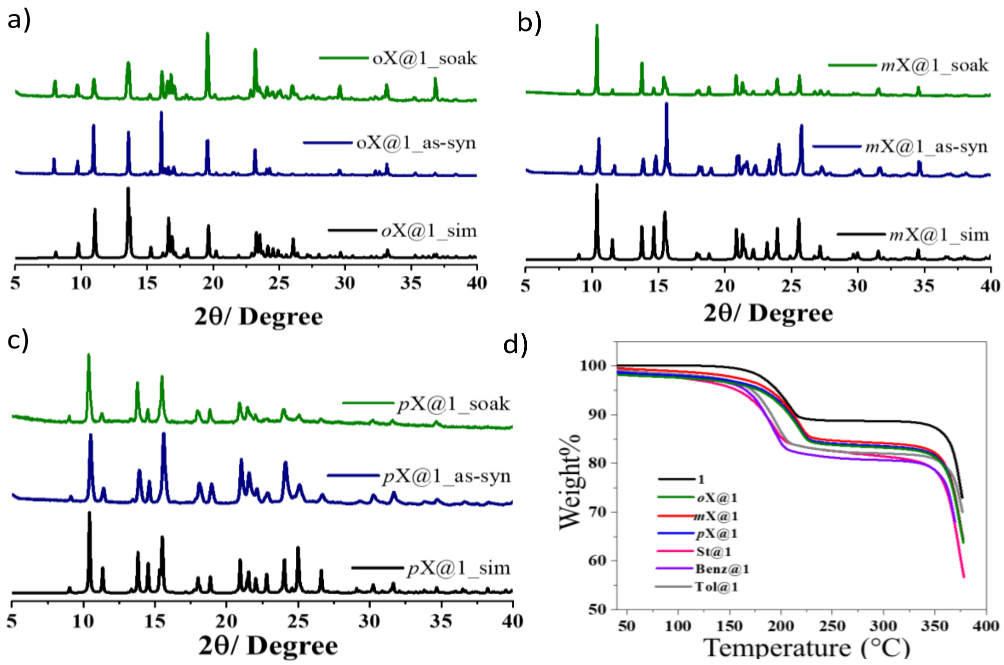

Figure 7: PXRD pattern of solvent soaking experiment exposing to (a) *ortho*-xylene (b) *meta*-xylene (c) *para*-xylene and compared with as-synthesized and simulated pattern. (d) Thermogravimetry profiles of the different guest (*o*X, *m*X, *p*X, Tol and St) encapsulated PCP.

separation, the smaller size of Benz compared Tol kinetically favored Benz (steeper vapor uptake at low pressure, Figure 2f); and iii) for Benz/cyHex separation, aromatic molecule preference of the dynamic space excludes cyHex. But for the xylenes, selectivity order is astonishing.

3.3.4.4: Guest encapsulated single-crystal structural analysis

To comprehend this, the xylenes, St and Tol[14] encapsulated PCPs as single crystals were synthesized and examined their crystal structure (Figure 6). To obtain single crystals, an in-situ reaction methodology has been adopted as described in the experimental section. The details of crystallographic parameters are listed in Table 3. Eb and cyHex encapsulated 1 crystal could not be obtained, confirming the adsorption experiment results (Benz encapsulated crystals were not of good quality, for structure determination, thermogravimetric analysis shown in Figure 7d). The xylene encapsulated frameworks (*o*X@1, *m*X@1 and *p*X@1) crystallized in primitive crystal system with different space groups (Table 3, Figure 7a-c XRD patterns). Xylenes occupied the dynamic nanospace between the *o*-phen groups from neighboring 1D chains (Figure 6a-c); i.e., just replacing

DMF from 1, as shown in Figure 1a. St and Tol encapsulation also exhibited similar crystal system and spatial position (Figure 6d-e). Note that to accommodate the guests, *o*-phen groups become parallel to each other, possibly to enhance π-π interaction (compare Figure 1a and 6). A careful look revealed that the spatial arrangements are distinctive for each isomer. Important parameters are: i) *o*-phen-guest π-π distances, and ii) methyl group orientations. To understand these differences, the chemical space position made simplified by drawing two parallel planes along *b* and *c*-axes, and thus the rectangular area (marked by the dotted line) formed houses the xylene isomer in the *ab*-plane (Figure 6a-c left). The distances between *o*-phen-*o*-phen along the *a*-axis are shown in Figure 3a-c middle. Comparisons of these dimensions revealed the order of space requirements for each isomer. Along the *a*-axis, *o*X<*m*X<*p*X, and along the *ab*-plane *p*X<*m*X<*o*X. According to the vapor adsorption profiles, *m*X interacts with the host structure strongest with lowest structure transition pressure of ~ 34 Pa. Hence, the host structure of **1a** quickly adopts the required space for mX (1284.758 Å^3). This is the lowest volume requirement, in comparison to the *o*X (1322.645 Å^3) and *p*X (1294.432 Å^3). Hence, the surprising preferential adsorption of *m*X and nearly complete rejection of other C_8-isomers from a mixture of the isomers is very evident.

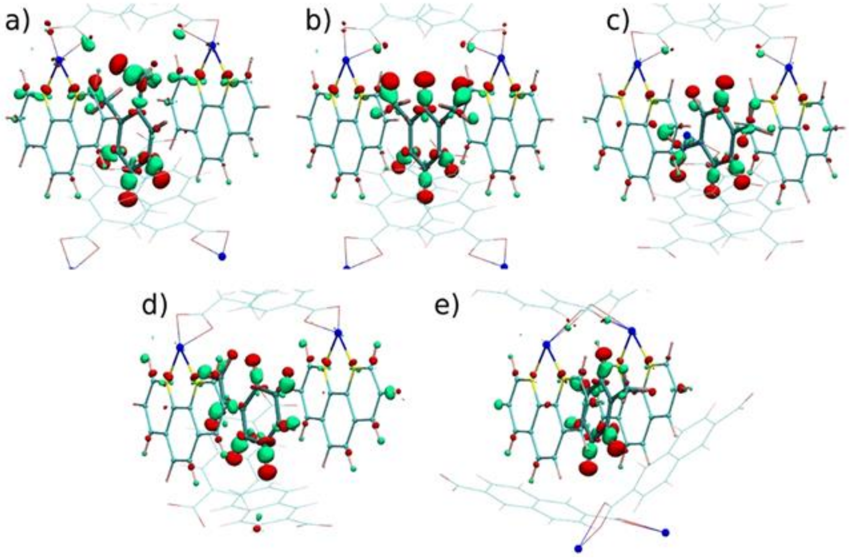

Figure 8: Electron density difference maps of the adsorbate encapsulated PCPs: a-c) *o*X, *m*X and *p*X, respectively, d) St, and e) Tol; Red and Green surfaces correspond to loss and gain in electron density, respectively. Both surfaces represent a magnitude of 1.58×10^{-3} e/Å^3 change. Pink, Cyan, Yellow, Red and Blue beads indicate Hydrogen, Carbon, Nitrogen, Oxygen, and Zinc atoms, respectively. Adsorbate molecules are shown in a darker shade.

3.3.4.5: Computational studies; binding insight in molecular level

The impact of different methyl group orientation is a determining factor to the binding energy and selectivity. Hence, to estimate the binding energies periodic density functional theory (DFT) calculations were carried out (see computational details in the supporting information). Among the xylenes, higher binding energy favored *m*X (146.1 kJ/mol) over *p*X (139.7 kJ/mol) or *o*X (123.6 kJ/mol) (Table 4). This difference is attributed to the additional C-H⋯π interaction between *m*X and the host framework. The

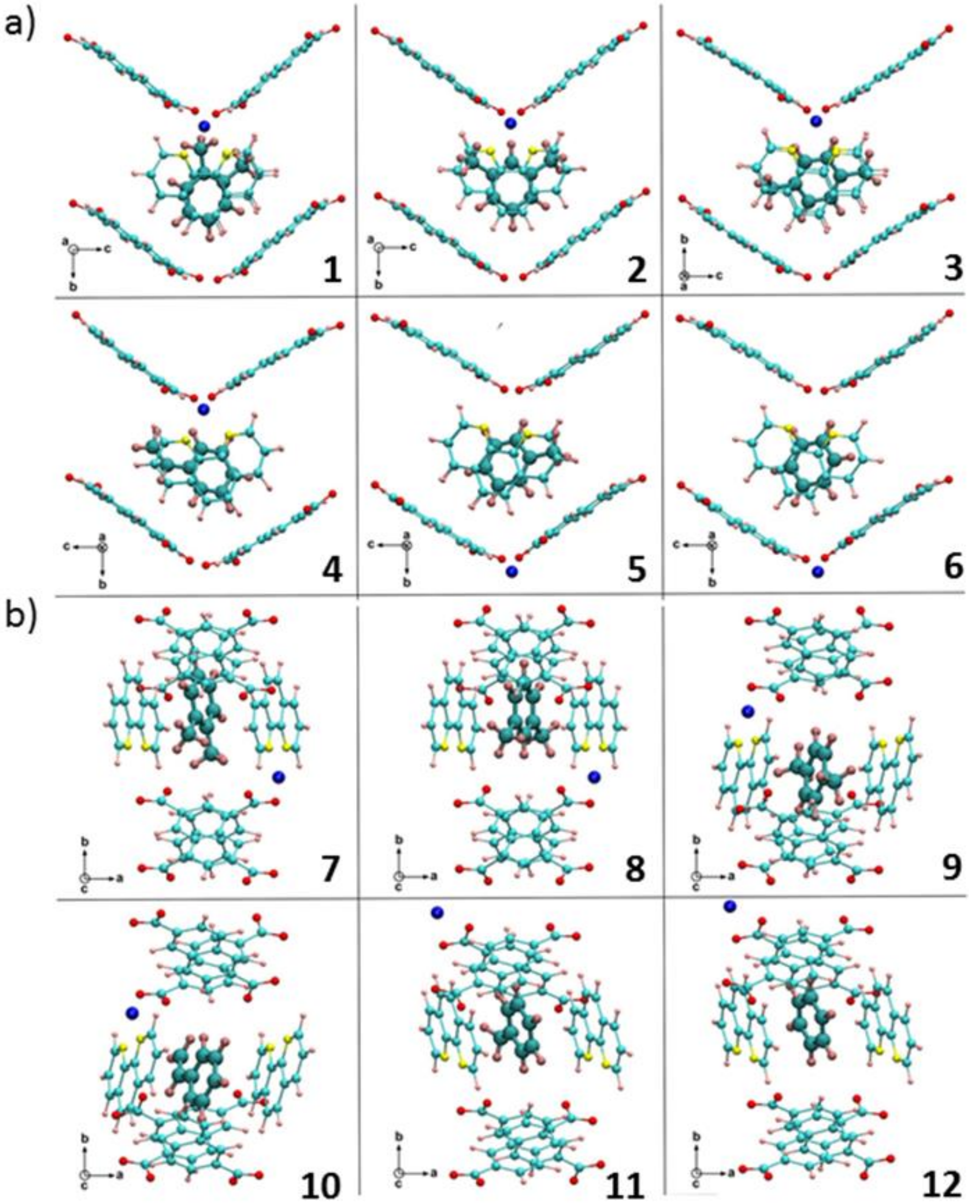

Figure 9: Showing the position of *ortho*-xylene (1, 7), *meta*-xylene (2, 8), *para*-xylene (3, 9), styrene (4, 10), toluene (5, 11) and benzene (6, 12). (a) Top view, (b) side view.

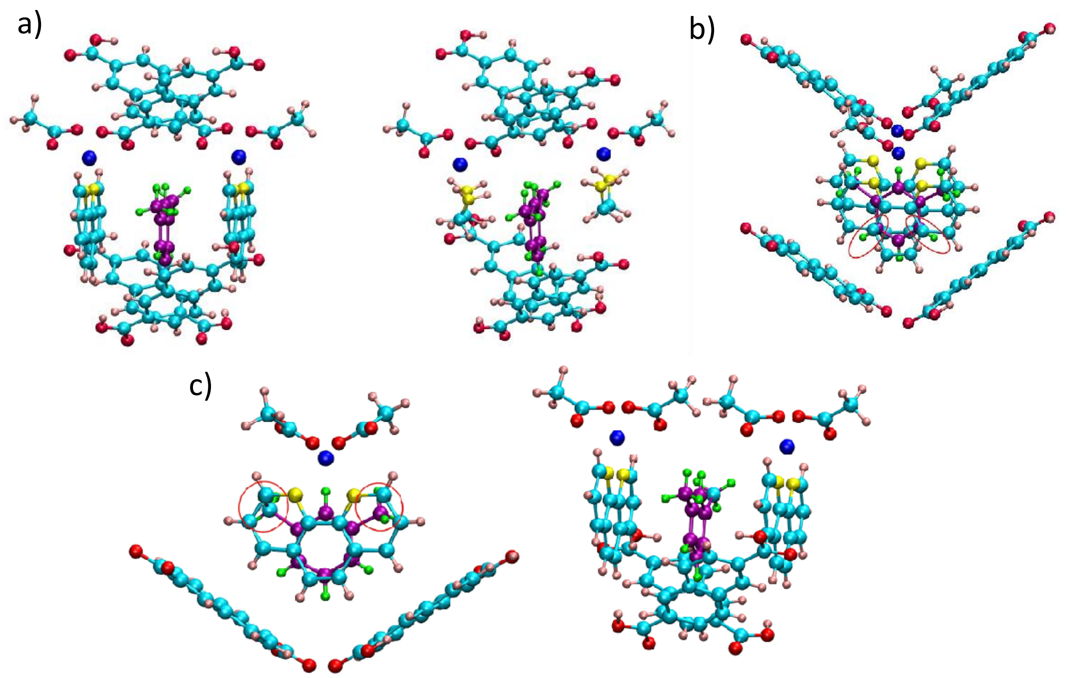

Figure 10: Fragments used in masked calculations: (a) Identifying contributions from π⋯π and methyl C-H⋯π interactions (i) original complete fragment (same as that seen in Figure 8). Two π systems of the framework can be seen on either side of the central *m*-xylene (ii) the two π systems discussed in (i) are changed to $H_2N-CH_2-CH_2-NH_2$. In this process, the π⋯π interactions between these two π systems and *m*X is removed. Further, the interaction between the methyl C-H and the π systems is also removed; (b) Interaction between the aromatic C-H of *m*X with the framework π systems. The former, oriented towards the latter are circled. The contribution of this interaction to the stabilization energy is obtained by masking out the two π systems of the framework that are shown below *m*X on its left and right; (c) Contribution from methyl C-H of xylene and π system of framework. Two orientations are shown. In (i), the specific methyl C-H bonds which are oriented towards these π systems are circled, in (ii), the π systems on top of the xylene are changed to acetate which coordinates the zinc atom.

methyl groups in *m*X are oriented in such a manner as to enable C-H (of the methyl) to interact with the π-cloud of 2,6-ndc in the framework. The revealed primary interactions for the xylene encapsulated frameworks are following and illustrated in Figure 8 and 9: i) π-π interaction between the phenyl ring of the xylenes with *o*-phen linker of the framework, ii) C-H⋯π interactions are as follows: (a) in *o*X, between aromatic C-H and 2,6-ndc, (b) in *m*X, between aromatic C-H and 2,6-ndc as well as between methyl C-H and 2,6-ndc, (c) In *p*X, none. iii) H-bonding interaction between aromatic C-H of *o*X/*p*X and carboxylate oxygen of 2,6-ndc; in the case of *m*X, the H-bond is present between methyl C-H and carboxylate oxygen of 2,6-ndc. To identify the specific interactions, selected regions of the host framework was identified, which are proximal to the adsorbed xylenes

Table 4: Comparison of cell parameters determined experimentally and by cell optimization for PCP encapsulating different guests and the corresponding binding energies (BE) per guest molecule.

isomer@**1**			a (Å)	b (Å)	c (Å)	α (°)	β (°)	γ (°)	Volume Error (%)	BE (kJ/mol)
oX@**1**		Expt.	15.35	19.63	17.06	90.0	90.7	90.0	0.66	-123.6
		Theory	15.30	19.85	17.04	90.5	91.1	90.0		
mX@**1**		Expt.	15.35	19.63	17.06	90.0	90.7	90.0	-0.55	-146.1
		Theory	15.30	19.62	17.03	90.0	90.7	90.0		
pX@**1**		Expt.	15.60	19.57	16.97	90.0	90.8	90.0	-0.82	-139.7
		Theory	15.54	19.60	16.87	89.9	91.0	90.0		
St@**1**		Expt.	15.76	19.27	16.51	90.0	92.5	90.0	-0.70	-131.3
		Theory	15.70	19.21	16.51	90.0	92.6	90.0		
Tol@**1**		Expt.	15.83	19.25	16.43	90.0	93.0	90.0	-0.18	-125.1
		Theory	15.82	19.24	16.42	89.9	93.1	90.0		
Benz@**1**		Expt.	15.83	19.25	16.43	90.0	93.0	90.0	-0.18	-104.0
		Theory	15.82	19.24	16.42	89.9	93.1	90.0		

Table 5: Energy contributions obtained from the masked calculations in the gas phase.

Xylene Isomers	Energy contribution from interaction (a) (kJ/mol)	Energy contribution from interaction (b) (kJ/mol)	Energy contribution from interaction (c) (kJ/mol)
meta-xylene	-66.872	-24.402	-4.109
para-xylene	-25.098	-27.424	-4.375
ortho-xylene	-3.893	-3.741	-12.672

and terminated it sensibly with hydrogen atoms. Calculations were carried out in the gas phase, at M06/6-31g(d,p) level of theory which treats non-covalent interactions well. Single point energies were calculated for i) isolated xylenes, ii) framework fragments and for iii) xylenes interacting with the selected fragments to yield binding energies (Figure 10). The strongest interaction was realized for *m*X, confirming the results obtained from periodic PBE-D3 calculations. The trend in binding energies can be explained as follows: for *m*X, the aromatic C-H is oriented towards the centroid of the π system of 2,6-ndc, whereas for *p*X and *o*X, it is absent (Figure 10, Table 5). For the St and Tol, the calculated binding energies were 131.3 and 125.1 kJ/mol. The specific interactions and electron density difference maps are shown in Figures 8 and 9. The binding energy of Benz encapsulated structure (by manually placing Benz in the void space and subsequent geometry optimization) has been also calculated and found that Benz:host interaction (104 kJ/mol) is weaker than Tol:host. This additional stability gained by Tol can be attributed to a C-H-π interaction between CH_3 of Tol and 2,6-ndc aromatic π-surface. However, this is contradictory to the experimental observation (Figure 2b). In this case, the thermodynamic stability (binding energy) is overcome by the kinetic factor (smaller size of Benz compared to Tol), as observed in the vapor adsorption profiles (Figure 2b, d).

3.3.4.6: Computational studies: corresponding mixture adsorption and selectivity

All the adsorption isotherms in **1a** have concave upward at low pressure (S-shape), which shows either weak vapor-framework affinity or presence of flexibility in the framework. Here, high vapor-framework binding energy of more than 100 kJ/mol (Table 4) was observed. This indicates that S-shape of adsorption isotherms is due to guest-induced flexibility in the PCP. In presence of flexibility, theoretical estimation of mixture adsorption selectivity, for a dynamic chemical space presented here, is not suitable using ideal adsorbed solution theory (IAST).[33] Therefore, osmotic framework adsorbed solution theory[30, 34] (OFAST) has been utilized to determine mixture adsorption isotherms and selectivity in **1a**. The OFAST method considers the thermodynamics of

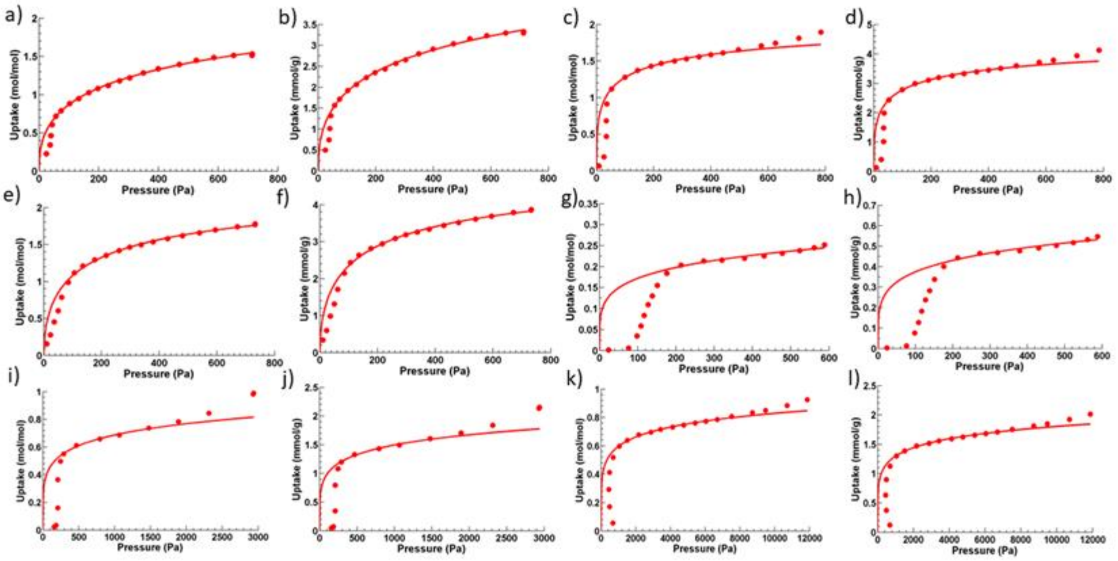

Figure 11: Fitting (line) of Langmuir adsorption isotherm to the experimental data (circle) of *o*X (a, b), *m*X (c, d), *p*X (e, f), St (g, h), Tol (I, j) and Benz (k, l) in the open state of **1a**. Uptake quantity is presented in mol/mol and mmol/g unit, respectively. For xylenes, good fittings were obtained below 500 Pa.

structural variations in nanoporous materials due to adsorbate-adsorbent interaction. Using OFAST, the estimated free energy change (ΔF)[31] is to be found of **1a** upon adsorption of various adsorbates varies in the range of 2-8 kJ/mol, and the energy order followed the experimental observations (Table 5). The calculated single, bi-and tri-component xylene mixture adsorption isotherms are shown in Figures 11-13. Particularly for the equimolar mixture of *m*X:*p*X:*o*X, the selectivity[15b] order is of *m*X>*p*X>*o*X ($S_{mX/pX}$ ~ 8, $S_{mX/oX}$ ~ 5.8 and $S_{pX/oX}$ ~ 1.5), which is in accordance with the experimental vapor diffusion kinetics (Figure 12-14). These estimated selectivity values, together with experimental separation and structure elucidation unequivocally establish the working principle of the dynamic chemical space in the coordination polymer.

Table 5: Saturation vapor pressure (P_0), guest induced transition pressure (P_{Trans}) for structural transition of **1a** from closed to open phase, fitted Langmuir-Freundlich isotherm model parameters (n_s, b, and t), and change in Helmholtz free energy (ΔF) of the guest encapsulated PCP.

	Guest	P_0 (kPa)	P_{Trans} (Pa)	n_s (mol/mol)	b (Pa^{-t})	t	ΔF (kJ/mol)
1	Benzene	12.601	468	2.0446	0.0903	0.2196	6.895

3	Toluene	2.92	207	2.3107	0.0821	0.2373	6.163
4	Styrene	0.65	113	1.5147	0.0444	0.2301	2.017
5	*m*Xylene	0.833	34	2.3707	0.1808	0.4042	8.169
6	*p*Xylene	0.7866	45	2.533	0.0557	0.5622	4.327
7	*o*Xylene	0.7666	39	3.5637	0.0425	0.4405	3.861

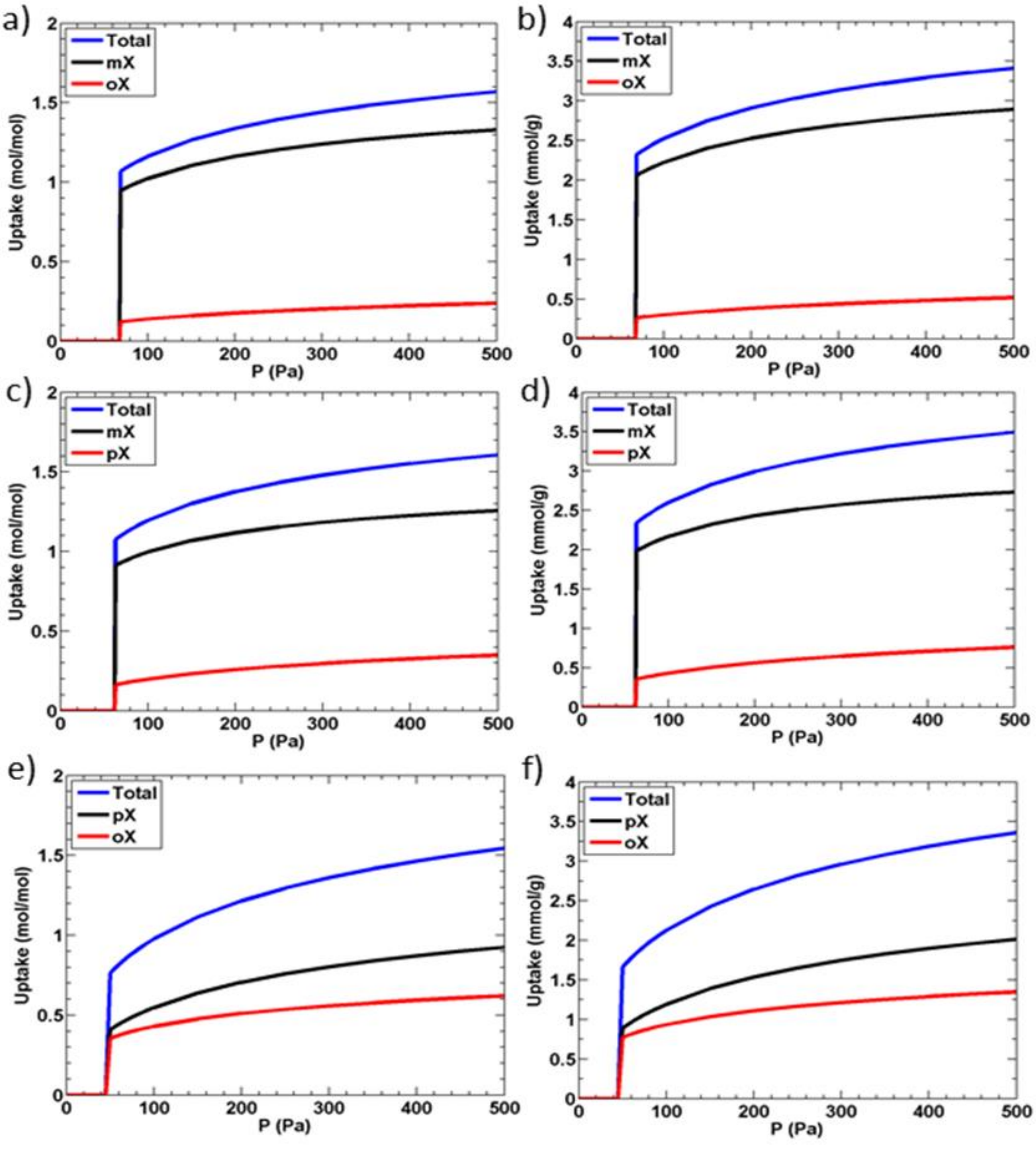

Figure 12: Calculated mixture adsorption isotherms (using OFAST) for equimolar mixture of (a, b) *m*X:oX, (c, d) *m*X:pX, and (e, f) *p*X:*o*X in mol/mol and mmol/g unit (left and right, respectively).

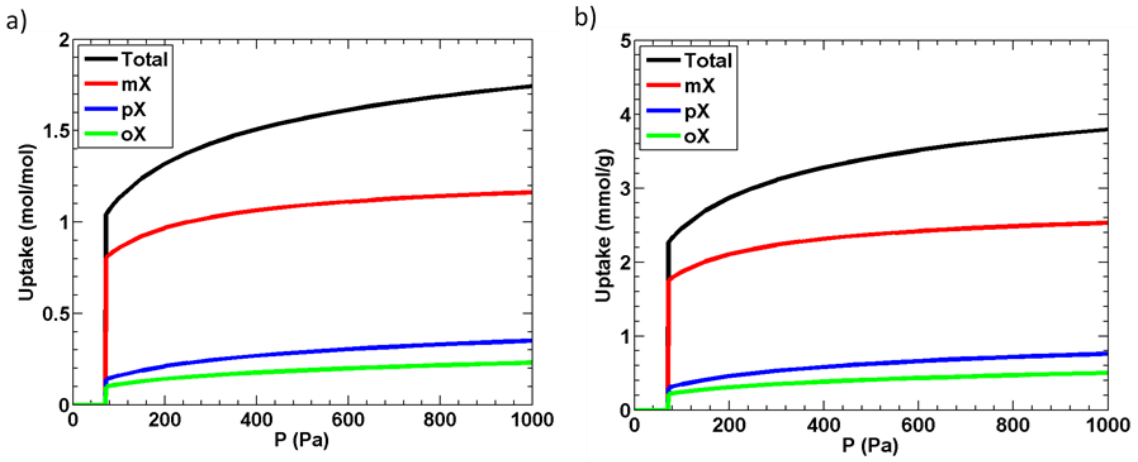

Figure 13: Calculated mixture adsorption isotherms (using OFAST) for equimolar mixture of equimolar ternary mixture of *m*X:*p*X:*o*X in mol/mol and mmol/g unit (left and right, respectively).

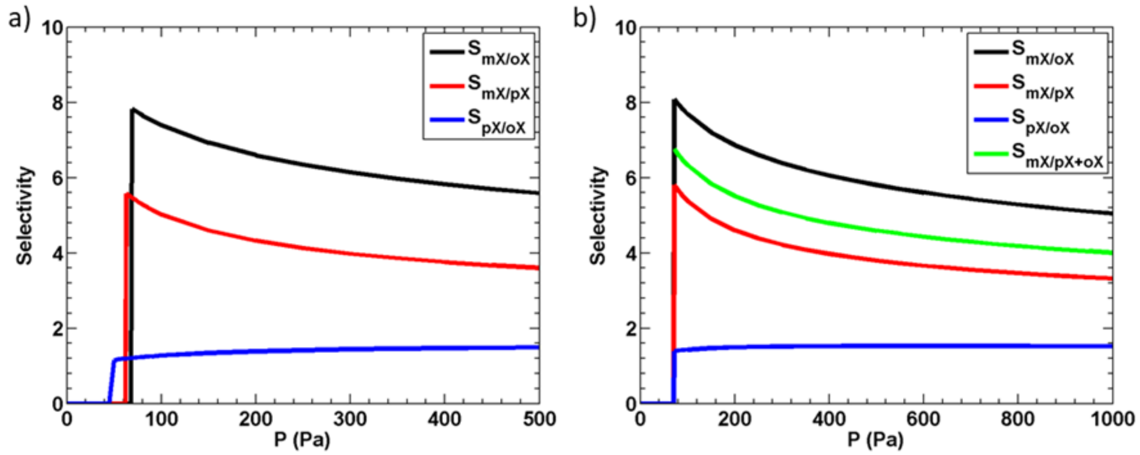

Figure 14: Mixture adsorption selectivity (S_{ab}) of **1a** calculated using OFAST for equimolar (a) binary and (b) ternary mixture of the xylene isomers. S_{ab} was calculated as, $S_{ab} = \left(\frac{x_a}{y_a}\right)\left(\frac{x_b}{y_b}\right)^{-1}$, where x_a and y_a are the mole fraction of the component a in the adsorbed and gas phase, respectively.

3.3.5: Conclusion

In conclusion, this chapter unfolds a dynamic chemical clipping in a supramolecular framework. This process can separate the individual chemical isomers from their mixture in liquid-phase. The chapter further demonstrates the success of such material design approach by realizing highly selective separation of BTEX chemical isomers, which are considered among the “seven chemical separations to change the world”.[2] The unveiled dynamic porous structure exhibited remarkably high meta-xylene selectivity and could efficiently sort out C_8 isomers in liquid-phase. A combinatorial approach of i) experimental separation efficiency estimation by breakthrough column and the batch in the liquid-phase, ii) crystallographic insight of adsorption site and iii) theoretical estimation of specific host-guest interaction energy has revealed the separation capability of the adsorbent. The present findings emphasize the significance of dynamic host-guest interaction, rather than having a fixed, rigid porous structure for achieving remarkable selectivity and separation performance. The new material design concept of the type presented here renders a step forward towards “new generation chemical adsorbent” for energy-efficient separation technology.

3.3.6: References

[1] a) Materials for Separation Technologies: Energy and Emission Reduction Opportunities **2005**; b) Bandwidth Study on Energy Use and Potential Energy Saving Opportunities in U.S. Petroleum Refining **2015**.
[2] D. S. Sholl and R. P. Lively, *Nature* **2016**, *533*, 316-316.
[3] a) H. Wang, X. Dong, V. Colombo, Q. Wang, Y. Liu, W. Liu, X.-L. Wang, X.-Y. Huang, D. M. Proserpio, A. Sironi, Y. Han and J. Li, *Adv. Mat.* **2018**, *30*, 1805088; b) Z. Song, Y. Huang, W. L. Xu, L. Wang, Y. Bao, S. Li and M. Yu, *Sci. Rep.* **2015**, *5*, 13981; c) J.-R. Li, R. J. Kuppler and H.-C. Zhou, *Chem. Soc. Rev.* **2009**, *38*, 1477-1504.
[4] Y. Yang, P. Bai and X. Guo, *Ind. Eng. Chem. Res.* **2017**, *56*, 14725-14753.
[5] a) H. Furukawa, K. E. Cordova, M. O’Keeffe and O. M. Yaghi, *Science* **2013**, *341*, 1230444; b) S. Kitagawa, R. Kitaura and S.-i. Noro, *Angew. Chem. Int. Ed.* **2004**, *43*, 2334-2375; c) M. L. Foo, R. Matsuda and S. Kitagawa, *Chem. Mater.* **2014**, *26*, 310-322.
[6] O. K. Farha, I. Eryazici, N. C. Jeong, B. G. Hauser, C. E. Wilmer, A. A. Sarjeant, R. Q. Snurr, S. T. Nguyen, A. Ö. Yazaydın and J. T. Hupp, *J. Am. Chem. Soc.* **2012**, *134*, 15016-15021.
[7] a) H. Deng, S. Grunder, K. E. Cordova, C. Valente, H. Furukawa, M. Hmadeh, F. Gándara, A. C. Whalley, Z. Liu, S. Asahina, H. Kazumori, M. O’Keeffe, O. Terasaki, J. F. Stoddart and O. M. Yaghi, *Science* **2012**, *336*, 1018-1023; b) R. Banerjee, H. Furukawa, D. Britt, C. Knobler, M. O’Keeffe and O. M. Yaghi, *J. Am. Chem. Soc.* **2009**, *131*, 3875-3877.
[8] O. M. Yaghi, M. O'Keeffe, N. W. Ockwig, H. K. Chae, M. Eddaoudi and J. Kim, *Nature* **2003**, *423*, 705-714.
[9] H. Deng, C. J. Doonan, H. Furukawa, R. B. Ferreira, J. Towne, C. B. Knobler, B. Wang and O. M. Yaghi, *Science* **2010**, *327*, 846-850.
[10] a) X. Zhao, Y. Wang, D.-S. Li, X. Bu and P. Feng, *Adv. Mat.* **2018**, *30*, 1705189; b) B. Van de Voorde, B. Bueken, J. Denayer and D. De Vos, *Chem. Soc. Rev.* **2014**, *43*, 5766-5788; c) R.-B. Lin, S. Xiang, H. Xing, W. Zhou and B. Chen, *Coord. Chem. Rev.* **2019**, *378*, 87-103; d) D.-D. Zhou, P. Chen, C. Wang, S.-S. Wang, Y. Du, H. Yan, Z.-M. Ye, C.-T. He, R.-K. Huang, Z.-W. Mo, N.-Y. Huang and J.-P. Zhang, *Nat. Mater.* **2019**, *18*, 994-998.
[11] a) S. Horike, S. Shimomura and S. Kitagawa, *Nat. Chem.* **2009**, *1*, 695-704; b) A. Schneemann, V. Bon, I. Schwedler, I. Senkovska, S. Kaskel and R. A. Fischer, *Chem. Soc. Rev.* **2014**, *43*, 6062-6096; c) I. Beurroies, M. Boulhout, P. L. Llewellyn, B. Kuchta, G. Férey, C. Serre and R. Denoyel, *Angew. Chem. Int. Ed.* **2010**, *49*, 7526-7529; d) T. K. Maji, R. Matsuda and S. Kitagawa, *Nat. Mater.* **2007**, *6*, 142-148; e) J. D. Evans, V. Bon, I. Senkovska,

H.-C. Lee and S. Kaskel, *Nat.Commun.* **2020**, *11*, 2690; f) S. Krause, N. Hosono and S. Kitagawa, *Angew. Chem. Int. Ed.* **2020**, *59*, 15325-15341.

[12] a) P. Kanoo, R. Haldar, S. K. Reddy, A. Hazra, S. Bonakala, R. Matsuda, S. Kitagawa, S. Balasubramanian and T. K. Maji, *Chem.–Euro. J.* **2016**, *22*, 15864-15873; b) P. Kanoo, R. Haldar, P. Sutar, A. Chakraborty and T. K. Maji in *Gated and Stepwise Sorption Processes in Functional Metal-organic Frameworks*, The Royal Society of Chemistry, **2017**, pp. 412-453; c) L. Li, R.-B. Lin, R. Krishna, X. Wang, B. Li, H. Wu, J. Li, W. Zhou and B. Chen, *J. Am. Chem. Soc.* **2017**, *139*, 7733-7736; d) P. A. P. Mendes, P. Horcajada, S. Rives, H. Ren, A. E. Rodrigues, T. Devic, E. Magnier, P. Trens, H. Jobic, J. Ollivier, G. Maurin, C. Serre and J. A. C. Silva, *Adv. Funct. Mater.* **2014**, *24*, 7666-7673.

[13] J. P. Garcia Villaluenga and A. Tabe-Mohammadi, *J. Membr. Sci.* **2000**, *169*, 159-174.

[14] R. Haldar, R. Matsuda, S. Kitagawa, S. J. George and T. K. Maji, *Angew. Chem. Int. Ed.* **2014**, *53*, 11772-11777.

[15] a) J. E. Warren, C. G. Perkins, K. E. Jelfs, P. Boldrin, P. A. Chater, G. J. Miller, T. D. Manning, M. E. Briggs, K. C. Stylianou, J. B. Claridge and M. J. Rosseinsky, *Angew. Chem. Int. Ed.* **2014**, *53*, 4592-4596; b) M. I. Gonzalez, M. T. Kapelewski, E. D. Bloch, P. J. Milner, D. A. Reed, M. R. Hudson, J. A. Mason, G. Barin, C. M. Brown and J. R. Long, *J. Am. Chem. Soc.* **2018**, *140*, 3412-3422; c) R. El Osta, A. Carlin-Sinclair, N. Guillou, R. I. Walton, F. Vermoortele, M. Maes, D. de Vos and F. Millange, *Chem. Mater.* **2012**, *24*, 2781-2791; d) M. Zaworotko, N. Kumar, Z. Chang, M.-H. Yu, A. Kumar, D. O'Nolan, X.-H. Bu, E. Patyk-Kaźmierczak, A. A. Bezrukov, S. Mukherjee and S.-Q. Wang, *Chem. Sci.* **2020**; e) A. S. Münch and F. O. R. L. Mertens, *J. Mater. Chem. A* **2012**, *22*, 10228-10234; f) A. Ahmed, M. Forster, R. Clowes, D. Bradshaw, P. Myers and H. Zhang, *J. Mater. Chem. A* **2013**, *1*, 3276-3286; g) B. Saccoccia, A. M. Bohnsack, N. W. Waggoner, K. H. Cho, J. S. Lee, D.-Y. Hong, V. M. Lynch, J.-S. Chang and S. M. Humphrey, *Angew. Chem. Int. Ed.* **2015**, *54*, 5394-5398; h) V. Finsy, H. Verelst, L. Alaerts, D. De Vos, P. A. Jacobs, G. V. Baron and J. F. M. Denayer, *J. Am. Chem. Soc.* **2008**, *130*, 7110-7118; i) B. Barton, E. C. Hosten and P. L. Pohl, *Tetrahedron* **2016**, *72*, 8099-8105; j) T. C. T. Pham, H. S. Kim and K. B. Yoon, *Science* **2011**, *334*, 1533-1538; k) D.-Y. Koh, B. A. McCool, H. W. Deckman and R. P. Lively, *Science* **2016**, *353*, 804-807; l) C.-T. He, L. Jiang, Z.-M. Ye, R. Krishna, Z.-S. Zhong, P.-Q. Liao, J. Xu, G. Ouyang, J.-P. Zhang and X.-M. Chen, *J. Am. Chem. Soc.* **2015**, *137*, 7217-7223; m) J. M. Holcroft, K. J. Hartlieb, P. Z. Moghadam, J. G. Bell, G. Barin, D. P. Ferris, E. D. Bloch, M. M. Algaradah, M. S. Nassar, Y. Y. Botros, K. M. Thomas, J. R. Long, R. Q. Snurr and J. F. Stoddart, *J. Am. Chem. Soc.* **2015**, *137*, 5706-5719; n) M. Lusi and L. J. Barbour, *Angew. Chem. Int. Ed.* **2012**, *51*, 3928-3931; o) D. Peralta, G. Chaplais, A. Simon-Masseron, K. Barthelet, C. Chizallet, A.-A. Quoineaud and G. D. Pirngruber, *J. Am. Chem. Soc.* **2012**, *134*, 8115-8126; p) S. Mukherjee, B. Joarder, A. V. Desai, B. Manna, R. Krishna and S. K. Ghosh, *Inorg. Chem.* **2015**, *54*, 4403-4408; q) M. Maes, F. Vermoortele, L. Alaerts, S. Couck, C. E. A. Kirschhock, J. F. M. Denayer and D. E. De Vos, *J. Am. Chem. Soc.* **2010**, *132*, 15277-15285; r) K. Jie, M. Liu, Y. Zhou, M. A. Little, S. Bonakala, S. Y. Chong, A. Stephenson, L. Chen, F. Huang and A. I. Cooper, *J. Am. Chem. Soc.* **2017**, *139*, 2908-2911; s) Q.-K. Liu, J.-P. Ma and Y.-B. Dong, *Chem.-Euro. J.* **2009**, *15*, 10364-10368; t) B. Moosa, L. Alimi, A. Shkurenko, A. Fakim, P. Bhatt, G. Zhang, M. Eddaoudi and N. Khashab, *Angew. Chem. Int. Ed.* **2020**, 59, 21367– 21371; u) M. du Plessis, V. I. Nikolayenko and L. J. Barbour, *J. Am. Chem. Soc.* **2020**, *142*, 4529-4533.

[16] SMART (V 5.628), SAINT (V 6.45a), XPREP, SHELXTL; Bruker AXS Inc. Madison, Wisconsin, USA. **2004**.

[17] G. M. Sheldrick, Siemens Area Detector Absorption Correction Program, University of Götingen, Götingen, Germany. **1994**.

[18] A. Altomare, G. Cascarano, C. Giacovazzo and A. Guagliardi, *J. Appl. Crystallogr.* **1993**, *26*, 343-350.

[19] G. M. Sheldrick, SHELXL-97, Program for Crystal Structure Solution and Refinement; University of Götingen, Götingen, Germany. **1997**.

[20] A. Spek, *J. Appl. Crystallogr.* **2003**, *36*, 7-13.

[21] G. M. Sheldrick, SHELXS 97, Program for the Solution of Crystal Structure, University Götingen, Germany. **1997**.

[22] L. Barbour, *J. Appl. Crystallogr.* **2020**, *53*, 1141-1146.

[23] J. Hutter, M. Iannuzzi, F. Schiffmann and J. VandeVondele, *WIREs Comput. Mol. Sci.* **2014**, *4*, 15-25.

[24] B. G. Lippert, J. H. Parrinello and Michele, *Mol. Phys.* **1997**, *92*, 477-488.

[25] J. VandeVondele, M. Krack, F. Mohamed, M. Parrinello, T. Chassaing and J. Hutter, *Comput. Phys. Commun.* **2005**, *167*, 103-128.

[26] a) S. Goedecker, M. Teter and J. Hutter, *Phys. Rev. B* **1996**, *54*, 1703-1710; b) M. Krack, *Theor. Chem. Acc.* **2005**, *114*, 145-152; c) C. Hartwigsen, S. Goedecker and J. Hutter, *Phys. Rev. B* **1998**, *58*, 3641-3662.

[27] J. VandeVondele and J. Hutter, *J. Chem. Phys.* **2007**, *127*, 114105.

[28] a) S. Grimme, J. Antony, S. Ehrlich and H. Krieg, *J. Chem. Phys.* **2010**, *132*, 154104; b) S. Grimme, S. Ehrlich and L. Goerigk, *J. Comput. Chem.* **2011**, *32*, 1456-1465.

[29] F.-X. Coudert, M. Jeffroy, A. H. Fuchs, A. Boutin and C. Mellot-Draznieks, *J. Am. Chem. Soc.* **2008**, *130*, 14294-14302.

[30] G. Fraux, A. Boutin, A. H. Fuchs and F.-X. Coudert, *Adsorption* **2018**, *24*, 233-241.

[31] S. Couck, T. R. C. Van Assche, Y.-Y. Liu, G. V. Baron, P. Van Der Voort and J. F. M. Denayer, *Langmuir* **2015**, *31*, 5063-5070.

[32] a) D. Tanaka, A. Henke, K. Albrecht, M. Moeller, K. Nakagawa, S. Kitagawa and J. Groll, *Nat. Chem.* **2010**, *2*, 410-416; b) N. Sikdar, A. Hazra and T. K. Maji, *Inorg. Chem.* **2014**, *53*, 5993-6002; c) N. Sikdar, M. Bhogra, Umesh V. Waghmare and T. K. Maji, *J. Mater. Chem. A.* **2017**, *5*, 20959-20968.

[33] A. L. Myers and J. M. Prausnitz, *AIChE Journal* **1965**, *11*, 121-127.

[34] F.-X. Coudert, C. Mellot-Draznieks, A. H. Fuchs and A. Boutin, *J. Am. Chem. Soc.* **2009**, *131*, 11329-11331.

Chapter 4

Water-Energy Nexus: Storage, Harvesting and Dehumidification

4.1: Investigating Binary and Ternary MOF Nanocomposites for Adequate Multi-environment Indoor Water Harvesting

Manuscript under preparation

Abstract

Introducing atmospheric water generation (AWG), beyond the arid atmosphere, under comfortable indoor humidity and temperature regime has its urgency in terms of commercialization and to address demolishing worldwide fresh water crisis. This chapter reports synthesis and characterization of a series of binary (aminoclay and Cu-BTC) and ternary (aminoclay, graphene oxide and Cu-BTC) MOF nanocomposites and their water storage and harvesting properties from the indoor atmosphere. The nanocomposites show enhanced hydrothermal stability and 63.4% of utmost water harvesting efficiency by blending aminoclay and graphene-oxide with Cu-BTC MOF. The study further extrapolates the water collection dynamics by varying ambient humidity, release temperature and on-demand sorption/desorption cycle under the ordinary indoor condition without any solar irradiation. The composite enables 0.431 Lg^{-1} of water at 90% relative humidity with a maximum value of 0.445 Lg^{-1} indoor water collections per day.

4.1.1: Introduction

Today's world witnessed the struggle of more than 4.3 billion people (71% of the global population) for clean, ample and safe drinking water.[1] The terrestrial renewable fresh water supply depends on two major sources; airborne moisture and other fresh water resources.[2] The quantity of ground water, as well as surface water, drops abruptly with increasing population, industrialization, climate interpolation, vegetation and also based on soil characteristics in different geographic zones.[3] In search of alternative water sources, desalination and atmospheric water harvesting are found to be most promising.[4] Whereas desalination provides fresh drinking water at a relatively low-cost, it requires brackish water availability, skilled labor for operation, and support that drives down the implementing condition.[5] Conversely, extracting water from the atmosphere is much easier and accessible everywhere. As sorption-based water harvesting is guided mainly by water storage, extensive research has been dedicated in search of smart and efficient materials. The classical desiccants (e.g., $CaCl_2$, silica gel, alumina or zeolites) unfortunately offer high energy expenditure and low regeneration capacity.[6]

Metal-organic frameworks (MOFs) have been recently investigated for several water-related studies for their exceptional porosity, structural stability under moisture exposure within working pressure range and moderate regeneration temperature. These characteristics make them auspicious for practical applications such as adsorption heat pumps,[7] thermal batteries, desalination,[8] indoor humidity control, [9] dehumidification[10] and atmospheric water harvesting.[4, 11] To date, all reported MOF-based air-to-water production technologies are functional through typical interfacial solar (artificial/natural) heating with a passive dew water collector, making their implementation and water generation restricted by climatic constrain.[12] Such atmospheric MOF-based water harvesting can be categorized into two parallel groups. At one end, Zr/Al based water-stable MOFs (MOF-808, MOF-303) are utilized under arid regions facilitated by steep water uptake at low relative humidity (RH).[12b-e] The underlying idea for such water harvesting is to show the threshold level of water uptake along with the effective solar heat that stands for energy-efficient and inexpensive water harvesting technology at low-humid arid regions. On the other hand, highly

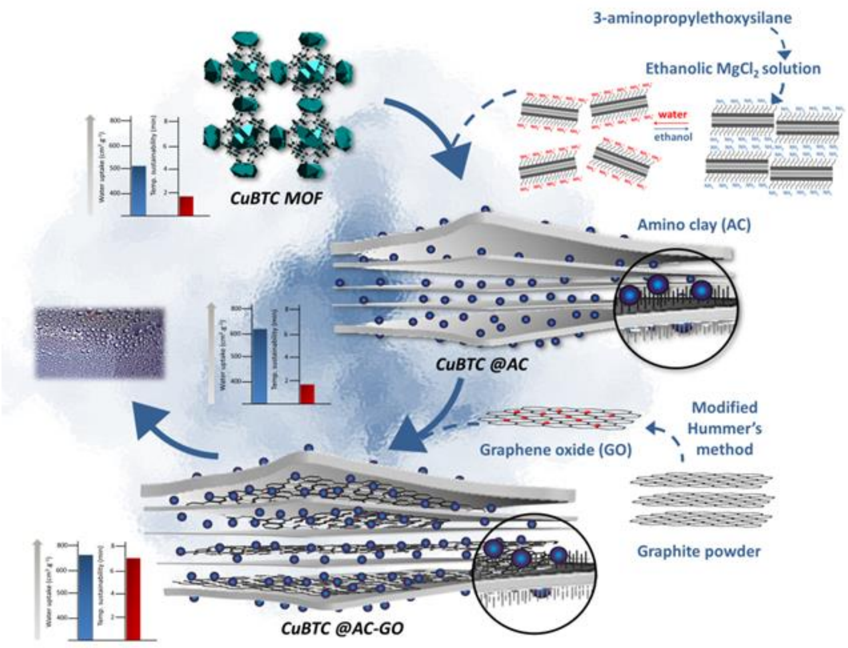

Scheme 1: Schematic illustration shows the stabilization of MOF nanoparticles on aminoclay (AC) and aminoclay-graphene (AC-GO) mixed matrix template. The bar diagram indicates thermal sustainability and water uptake capacity per gram of material.

efficient composites were designed by using crosslinked polymer (poly(N-isopropylacrylamide) or hygroscopic salt with mesoporous MIL-101(Cr) MOF to study its best performance after exposure to maximum relative humidity (~90% RH).[12g, 13] Although, in each case, the system involves capturing atmospheric water at night and evaporating during daytime with the assistance of solar irradiation. Thus an important question arises: how this atmospheric water harvesting can address the world's thirst where the availability/intensity of solar radiation along with the distribution of global fresh-water among the continent is extremely partial.[4]

In this work, a facile strategy for developing MOF based nanocomposites has been demonstrated to modulate water harvesting properties from the atmosphere by incorporating two layered templates (aminoclay [AC] and graphene oxide [GO]) of different proportions into typical MOF (CuBTC), affording CuBTC@AC-GO nanocomposite. CuBTC [formulated as $Cu_3(BTC)_2(H_2O)_3$; BTC= benzene-1,3,5-tricarboxylate], could be considered as an appropriate sorbent for multi-environment (arid-humid-fog) harvesting study, exhibits moderate water uptake with two inflection points at 25 and 70% RH, restricts its application because of instability under humid condition.[14] Aminoclay allows nano-structuring of MOF nanoparticles and the interfacial void provides a higher surface-to-volume ratio. The dynamic water-dispersible feature of AC provides additional water stability to the composite.[15] The purpose of combining graphene oxide is predominantly for its prolonged heat conduction capacity that would help facile water release during desorption (Scheme 1).[16] The water uptake was enhanced ~39% for CuBTC@AC-GO compared to bulk CuBTC, due to the additional interfacial void space and presence of hydrophilic functional groups (amine for AC, epoxy, hydroxyl, carboxyl for GO) from the 2D matrices.[15a, 17] This, in turn, enables autonomous water harvesting modulated by varying temperature (65, 75, 85, 90°C), humidity (10, 30, 50, 70, 90% RH) and indoor airborne moisture under laboratory condition. The work demonstrates continuous water supply for 120 h (1 cycle per day) and 79 h (1 and half-cycle per day), producing total 1.34 (best value 0.337 $Lg^{-1}day^{-1}$) and 10.5 litres (best value 0.445 $Lg^{-1}day^{-1}$) of drinkable atmospheric water per gram of material without any solar-irradiation.

4.1.2: Experimental section

4.1.2.1: Materials

All the reagents and solvents employed are commercially available and used as supplied without further purification. Chemicals were obtained from Sigma-Aldrich Chemicals Company.

4.1.2.2: Synthesis

CuBTC@AC Synthesis: Aminoclay (AC) was prepared by mixing 3-aminopropyltriethoxysilane and ethanolic solution of Magnesium chloride following typical reaction conditions reported by Mann and coworkers.[18] Freshly prepared AC has been blended with HKUST by varying it’s concentration 4.6, 9.6 and 15.3 wt% (analyzed from ICP-AES data) aminoclay, respectively. A similar procedure, reported by our group, was repeated to synthesize CuBTC@AC-1 (or, CuBTC@AC), CuBTC@AC-2, and CuBTC@AC-3.

CuBTC@GO Synthesis: Graphite oxide was synthesized by oxidation of graphite using a modified Hummers method.[19] Similar to the previous report, CuBTC@GO was prepared by exfoliating GO in de-ionized water followed by the addition of MOF precursors. 0.34 g (9wt% GO considering 100% CuBTC) was dispersed in 8 mL water. Then 0.241 g Copper nitrate trihydrate (1 mmol) and 0.147 g 1,3,5-benzenetricarboxylic acid (0.67 mmol) were added to the above solution with 12 mL DMF and 12 mL ethanol. The complete reaction mixture was transferred to a Teflon-lined stainless-steel autoclave and stirred for 10 minutes. The autoclave was tightly sealed and placed in an oven at 80 °C for 24 h. The resulting sky-blue product was washed in fresh DMF and finally with ethanol, and the collected product was dried under 60 °C oven.

CuBTC@AC-GO Synthesis: At first, 0.34g (9wt% GO considering 100% CuBTC) was dispersed in 8 mL water and sonicated for 1 h. 5 mg of AC in 4 mL ethanol was added to the above solution and stirred for another 5 minutes by maintaining neutral pH. Now, as described earlier similar concentration of precursor solution was added and kept reaction under 80 °C. The dark-blue product was washed repeatedly with fresh DMF and ethanol and referred to as CuBTC@AC-GO-1 (or, CuBTC@AC-GO). A similar procedure was repeated by loading 10 mg and 20 mg of AC and collected composites are denoted as CuBTC@AC-GO-2 and CuBTC@AC-GO-3, respectively.

4.1.2.3: Physical measurements

Powder X-ray diffraction (PXRD) patterns were recorded using a Bruker D8 Discover instrument using Cu–Kα radiation. Inductively Coupled Plasma-Atomic Emission Spectroscopy (ICP-AES) measurements were recorded on the Perkin Elmer Optima 7000dv ICP-AES instrument. The FT-IR experiments were carried out by utilizing a Bruker (Vortex 70V) spectrophotometer. The samples were prepared by dispersing the sample in MeOH and then dropping 5 μL of the solution onto a small piece of silicon wafer and drying it into the air. Transmission electron microscopy (TEM) images were taken with a JEOL JEM-3010 transmission electron microscope operating at 200 kV. The samples were prepared in the same way as described above, but the drop cast was made onto a carbon-coated TEM grid. Adsorption isotherms were recorded with the desolvated samples using QUADRASORB-SI analyzer and AUTOSORB IQ_2 instrument. Water vapor adsorption isotherm measurements at 298 K were carried out on a fully

BELSORP-aqua volumetric adsorption instrument from BEL, Japan. The helium used for the adsorption measurements is of scientific/research grade with 99.999% purity. To prepare the desolvated samples, approximately 100-150 mg of sample was degassed under 10^{-1} Pa vacuum for overnight (~12-16 h) prior to the measurements.

4.1.2.4: Device fabrication

4.1.2.4.1: Atmospheric water harvesting

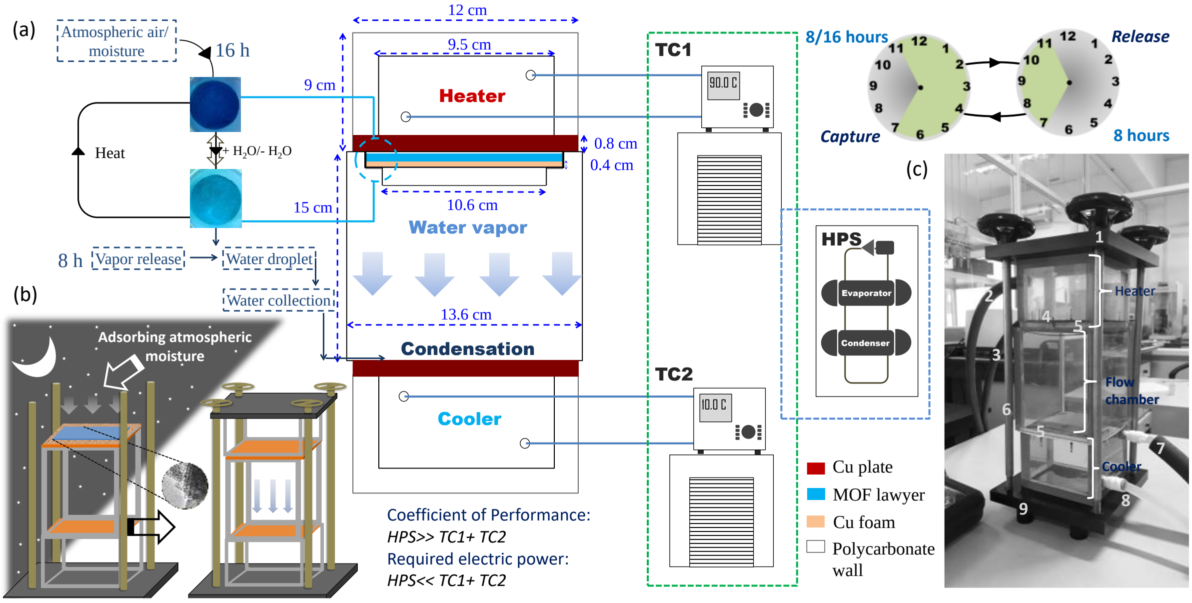

Figure 1: Detailed overview of all-in-one lab made indoor atmospheric water generator (IAWG). (a) Mechanism of continuous atmospheric water sorption and release with a detailed instrumental overview. (b) Schematic (illustrative (b) and pictographic (d)) representation of prototype device and the time cycle (c). [1: Aluminum plate, 2: hot water outlet, 3: hot water inlet, 4: Copper foam, 5: Copper plate, 6: Steel screw, 7: cold water outlet, 8: cold water inlet, 9: Aluminum base].

Our all-in-one prototype device of water generation comprises of three compartments. The 1st and 3rd compartments are connected to the temperature controller whereas the 1st one generates high temperatures (65, 75, 85 and 90 °C) and the bottom part is working as a condenser (depends upon the dew-point temperature). The middle part, sandwiched between heater and condenser, allows the water vapor to flow towards the condenser where water droplets are collected (Figure 1a, b). The efficiency of such a water collecting device depends upon the water release and water capture. However, water release time at certain elevated temperature from the MOF should be significantly faster than the capture from atmosphere. This is why, in a 5-cycle harvesting course, the material was allowed to adsorb moist for 16 h (7:00 pm to 11:00 am) and release for rest 8 h (11:00 am to 7 pm) in a day (M_a). In another method (M_b), the sorption and release time was restricted to 8 h each and five consecutive cycles were performed accordingly within 79 h. Fig. 1, 8 and 9 discloses associated significant parameters with defining harvesting phenomena. T_{ih}, the input heater temperature was kept constant at 90 °C to avail highest possible water collection. Relative humidity points refer the average atmospheric relative humidity value experienced by MOF during the interval of 16 h or 8 h. Similarly, ambient humidity and corresponding room temperature, defines the dew point limit and corresponding values during the process of water harvesting, especially at the time of water release and collection (8 h). The dew point (T_{dp}) is an edge temperature to which air must be cooled and to become saturated with the moisture present in the air. This is explained by this well-known approximation (Eqn. 2, 3 and 4) which reflects its strong association with RH% and ambient temperature. As a consequence, the dew point relocated with other parameters from one day to other. And finally, T_{sc}, sensible condenser temperature was kept on or above to T_d to minimize the error in water content generated by the moisture present in that chamber.

$$\gamma\ (T_a, RH) = \ln(\frac{RH}{100}) + bT_a/\ (c + T_a) \qquad \text{(eqn. 2)}$$

$$T_{dp} = c\gamma\ (T_a, RH)/\ b - \gamma\ (T_a, RH) \qquad \text{(eqn. 3)}$$

Eqn. 2 exhibits a well-known approximation used to calculate the dew point, T_{dp}. Given the actual air temperature, T_a in °C and relative humidity RH%. Where b and c are constants varied with temperature range. However, this approximation can further be simplified in Eqn. 4.

$$T_{dp} \sim T_a - \frac{100-RH}{5} \qquad \text{(eqn. 4)}$$

$$RH \sim 100 - 5(T_a - T_{dp}) \qquad \text{(eqn. 5)}$$

In addition, the efficiency of each water generation cycle is further calculated. W_{cap}, W_{rel} are the amount of water captured and released by MOF (Table 2). For a five days' continuous cycle (120 h), as MOF is externally activated under vacuum for single time

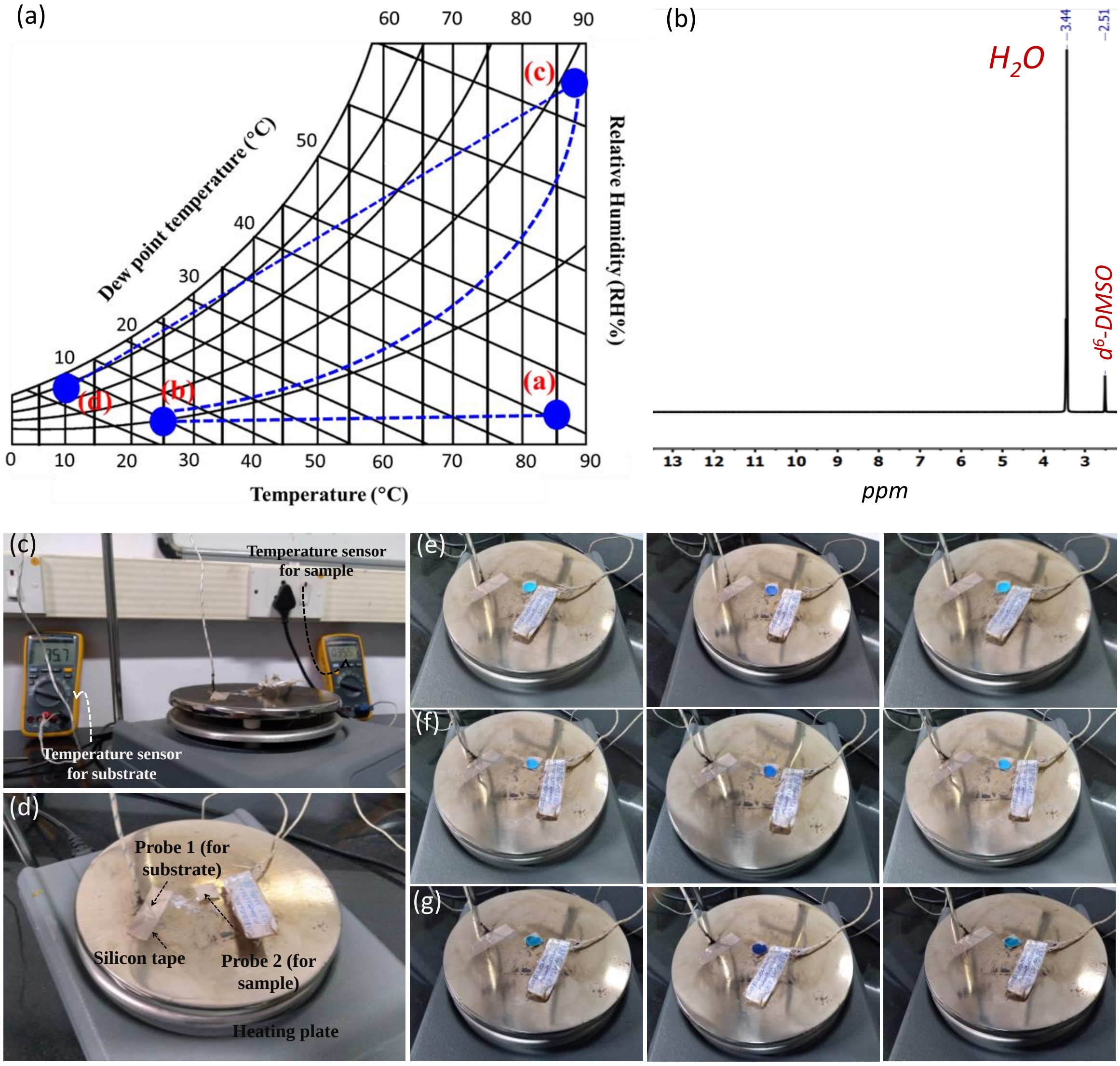

Figure 2: (a) The water collecting cycle defined by psychometric chart referring the several stages of MOF and water collection presented in Figure 1. (b) ^{1}H-NMR of collected water collected from CuBTC@AC-1. (c-g) Customized experimental arrangement for Figure 3h experiments. Pictorial representation of all three materials (CuBTC, e; CuBTC@AC-1, f; CuBTC@AC-GO-1, g) under experimental conditions (a, b) at three different conditions (ambient-90°C-ambient, e-g).

only before the measurement, W_{cap} is considered the same for each cycle. The η_{WHC}, product of water release (η_R) and capture efficiency (η_C), represents efficiency of each water harvesting cycle. 1.1862 g of activated CuBTC@AC-1 was saturated for 16 h at 45-55% RH on the copper foam. After saturation, the heating compartment of the device connected to the temperature controller was placed on the composite layer packed over the copper foam. Beneath the porous foam, it contains one metal plate that transfers the heat to the material at 90 °C. The first droplet on the inner wall of the middle part appears within 30 minutes. After 8 h, when water release was completed, droplets were collected from the surface of the other copper plate. This copper plate is connected to a temperature circular act as a condenser in the device.

4.1.2.4.2: Water harvesting under arid, humid and fog condition

The development of such composite material in a wide range inspired us to explore its acceptability from low to high humid regions. A three-neck round bottom flux was customized where one neck was fitted with a humidity sensor, one for sample loading, and the other one to alter the chamber environment depending upon its necessity, as shown in Figure 3. The activated MOF samples (~2.0 g, both CuBTC@AC and CuBTC@AC-GO) were loaded and chamber humidity was controlled either by purging water vapor, allowing an inert environment (N_2/Ar gas), or by creating a vacuum by using pump. The amount of water collection obeys linear relationship with the RH% present inside the 3-neck RB experienced by composites. The same batch of composites are further used to study non-equilibrium ads/des cycle (Figure 7d, e), and finally, the purity of the collected water has been tested by ^{1}H-NMR analysis that ensures zero leaching of MOF or organic fragments (Figure 2b).

4.1.2.4.3: Prototype fabrication and data collection of related parameters to count overall water harvesting

On average, any atmospheric water generation device should obey few primary criteria in order to produce energy-efficient technology. The applied material should be atoxic, cheap, scalable, wide-band sorption capacity and fairly stable to operate over a great deal of time. In addition, the prototype device needs to be efficient enough in terms of commercial sustainability and energy-saving. Unfortunately, none of this existing atmospheric water generator meets all these mentioned criteria neither in material development nor from device fabrication. To date, the reported MOF water harvesters are functional through the help of two distinct energy input sources: solar module (photovoltaic/ solar-thermal) and condenser (natural/ compressor/ chiller/ heat sink/ thermo-electric based). Such devices are violating energy-efficient norms predominantly from a thermodynamic standpoint.

It has been already mentioned, our device is made of three primary compartments. The 1st and 3rd compartments are connected to the temperature controller, while the 1st one act as a heater (>90 °C) and the bottom one as a condenser (8-13 °C). The middle part allows the water vapor to flow towards the condenser where water droplets are formed and collected subsequently. Each compartment unit was made of a 1.2 cm thick polycarbonate sheet. The two temperature controller compartments (9cm×12cm×12cm) are quite similar in size and one of the side 0.7 cm thick copper plates was screwed and sealed with a rubber gasket (Figure 1, 3). This copper plate is used either as a heater to transfer heat to the material or as a condenser to shelter the water droplets. The middle cubicle (15cm×13cm×13cm) is sandwiched in between with a 10.6cm×10.6cm slot to hold copper foam (with 80% porosity, 0.4 cm thickness, pore size 1-2 mm, thermal conductivity 401 W m^{-1} k^{-1}, 50 PPI). The activated composite was blown out over (2×21) cm^2 area on the copper foam supported by aluminium foil beneath it. This Al-foil was covered from the reverse side of the foam with sixteen holes (~1 cm diameter), allowing water vapor through it. And finally, to make it air-tight, it was fixed from the top by using four steel stand and one aluminium lid. The change in temperature (room and dew point temperature) and relative humidity (day/ night) was monitored by a humidity-temperature sensor (EE355-PAISAL-100, Model: IP65, 20-200,000 ppm, 0-100% RH, -60 to 100 °C, 4-20 mA, 18.28 V DC) during WGC by placing it at different positions in the IAWG. The energy consumption (or the measurement of current in a circuit) of the system during harvesting was calculated by Ammeter. The temperatures of 1st and 3rd blocks are adjusted by the temperature controller (Julabo; F25 MH, Operative: -28-200 °C, 230 V, 100 Amp, 50-60 Hz). As a carrier of heat, water has been used, which normally fills into the blocks and transfer the heat to the copper plate as programmed by the controller. However, these two different temperature controllers could be integrated into a single system by using simultaneous heating and cooling pump (HPS) (Figure 1a). Long before 1982, Lecrivain *et al.* first fabricated a HPS that produce hot water as high as 95 °C with a chilled water source at 0 °C.[20] In a recent review, Byrne and his team demonstrated that such a simultaneous systems are 65 to 82% more efficient with respect to each pump (heating or cooling) in terms of their coefficient of performance.[21] Nevertheless, an adaptation of temperature controller as an energy input has radically changed the impact in several ways. First, a temperature controller can expand its operational window to achieve maximum efficiency while solar-assisted devices are dependent on ambient solar, air, and humid condition. Secondly, the necessary expansive equipment for other solar-induced harvesters such as OTTI aerogel, pyro mark paint, pyrometer, biconvex lens loses its importance in indoor water harvesting. And finally, the idea of incorporating temperature controller allows the system to work under indoor condition and make the device portable, cheap and accessible worldwide.

Heat transfer in porous media

The analysis of heat transfer in porous media involves solving two coupled energy equations, one for the porous material and one for the fluid. The solution is represented by two energy functions. Porosity is defined as P; V_f is fluid or pore volume and V represents total volume.

$$P = V_f / V \qquad \text{(eqn. 6)}$$

Considering for a porous wall with thickness L and face area A, the volume expressed as;

$$V = AL \qquad \text{(eqn. 7)}$$

If model the pores as straight channel;

$$V_f = A_f L \qquad \text{(eqn. 8)}$$

If A_f is the total fluid flow area, then substituting eqn. 7 and eqn. 8;

$$P = A_f / A \qquad \text{(eqn. 9)}$$

Thus,

$$A_f = PA \qquad \text{(eqn. 10)}$$

It follows that the area of solid material, represented by A_s

$$A_s = (1-P)A \qquad \text{(eqn. 11)}$$

Now, considering one-dimensional transient conduction in a porous wall; fluid flows through the wall at a rate m. The wall generates energy at a rate q^m per unit volume.

If, constant porosity, constant flow rate, constant properties and temperature are identical for solid and fluid then,

$$E = E_{in} + E_g - E_{out} \qquad \text{(eqn. 12)}$$

If E is the rate of energy change within the element, then E_{in}, E_g and E_{out} are the rate of energy added to the element, rate of energy generated within the element, and rate of energy removed from the element, respectively.

Adapting Fourier's law to determine heat conduction through the solid and fluid, E_{in} is given by,

$$E_{in} = - k_s(1-p)A\frac{\partial T}{\partial x} - k_f PA\frac{\partial T}{\partial x} + mc_{pf}T \qquad \text{(eqn. 13)}$$

Where, c_{pf}, k_f are specific heat and thermal conductivity of fluid, k_s, thermal conductivity of solid material and x is the distance in between.

Defining thermal conductivity of solid-fluid matrix, $\bar{k}$ *as,*

$$\bar{k} = (1-p)k_s + Pk_f \qquad \text{(eqn. 14)}$$

Then,

$$E_{in} = \bar{k}A\frac{\partial T}{\partial x} + mc_{pf}T \qquad \text{(eqn. 15)}$$

Eqn. 14 is further used,

$$E_{out} = - \bar{k}A\frac{\partial T}{\partial x} - \bar{k}A\frac{\partial 2T}{\partial x2} + mc_{pf}(T + \frac{\partial T}{\partial x}dx) \qquad \text{(eqn. 16)}$$

Again, E_g is given by,

$$E_g = q^m A\, dx. \qquad \text{(eqn.17)}$$

So, E can be calculated from eqn. 12 by adding eqn. 15, 16 and 17. Where E represents the changes in the energy of the solid and the fluid. Each component is proportional to its mass within the element.

The efficiency calculation of lab-made atmospheric water harvester (AWH)

The highest water capacity by the MOF under certain temperature and relative humidity is called the saturation of MOF. W_{cap}, water captured in per gram of MOF, is termed as water capture capacity calculated by water filling within the time span of 16h at night. Our atmospheric water generator is made of three compartments. The top part is considered a heat source that basically transfers heat to the material to release water. Now, the total energy absorbed or total heat transferred to the sample is $q_{H,\,total}$

Then,

$$q_{H,\,total} = q_{H,\,latent} + q_{H,\,material} + q_{H,\,loss}$$

Now, $q_{H,\,latent}$ is required to overcoming MOF-water interaction. The heat is required for increasing the temperature of MOF or the desiccant material. The heat loss for during this operation is represented as $q_{H,\,loss}$. For a thermally isolated and closed system,

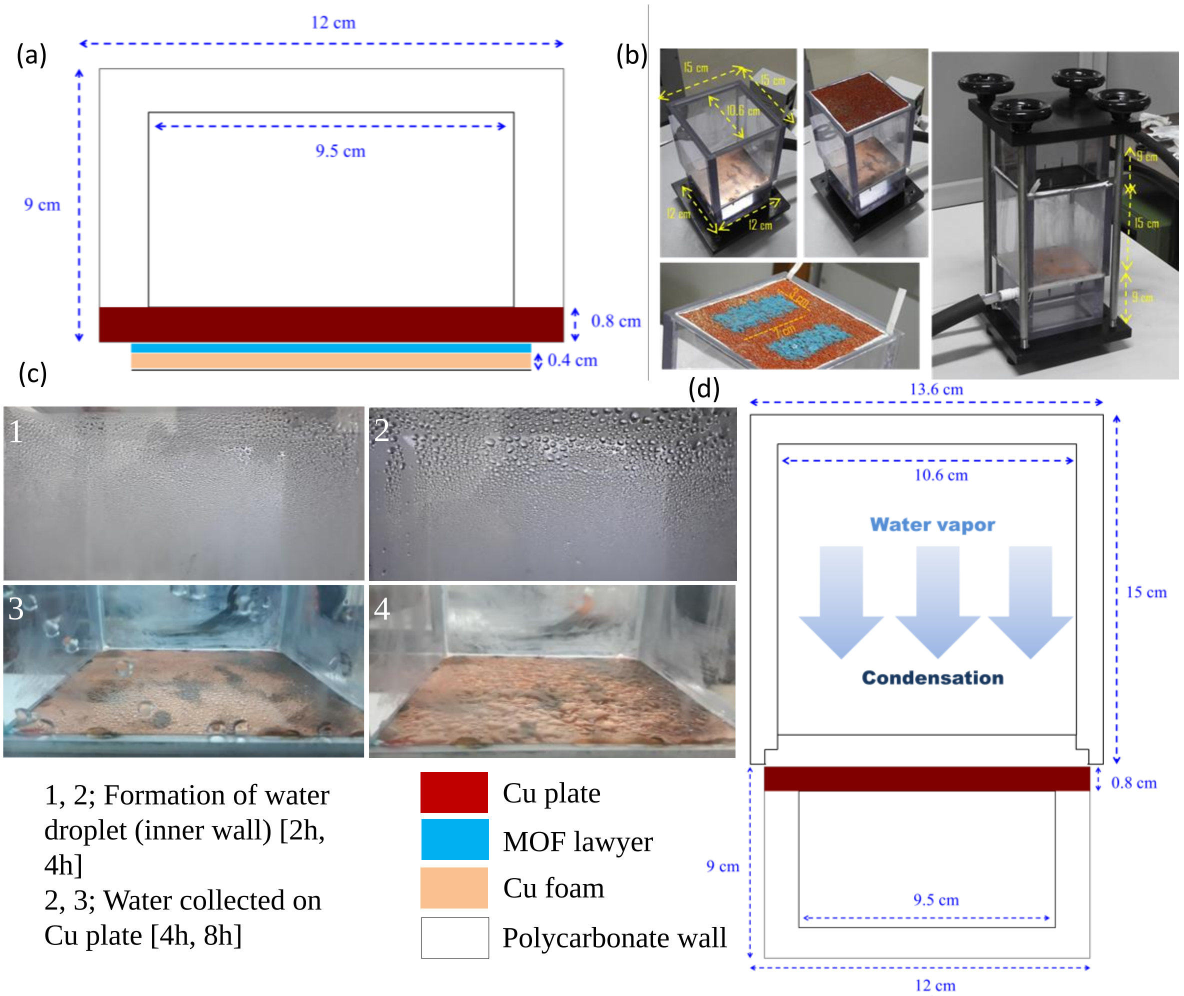

Figure 3: (a) Schematic presentation of heater (top part) of atmospheric water generator. (c) Photo of prototype test apparatus during sample loading. (c) Photograph of water condensation inside the wall of an enclosure (1, 2) and final collection on top of the cupper plate (3, 4). (d) Schematic presentation of middle part and condenser of atmospheric water generator.

heat loss is considered negligible and then;

$$q_{H,\ total} = q_{H,\ latent} + q_{H,\ material}$$

By considering, $q_{H,\ material} >> q_{H,\ loss}$, and for an efficient system, generally, $q_{H,\ latent} > q_{H,\ material}$. The total latent energy is defined as the amount of energy per unit mass or gram of MOF spent to desorb the entire amount of captured water from the pore of the MOF.

$$q_{H,\ latent} = W_{cap}.q_{st}$$

q_{st} is isosteric heat of adsorption of corresponding desiccant (here, MOF) material. In addition, other parameters such as heat capacity of the desiccant material, temperature during water adsorption (T_{cap}) and release ($T_{release}$). For complete heat transfer in a closed system, it could be assumed $T_{release} \sim T_H$ and $T_{cap} \sim T_a$. For this AWG, $T_H = 90$ °C and T_a, varies from 20-28 °C (depending upon the exact room temperature of that corresponding date). For an ideal harvester system, the results indicate that the $q_{H,\ material} >> q_{H,\ loss}$ during the release process; therefore, almost all the incident energy is spent on overcoming the MOF-water interactions.

The performance of the water capture cycle can be evaluated by water release efficiency. The release efficiency, η_R, is the ratio of the amount of water being captured during 16 h/8 h and released in the next 8 h.

$$\eta_R = W_{rel}/ W_{cap}$$

Similarly, the cooling energy required to condense the water vapor released from the MOF is spent on three processes:

$$q_{C,\ total} = q_{C,\ latent} + q_{C,\ material} + q_{C,\ loss}$$

The heat required for condensation of released water vapor from MOF $q_{C,\ total,}$ is dependent on three energy parameters. $q_{C,\ latent}$, the required energy (in terms of heat) to reduce the temperature of released water, and $q_{C,\ material}$ the sensible heat to liquefy water vapor into droplets. A portion of total energy $q_{C,\ loss}$ is being lost to the surrounding considered negligible with respect to other temperature factors as the device is isolated. Thermodynamically, drop-wise condensation may occur on a hard surface cooled below the saturation temperature of a surrounding vapor as the surface is poorly wetted excluding at locations where well-wetted contaminant nuclei exist.

$$q_{C,\ material} = W_{cap}.C_{p,wv}(\mathrm{T_{wv}}\text{-}\mathrm{T_{dp}})$$

$$q_{C,latent} = m_{air}/\ m_{MOF}.C_{p,a}(\mathrm{T_a}\text{-}\mathrm{T_{dp}}) + W_{cap}.h_{fg}$$

T_{wv}, T_a, T_{dp} are the temperature of water vapor, dry air and dew point, respectively. Hence, $C_{p,wv}$ and $C_{p,a}$ represents the respective heat capacity of water vapor and air. The specific heat of phase change of water vapor to liquid is expressed as h_{fg}.

Considering $q_{C,loss}$ is negligible, the water vapor temperature and air temperature is in equilibrium ($T_{wv} = T_a$). Subsequently, for maximum efficient system, the amount of condensed water capture is equal to the water released in the air by MOF after experiencing high temperature (90 °C). Hence, the condenser temperature is also in equilibrium with air temperature during condensation. So, the previous equation can be represented as;

$$q_{C,\ total} = (\mathrm{T_a}\text{-}\mathrm{T_{dp}})\ (W_{cap}.C_{p,wv} + m_{air}/\ m_{MOF}.C_{p,a}) + W_{cap}.h_{fg}$$

It could be further approximated that the quantity of energy required for condensation of released water can be determined by neglecting other parameters such as sensible heating required to liquefy water vapor into droplets and so on. However, from thermodynamic point of view, any device fabrication for atmospheric water generation should consider a minimum heat necessity, $q_{c,min}$, that theoretically allows the condensation of entire amount of released water. Thus, considering all these approximations, the performance of collecting cycle (η_C) is expressed as;

$$\eta_R = W_{rel}.(m_{col}/m_{MOF})$$

Where, m_{col} and m_{MOF} are the mass of collected water on the condenser (collected from solid surface of the copper plate) and MOF, respectively.

Hence, for an isolated system condenser temperature, T_c, should always be higher than ambiance dew point temperature (T_{dp}). The dew point represents a particular point with respect to the present temperature and relative humidity of air (RH%) to which air must be cooled to become saturated with water vapor. That means, under a certain temperature, air has not been able to hold the moisture and subsequently condense into liquid water.

To calculate the exact amount of water collected (m_{col}), as $T_c > T_{dp}$, only water released from the MOF is considered because apparently there is no chance of moisture liquefaction from the air. Then, the overall efficiency of WHC is calculated as;

$$\eta_{WHC} = \eta_R . \eta_C$$

$$\eta_{WHC} = W_{cap} . (m_{col}/m_{MOF})$$

Theoretically, to achieve maximum possible efficient water generation is only possible if the amount of water released from the MOF equals the captured amount and if all the released water is condensed. So that, ($\eta_R \to 1$); and ($\eta_C \to 1$).

During each continuous water harvesting cycle, W_{cap} is considered the same and only calculated from initial water capture.

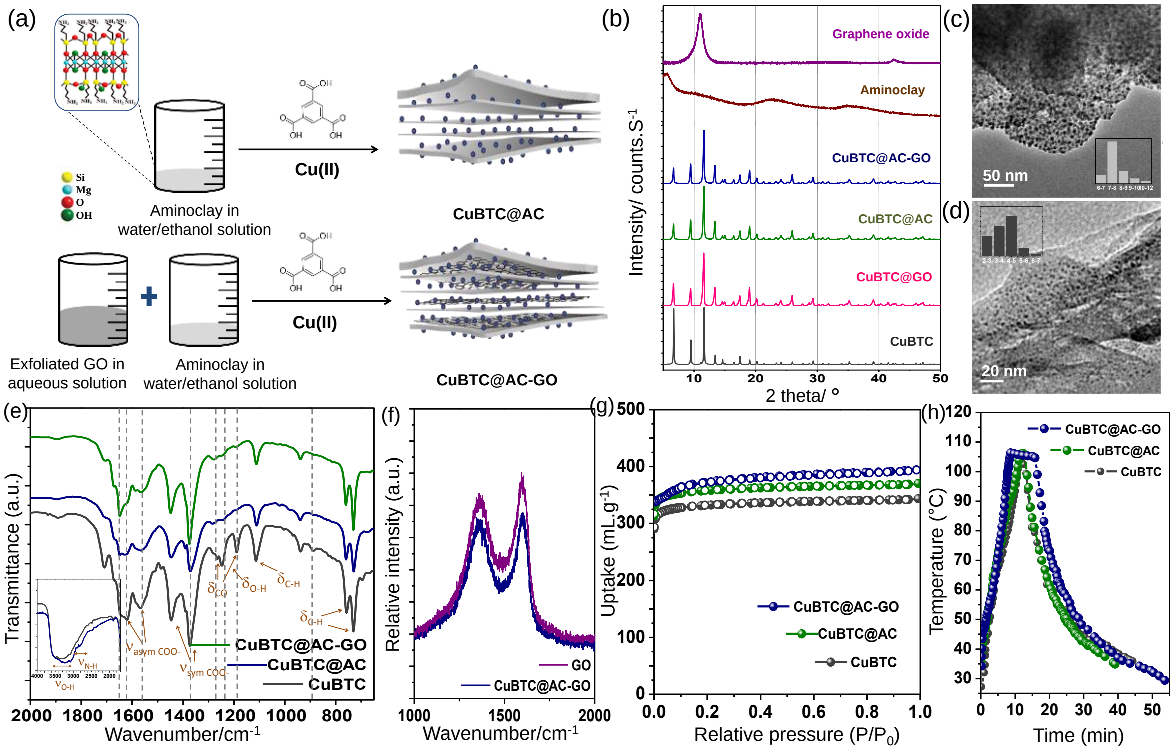

Figure 4: (a) Synthetic scheme of CuBTC@AC and CuBTC@AC-GO. (b) Powder X-ray pattern of parent material and composites. (c, d) TEM images of CuBTC@AC and CuBTC@AC-GO with particle size distribution histogram plots in inset. (e) FT-IR spectra of composites and bulk-CuBTC. (f) Raman spectra of CuBTC@AC-GO indicate overlap with pure graphene oxide. (g) N_2 adsorption-desorption isotherm at 77 K. (h) Control increase of the sample temperature with time from ambient to heater temperature (105 °C) to study heat conduction of the materials.

4.1.3: Result and discussion

4.1.3.1: Fabrication and characterization of nanocomposites

The growth and stabilization of MOF nanoparticles on multiple templates (aminoclay and graphene oxide) was fabricated through an *in-situ* hydrothermal synthesis route, as illustrated in Figure 4a. Here, bicomponent composites CuBTC@AC-1 (or, CuBTC@AC), CuBTC@AC-2, and CuBTC@AC-3 were resynthesized by following a previously reported method by varying clay concentration.[15a] PXRD, surface area and TEM analysis revealed the successful formation of the composites. The tri-component composites have been prepared by adding 9 wt% of graphene oxides (w.r.t 100% MOF formation) into the bicomponent mixture. Three new composites are denoted as CuBTC@AC-GO-1, CuBTC@AC-GO-2, and CuBTC@AC-GO-3. In addition to these six compounds, CuBTC and CuBTC@GO (GO ~9 wt%) were also prepared by following the similar synthetic methodology. Each of them showed good agreement with the powder pattern of pristine MOF (Figure 4b, 5a). As shown in the size distribution histogram plot in Figure 5c, the NPs are in the range of 2-5 nm for CuBTC@AC-GO-1 (or, CuBTC@AC-GO), but less equally and evenly distributed than CuBTC@AC-GO-2 of average particle size 8-12 nm. In the case of CuBTC@AC-GO-3, where clay content is 15.3 wt%, MOF particles appear with 15-30 nm size large with uneven distribution (Figure 5d [7, 8]; d). The Energy dispersive X-ray spectroscopy (EDX) analysis of CuBTC@AC-GO-1 clearly confirms the presence of Mg and Si that comes from AC and corresponding elemental mapping suggests the homogeneous distribution of other elements throughout the sample (Figure 5b). Hence, the architecture of such a composite material obtained is dictated by the highest degree of freedom in three distinct components, the shape-size of the nanoparticles and the defined alignment of the other two templates.

For reference, the N_2 adsorption isotherm of bulk CuBTC was measured and it showed a characteristic type-I isotherm with BET (Brunauer-Emmett-Teller) surface area of 1253 m^2g^{-1}, attributed to its microporous nature, while densely stacked clay does not uptake N_2 at 77 K (Figure 6a). In fact, the bi-component materials, CuBTC@AC-1 and CuBTC@AC-2 revealed an improved BET surface area of 1305 and 1381 m^2g^{-1}, respectively. Contrastingly, the trace amount of GO loading further increased the surface area. CuBTC@GO, CuBTC@AC-GO-1, and CuBTC@AC-GO-2 showed enhanced BET surface area of 1486 m^2g^{-1}, 1425 m^2g^{-1}, and 1569 m^2g^{-1}, respectively (Table 1).

Further to understand the importance of nanocomposite fabrication, N_2 and water adsorption were performed with of the physical mixture (50:50) of CuBTC@AC and CuBTC@GO that revealed an average surface area and water uptake (1294 m^2g^{-1}, 574 cm^3g^{-1}, respectively; Figure 6b). Therefore, the enhanced surface area in tricomponent nanocomposite could be attributed to the formation of some interfacial voids between three individual components (MOF on AC matrix, MOF on GO matrix and in between MOF@AC and MOF@GO lamina). The detailed sorption property is represented in detail in Table 1.

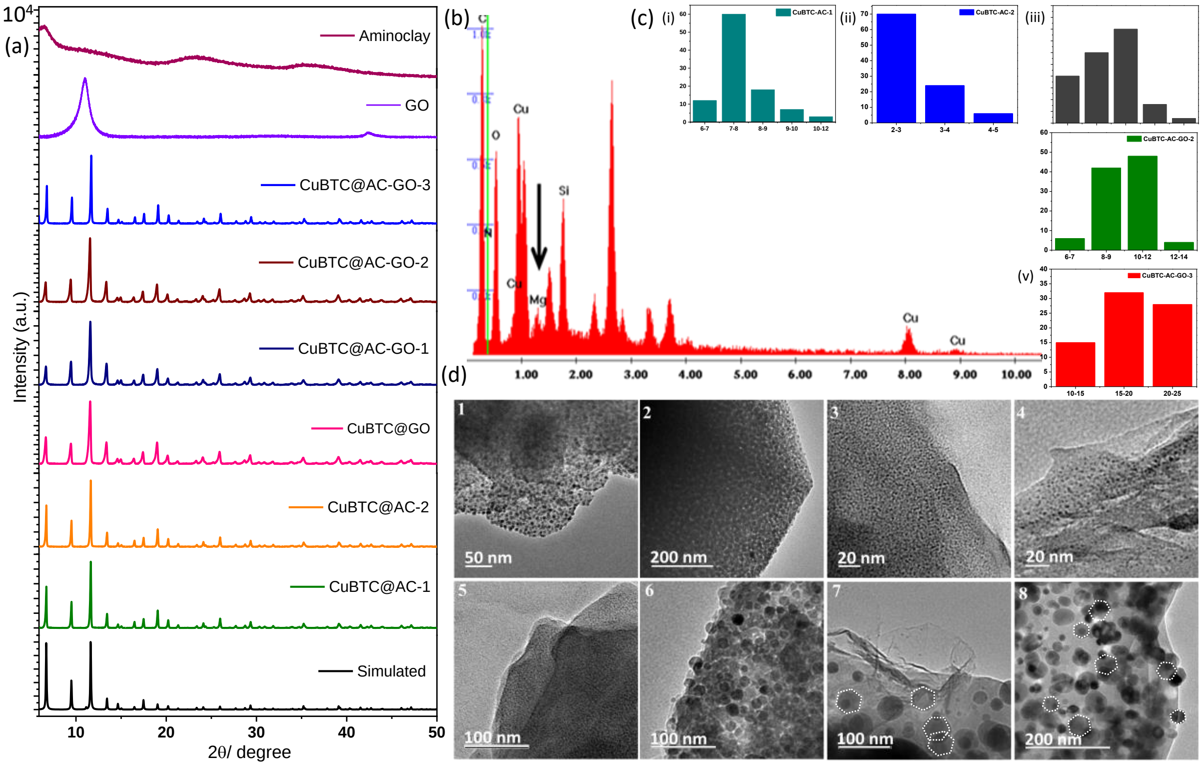

Figure 5: (a) Comparative powder X-ray pattern of additional composites with parent materials. (b) EDX analysis of CuBTC@AC-GO-1. (d) TEM images and (c) particle size distribution histogram of CuBTC@AC-1 (1, 2), CuBTC@AC-GO-1 (3, 4), CuBTC@AC-GO-2 (5, 6), CuBTC@AC-GO-3 (7, 8).

Among bi-component composites, CuBTC@AC-1 and CuBTC@AC-GO-1 from tri-component composites exhibited maximum water storage capacity (Table 1) under ambient condition (298 K), and thus these two composites are extensively studied and harvesting efficiency has been performed by using these two materials under various experimental conditions.

For bi-component, the AC layers played a crucial role in the nucleation and stabilization of CuBTC nanoparticles, which is further supported by the uniform growth of MOF particles on clay surface (Figure 4c, *inset*). Similarly, the well-defined flakes of graphene oxide layers are shown in Figure 4d validated the successful formation of tri-composite. Raman analysis of CuBTC@AC-GO (or CuBTC@AC-GO-1) depicted the broad bands at 1366 and 1602 cm^{-1} merging with the MOF bands in the 1150–1670 cm^{-1} range, attributable to the D and G bands of GO, suggests its presence in the composites (Figure 4f). FTIR spectra of composites were recorded from 4000 to 600 cm^{-1} on an attenuated total reflection (ATR), and the spectra of CuBTC tie well with that reported in the literature. Various bands in the 1300-600 cm^{-1} region attributed to the out-of-plane vibration of ligand (BTC; benzene-1,3,5 tricarboxylate).[22] Hence, the significant reduction in intensity at 880, 1193, 1243, 1268 cm^{-1} may be ascribed to the successful wrapping of templates (clay and GO layers) around MOF nanoparticles. Whereas, the new band appears at 1595 cm^{-1} for CuBTC@AC-GO and a shoulder hump around 2790 cm^{-1} for CuBTC@AC (or CuBTC@AC-1) can be assigned for O-H bond of oxygen-surface group and N-H stretching vibrations, respectively (Figure 4f, *inset*). The N_2 adsorption-desorption isotherms of CuBTC@AC (1305 m^2g^{-1}) and CuBTC@AC-GO (1425 m^2g^{-1}) showed with respect to parent CuBTC (1253 m^2g^{-1}, Figure 4g). The speck loading of AC makes the material accessible to more N_2 uptake by restricting aggregation between crystallites and reduction in diffusion barrier by the successful formation of MOF NPs.

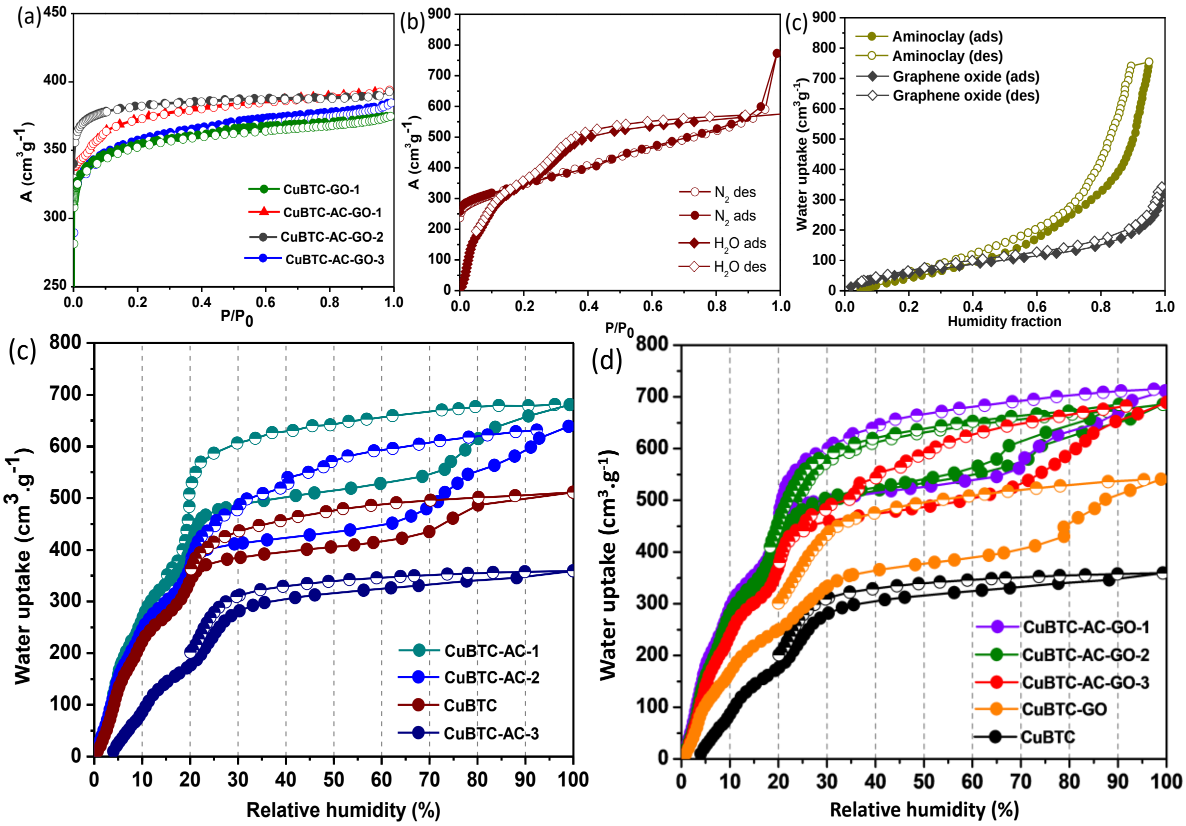

Figure 6: (a) N_2 adsorption-desorption isotherm measured at 77 K for CuBTC@GO and other tri-component composites. (b) N_2 and H_2O adsorption isotherm of the physical mixture (CuBTC@AC-1+ CuBTC@GO-1) at 77 K and 298 K, respectively. (c, d) Water adsorption isotherm at 298 K for all bi-component and tri-component composites in comparison with bulk-CuBTC MOF.

4.1.3.2: Water adsorption performance

Pure CuBTC has an "*S-shaped*" water adsorption isotherm with two inflections of water intake in the range of 20-30% (arid to humid) and 60-80% (humid to fog) relative humidity, maintains all qualities of a multi-environment desiccant material (Figure 2a, j). The water uptake capacity at P/P_0 ~0.99 (~99% RH) of CuBTC@AC-GO-2 and CuBTC@AC-GO-3 are considerably high**,** which is increased by 33.9% (687 cm^3g^{-1}) and 34.3% (689 cm^3g^{-1}) compared to CuBTC (Figure 6c, d) at 298 K (Table 1;). Nevertheless, as shown in Figure 6d, the water storage capacity at arid-humid (30% RH), and humid-fog (70% RH) interfaces along with extreme fog conditions (100% RH) increases 31%, 35%, and 40% with reference to CuBTC. With maximum AC-GO combination in CuBTC@AC-GO-3 the water uptake is more than CuBTC@AC-GO-2, while shows the least surface area in respect to all other tri-component. As observed from the water adsorption isotherm at 298 K, two other associate components, AC and GO show very low water adsorption capacity below 80% RH (Figure 6c). Although keeping consistency with enhanced surface area, composites showed improved water uptake under the arid-humid-fog region. The water uptake capacity at maximum RH at 298 K for CuBTC@AC is 680 cm^3g^{-1}, and for CuBTC@AC-GO it further reaches 716 cm^3g^{-1} (39.5% increase with respect to bulk-CuBTC), outclasses many desiccant porous materials reported so far and is only comparable to that few benchmark water-stable MOFs (Figure 7j).[23]

The enhanced hydrothermal stability of each composite was analyzed through powder X-ray diffraction (PXRD), *in-situ* diffuse reflectance infrared Fourier transform (DRIFT) spectroscopy and by performing multiple non-equilibrium adsorption/desorption cycle within 45-75% relative humidity under a mild temperature swing. Each composite was placed by spreading ~100 mg of sample in an open 30 ml scintillation vial which was kept in a custom-made chamber set to 20, 50, 70, and 90% RH for more than an hour. The PXRD patterns for both the composites show no indication of structural decomposition upon high concentration moisture treatment. Likewise, as depicted in Figure 7d, and e, the reusability of the composites was tested by executing sequential atmospheric moisture sorption-desorption. These continuous non-equilibrium cycling performances with the help of mild temperature swings indicate no decline in efficiency even after eight cycles. Interestingly, CuBTC@AC and CuBTC@AC-GO produce stable dispersion in water for more than 6 h, while the bulk CuBTC settle down within 15 minutes (Figure 7f). Under a set condition, CuBTC@AC-GO consumes more time (~3.5 h) for 8 consecutive recycling compared to CuBTC@AC, which requires approximately 2 hours. Furthermore, and water-adsorption kinetics and isosteric heats of adsorption were calculated for better understanding the water sorption-desorption dynamics. The water-adsorption kinetic data are fitted into LDF (linear driving force) model by using the equation $M_t/M_e=1-\exp(-kt)$. Figure 7g represents M_t/M_e vs. t that represents the mass transfer coefficient for diffusion between adsorbent particle and adsorbate pore. CuBTC@AC-GO shows faster rate of adsorption with a rate constant value 9.65×10^{-3} S^{-1} (α 0.139; P/P_0 at 0.10), while rate constant for CuBTC@AC and CuBTC are 4.61×10^{-3} S^{-1} (α 0.054; P/P_0 at 0.10) and 2.4×10^{-3} S^{-1} (P/P_0 at 0.10), respectively. These results disclose the accelerated water sorption kinetics in composites upon pristine MOF. Benefiting from multiple adsorption-desorption isotherms under various temperatures;

isosteric heat of adsorption (Q_{st}) was calculated from *Clausius-Clapeyron* equation in order to estimate the released energy developed from material-water interaction (Figure 7h, i). At zero loading, the isosteric heats of adsorption for CuBTC@AC and CuBTC@AC-GO are 98.6 and 62.1 kJmol^{-1}, respectively, were measured from two different analysis temperatures (25 °C and 35°C). For natural water harvesting lower Q_{st} value is preferred, where it could be considered that the lower value reflects minimum energy consumption for water release with weak MOF-water interaction.

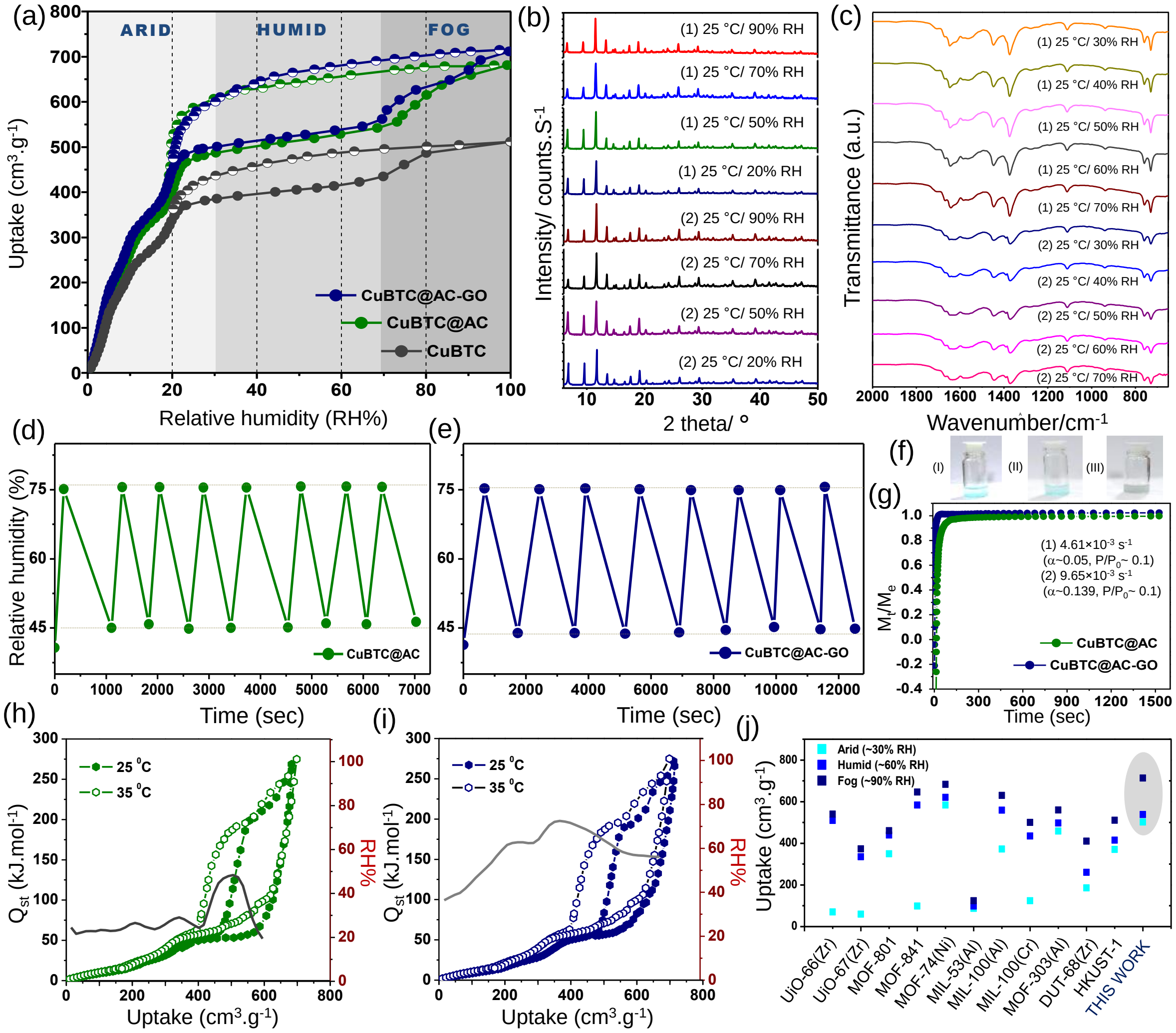

Figure 7: (a) Water adsorption isotherm of CuBTC, CuBTC@AC and CuBTC@AC-GO at 25°C. (b, c) PXRD pattern and *in-situ* FT-IR spectra of CuBTC@AC (1) and CuBTC@AC-GO (2) under different humid environment. (d, e) non-equilibrium water adsorption/desorption cycle within 45-75% relative humidity under a mild temperature swing. (f) Images of (1) CuBTC, (2) CuBTC@AC (3) CuBTC@AC-GO after 6 hours of preparation of dispersion in aqueous medium. (g) Kinetic plots of water vapor diffusion at 293 K considering 1500 sec equilibrium time. Isosteric heat of adsorption (Q_{st}) with water adsorption

isotherm calculated from respective sorption isotherm at 35 °C and 25°C for (h) CuBTC@AC and (i) CuBTC@AC-GO. (j) Comparative benchmark water stable MOF and their water uptake under arid, humid and fog region.

4.1.3.2: Temperature and humidity modulated indoor water harvesting

From the assessment of adsorption isotherm, isosteric heat of adsorption, adsorption kinetics and moisture capture-release cycle, it could be estimated that the CuBTC@AC-GO demonstrates higher interaction with water with respect to CuBTC@AC. To evaluate successful water harvesting, oozing efficiency affects more compare to water storage capacity. The CuBTC@AC-GO exhibits rapid heat reception from the heating plate, and it is sustainable for more than 7 min at 90°C, while for CuBTC and CuBTC@AC the sustainability perceives for approximately 2 minutes (Figure 4h, 2c-g). Therefore, to study temperature modulated water harvesting, CuBTC@AC-GO was chosen at first as it

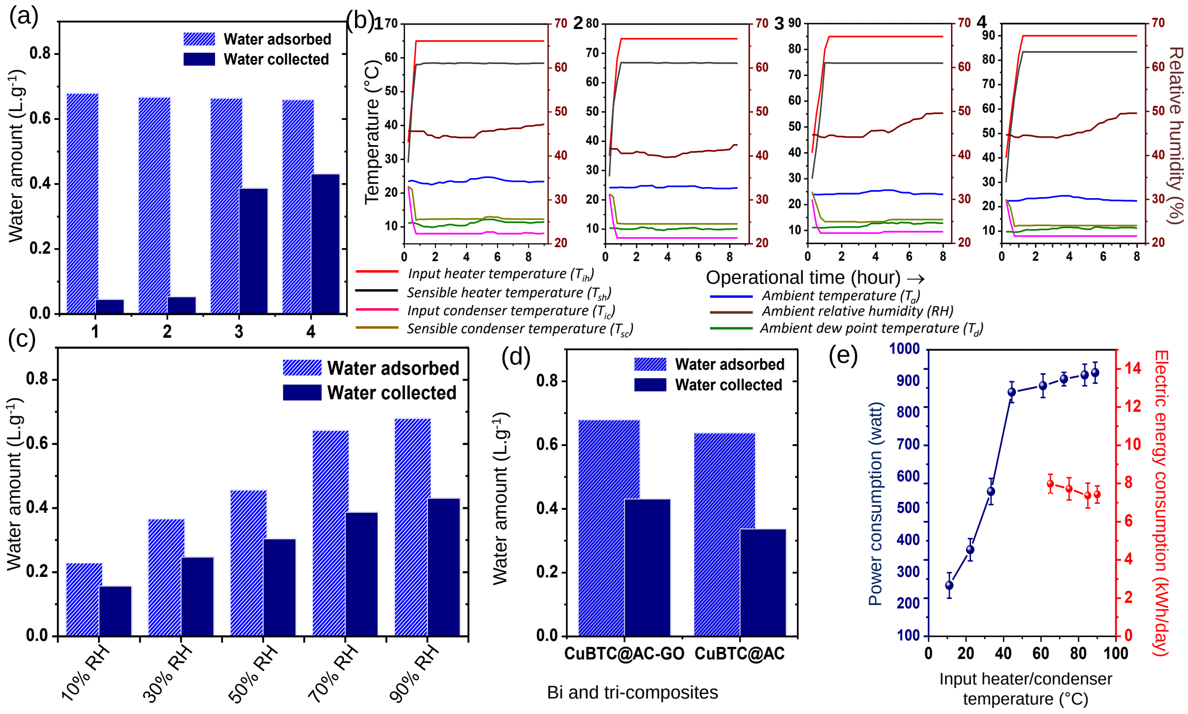

Figure 8: (a) Total amount of water uptake and capture of CuBTC@AC-GO under different desorption temperature. (b) Representative temperature (input heater temperature, sensible heater temperature, input condenser temperature, sensible condenser temperature, ambient temperature, ambient dew point temperature) and ambient relative humidity with respect to complete operational time. (c) Water capture and release study of CuBTC@AC-GO after exposed to 10, 30, 50, 70 and 90% RH. (d) Comparative water production graph of CuBTC@AC and CuBTC@AC-GO at 90% RH. (e) Power consumption and electric energy consumption plot as a function of input temperature. (f) Photo of prototype test apparatus during sample loading.

shows high water storage as well as prolonged thermal sustainability. In a typical laboratory experiment, the CuBTC@AC-GO (~1.85 g) was saturated overnight (RH 85-90%; 20-25°C, 16 h) in a custom-made chamber. After saturation, the sorbent was taken out and packed on the enclosure (Figure 3b). Harvesting data were collected under different input heater temperatures such as 65, 75, 85, 90°C (Figure 8b). Associated boundary conditions during water condensation such as input heater temperature (T_{ih}), sensible heater temperature (temperature sensed close to sorbent, T_{sh}), input condenser temperature (T_{ic}), sensible condenser temperature (temperature where water droplets are collected, T_{sc}), ambient temperature (T_a), ambient dew point temperature (T_d) and ambient relative humidity (RH) were stated in Figure 8b, 1-4. Note that, for each case, the T_{sc} is maintained below ambient but slightly above dew point to restrict atmospheric vapor condensation inside the enclosure. Collected water amount increases with sensible heater temperature. At 90% RH, CuBTC@AC-GO adsorbs a total water amount of 0.67 Lg^{-1} (0.53 gg^{-1}), from which 0.045, 0.053, 0.38 and 0.43 Lg^{-1} were directly collected after 8-9 h of water release by applying 58.4, 66.8, 74.7 and 83.5 °C desorption temperature (or T_{sh}), respectively. The harvestable water amount sharply increases from 65 to 90 °C with input heating by electrical power varying between 867 and 928 watts (Figure 8e). Interestingly, at higher temperature the water seepage became faster, and the consequent total energy consumption reduces from 7.98 to 7.42 kWh/day (for heater only). Thus, water was further harvested using a heater maintained at 90°C input temperature.

Next, the material was exposed to different humidity to study its potential in water harvesting across the globe. CuBTC@AC-GO was placed in a custom-made chamber set to either 10, 30, 50, 70 or 90% RH and kept for overnight airborne moisture adsorption (20-25°C, 16 hours). Water harvesting performance was studied under the similar release condition described above and found 0.15, 0.24, 0.3, 0.38 and 0.43 Lg^{-1} of water production with an overall harvesting efficiency of 68.5, 67.4, 66.6, 60.2 and 63.4%, respectively (Figure 8c). For comparison, CuBTC@AC was tested under identical sorption and release environment (during sorption: RH 90%, 20-26 °C, 16 h; during release: RH 45-55%, 22-28 °C, 8 h) and it shows 10.6% reduction in overall water harvesting efficiency with respect to CuBTC@AC-GO.

4.1.3.3: Autonomous indoor atmospheric water harvesting

All the aforementioned experiments were performed by spreading the material for 16 hours under a set humid environment. To study harvesting performance from indoor airborne moisture, our material was exposed (~2.02 g) overnight under an ambient environment. Here, the mechanism involves a continuous five capture-release cycle, where adsorption occurs during night time (7:00 pm to 11:00 am; 16 h) and heat-assisted desorption occurs during day-time (11:00 am to 7 pm; 8 h), schematically described in Figure 9a. The representative parameters are portrayed in Figure 9b and

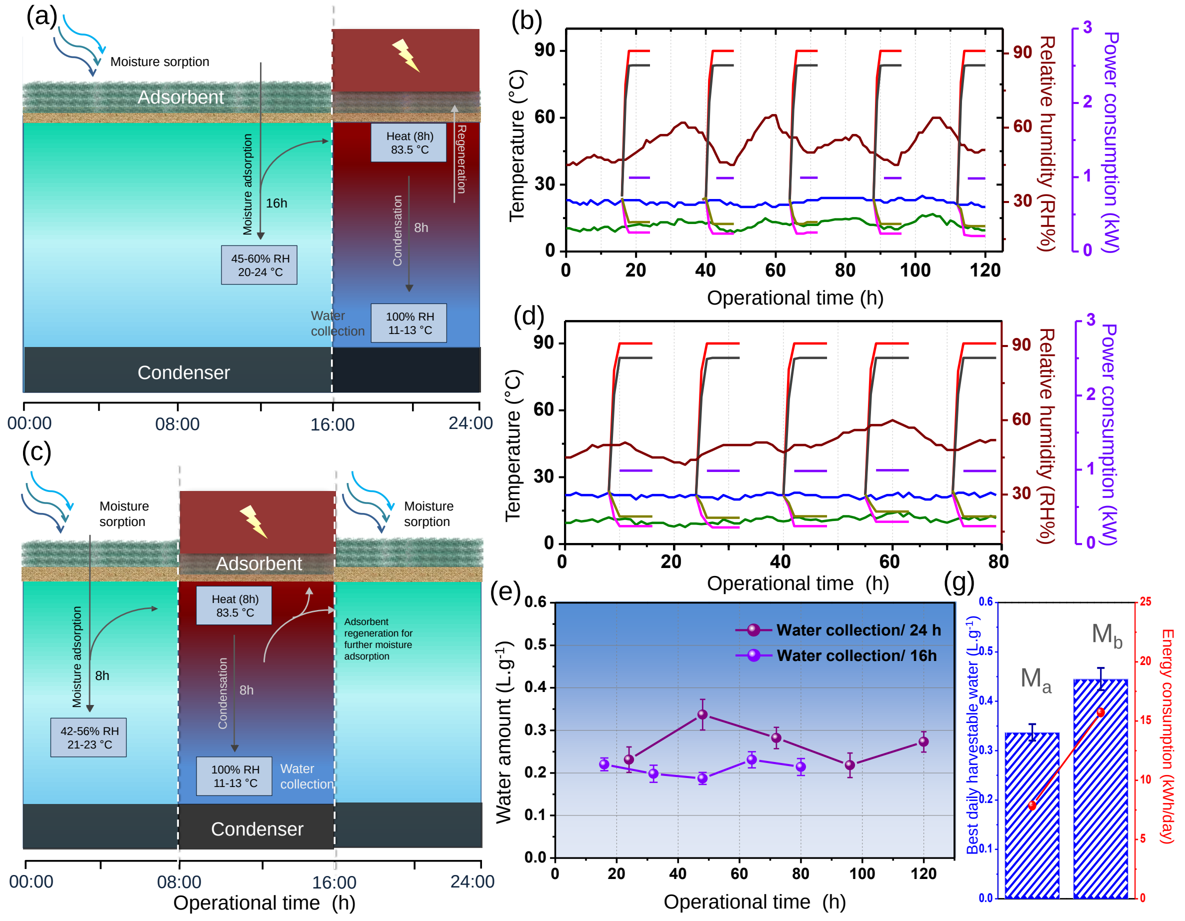

Figure 9: (a) Schematic of indoor water harvesting device and (b) the corresponding boundary conditions for 120 hours sorption-desorption cycle operated through active cooling and heating. (c) Schematic of indoor water generation with one and half cycle per day (capture-release-capture per day) with (d) corresponding boundary conditions for 79 h. (e) Total harvestable water amount after each cycle. (f) Photograph of water condensation inside the wall of the enclosure (1, 2) and final collection on top of the cupper plate (3, 4). (g) Comparative plot with a representation of best water collection rate and corresponding energy consumption per day.

after five days the total estimated water production is 1.34 Lg^{-1} (1.07 gg^{-1}) (Figure 9b). Obviously, this method (M_a) is more realistic compared to the previous experiments because in the course of cyclic studies, the sorbent was activated for the next adsorption during the process of regeneration and subsequently saturated by indoor airborne moisture. As a matter of course, this method actually mimicked the solar-induced atmospheric water harvesting, where water production is governed by solar (natural/artificial) heat during the daytime. Side by side, it is observed that the atmospheric water uptake capacity of the material was not predominantly altered if the sorption time could be reduced from 16 h to 8 h. Thus, the new method (M_b) involves an uninterrupted capture-release-capture cycle per day, where the time limit for each capture and release is 8 h (Figure 9c). To process five consecutive cycles, it requires only 79 h and the corresponding boundary conditions with per cycle water production is recorded in Figure 8d and e. However, the best water collection per day for M_b enhanced 1.32 times (0.445 $Lg^{-1}day^{-1}$) with respect to M_a with an additional energy penalty of 7.76 to 7.93 kWh/day (Figure 9g).

Table 1: Sorption properties of pristine and composite materials.

Sl. No.	MOF	BET Surface area (m^2/g)	Water uptake (ml/g) at P/P_0 = 1.0 (RH% 100)	Water uptake (ml/g) at P/P_0 = 0.3 (RH% 30)
1.	CuBTC	1253	513	386
2.	CuBTC@AC-1	1305	680	487
3.	CuBTC@AC-2	1381	632	415
4.	CuBTC@AC-3	917	355	287
5.	CuBTC@GO	1486	537	356
6.	CuBTC@AC-GO-1	1425	**716**	506
7.	CuBTC@AC-GO-2	1569	687	494
8.	CuBTC@AC-GO-3	1328	689	459

Table 2: Measurement of harvested water amount.

Sample	Date	W_{cap} (Lkg^{-1})	W_{rel} (Lkg^{-1})	η_R (%)	η_{WGC} (%)
CuBTC@AC	25 July	1.506	1.209	80	67.7

CuBTC@AC	26 July	1.506	1.079	71.6	60.40
CuBTC@AC	27 July	1.506	1.138	75.5	63.72
CuBTC@AC	28 July	1.506	1.067	70.8	59.73
CuBTC@AC	29 July	1.506	0.972	64.56	54.42
CuBTC@AC-GO	5 Aug	2.417	1.925	79.67	40.54
CuBTC@AC-GO	6 Aug	2.417	2.161	89.43	45.50
CuBTC@AC-GO	7 Aug	2.417	1.925	79.67	40.54
CuBTC@AC-GO	8 Aug	2.417	1.631	67.48	34.33
CuBTC@AC-GO	9 Aug	2.417	1.513	62.60	31.85
	Relative humidity (%)				
CuBTC@AC-GO	90	0.679	0.431	63.4	51.5
CuBTC@AC-GO	70	0.642	0.387	60.2	52.4
CuBTC@AC-GO	50	0.456	0.242	61.5	53.0
CuBTC@AC-GO	30	0.366	0.247	72.4	67.4
CuBTC@AC-GO	10	0.229	0.157	74.2	68.5

4.1.4: Conclusion

In summary, this chapter has delineated an indoor, portable, widely functional water generator empowered by ternary MOF-clay-graphene composite with the assistance of usual electrical input. Two non-porous templates with hydrophilic sites and integrated with a MOF particle serves as a stimulus to modulate hydrothermal stability and increase the water uptake. The ternary composite exhibits a significant sorption capacity (0.67 Lg^{-1} at 90% RH) and direct water release property regulated by various desorption temperatures, humid environments and multiple sorption-release studies. This enables an uninterrupted water collection with the best value of 0.445 $Lg^{-1}day^{-1}$ through two desorption cycles a day. On the other hand, 0.431 $Lg^{-1}day^{-1}$ of fresh water is collected by regenerating the composite after being exposed to 90% relative humidity. This facile and economic development of materials with adequate water capture-to-release ability for stand-alone indoor atmospheric water generation would pave a way to translate such atmospheric harvester from laboratory to daily life needs.

4.1.5: References

[1] M. M. Mekonnen and A. Y. Hoekstra, *Sci. Adv.* **2016**, *2*, e1500323.
[2] S. L. Postel, G. C. Daily and P. R. Ehrlich, *Science* **1996**, *271*, 785-788.
[3] a) C. J. Vörösmarty, P. Green, J. Salisbury and R. B. Lammers, *Science* **2000**, *289*, 284-288; b) J. Schewe, J. Heinke, D. Gerten, I. Haddeland, N. W. Arnell, D. B. Clark, R. Dankers, S. Eisner, B. M. Fekete, F. J. Colón-González, S. N. Gosling, H. Kim, X. Liu, Y. Masaki, F. T. Portmann, Y. Satoh, T. Stacke, Q. Tang, Y. Wada, D. Wisser, T. Albrecht, K. Frieler, F. Piontek, L. Warszawski and P. Kabat, *PNAS* **2014**, *111*, 3245-3250.
[4] Y. Tu, R. Wang, Y. Zhang and J. Wang, *Joule* **2018**, *2*, 1452-1475.
[5] a) T. Mezher, H. Fath, Z. Abbas and A. Khaled, *Desalination* **2011**, *266*, 263-273; b) V. G. Gude, *Water Research* **2016**, *89*, 87-106; c) M. A. Shannon, P. W. Bohn, M. Elimelech, J. G. Georgiadis, B. J. Mariñas and A. M. Mayes, *Nature* **2008**, *452*, 301-310; d) M. Elimelech and W. A. Phillip, *Science* **2011**, *333*, 712-717.
[6] a) G. Restuccia, A. Freni, S. Vasta and Y. Aristov, *Int. J. Refrig.* **2004**, *27*, 284-293; b) E.-P. Ng and S. Mintova, *Micropor. Mesopor. Mat.* **2008**, *114*, 1-26.
[7] a) D. Lenzen, J. Zhao, S.-J. Ernst, M. Wahiduzzaman, A. Ken Inge, D. Fröhlich, H. Xu, H.-J. Bart, C. Janiak, S. Henninger, G. Maurin, X. Zou and N. Stock, *Nat. Commun.* **2019**, *10*, 3025; b) K. H. Cho, D. D. Borges, U. H. Lee, J. S. Lee, J. W. Yoon, S. J. Cho, J. Park, W. Lombardo, D. Moon, A. Sapienza, G. Maurin and J.-S. Chang, *Nat. Commun.* **2020**, *11*, 5112; c) S. K. Henninger, H. A. Habib and C. Janiak, *J. Am. Chem. Soc.* **2009**, *131*, 2776-2777.
[8] a) X. Liu, N. K. Demir, Z. Wu and K. Li, *J. Am. Chem. Soc.* **2015**, *137*, 6999-7002; b) R. Ou, H. Zhang, V. X. Truong, L. Zhang, H. M. Hegab, L. Han, J. Hou, X. Zhang, A. Deletic, L. Jiang, G. P. Simon and H. Wang, *Nat. Sustain.* **2020**, *3*, 1052-1058.
[9] a) D. Ma, P. Li, X. Duan, J. Li, P. Shao, Z. Lang, L. Bao, Y. Zhang, Z. Lin and B. Wang, *Angew. Chem., Int. Ed.* **2020**, *59*, 3905-3909; b) P. K. Tsobnang, E. Hastürk, D. Fröhlich, E. Wenger, P. Durand, J. L. Ngolui, C. Lecomte and C. Janiak, *Cryst. Growth Des.* **2019**, *19*, 2869-2880; c) R. G. AbdulHalim, P. M. Bhatt, Y. Belmabkhout, A. Shkurenko, K. Adil, L. J. Barbour and M. Eddaoudi, *J. Am. Chem. Soc.* **2017**, *139*, 10715-10722.
[10] Y. Zhang, L. Wu, X. Wang, J. Yu and B. Ding, *Nat. Commun.* **2020**, *11*, 3302.
[11] a) W. Xu and O. M. Yaghi, *ACS Cent. Sci.* **2020**, *6*, 1348-1354; b) M. J. Kalmutzki, C. S. Diercks and O. M. Yaghi, *Adv. Mater.* **2018**, *30*, 1704304.
[12] a) N. Hanikel, M. S. Prévot and O. M. Yaghi, *Nat. Nanotech.* **2020**, *15*, 348-355; b) H. Kim, S. Yang, S. R. Rao, S. Narayanan, E. A. Kapustin, H. Furukawa, A. S. Umans, O. M. Yaghi and E. N. Wang, *Science* **2017**, *356*, 430; c) F. Fathieh, M. J. Kalmutzki, E. A. Kapustin, P. J. Waller, J. Yang and O. M. Yaghi, *Sci. Adv.* **2018**, *4*, eaat3198; d) N. Hanikel, M. S. Prévot, F. Fathieh, E. A. Kapustin, H. Lyu, H. Wang, N. J. Diercks, T. G. Glover and O. M. Yaghi, *ACS Cent. Sci.* **2019**; e) H. Kim, S. R. Rao, E. A. Kapustin, L. Zhao, S. Yang, O. M. Yaghi and E. N. Wang, *Nat. Commun.* **2018**, *9*, 1191; f) A. J. Rieth, S. Yang, E. N. Wang and M. Dincă, *ACS Cent. Sci.* **2017**, *3*, 668-672; g) J. Xu, T. Li, J. Chao, S. Wu, T. Yan, W. Li, B. Cao and R. Wang, *Angew. Chem., Int. Ed.* **2020**, *59*, 5202-5210.
[13] a) A. Karmakar, P. G. M. Mileo, I. Bok, S. B. Peh, J. Zhang, H. Yuan, G. Maurin and D. Zhao, *Angew. Chem., Int. Ed.* **2020**, *59*, 11003-11009; b) G. Yilmaz, F. L. Meng, W. Lu, J. Abed, C. K. N. Peh, M. Gao, E. H. Sargent and G. W. Ho, *Sci. Adv.* **2020**, *6*, eabc8605.
[14] a) P. Küsgens, M. Rose, I. Senkovska, H. Fröde, A. Henschel, S. Siegle and S. Kaskel, *Micropor. Mesopor. Mater.* **2009**, *120*, 325-330; b) N. C. Burtch, H. Jasuja and K. S.

Walton, *Chem. Rev.* **2014**, *114*, 10575-10612; c) J. B. DeCoste, G. W. Peterson, B. J. Schindler, K. L. Killops, M. A. Browe and J. J. Mahle, *J. Mater. Chem. A.* **2013**, *1*, 11922-11932.

[15] a) A. Chakraborty, A. Achari, M. Eswaramoorthy and T. K. Maji, *Chem. Commun.* **2016**, *52*, 11378-11381; b) A. Chakraborty, S. Roy, M. Eswaramoorthy and T. K. Maji, *J. Mater. Chem. A.* **2017**, *5*, 8423-8430; c) A. Chakraborty, S. Laha, K. Kamali, C. Narayana, M. Eswaramoorthy and T. K. Maji, *Inorg. Chem.* **2017**, *56*, 9426-9435; d) K. K. R. Datta, M. Eswaramoorthy and C. N. R. Rao, *J. Mater. Chem.* **2007**, *17*, 613-615.

[16] S. Yang, X. Huang, G. Chen and E. N. Wang, *J. Porous Mater.* **2016**, *23*, 1647-1652.

[17] a) J. E. Martin, A. J. Patil, M. F. Butler and S. Mann, *Adv. Func. Mater.* **2011**, *21*, 674-681; b) K. K. R. Datta, C. Kulkarni and M. Eswaramoorthy, *Chem. Commun.* **2010**, *46*, 616-618; c) K. V. Rao, K. K. R. Datta, M. Eswaramoorthy and S. J. George, *Angew. Chem., Int. Ed.* **2011**, *50*, 1179-1184; d) K. K. R. Datta, A. Achari and M. Eswaramoorthy, *J. Mater. Chem. A.* **2013**, *1*, 6707-6718; e) S. Liu, L. Sun, F. Xu, J. Zhang, C. Jiao, F. Li, Z. Li, S. Wang, Z. Wang, X. Jiang, H. Zhou, L. Yang and C. Schick, *Energy Environ. Sci.* **2013**, *6*, 818-823.

[18] A. J. Patil, E. Muthusamy and S. Mann, *Angew. Chem., Int. Ed.* **2004**, *43*, 4928-4933.

[19] a) H.-J. Shin, K. K. Kim, A. Benayad, S.-M. Yoon, H. K. Park, I.-S. Jung, M. H. Jin, H.-K. Jeong, J. M. Kim, J.-Y. Choi and Y. H. Lee, *Adv. Func. Mater.* **2009**, *19*, 1987-1992; b) Z.-J. Fan, W. Kai, J. Yan, T. Wei, L.-J. Zhi, J. Feng, Y.-m. Ren, L.-P. Song and F. Wei, *ACS Nano* **2011**, *5*, 191-198.

[20] E. Lecrivain, G. Laroche and A. Vallot, *Inter. J. Refrig.* **1982**, *5*, 221-225.

[21] P. Byrne and R. Ghoubali, *Appl. Therm. Eng.* **2019**, *149*, 414-424.

[22] D.-D. Zu, L. Lu, X.-Q. Liu, D.-Y. Zhang and L.-B. Sun, *J. Phys. Chem. C .* **2014**, *118*, 19910-19917.

[23] X. Liu, X. Wang and F. Kapteijn, *Chem. Rev.* **2020**, *120*, 8303-8377.

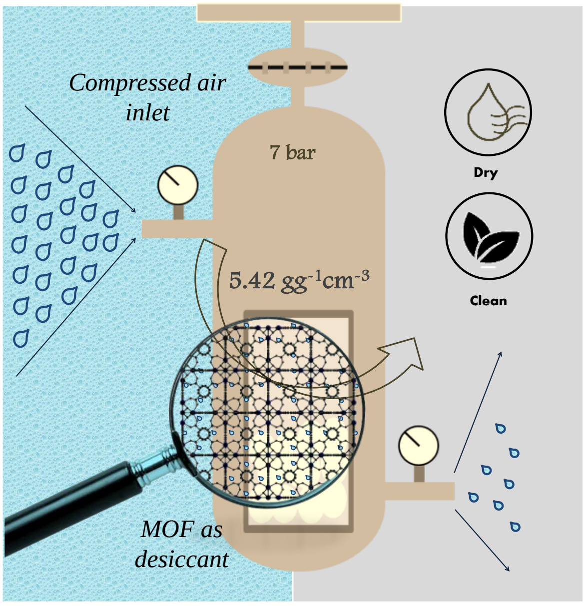

4.2: Metal-Organic Framework as Next-Generation Dehumidifier Desiccant for Compressed Air Dryer

Manuscript under preparation

Abstract

Urbanization is inevitable. Rapid growth in population and massive rural-to-urban migration has steadily increased building energy account 20-40% of total energy consumption in the last two decades. In most urban areas the electricity demand for indoor heating, ventilation and air conditioning (HVAC) grabbed the lion's share of total power consumption. In this context, a desiccant cooling system (DCS) is extremely efficient to provide satisfied air supply with a convenient temperature and humidity ratio compared to the traditional compression cooling system (CCS). This chapter reveals the design and manifestation of a prototype device based on MOF (UiO-66) and MOF-composite (UiO-66@Aminoclay) that captures moisture from compressed air under ambient to 7 Bar pressure. The device exhibits a 54% improvement in operational time and a 44% increase in moisture sorption efficiency (5.42 gm^{-3} of moisture capture per gram of material) compared to commercially used activated alumina. The study also considers the total change in heat allocation and reduction in atmospheric carbon concentration throughout the measurements.

4.2.1: Introduction

As the world continuous to urbanize, the incessant advancement and deployment of energy-saving technologies offer the outstanding potential to uphold ever-increasing energy demand. These developments also, subsequently support the reduction in carbon footprint and worldwide consumption of renewable energy.[1] To affords a better living quality; it consumes approximately 40% of total global energy needs which is not less than the quantity consumed by industry and transport.[2] For domestic and non-domestic buildings, combining the rise in duration spent inside, the enhancement in building facility and comfort level have elevated electricity demand for heating, ventilation and air conditioning systems (HVAC) to regulate indoor temperature, humidity and air circulation.[3] From the perspective of indoor air constitution, thermally driven adsorption-based heat pumps (AHP) or desiccant cooling systems (DCS) are considered because of their significant productivity quotient, labor reduction, and sensible consumption of electric power.[4] In a typical desiccant cooling system, the compressed air is passed through a desiccant 'bed' that attracts moisture from the air by providing an area of low vapor pressure at the surface of desiccants. As the partial pressure of the water in compressed air is more, thereby the water molecules move from the air to the desiccant by making adjacent air dehumidified. The complete process is regenerative. After being saturated by the humidity, the desiccants release their moisture into the reactivation air, when submitted to regeneration energy (heating or hot air circulation).[5] The energy efficiency, working capacity and coefficient of performance of such compressed air desiccant cooling system (DCS) are directly proportional to the water storage capacity of the desiccant.[6] However, these materials offer extensive research has been dedicated in search of smart and efficient material including industrially surviving materials such as zeolite, silica and alumina that unfortunately offerings high energy expenditure with low regeneration capacity.[7]

Metal-organic frameworks, or MOFs, a unique class of crystalline porous material with exceptional porosity, unprecedented surface area, tunable pore size, remarkable chemical and thermal stability, have enjoyed widespread acceptance for addressing enduring social challenges, such as environmental deterioration and energy crisis.[8] Despite having so many attractive features, until the previous decade, MOF was inapt for commercial implementation due to lack of water stability. Generally, most of the MOFs with moisture treatment could lead to structural decomposition, phase transformation, or ligand displacement.[9] However, with an improved understanding of structural stability under moisture exposure, plenty of water-stable MOFs are being published that paving the way towards many important applications such as heat pump[10], humidity control[11], dehumidification[12], thermal batteries[13] and water harvesting[14]. From the mechanistic point of view, the diverse range of water adsorption behavior of MOF makes them promising in terms of facile water capture at low relative pressure range and the associated stability, recyclability and high uptake leading to superior working efficiency.[6, 9b, c, 13, 15]

In this respect, Zirconium-based MOFs taking the leading position because of their notably high surface area and steadiness against both thermal and humid conditions.[13, 16] UiO-66 is regarded as a typical MOF is built up from the inorganic building blocks Zr_6-octahedra with an inner $Zr_6O_4(OH)_4$ core bonded to twelve 1,4-benzene dicarboxylate (BDC) linkers, has attracted overly attention due to its high water resistance, along with a high chemical, thermal and mechanical stability.[17] Furthermore, the UiO-66 exhibited type-V reversible water adsorption isotherm with gradual uptake by keeping condensation step far from low relative pressure. These features make UiO-66 a potential material for water adsorption in a broad working humidity range.[13, 18] The fast (simple sorption-desorption kinetics), energy efficient (low-temperature heating) and facile (low isosteric heat of adsorption) regeneration *via* simple pressure/temperature swing and high-pressure sustainability make it an appropriate choice for desiccant air dryer.[17c, 19] Herein, the chapter unfolds a strategy of synthesizing UiO-66 under the microwave (UiO-66M) and its stabilization on 2D functional scaffold such as aminoclay (UiO-66M@AC-*x*). Recently, Maji *et al.* have demonstrated the growth and stabilization of MOF nanoparticles on layered materials namely nanoclay[20], aminoclay[21], graphene oxide[22], and functional graphene oxide[23]. Aminoclay (AC) or Aminopropyl-functionalized magnesium (organo) phyllosilicate, is a highly water dispersible two-dimensional synthetic layered compound, commonly perform as a functional template to house metal nanoparticles or organic chromophores for several photo and electrocatalytic applications.[24] Particularly, four composites (UiO-66M@AC-*x*; *x* depends on added clay concentration) were synthesized under microwave conditions by dispersing AC in a water-ethanol mixture followed by the addition of the precursor solution of UiO-66. The amine group in AC, as anticipated, can act as a metal-binding site to stabilize MOF particles; likewise, it can also offer additional hydrophilic sites for water adsorption. The resulting composite, as expected, would show enhanced water uptake through the passage between AC layers and particles' interfaces (Scheme 1). Such integration of two or three components provides a synergistic effect to achieve improved surface area, and superior water adsorption and release efficiency under atmospheric or compressed humid environment.

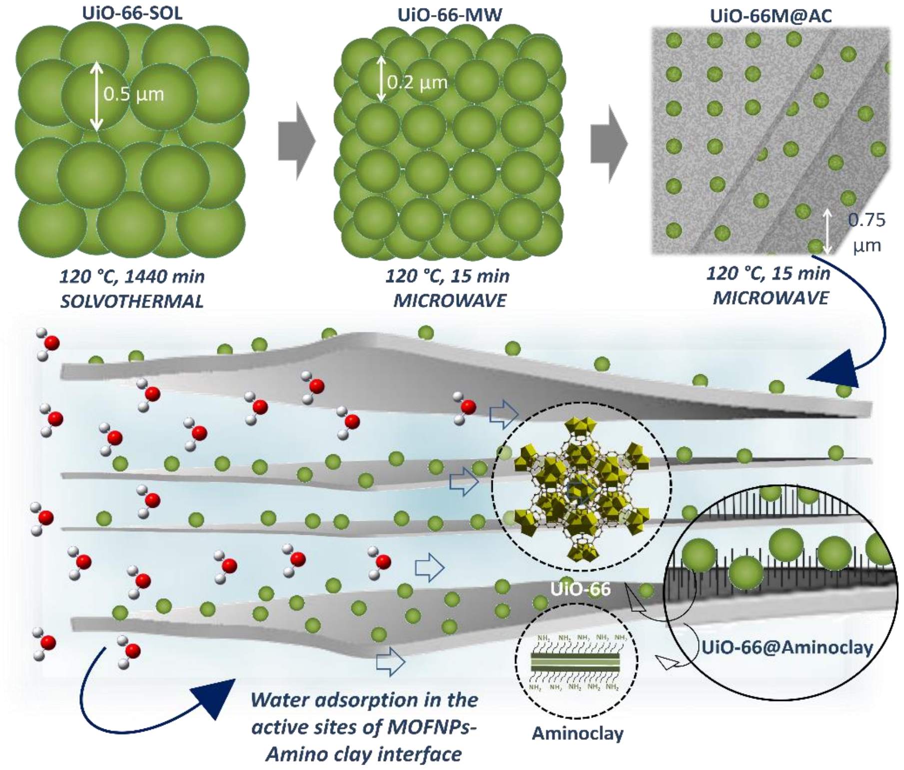

Scheme 1: Downsizing MOF particles by using microwave heating method and further reduction is achieved by a synergistic effect of template-assisted MOF growth and microwave stimuli (top). Schematic representation of composite for water sorption in hydrophilic MOF surface and MOF-aminoclay interfaces (bottom).

In industries, desiccant air dryers are comprised of two adjacent towers filled with desiccant materials. At a time one tower is used for drying and another tower is for regeneration. The compressed air passes through the piston valve and enters the drying tower where the desiccants adsorb its moisture and then release it downstream. Thereafter, the dry air travels through the saturated desiccant and pulls off the water while the alternate tower dries the incoming air. The complete process operates on the principle of heatless regeneration and the physical property of desiccant to adsorb and release moisture.[25] Finally, a prototype MOF based compressed air dryer prototype was built and that demonstrated the efficiency of MOF and MOF composite materials as next-generation desiccant material. Experiments were performed in this prototype with MOF (UiO-66, UiO-66M) and MOF-composites (UiO-66M@AC-10) under the working range of ambient to 7 bar pressures. The best performance is achieved with a composite having ~7.3% AC content, which shows a 44% increase in moisture sorption performance compared to commercial desiccant (activated alumina) under a compressed-pressure chamber.

4.2.2: Experimental section

4.2.2.1: Materials

All the reagents and chemicals are commercially available and used without additional purification. Zirconium(IV) chloride (anhydrous, powder, 99.99% trace metals basis), Benzene-1,4-dicarboxylic acid (H_2BDC), 3-aminopropyltriethoxysilane, Magnesium chloride, N, N`- dimethylformamide were obtained from the Sigma-Aldrich Chemical Co.

4.2.2.2: Synthesis

AC synthesis: Aminoclay (AC) was synthesized following typical reaction conditions as reported by Mann and co-workers.[25] 3-aminopropyltriethoxysilane (5.85 mmol, 1.3 mL) was added dropwise to an ethanolic solution of $MgCl_2$ (3.62 mmol, 0.84 g) in ethanol (20 g). The obtained white slurry was stirred overnight and the precipitate was isolated by centrifugation, further washed in ethanol, and dried at 40 °C.

UiO-66-SOL: UiO-66, prepared under solvothermal condition, synthesized by following previously reported method.[17a] 0.053 g of $ZrCl_4$ (0.227 mmol) and 0.034 g (0.227 mmol) H_2BDC was dissolved using in 25 g DMF and the obtained mixture was sealed and placed in an oven at 120 °C for 24 h. Further the resulting solid was filtered, frequently washed in DMF, and dried under ambient temperature.

UiO-66M: Microwave-assisted UiO-66 synthesis was performed by following previously reported procedure.[26] Here, 'M' stands for microwave. 0.29 g of $ZrCl_4$ (1.25 mmol) and

0.034 g H_2BDC (1.25 mmol) was dissolved in 10 mL DMF. Further 2.1 mL of acetic acid (7.5 mmol) and 0.135 mL water (7.5 mmol) were added to the above reaction mixture. The precursor solution was subjected to microwave heating (MONOWAVE 200) at 120 °C for 15 mins. Thereafter, the reaction container is cooled to room temperature, centrifuged to obtain the product, washed multiple times by using DMF and acetone and finally dried at 60 °C.

UiO-66M@AC-x: 5/10/15/20 mg (x) of AC dissolved in 3 mL water and 2 mL water, stirred for 30 mins. Therefore, MOF precursors were added to the previous solution in DMF. The rest of the reaction condition is similar as it is mentioned above (UiO-66M).

The materials are synthesized approximately 3 g each by combining multiple reaction products of several batches. The combined precipitate was collected and washed 4-5 times daily with DMF and acetones and subsequently dried in air. Air-dried samples were transferred into a vacuum chamber. The chamber was first evacuated at room temperature for few hours until the pressure drops below 10^{-1} Pa. After that, the sample was heated in a vacuum at 140 °C for 18 hours.

Prior to every experiment in the compressed chamber, the synthesized material was evacuated at high temperature (120 °C) and high vacuum (<1 Pa). The sample weight was estimated before and after the evacuation of every measurement and readily transferred to the compressed/dehumidifier chamber.

4.2.2.3: Physical measurements

Powder X-ray diffraction (PXRD) patterns were recorded using a Bruker D8 Discover instrument using Cu–Kα radiation. In-situ DRIFT spectra were recorded on a Bruker, Vortex 70v, equipped with an in-situ diffuse reflection chamber and highly sensitive MCT detector cooled by liquid N_2. The sample (~15 mg) was finely ground and placed into a designed reaction cell equipped with a ZnSe window. The cell was connected with three connectors, one for flowing humid air, one for creating a vacuum and the other one for acquainting the chamber's relative humidity. The sample was treated with exact humidity by adjusting humid flow and vacuum creation. Inductively Coupled Plasma-Atomic Emission Spectroscopy (ICP-AES) measurements were recorded on Perkin Elmer Optima 7000dv ICP-AES instrument. The samples were prepared by dispersing the sample in

MeOH and then dropping 5 μL of the solution onto a small piece of silicon wafer and drying it into the air. Transmission electron microscopy (TEM) images were taken with a JEOL JEM-3010 transmission electron microscope operating at 200 kV. The samples were prepared in the same way as described above, but the drop cast was made onto a carbon-coated TEM grid. Reactions under microwave stimuli were carried by transferring reaction mixture in 30 mL wide-neck vials by using MONOWAVE 200 (Anton Paar Monowave Series; Serial Number: 81919734; Instrument Software Version: 4.10.9376.7) microwave reactor. Adsorption isotherms were recorded with the desolvated samples using QUADRASORB-SI analyzer and AUTOSORB IQ$_2$ instrument. Water vapor adsorption isotherm measurements at 298 K were carried out on a fully BELSORP-aqua volumetric adsorption instrument from BEL, Japan. The helium used for the adsorption measurements is of scientific/research grade with 99.999% purity. To prepare the desolvated samples, approximately 100-150 mg of sample was degassed under 10^{-1} Pa vacuum for overnight (~12-16 hours) before the measurements. To understand released air quality the relative percentage of outlet gas was analyzed by gas chromatography (Agilent 7890 B).

4.2.2.4: Device fabrication

The dehumidifier chamber, as shown in Figure 1, is comprised of three compartments, where the bottom one is made up of hard polycarbonate to minimize temperature transfer to the environment. Three respective sensors; pressure, dew point and temperature were fixed with the middle part of the dehumidifier to evaluate the change in such physical parameters before, after and during experimental conditions. This chamber temperature was maintained at ~25 °C throughout the entire process. It is connected to the compressed air pump (BAC compressor) which can dose approximately 8 Bar pressure to the chamber starting from the ambient pressure. The compressed air pressure was maintained at around 1, 2, 3, 4, 5, 6 and 7 Bar, monitored by using an integrated pressure sensor (Measurements Specialities, INC, Hampton, VA, USA; Model no., MS 256-000012-016BG) and inlet/outlet digital pressure gauge (Equinox, EQ-DPG-801). Adjusted flow control, flow regulatory valves and stainless-steel lines are obtained from Chemix Speciality Gases and Equipment, Bangalore. All the associated parameters such as dew point, dew frost point, wet bulb temperature, water content, volume

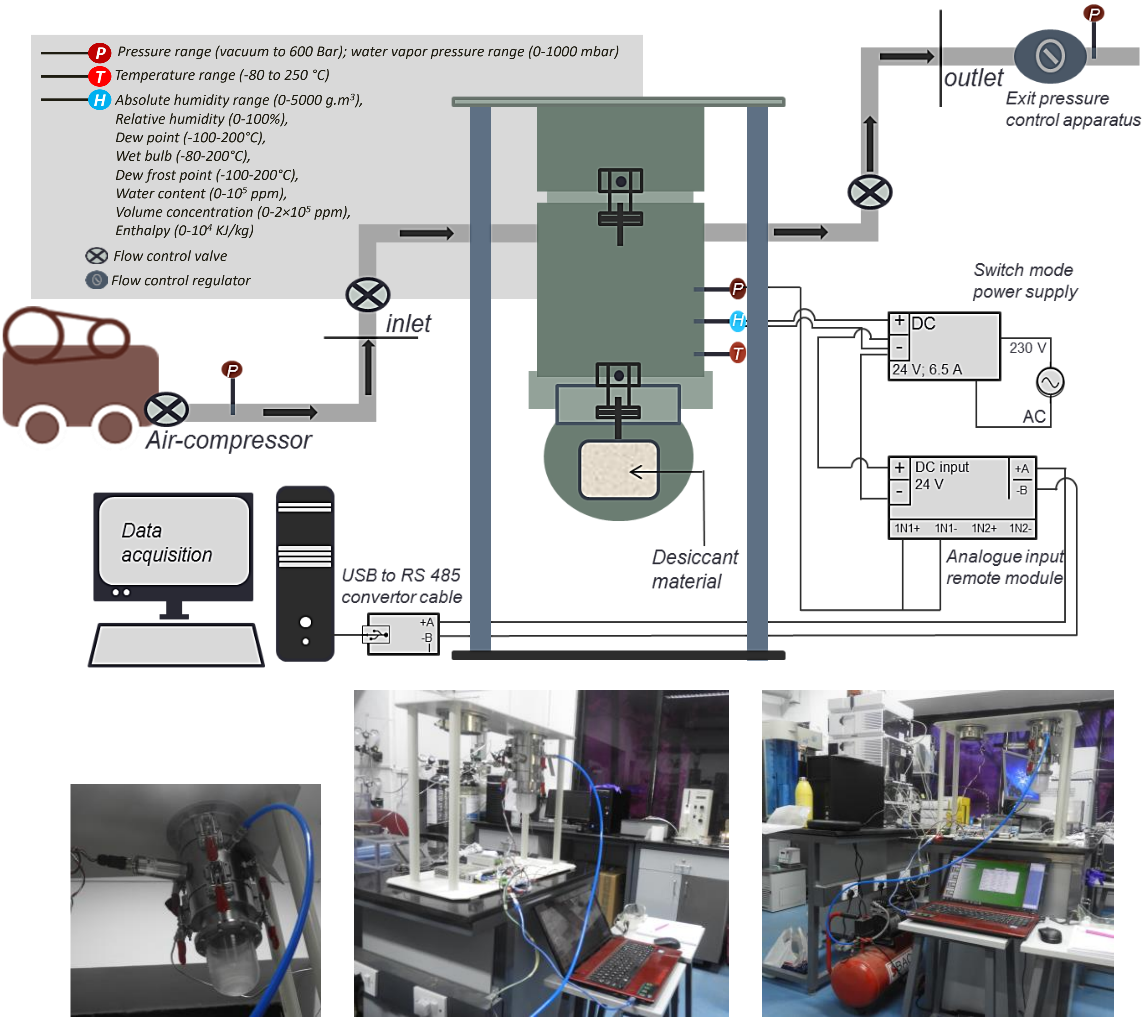

Figure 1: A detailed device blueprint and corresponding sensors' specification (top) with the photograph of the customized set-up (bottom).

concentration, enthalpy, absolute and relative humidity were described by humidity or dew-point sensor (EE355-PA1SAL-100; Model IP65) across the measurement. The electronic data was translated through USB to RS485 serial converter and recorded by software (EE configurator and Docklight). Industrially obtained activated alumina (identical amount, ~ 3 g) was treated equally and the time of saturation is approximately double as compared with MOF materials. However, the additional air quality tests were performed by considering the inlet and outlet concentration of N_2, O_2 and CO_2 through gas chromatographic technique (Agilent 7890B) by using polymer-grade Argon as carrier gas. The relative decrease in CO_2 gas concentration in the outlet with respect to the inlet exhibits the DAC capacity of the MOF under a compressed environment (Figure 9).

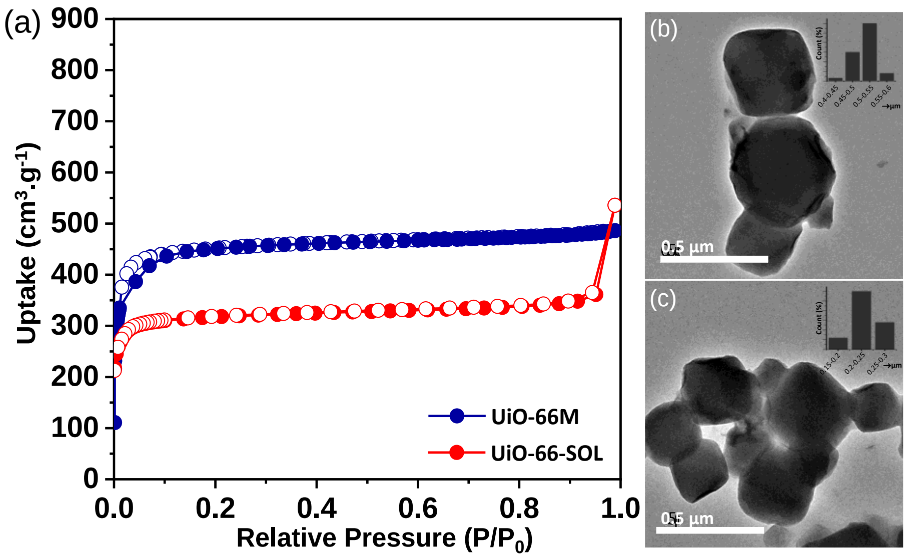

Figure 2: (a) N_2 adsorption-desorption isotherm measured at 77 K. (b) TEM images of (b) UiO-66-SOL and (c) UiO-66M with particle size distribution histogram (*inset*).

4.2.3: Results and discussion

Various rational downsizing techniques that bring micro-sized MOF into nano-domain were shown to further benefit from the inherent properties of the MOF by retuning their surface-to-volume ratio.[27] Here, the fast nucleation technique such as microwave heating has been adopted, while the BET surface area is improved from 1294 (UiO-66-SOL) to 1574 (UiO-66M) m^{2}g^{-1}, by reducing particle size and increasing surface-to-volume ratio (Figure 2). However, the N_2 adsorption isotherm at 77 K for UiO-66-SOL and UiO-66M exhibits a characteristic type-I adsorption profile with micropore entered at 1.2 nm (as calculated from NLDFT pore size distribution). TEM images with corresponding size distribution revealed the reduction in particle size from 500-550 nm to 200-250 nm as a consequence of faster nucleation through microwave heating (Figure 2b, c). Furthermore, by combining two approaches, template-assisted and bottom-up microwave heating, 20-25 nm sized UiO-66NPs were accustomed on aminoclay 2D matrix (UiO-66M@AC). To prepare UiO-66M@AC composites, the clay concentration was varied by keeping a fixed precursor ratio of MOF and the respective composites are designated as UiO-66M@AC-5, UiO-66M@AC-10, UiO-66M@AC-15 and UiO-66M@AC-20. The clay contents were found to be 2.48, 5.95, 6.2 and 7.3%, respectively for UiO-66M@AC-5, UiO-66M@AC-10, UiO-66M@AC-15 and UiO-66M@AC-20, as obtained from the inductively

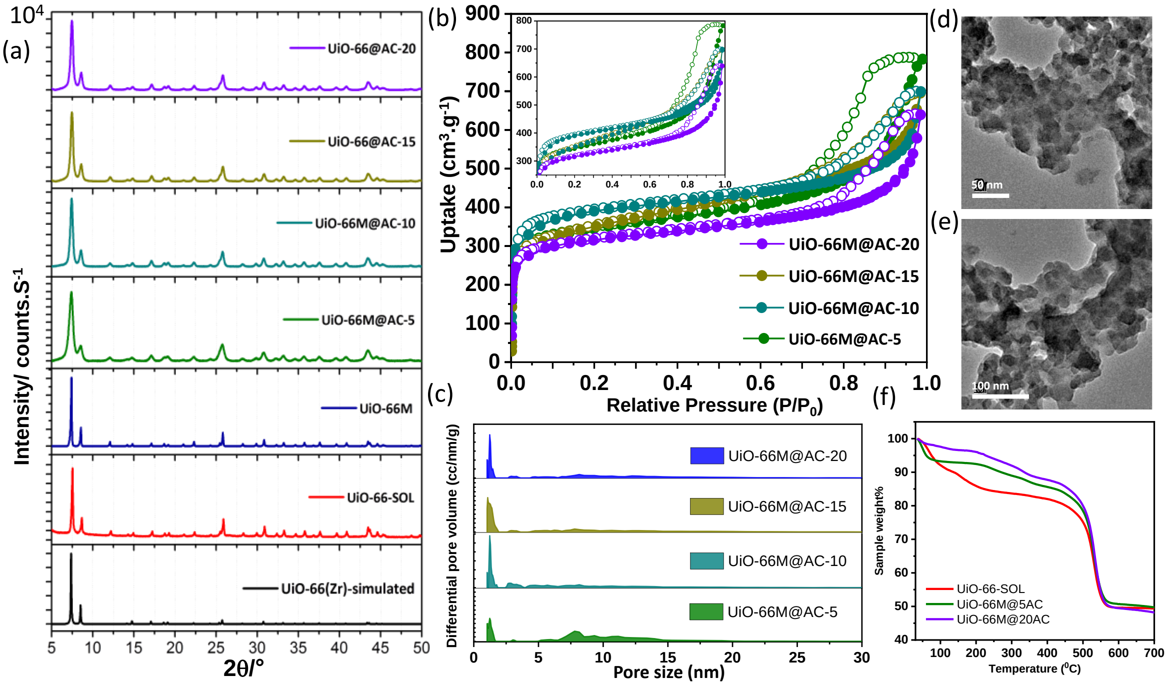

Figure 3: (a) PXRD patterns of MOF and related composites, (b) N_2 ads-des isotherm measured at 77 K for all composites and (c) calculated NLDFT pore size distribution, (d, e) TEM images of UiO-66M@AC-10 showing the distribution of MOF nanoparticles on clay matrixes, (f) TGA profile of two composites with solvothermally prepared parent MOF.

coupled plasma atomic emission spectrometry. The well-correspondence of powder X-ray diffraction patterns of UiO-66-SOL, UiO-66M and four composites are with pristine framework approves the formation of pure crystalline phase of the materials in UiO-66M@AC. The slight peak broadening in composites compared to UiO-66-SOL and UiO-66M pattern esteems the wide reduction in particle size (Figure 3a). The loading of aminoclay template provides thermal stability to the overall composites as revealed from thermogravimetric analysis (Figure 3f). TEM images showed further downsizing of the MOF particles in the range of 20-25 nm, which are distributed on the clay surface. Aminoclay template can be instrumental towards variation in porosity of the composites as observed in morphology and thermal stability test. The N_2 adsorption-desorption measurement was performed at 77 K for all synthesized composites and the calculated BET surface areas of composites, are found to be 1096, 1236, 1142, and 996 m^2g^{-1}, respectively (Figure 3b). Interestingly, these isotherms largely differ from pristine profile and exhibits a combine isotherm of type-I and type-IV. One of the major characteristics of type-IV is its hysteresis, which is associated with capillary condensation in mesopores, observed a limiting uptake in the range of high relative pressure (P/P_0). As observed in Figure 1b (also in inset), the hysteresis loop was found in P/P_0 ~ 0.75-0.99 resembling H4 type that attributes particle with internal voids of narrow slit-like pores irregular shape and broad size distribution.[28] Obviously, the free amine groups of exfoliated AC act as a seed to grow the MOF nanoparticles offered some interfacial voids between multiple-stacked MOF@clay matrixes. This was validated by the formation of these additional pores as evidenced from the NLDFT pore size distribution (PSD) plot (Figure 3c). The PSD of UiO-66M@AC showed the additional pore population at mesoporous range of 3, 5-11 nm including its intrinsic microporosity at 1.2 nm. The pores in different regions and the corresponding micro and mesopore volume ratios for all the composites are documented in Figure 1c and Table 1.

Table 1: Physical characteristics and sorption properties of UiO-66 MOF and composites.

Sample	Aminoclay weight%	Particle size (µm)	Total BET surface area (m^2g^{-1})	PSD (nm)	V_{micro}/V_{meso}
UiO-66-SOL	--	0.5	1294	1.2	--
UiO-66M	--	0.25	1574	1.2	--
UiO-66M@AC-5	2.48	--	1096	1.2, 3, 5-11	0.357
UiO-66M@AC-10	5.95	0.025	1236	1.2, 2.5-3.8	1.024
UiO-66M@AC-15	6.20	--	1142	1.2, 3, 7-8.5	0.745
UiO-66M@AC-20	7.30	--	996	1.2, 3, 7-8.5	0.696

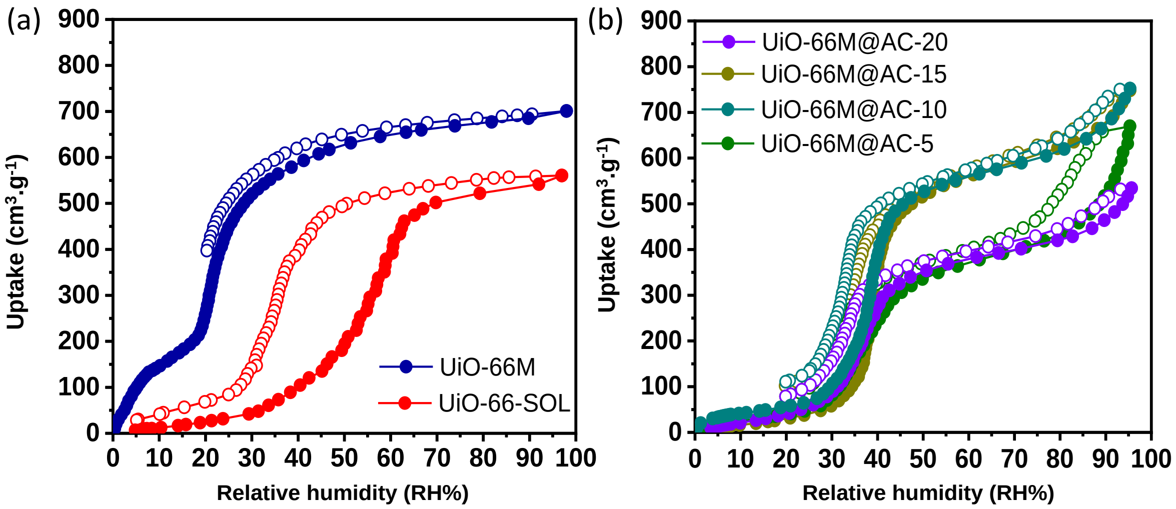

Figure 4: Water adsorption-desorption isotherm for (a) UiO-66-SOL, UiO-66M; and (b) composites (UiO-66M@AC-5)

4.2.3.1: Water sorption towards air-drying: ambient and high-pressure conditions

Having observed bimodal porosity of the composites, its water sorption profile was further studied along with UiO-66-SOL and UiO-66M. The water sorption studies for UiO-66-SOL exhibited 545 ml/g maximum water storage capacity (W_c),[13, 29] while UiO-66M showed comparatively higher W_c (692 ml/g) with sharp low-pressure uptake at 0.18 P/P_0 (18.42% relative humidity or RH, Figure 4a). Remarkably, in association with aminoclay, the water sorption isotherm revealed an *S*-shaped profile at 298 K, exhibiting a sharp uptake between ~30-40% relative humidity with a W_c for UiO-66M@AC-5, UiO-66M@AC-10, UiO-66M@AC-15 and UiO-66M@AC-20 are 669, 751, 748 and 534 mL/g, respectively under ambient temperature and pressure condition (Figure 4b). As observed from the sorption profile in Figures 4a and b, the composites differ predominantly in two respects from the pristine MOF. First, UiO-66M@AC-10 and UiO-66M@AC-15 exhibited enhanced W_c than pristine MOF (UiO-66-SOL and UiO-66M). Second, the composites show typical *S*-type isotherm with one major and minor steep in water uptake at 0.25-0.35 P/P_0 (25-35% RH) and ~ 0.8 P/P_0 (>80% RH), while MOF shows a typical type-V sorption curve with major uptake at 0.3 (33% RH for UiO-66-SOL) and 0.18 P/P_0 (UiO-66M). However, the minor steep in water sorption (at >0.8 P/P_0) for composites are generated due to the capillary condensation at the MOF-clay interfaces,

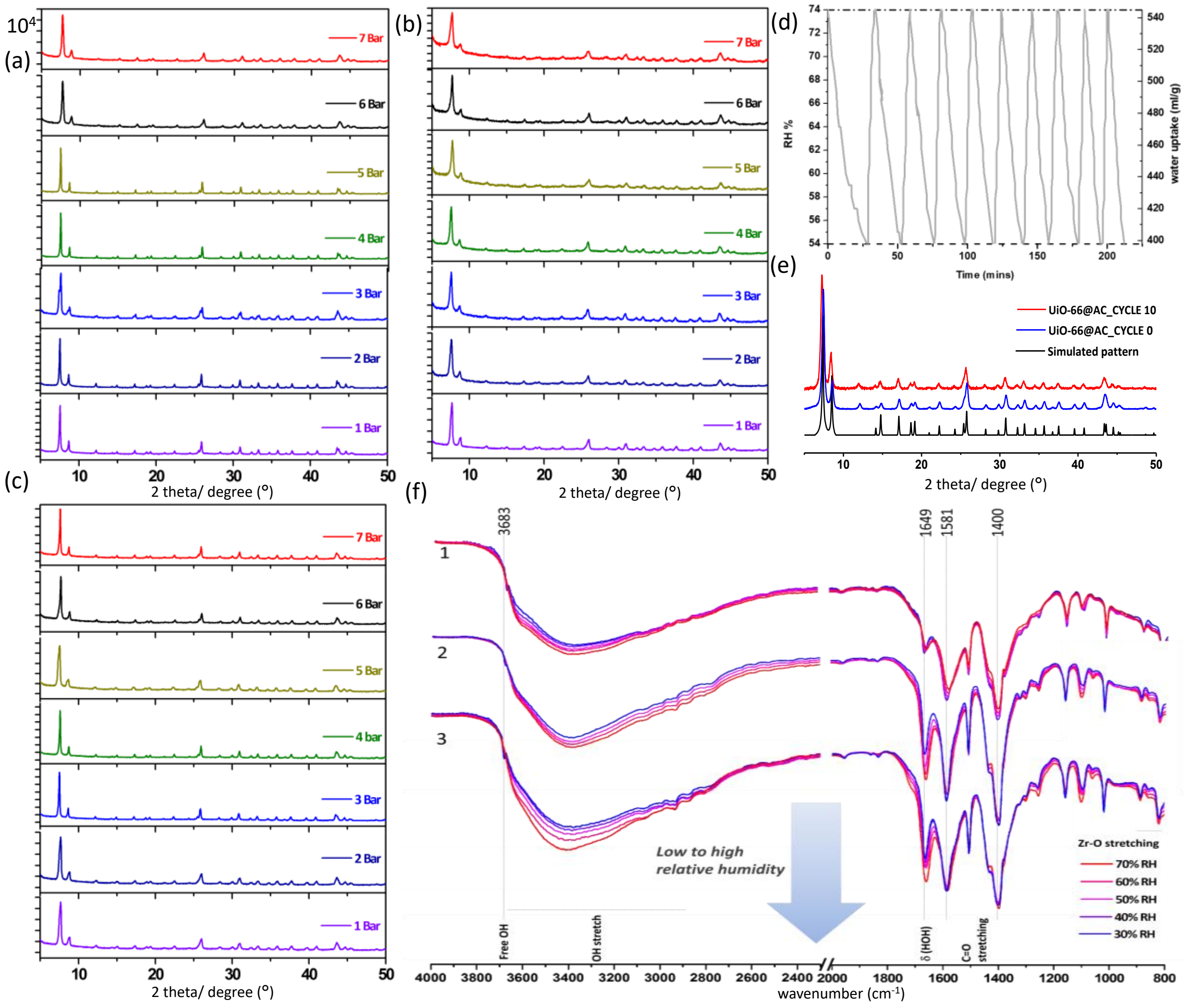

Figure 5: PXRD patterns of (a) UiO-66-SOL, (b) UiO-66M, and (c) UiO-66M@AC-10 after keeping it in high-pressure chamber at varied compressed air pressure (1-7 Bar). (d) 10 cycles of water uptake profile to relative humidity at 298 K. (e) Stability study of UiO-66M@AC-15 after 10 cycles and compared concerning its initial and pristine pattern by powder-XRD. (f) In-situ FTIR of UiO-66-SOL (1), UiO-66M (2), and UiO-66M@AC-15 (3) at different humid environment (30-70% RH).

rapidly filled with the clustered water molecules at a higher relative humidity regime (>0.8 P/P_0 or 80% RH). To put these results in perspective with the atmospheric moisture sorption beyond ambient pressure, a series of comparative studies under 1 to 7 Bar compressed air pressure was performed aiming at determining which composite (UiO-66M@AC-10) had the best performing water sorption capacity at 298 K under ambient pressure. The study has been restricted only to comparing UiO-66 (prepared through both solvothermal and microwave heating) to commercial desiccants (activated alumina); however, other hydrophilic sorbents might be fascinating for such benchmark experiments.

As shown in Figure 1, experiments were performed in a pressure-controlled chamber (operated ambient to 7 bar air-pressure) associated with air-compressor, humidity, temperature and pressure sensor. Further, the structural durability of UiO-66-SOL, UiO-66M and UiO-66M@AC-10 was examined by in-situ DRIFT and powder X-ray study by increasing humidity (30-70% RH) and compressed air-pressure (~1 to 7 bar), respectively. The results exhibited the structural integrity of all adsorbents under such rugged conditions (Figure 5). Similarly, as shown in Figure 3e, the composites recyclability was tested by executing sequential non-equilibrium sorption-desorption (in the range to near comfortable humidity[30] i.e., 55 to 75% RH) with the assistance of mild temperature swing. The plot exhibits no significant deterioration in efficiency even after 10 cycles (Figure 5d, e).

Table 2: Water sorption properties of parent MOF and composite materials.

Sample id	BET surface area (m^2g^{-1})	Water sorption (mLg^{-1})	High pressure moisture sorption ($gg^{-1}m^{-3}$)
UiO-66-SOL	1294	545	4.15
UiO-66M	1574	692	5.02
UiO-66M@AC-5	1096	669	--
UiO-66M@AC-10	1236	751	--
UiO-66M@AC-15	1142	748	5.42
UiO-66M@AC-20	996	534	--

It is worth noting that compressed air is nothing more than a form of condensed atmospheric air at higher concentrations. The diffusion rate of water molecules could be different at different locations depending on their atmospheric moisture content. Therefore, the water concentration in various forms (water vapor pressure, water content in ppm, absolute and relative humidity) through the inlet humidity sensor prior to the sorption experiments were also measured (Figure 7). For effective dehumidification, water sorption was measured at high pressure, and evidently, as revealed from Figure 6a, the moisture sorption capacity at ~7 bar of UiO-66M@AC-10 is 5.42 $gg^{-1}m^{-3}$, which is more than that of UiO-66M (5.02 $gg^{-1}m^{-3}$) and UiO-66-SOL (4.15

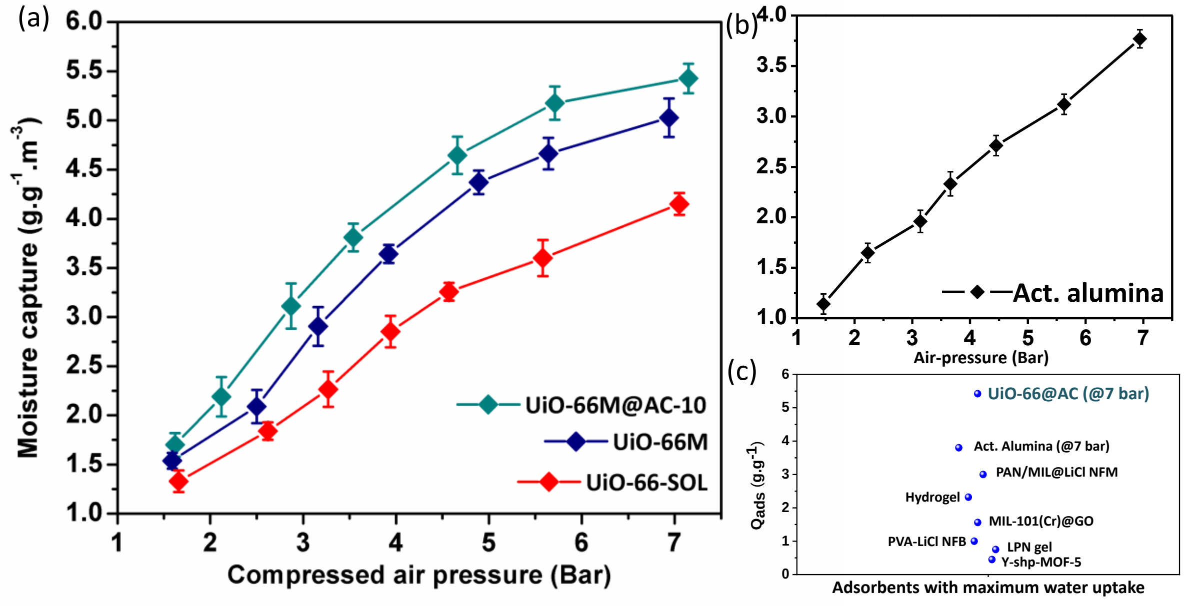

Figure 6: (a) Moisture uptake for UiO-66-SOL (red), UiO-66M (blue) and UiO-66M@AC-10 (cyan) in respect to compressed air pressure (b) Moisture sorption capacity of commercially available activated alumina under same pressure window. (c) A comparative chart of the moisture absorption capacity for some reported representative desiccant materials.

gg^{-1}m^{-3}) under the same compressed air pressure (P_c) (Figure 4a). Note that, moisture capture at each pressure was acquired individually by using activated materials. Accordingly, the total measurement time has been reported by taking ~3 g of activated material in each case and compared them in Figure 7c. However, the measurement uncertainty of all experimental moisture sorption and other related parameters are studied against air pressure was in 10% error bars. Significantly, the pore geometry of UiO-66 and the non-porous amine-functionalized layered structure of clay (AC) provides good support for the successful growth and stabilization of MOF NPs.

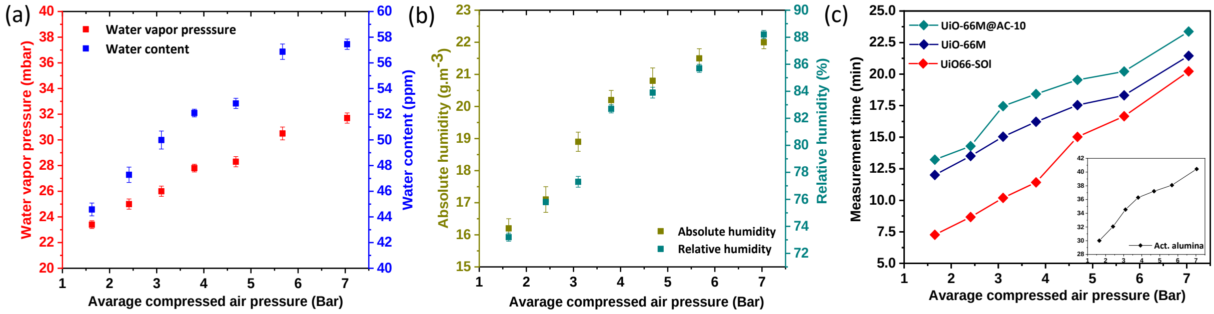

Figure 7: (a), (b) Water content status (vapor pressure, concentration in ppm, absolute and relative humidity) prior to sorption measurement. (e) Measurement time vs. average compressed air pressure (P_{avg}) reveals the faster kinetics of moisture storage to the material as compared to alumina.

With the assistance of superior structural dynamicity of clay and interfacial voids between MOF-clay and clay-clay surfaces, thus generated, enhanced the water holding capacity and long-term stability of the composite. To further evaluate the advantages of UiO-66M@AC-10 for moisture sorption, the capacity is quantitatively compared and this composite possesses the highest rank over all other previously reported materials.[31] Such moisture capacity was measured at each pressure based on the weight of activated materials, calculate it as follows;

$$Moisture\ capture = (W_a - W_d)/\mathrm{d} \qquad (1)$$

Where, W_a absolute humidity ratio of the air stream ($\mathrm{gm^{-3}}$); W_d humidity ratio in equilibrium with the desiccant ($\mathrm{gm^{-3}}$) and d represents the activated weight of the material (g).

Moreover, the change in water content both in ppm and relative humidity has been recorded in Figure 7a, b concerning average compressed air pressure (P_{avg}). Further, the water adsorption performance with time was evaluated and compared with respect to alumina beads (Figure 7c, *inset*). As shown in Figure 7c, the complete measurement time at P_{avg} was recorded and at 7 bar pressure, all UiO-66 series shows on an average ~21 min time (23.37, 21.44 and 20.21 min for UiO-66M@AC-10, UiO-66M and UiO-66-SOL, respectively) for moisture sorption, while for alumina it is 44.4 min.

4.2.3.2: Internal heat allocation towards cooling

The resulting air temperature though out the process is difficult to measure as 75% of the total device is made up of stainless steel which is a good conductor of heat. Thus, the overall heat rejection or adsorption was accounted as a function of internal energy (or enthalpy) inside the closed chamber. The change in enthalpy was identified by the respective sensor mounted inside and the value of total enthalpy was calculated independently at each pressure point from ambient to 7 bar. First, the total enthalpy of the chamber was measured under blank conditions by only purging atmospheric air into it. A regular increase in enthalpy was monitored with increasing air pressure as a consequence of air particle (mostly the airborne moisture) accumulation inside the

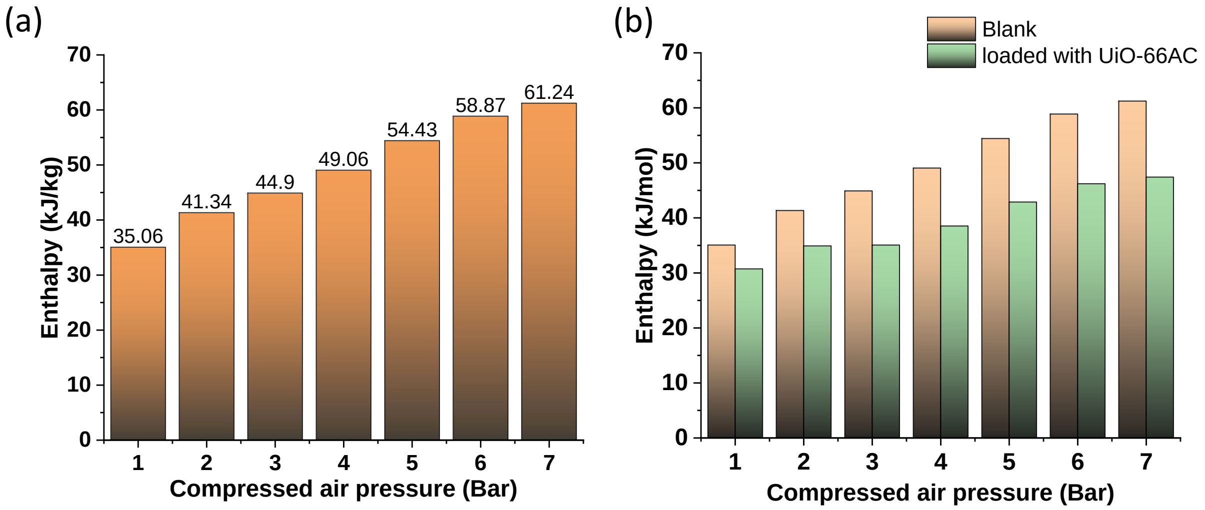

Figure 8: The accounted total enthalpy inside the chamber under (a) blank condition and (b) with loading ~3 g of activated UiO-66M@AC-10.

closed chamber (Figure 8a). The value rises significantly from 35.06 to 61.24 kJkg^{-1} as dosing pressure intensifies from ambient to 7 bar. Similar experiments were performed by loading UiO-66M@AC-10 in the chamber during moisture sorption and enthalpies were compared with the enthalpies measured with no loading. A substantial decrease in total enthalpy was observed even under ambient conditions and regularly increased with a rise in the air-pressure. At 7 bars, the maximum enthalpy change (ΔH) was found to be 13.84 kJkg^{-1} with a total enthalpy value of 47.4 kJkg^{-1} (Figure 8b). Nevertheless, as it has been understood, two contradictory factors worked together; (i) as the air particles were flushed inside the chamber, the large number of particles are agglomerated in one confined place, and the random collisions among the particle enhance the total enthalpy of the system, (ii) in presence of the adsorbent, water molecules get adsorbed and as the adsorption is an exothermic process it will release energy in form of heat to the surroundings (i.e., inside the chamber). Here, the former factor surpassed the second one and the observed drop in enthalpy is found because of the plunge in collision density as an outcome of the higher amount of moisture sorption by the composite. Moreover, the isosteric heat of adsorption for UiO-66 was not too high and the estimated average value is around 41.3 kJmol^{-1}.[19b] However, if the device could be improved to completely thermally insulative, such a drop in enthalpy might be translated to cooling. However, as the moisture sorption was performed under high

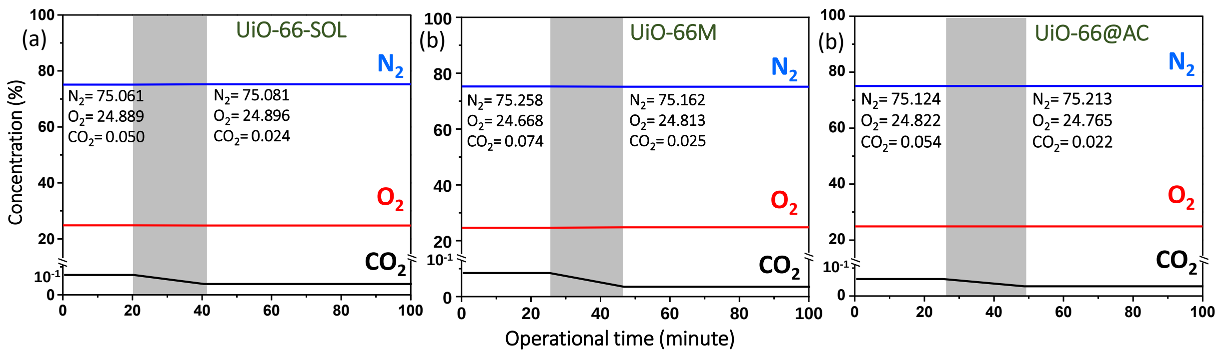

Figure 9: Direct air capture by (a) UiO-66-SOL, (b) UiO-66M and (c) UiO-66@AC-10 under 7 bar compressed air pressure, analyzed by GC at before and after atmospheric moisture adsorption by the materials.

pressure, the outlet release of air with a pressure drop will further amplify the cooling phenomena as an influence of the J-T(Joule-Thompson) expansion principle.[32]

4.2.3.3: Direct carbon capture from compressed air

Recently, direct air capture (DAC) of CO_2 by physisorption has attracted immense attention because of its potential from sequestering atmospheric CO_2 even under humid conditions.[33] Few benchmark MOF materials have been tested and many of them exhibited promising sorption of moist CO_2 by unaffecting structural integrity and native porosity.[34] Fortunately, UiO-66 has been considered as one of them and at 49% humidity (at 1 atm) it showed 0.36Lkg^{-1} uptake capacity of CO_2. With decreasing atmospheric pressure (at 0.15 atm), the uptake value increase to 4.28 Lkg^{-1} even with an improved relative humidity of 75%.[34b] DAC remains challenging under the ambient condition as a result of trace CO_2 concentration and high water vapor pressure. The accumulation of air through compression could also enhance the local CO_2 concertation in the enclosure chamber and that might help to improve the CO_2 adsorption capacity of the adsorbents. To understand the released air quality by dehumidifier chamber, the relative concentration of N_2, O_2 and CO_2 has been tested before measurement and after saturation of the material. The relative decrease in CO_2 concentrations was found to be 52, 66.2 and 59.3% for UiO-66-SOL, UiO-66M and UiO-66M@AC-10, respectively. The outlet air concentrations were tested by gas chromatographic technique and the measured values are showed in Figure 9 at 7 bar compressed air pressure. In this contribution, one could address how atmospheric moisture impacts two aspects of significant practical consideration with respect to DAC, in particular, and carbon capture, in overall the conflict between water vapor and CO_2 in atmospheric air even in the high-pressure environment.

4.2.4: Conclusion

In conclusion, ultra-hydrophilic nano-MOF composites have been synthesized by the synergistic effect of microwave stimuli and AC-template support. This work demonstrates that AC can act as an efficient template to assist the growth of UiO-66 nanoparticles. The additional mesopores generated at the MOF-clay interfaces provides additional space for water storage at higher relative humidity. Inspired by this observation, for the first time, a high-pressure moisture trapping device was fabricated that allows water vapor sorption far beyond atmospheric pressure using MOF (UiO-66-SOL and UiO-66M) and MOF-composites (UiO-66M@AC-10). A substantial increase in moisture sorption (as high as 5.42 $gg^{-1}m^{-3}$) is achieved at ~7 bar compressed air pressure for composite. This result is 44% higher in moisture sorption compared to current commercial desiccants (3.76 $gg^{-1}m^{-3}$; activated alumina). Furthermore, based on remarkably high moisture storage and fast sorption kinetics of MOFs under compressed air pressure, one could pave the way for the fabrication of MOF-composites for widespread application of moisture capture far beyond arid, semi-arid and atmospheric conditions. Finally, a proof-of-concept MOF-based high-pressure moisture trapping prototype was built to validate the viability of these approaches to offer *dry-cool-clean* air to maintain sustainable indoor weather quality.

4.2.5: References

[1] a) W. SIMPSON, *Science* **1983**, *220*, 1226-1226; b) T. Mimura, S. Shimojo, T. Suda, M. Iijima and S. Mitsuoka, *Energy Convers. Manag.* **1995**, *36*, 397-400; c) S. Carley and D. M. Konisky, *Nat. Energy* **2020**.
[2] a) L. Pérez-Lombard, J. Ortiz and C. Pout, *Energy and Buildings* **2008**, *40*, 394-398; b) P. Nejat, F. Jomehzadeh, M. M. Taheri, M. Gohari and M. Z. Abd. Majid, *Renew. Sustain. Energy Rev.* **2015**, *43*, 843-862; c) A. L. Webb, *Renew. Sustain. Energy Rev.* **2017**, *77*, 748-759.
[3] a) B. Tashtoush, M. Molhim and M. Al-Rousan, *Energy* **2005**, *30*, 1729-1745; b) A. P. Raman, M. A. Anoma, L. Zhu, E. Rephaeli and S. Fan, *Nature* **2014**, *515*, 540-544; c) K. Lundgren-Kownacki, E. D. Hornyanszky, T. A. Chu, J. A. Olsson and P. Becker, *Int. J. Biometeorol.* **2018**, *62*, 401-412; d) C. Jia, C. Chen, R. Mi, T. Li, J. Dai, Z. Yang, Y. Pei, S. He, H. Bian, S.-H. Jang, J. Y. Zhu, B. Yang and L. Hu, *ACS Nano* **2019**, *13*, 9993-10001; e) T. Li,

M. Zhu, Z. Yang, J. Song, J. Dai, Y. Yao, W. Luo, G. Pastel, B. Yang and L. Hu, *Adv. Energy Mater.* **2016**, *6*, 1601122.
[4] a) S. K. Henninger, H. A. Habib and C. Janiak, *J. Am. Chem. Soc.* **2009**, *131*, 2776-2777; b) W. Wang, L. Wu, Z. Li, Y. Fang, J. Ding and J. Xiao, *Dry. Technol.* **2013**, *31*, 1334-1345.
[5] M. Sahlot and S. B. Riffat, *Int. J. Low-Carbon Technol.* **2016**, *11*, 489-505.
[6] S. M. Towsif Abtab, D. Alezi, P. M. Bhatt, A. Shkurenko, Y. Belmabkhout, H. Aggarwal, Ł. J. Weseliński, N. Alsadun, U. Samin, M. N. Hedhili and M. Eddaoudi, *Chem* **2018**, *4*, 94-105.
[7] a) E.-P. Ng and S. Mintova, *Micropor. Mesopor. Mater.* **2008**, *114*, 1-26; b) S. Kittaka, S. Ishimaru, M. Kuranishi, T. Matsuda and T. Yamaguchi, *Phys. Chem. Chem. Phys.* **2006**, *8*, 3223-3231; c) R. B. Derr, *Ind. Eng. Chem.* **1938**, *30*, 384-388.
[8] a) H.-C. J. Zhou and S. Kitagawa, *Chem. Soc. Rev.* **2014**, *43*, 5415-5418; b) C. A. Trickett, A. Helal, B. A. Al-Maythalony, Z. H. Yamani, K. E. Cordova and O. M. Yaghi, *Nat. Rev. Mater.* **2017**, *2*, 17045; c) H. Wang, Q.-L. Zhu, R. Zou and Q. Xu, *Chem* **2017**, *2*, 52-80; d) H. Furukawa, K. E. Cordova, M. O'Keeffe and O. M. Yaghi, *Science* **2013**, *341*, 1230444; e) *Chem. Rev.* **2012**, *112*, 673-674; f) S. Roy, S. Laha and T. K. Maji in *10 - Potential of hydrophobic metal-organic framework-based materials for environmental applications*, (Ed. S. K. Ghosh), Elsevier, **2019**, pp. 319-354; g) D. Samanta, S. Roy, R. Sasmal, N. D. Saha, P. K R, R. Viswanatha, S. S. Agasti and T. K. Maji, *Angew. Chem., Int. Ed.* **2019**, *58*, 5008-5012; h) S. Roy, A. Chakraborty and T. K. Maji, *Coord. Chem. Rev.* **2014**, *273-274*, 139-164; i) A. Hazra, S. Jana, S. Bonakala, S. Balasubramanian and T. K. Maji, *Chem. Commun.* **2017**, *53*, 4907-4910.
[9] a) N. C. Burtch, I. M. Walton, J. T. Hungerford, C. R. Morelock, Y. Jiao, J. Heinen, Y.-S. Chen, A. A. Yakovenko, W. Xu, D. Dubbeldam and K. S. Walton, *Nat. Chem.* **2020**, *12*, 186-192; b) C. Wang, X. Liu, N. Keser Demir, J. P. Chen and K. Li, *Chem. Soc. Rev.* **2016**, *45*, 5107-5134; c) N. C. Burtch, H. Jasuja and K. S. Walton, *Chem. Rev.* **2014**, *114*, 10575-10612.
[10] a) S. Cui, M. Qin, A. Marandi, V. Steggles, S. Wang, X. Feng, F. Nouar and C. Serre, *Sci. Rep.* **2018**, *8*, 15284; b) M. F. de Lange, K. J. F. M. Verouden, T. J. H. Vlugt, J. Gascon and F. Kapteijn, *Chem. Rev.* **2015**, *115*, 12205-12250; c) S. K. Henninger, F. Jeremias, H. Kummer and C. Janiak, *Eur. J. Inorg. Chem.* **2012**, *2012*, 2625-2634.
[11] a) R. G. AbdulHalim, P. M. Bhatt, Y. Belmabkhout, A. Shkurenko, K. Adil, L. J. Barbour and M. Eddaoudi, *J. Am. Chem. Soc.* **2017**, *139*, 10715-10722; b) D. Ma, P. Li, X. Duan, J. Li, P. Shao, Z. Lang, L. Bao, Y. Zhang, Z. Lin and B. Wang, *Angew. Chem., Int. Ed.* **2020**, *59*, 3905-3909; c) M. Qin, P. Hou, Z. Wu and J. Wang, *Build Environ.* **2020**, *169*, 106581; d) P. K. Tsobnang, E. Hastürk, D. Fröhlich, E. Wenger, P. Durand, J. L. Ngolui, C. Lecomte and C. Janiak, *Cryst. Growth Des.* **2019**, *19*, 2869-2880.
[12] P. Guo, A. G. Wong-Foy and A. J. Matzger, *Langmuir* **2014**, *30*, 1921-1925.
[13] H. Furukawa, F. Gándara, Y.-B. Zhang, J. Jiang, W. L. Queen, M. R. Hudson and O. M. Yaghi, *J. Am. Chem. Soc.* **2014**, *136*, 4369-4381.
[14] a) H. Kim, S. Yang, S. R. Rao, S. Narayanan, E. A. Kapustin, H. Furukawa, A. S. Umans, O. M. Yaghi and E. N. Wang, *Science* **2017**, *356*, 430; b) H. Kim, S. R. Rao, E. A. Kapustin, L. Zhao, S. Yang, O. M. Yaghi and E. N. Wang, *Nat. Commun.* **2018**, *9*, 1191; c) F. Fathieh, M. J. Kalmutzki, E. A. Kapustin, P. J. Waller, J. Yang and O. M. Yaghi, *Science Advances* **2018**, *4*, eaat3198; d) N. Hanikel, M. S. Prévot, F. Fathieh, E. A. Kapustin, H. Lyu, H. Wang, N. J. Diercks, T. G. Glover and O. M. Yaghi, *ACS Cent. Sci.* **2019**, *5*, 1699-1706; e) J. Xu, T. Li, J. Chao, S. Wu, T. Yan, W. Li, B. Cao and R. Wang, *Angew. Chem., Int. Ed.* **2020**, *59*, 5202-5210; f) N. Hanikel, M. S. Prévot and O. M. Yaghi, *Nat. Nanotech.* **2020**, *15*, 348-355; g) M.

J. Kalmutzki, C. S. Diercks and O. M. Yaghi, *Adv. Mater.* **2018**, *30*, 1704304; h) Y. Tu, R. Wang, Y. Zhang and J. Wang, *Joule* **2018**, *2*, 1452-1475; i) M. W. Logan, S. Langevin and Z. Xia, *Sci. Rep.* **2020**, *10*, 1492.

[15] a) Y. Byun, S. H. Je, S. N. Talapaneni and A. Coskun, *Chem. Euro. J.* **2019**, *25*, 10262-10283; b) J. Canivet, A. Fateeva, Y. Guo, B. Coasne and D. Farrusseng, *Chem. Soc. Rev.* **2014**, *43*, 5594-5617; c) S.-Y. Zhang, S. Jensen, K. Tan, L. Wojtas, M. Roveto, J. Cure, T. Thonhauser, Y. J. Chabal and M. J. Zaworotko, *J. Am. Chem. Soc.* **2018**, *140*, 12545-12552; d) M. Mon, F. Lloret, J. Ferrando-Soria, C. Martí-Gastaldo, D. Armentano and E. Pardo, *Angew. Chem., Int. Ed.* **2016**, *55*, 11167-11172; e) A. J. Rieth, S. Yang, E. N. Wang and M. Dincă, *ACS Cent. Sci.* **2017**, *3*, 668-672; f) F. Jeremias, A. Khutia, S. K. Henninger and C. Janiak, *J. Mater.Chem. A.* **2012**, *22*, 10148-10151.

[16] a) P. Deria, D. A. Gómez-Gualdrón, W. Bury, H. T. Schaef, T. C. Wang, P. K. Thallapally, A. A. Sarjeant, R. Q. Snurr, J. T. Hupp and O. K. Farha, *J. Am. Chem. Soc.* **2015**, *137*, 13183-13190; b) V. Guillerm, F. Ragon, M. Dan-Hardi, T. Devic, M. Vishnuvarthan, B. Campo, A. Vimont, G. Clet, Q. Yang, G. Maurin, G. Férey, A. Vittadini, S. Gross and C. Serre, *Angew. Chem., Int. Ed.* **2012**, *51*, 9267-9271.

[17] a) J. H. Cavka, S. Jakobsen, U. Olsbye, N. Guillou, C. Lamberti, S. Bordiga and K. P. Lillerud, *J. Am. Chem. Soc.* **2008**, *130*, 13850-13851; b) M. Kandiah, M. H. Nilsen, S. Usseglio, S. Jakobsen, U. Olsbye, M. Tilset, C. Larabi, E. A. Quadrelli, F. Bonino and K. P. Lillerud, *Chem. Mater.* **2010**, *22*, 6632-6640; c) Q. Yang, A. D. Wiersum, P. L. Llewellyn, V. Guillerm, C. Serre and G. Maurin, *Chem. Commun.* **2011**, *47*, 9603-9605; d) S. Chavan, J. G. Vitillo, D. Gianolio, O. Zavorotynska, B. Civalleri, S. Jakobsen, M. H. Nilsen, L. Valenzano, C. Lamberti, K. P. Lillerud and S. Bordiga, *Phys. Chem. Chem. Phys.* **2012**, *14*, 1614-1626.

[18] a) M. I. Hossain and T. G. Glover, *Ind. Eng. Chem. Res.* **2019**, *58*, 10550-10558; b) J. Canivet, J. Bonnefoy, C. Daniel, A. Legrand, B. Coasne and D. Farrusseng, *New J. Chem.* **2014**, *38*, 3102-3111; c) P. M. Schoenecker, C. G. Carson, H. Jasuja, C. J. J. Flemming and K. S. Walton, *Ind. Eng. Chem. Res.* **2012**, *51*, 6513-6519.

[19] a) J. H. Cavka, C. A. Grande, G. Mondino and R. Blom, *Industrial & Engineering Chemistry Research* **2014**, *53*, 15500-15507; b) F. Jeremias, V. Lozan, S. K. Henninger and C. Janiak, *Dalton Trans.* **2013**, *42*, 15967-15973; c) Q. Yang , H. Jobic, F. Salles, D. Kolokolov , V. Guillerm, C. Serre and G. Maurin, *Chem. Euro. J* **2011**, *17*, 8882-8889.

[20] A. Chakraborty, P. Sutar, P. Yadav, M. Eswaramoorthy and T. K. Maji, *Inorg. Chem.* **2018**, *57*, 14480-14483.

[21] a) A. Chakraborty, A. Achari, M. Eswaramoorthy and T. K. Maji, *Chem. Commun.* **2016**, *52*, 11378-11381; b) A. Chakraborty, S. Roy, M. Eswaramoorthy and T. K. Maji, *J. Mater. Chem. A* **2017**, *5*, 8423-8430; c) A. Chakraborty, S. Laha, K. Kamali, C. Narayana, M. Eswaramoorthy and T. K. Maji, *Inorg. Chem.* **2017**, *56*, 9426-9435.

[22] R. Kumar, K. Jayaramulu, T. K. Maji and C. N. R. Rao, *Chem. Commun.* **2013**, *49*, 4947-4949.

[23] R. Kumar, K. Jayaramulu, T. K. Maji and C. N. R. Rao, *Dalton Trans.* **2014**, *43*, 7383-7386.

[24] a) J. E. Martin, A. J. Patil, M. F. Butler and S. Mann, *Adv. Func. Mater.* **2011**, *21*, 674-681; b) K. K. R. Datta, C. Kulkarni and M. Eswaramoorthy, *Chem. Commun.* **2010**, *46*, 616-618; c) K. V. Rao, K. K. R. Datta, M. Eswaramoorthy and S. J. George, *Angew. Chem., Int. Ed.* **2011**, *50*, 1179-1184; d) K. K. R. Datta, A. Achari and M. Eswaramoorthy, *J. Mater. Chem. A.* **2013**, *1*, 6707-6718.

[25] A. J. Patil, E. Muthusamy and S. Mann, *Angew. Chem., Int. Ed.* **2004**, *43*, 4928-4933.

[26] Y. Li, Y. Liu, W. Gao, L. Zhang, W. Liu, J. Lu, Z. Wang and Y.-J. Deng, *CrystEngComm* **2014**, *16*, 7037-7042.
[27] K. A. S. Usman, J. W. Maina, S. Seyedin, M. T. Conato, L. M. Payawan, L. F. Dumée and J. M. Razal, *NPG Asia Materials* **2020**, *12*, 58.
[28] K. S. W. Sing, **1985**, *57*, 603-619.
[29] P. Ghosh, Y. J. Colón and R. Q. Snurr, *Chem. Commun.* **2014**, *50*, 11329-11331.
[30] A. S. o. Heating, Refrigerating, A.-C. Engineers and A. N. S. Institute, *Ventilation for acceptable indoor air quality*, American Society of Heating, Refrigerating and Air-Conditioning Engineers, **2001**, p.
[31] Y. Zhang, L. Wu, X. Wang, J. Yu and B. Ding, *Nat. Commun.* **2020**, *11*, 3302.
[32] a) J. R. Roebuck, *Proc. Amer. Acad. Arts Sci.* **1925**, *60*, 537-596; b) H. N. Davis, *Proc. Amer. Acad. Arts Sci.* **1910**, *45*, 243-264.
[33] a) X. Shi, H. Xiao, H. Azarabadi, J. Song, X. Wu, X. Chen and K. S. Lackner, *Angewandte Chemie International Edition* **2020**, *59*, 6984-7006; b) E. S. Sanz-Pérez, C. R. Murdock, S. A. Didas and C. W. Jones, *Chemical Reviews* **2016**, *116*, 11840-11876.
[34] a) A. Kumar, D. G. Madden, M. Lusi, K.-J. Chen, E. A. Daniels, T. Curtin, J. J. Perry Iv and M. J. Zaworotko, *Angew. Chem., Int. Ed.* **2015**, *54*, 14372-14377; b) D. G. Madden, H. S. Scott, A. Kumar, K.-J. Chen, R. Sanii, A. Bajpai, M. Lusi, T. Curtin, J. J. Perry and M. J. Zaworotko, *Phil. Trans. R. Soc.* A. **2017**, *375*, 20160025.

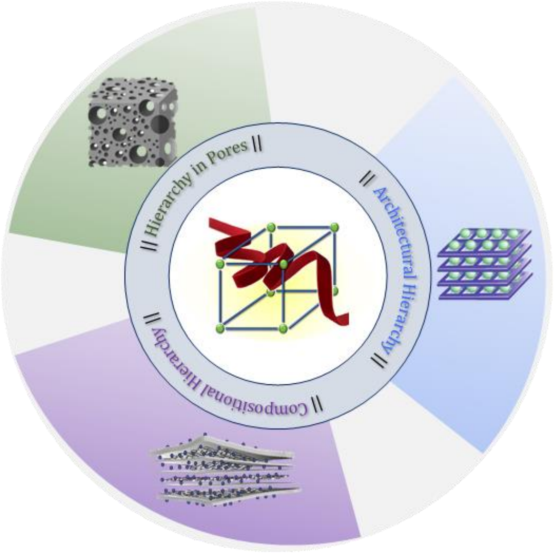

Chapter 5

Summary and Future Outlook

In the very first chapter i.e., the introduction of the thesis, the evolution of MOFs over the year has been portrayed from its synthesis, application and structural point of view. Such diversity affords MOFs to encompass a horizon of real applications from storage, separation, sensing to drug delivery, catalysis and various energy-environmental requisition. Chapter 1 categorizes hierarchy in MOFs in three major segments (i) Hierarchy in pores, (ii) Architectural hierarchy and (iii) Compositional hierarchy. The distribution of chapters across the thesis maintains the same rhythm as chapter 2 deals with 'MOFs with hierarchical porosity' where hierarchical pores are generated by adjusting synthetic conditions of intrinsically microporous MOFs. While, chapter 3 deals with rigid or dynamic frameworks for industrially important hydrocarbon separation and chapter 4 consists of the fabrication of MOF@composites for a verity of water-related applications that are entitled as 'Water-energy nexus: storage, harvesting and dehumidification', correspondingly (Scheme 1).

The second chapter assembles the novel strategies for designing hierarchical micro-mesoporous MOFs. This chapter primarily focused on creating additional mesoporosity by modulating reaction condition with the assistance of microwave heating. It provides a mechanistic understanding for generating structural bimodality in one case by providing perturbation in the system through stirring and in another case by using the solvent mixture as a cluster for breeding mesoscopic void. Nevertheless, the work only reveals the mechanism of pore engineering and the storage of nanoscale molecule in mesopore. However, these materials may perform in the province of catalysis, energy transfer, ion-transport, drug loading and delivery due to bigger pore and high mass transfer kinetics.

The main components for manufacturing fossil fuels, plastics and polymers are hydrocarbons. They are composed of carbon and hydrogen, derived from coal, petroleum (crude oil) and natural gas. In a recent *nature* article, Lively and Sholl listed out seven chemical separations including olefin/paraffin/alkyne, alkane and aromatic isomer separation, which are of great status for affording polymer-grade (>99.9% purity) production of pure raw materials to meet the necessities of downstream refinement. At present, the industry follows traditional separation methodologies such as solvent extraction and cryogenic distillation, predominantly suffer from high-energy intensive, low efficiency with the serious environmental hassle. The third chapter represents the design and synthesis of a dedicated metal-organic framework or porous coordination polymer (and related membrane; mixed matrix membrane) for hydrocarbon separation through a cooperative real-time breakthrough and computational approach. Moreover, it also summarizes the purification performance under gas as well as liquid phase by adopting underlying separation mechanism such as size-dependent molecular sieving, diffusion-based kinetic preferences and enthalpy have driven thermodynamic effect.

The fourth chapter depicts the preparation of MOF@Composites and its implication in higher water storage performance. Customized prototype devices are fabricated with the assistance of such materials, which are further employed for atmospheric moisture harvesting. The first subchapter unfolds the material-cum-device's efficacy for atmospheric water harvesting under all-environment indoor conditions, while the second segment reveals its potency towards clean-cool-dry air vindication. From the

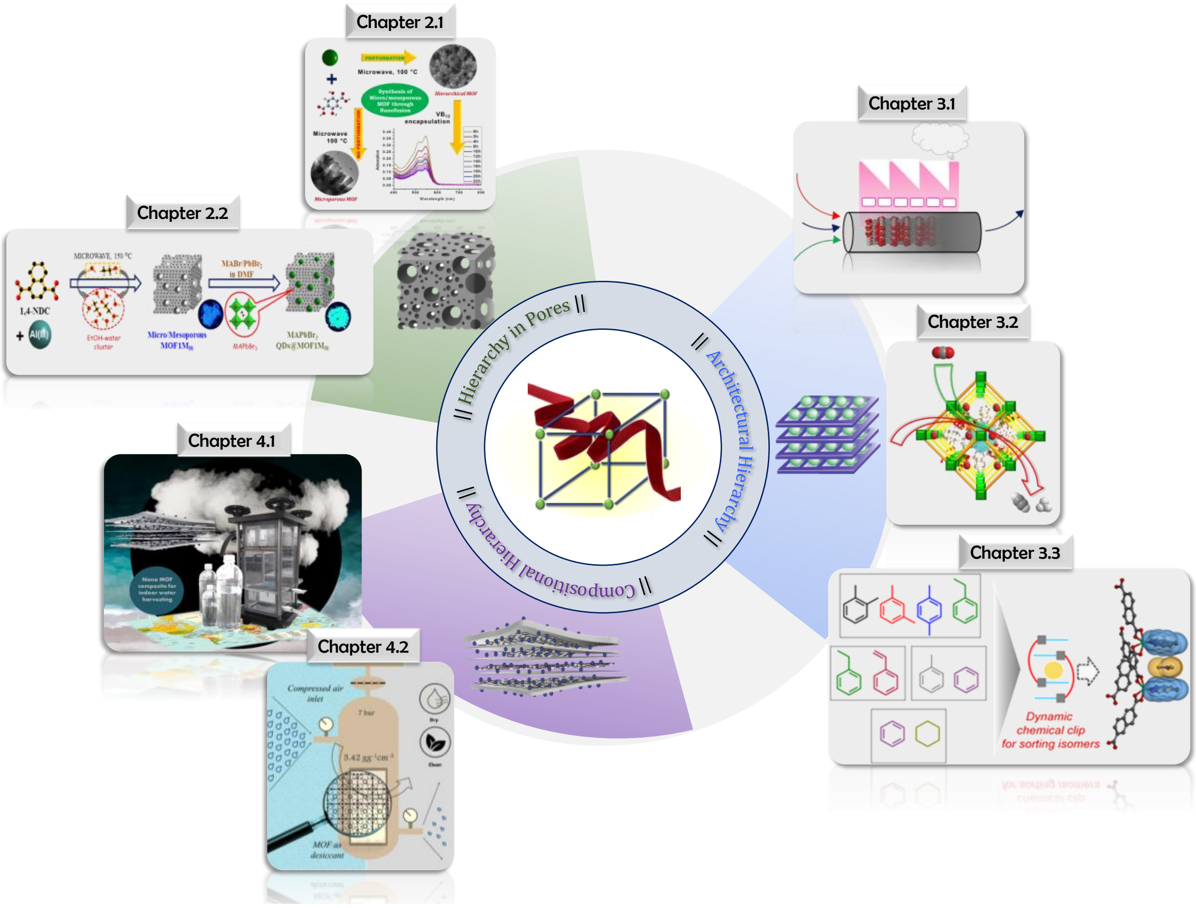

Scheme 1: Thesis at a glance; Summarizing the overall work of all chapters.

perspective of future endeavour, another application that has not been explored in this chapter but could be an offshoot of excellent water sustainability of such materials may exhibit profound photo or electrocatalytic application in atmospheric CO_2 reduction or to generate clean fuels (H_2 as an example) *via* water splitting.

List of Publications

❖ Articles

1. **S. Laha**, A. Chakraborty, T. K. Maji. Synergistic Role of Microwave and Perturbation toward Synthesis of Hierarchical Porous MOFs with Tunable Porosity. *Inorg. Chem.* 2020, **59**, 6, 3775.
2. **S. Laha**, D. Rambabu, S. Bhattacharyya, T. K. Maji. Modulating Hierarchical Micro/Mesoporosity by a Mixed Solvent Approach in Al-MOF: Stabilization of $MAPbBr_3$ Quantum Dots. *Chem. Eur. J.* 2020, **26**, 14671.
3. **S. Laha**, R. Haldar, N. Dwarkanath, S. Bonakala, A. Sharma, A. Hazra, S. Balasubramanian, T. K. Maji. A Dynamic Chemical Clip in Supramolecular Framework for Sorting Alkylaromatic Isomers using Thermodynamic and Kinetic Preferences. *Angew. Chem. Int. Ed.,* 2021, **60**, 2.
4. **S. Laha**, T. K. Maji. A Ternary MOF Nanocomposite for Adequate Multi-environment Indoor Water Harvesting. (*Manuscript to be submitted*).
5. **S. Laha**, N. Dwarkanath, A. Sharma, D. Rambabu, S. Balasubramanian, T. K. Maji. Highly Selective Multicomponent Hydrocarbon Separation with a Tailor-made Al-MOF. (*Manuscript under preparation*).
6. **S. Laha**, S. Dias, V. R. Bakuru, V. Pulinkuzhi, A. Dey, Y. Pandit, T. K. Maji. Metal-Organic Framework as Next-Generation Dehumidifier Desiccant for Compressed Air Dryer. (*Manuscript under preparation*).
7. **S. Laha**, N. Sikdar, R. Jena, T. K. Maji. An Adsorbate Biased Dynamic 3D Porous Framework for Inverse CO_2 Sieving over C_2H_2. (*Manuscript under preparation*).
8. A. Chakraborty, **S. Laha**, K. Kamali, C. Narayana, M. Eswaramoorthy, T. K. Maji. In Situ Growth of Self-Assembled ZIF-8—Aminoclay Nanocomposites with Enhanced Surface Area and CO_2 Uptake. *Inorg. Chem.* 2017, **56**, 16, 9426.
9. A. Singh, P. Verma, **S. Laha**, D. Samanta, S. Roy, T. K. Maji. Photochromic Conjugated Microporous Polymer Manifesting BioInspired pcFRET and Logic Gate Functioning. *ACS Appl. Mater. Interfaces* 2020, **12**, 18, 20991.
10. P. Sutar, V. R. Bakuru, P. Yadav, **S. Laha**, S. Kalidindi, T. K. Maji. Nanocomposite Hydrogel of Pd@ZIF-8 and Laponite®: Size-Selective Hydrogenation Catalyst under Mild Conditions. *Chem. Eur. J.* 2021, **27** 10, 3268.
11. S. Roy, V. M. Suresh, A. Hazra, A. Bandyopadhyay, **S. Laha**, Swapan. K. Pati, T. K. Maji, Solvent-Modulated Emission Properties in a Superhydrophobic Oligo(p-phenyleneethynylene)-Based 3D Porous Supramolecular Framework. *Inorg. Chem.*, 2018, **57**, 8693.

❖ Patents

1. Process for Purification of Hydrocarbons. T. K. Maji, **S. Laha**, R. Haldar. Indian Patent Application Number: 202041001843 (Year 2020); PCT/IN2021/050040.
2. Nanocomposite and implementations thereof. T. K. Maji, **S. Laha**, Indian Patent Application Number: 202041055639 (Year 2020).

❖ Book Chapters

1. S. Roy, **S. Laha**, T. K. Maji, Book Chapter in Potential of Hydrophobic Metal–Organic Framework-based Materials for Environmental Applications, *Elsevier* 2019, Chapter 10, 319.
2. K. P. Sonu, **S. Laha**, M. Eswaramoorthy, T. K. Maji, Book Chapter in Porous Materials: Recent Developments, *World Scientific* 2019, Chapter 7, 148.

Biography

Subhajit Laha obtained his B.Sc. degree from Scottish Church College, Kolkata, University of Calcutta, in 2013. He obtained his master's degree from the Indian Institute of Technology Hyderabad, in 2015. Presently, he is pursuing his Ph.D. under the supervision of Prof. Tapas K. Maji at the Jawaharlal Nehru Centre for Advanced Scientific Research (JNCASR), Bangalore, India. His research work focuses on synthesis and study of metal-organic frameworks and related composites for storage, separation and water harvesting.